



A NONLINEAR DYNAMICS PERSPECTIVE OF WOLFRAM'S NEW KIND OF SCIENCE. PART IV: FROM BERNOULLI SHIFT TO $1/f$ SPECTRUM

LEON O. CHUA, VALERY I. SBITNEV and SOOK YOON
*Department of Electrical Engineering and Computer Sciences,
 University of California at Berkeley,
 Berkeley, CA 94720, USA*

Received August 5, 2004; Revised November 10, 2004

By exploiting the new concepts of CA *characteristic functions* and their associated *attractor time- τ maps*, a *complete* characterization of the long-term time-asymptotic behaviors of all 256 one-dimensional CA rules are achieved via a single “probing” *random* input signal. In particular, the *graphs* of the *time-1 maps* of the 256 CA rules represent, in some sense, the *generalized Green's functions* for Cellular Automata. The asymptotic *dynamical evolution* on any CA *attractor*, or *invariant orbit*, of 206 (out of 256) CA rules can be predicted precisely, by *inspection*. In particular, a total of 112 CA rules are shown to obey a generalized *Bernoulli σ_τ -shift rule*, which involves the *shifting* of any binary string on an attractor, or invariant orbit, either to the *left*, or to the *right*, by *up to 3 pixels*, and followed possibly by a *complementation* of the resulting bit string.

The most intriguing result reported in this paper is the discovery that the four *Turing-universal* rules [\[110\]](#), [\[124\]](#), [\[137\]](#), and [\[193\]](#), and only these rules, exhibit a $1/f$ power spectrum.

Keywords: Cellular neural networks; CNN; cellular automata; Turing machine; universal computation; Green's function; Bernoulli shift; $1/f$ power spectrum; global equivalence classes; CA attractors; invariant orbits; garden of Eden; isle of Eden.

1. Introduction

The basic notations and concepts underlying this tutorial stem from [Chua, 1998; Chua & Roska, 2002] and from Part I [Chua *et al.*, 2002], Part II [Chua *et al.*, 2003], and Part III [Chua *et al.*, 2004]. Throughout this paper we are concerned exclusively with 2-state one-dimensional cellular automata consisting of $I + 1$ cells, $i = 0, 1, 2, \dots, I$ with periodic boundary conditions, as depicted in Fig. 1(a). Each cell i interacts only with its nearest neighbors $i - 1$ and $i + 1$, as depicted in Fig. 1(b). Here u_{i-1} , u_i and u_{i+1} denote the three inputs needed to compute the single output y_i by a three-input nonlinear function

$$y_i = N(u_{i-1}, u_i, u_{i+1}) \quad (1)$$

Boolean computations by this function are executed according to the truth table depicted in Fig. 1(c).

Each of the eight binary bits $\beta_0, \beta_1, \dots, \beta_7$ in the rightmost column of this figure is equal to either 0 or 1. There are 256 distinct combinations of “zeros” and “ones” among the eight binary bits $\beta_0, \beta_1, \dots, \beta_7$, each one defining a unique Boolean function of three binary variables. One-to-one correspondence of each of these 256 Boolean functions with its associated decimal number

$$\boxed{N} = \sum_{k=0}^7 \beta_k 2^k \quad (2)$$

determines a local rule \boxed{N} of the cellular automaton. Each coefficient $\beta_0, \beta_1, \dots, \beta_7$ is uniquely identified, via its coordinates (u_{i-1}, u_i, u_{i+1}) from Fig. 1(d) as a *vertex* of the *Boolean cube* shown in Fig. 1(e). A vertex \textcircled{k} is colored in blue if $\beta_k = 0$ and in red if $\beta_k = 1$. For example, the colored vertices in

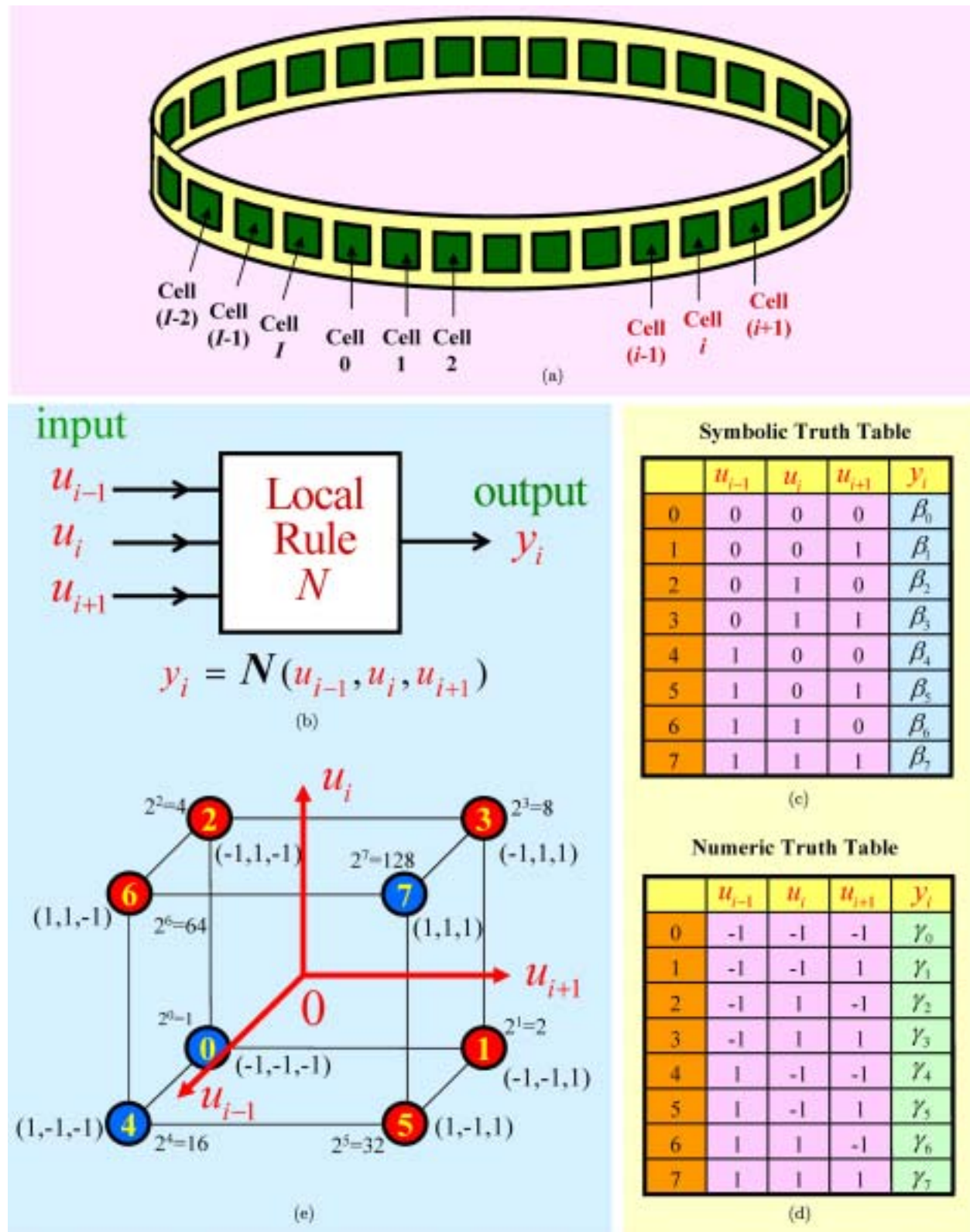


Fig. 1. (a) A one-dimensional Cellular Automata (CA) made of $(I + 1)$ identical cells with a periodic boundary condition. Each cell " i " is coupled only to its left neighbor cell $(i - 1)$ and right neighbor cell $(i + 1)$. (b) Each cell " i " is described by a local rule N , where N is a decimal number specified by a binary string $\{\beta_0, \beta_1, \dots, \beta_7\}$, $\beta_i \in \{0, 1\}$. (c) The symbolic truth table specifying each local rule N , $N = 0, 1, 2, \dots, 255$. (d) By recoding "0" to "-1", each row of the symbolic truth table in (c) can be recast into a numeric truth table, where $\gamma_k \in \{-1, 1\}$. (e) Each row of the numeric truth table in (d) can be represented as a *vertex* of a Boolean Cube whose color is red if $\gamma_k = 1$, and blue if $\gamma_k = -1$.

Fig. 1(e) correspond to the local rule

$$\boxed{N} = 0 \cdot 2^0 + 1 \cdot 2^1 + 1 \cdot 2^2 + 1 \cdot 2^3 + 0 \cdot 2^4 + 1 \cdot 2^5 + 1 \cdot 2^6 + 0 \cdot 2^7 = 110. \quad (3)$$

Depending on the context, each variable u_{i-1}, u_i, u_{i+1} , or y_i may assume a *symbolic* Boolean value “0” or “1”, as depicted in Fig. 1(c), or a *numeric* value, “−1” or “+1”, as depicted in Fig. 1(d). The symbolic and numeric representations are related to each other as follows¹:

$$\boxed{\text{numeric variable}} = 2 \cdot \boxed{\text{Boolean variable}} - 1 \quad (4)$$

$$\boxed{\text{Boolean variable}} = \frac{1}{2} (\boxed{\text{numeric variable}} + 1) \quad (5)$$

In particular, the real variables $\gamma_0, \gamma_1, \dots, \gamma_7$ in Fig. 1(d) are related to the Boolean variables $\beta_0, \beta_1, \dots, \beta_7$ in Fig. 1(c) via the formula

$$\gamma_k = 2\beta_k - 1 \quad (6)$$

Substituting Eq. (6) into Eq. (2), we obtain the following equivalent local rule number

$$\boxed{N} = \frac{1}{2} \left(255 + \sum_{k=0}^7 \gamma_k 2^k \right) \quad (7)$$

1.1. Computing all 256 rules from one CA difference equation

The cellular automaton evolves in discrete time steps $t = 0, 1, 2, \dots$. The output of the i th cell (in numeric representation) can be calculated analytically from the following nonlinear difference equation [Chua *et al.*, 2004] involving eight parameters:

$$\begin{aligned} &\textbf{CA Difference Equation 1: } u_i^t \in \{-1, 1\} \\ &u_i^{t+1} = \text{sgn}\{z_2 + c_2|(z_1 + c_1|(z_0 + b_1 u_{i-1}^t \\ &\quad + b_2 u_i^t + b_3 u_{i+1}^t)|)|)\} \end{aligned} \quad (8)$$

It is indeed remarkable that one equation suffices to define all $2^8 = 256$ Boolean functions of three variables u_{i-1}, u_i , and u_{i+1} by simply specifying eight *real* numbers. Even more remarkable is that the CA Difference equation (8) is *robust* in the sense that the eight parameter values defining each local rule \boxed{N} form a *dense* set. One set of parameters $\{z_2, c_2, z_1, c_1, z_0, b_1, b_2, b_3\}$ for realizing

each one of the 256 local rules is listed in Table 4 of Part II [Chua *et al.*, 2003]. The eight parameters $\{z_2, c_2, z_1, c_1, z_0, b_1, b_2, b_3\}$ in this equation can be used to derive the coefficients β_k in Fig. 1(c), $k = 0, 1, \dots, 7$ via the formula:

$$\beta_k = \frac{1}{2} (1 + \text{sgn}\{z_2 + c_2|(z_1 + c_1|(z_0 + b_1 u_{k,i-1} + b_2 u_{k,i} + b_3 u_{k,i+1})|)|)\}) \quad (9)$$

where the *numeric* coefficients $u_{k,i-1}, u_{k,i}$ and $u_{k,i+1}$ are given by row k of the truth table in Fig. 1(d). The state variables u_{i-1}^t, u_i^t , and u_{i+1}^t in Eq. (8) must be expressed in numeric values −1 and +1.

Since this paper (Part IV) will be devoted exclusively to Boolean variables $x_i \in \{0, 1\}$, it is more convenient to express Eq. (8) in terms of x_i via Eq. (4); namely,

$$\begin{aligned} &\textbf{CA Difference Equation 2: } x_i^t \in \{0, 1\} \\ &x_i^{t+1} = \frac{1}{2} (1 + \text{sgn}\{z'_2 + c_2|(z'_1 + c_1|(z'_0 + b_1 x_{i-1}^t \\ &\quad + b_2 x_i^t + b_3 x_{i+1}^t)|)|)\}) \\ &\text{where } z'_0 \triangleq \frac{1}{2} [z_0 - (b_1 + b_2 + b_3)], \quad z'_1 \triangleq \frac{1}{2} z_1, \\ &\quad z'_2 \triangleq \frac{1}{2} z_2 \end{aligned} \quad (10)$$

2. Mapping Local Rules onto Global Characteristic Functions

Given any local rule \boxed{N} , $N = 0, 1, 2, \dots, 255$, and any binary *initial configuration* (or *initial state* when used in the context of nonlinear dynamics)

$$\vec{\mathbf{x}}(0) = [x_0(0), x_1(0), \dots, x_{I-1}(0), x_I(0)] \quad (11)$$

for a one-dimensional Cellular Automaton with $I+1$ cells [see Fig. 1(a)], where $x_i(0) \in \{0, 1\}$, we can associate uniquely the *Boolean string* $\vec{\mathbf{x}}(0)$ with the *binary expansion* (in base 2) of a *real* number $0 \cdot x_0 x_1 \dots x_{I-1} x_I$ on the *unit interval* $[0, 1]$; namely,

$$\begin{aligned} &\vec{\mathbf{x}} \triangleq [x_0 x_1 \dots x_{I-1} x_I] \\ &\mapsto \phi \triangleq 0 \cdot x_0 x_1 \dots x_{I-1} x_I \end{aligned} \quad (12)$$

¹The Boolean variable is considered as a *real* number in Eqs. (4) and (5), or in any equation involving real-variable (i.e. nonlogic) operations.

where the *decimal* equivalent of Eq. (12) is given by

$$\phi = \sum_{i=0}^I 2^{-(i+1)} x_i \quad (13)$$

We will often need to consider also the *bilateral* image

$$\bar{\mathbf{x}}(0) = [x_I(0), x_{I-1}(0), \dots, x_1(0), x_0(0)] = \mathbf{T}^\dagger(\bar{\mathbf{x}}(0)) \quad (14)$$

henceforth called the *backward Boolean string* associated with the *forward Boolean string* $\bar{\mathbf{x}}$ from Eq. (12), where \mathbf{T}^\dagger is the $(I+1)$ -dimensional *left-right transformation* operator defined in Table 13 of [Chua et al., 2004], namely,

$$\mathbf{T}^\dagger[x_0 x_1 \cdots x_{I-1} x_I] = [x_I x_{I-1} \cdots x_1 x_0] \quad (15)$$

Each backward Boolean string $\bar{\mathbf{x}}$ in Eq. (14) maps into the real number ϕ^\dagger defined by

$$\bar{\mathbf{x}} \mapsto \phi^\dagger \triangleq 0 \bullet x_I x_{I-1} \cdots x_1 x_0 \quad (16)$$

where the decimal equivalent of Eq. (16) is given by

$$\phi^\dagger = \sum_{i=0}^I 2^{-(I+1)+i} x_i \quad (17)$$

where

$$\bar{\mathbf{x}} \triangleq [x_I x_{I-1} \cdots x_1 x_0]$$

2.1. CA characteristic functions

For a one-dimensional CA with $I+1$ cells, there are $n_\Sigma \triangleq 2^{I'}$ distinct Boolean strings, where $I' \triangleq I+1$. Let Σ denote the *state space* made of the collection of all n_Σ Boolean strings. Each local rule \boxed{N} induces a *global map*

$$T_{\boxed{N}} : \Sigma \rightarrow \Sigma \quad (18)$$

where each state $\mathbf{x} \in \Sigma$ is mapped into exactly one state $T_{\boxed{N}}(\mathbf{x}) \in \Sigma$. Since each state $\mathbf{x} \in \Sigma$ corresponds to one, and only one, point $\phi \in [0, 1]$ via Eq. (13), it follows that the global map (18) induces an *equivalent map* $\chi_{\boxed{N}}$ from the set of all *rational* numbers $\mathcal{R}[0, 1]$ over the unit interval $[0, 1]$ into itself; namely,

$$\chi_{\boxed{N}} : \mathcal{R}[0, 1] \rightarrow \mathcal{R}[0, 1] \quad (19)$$

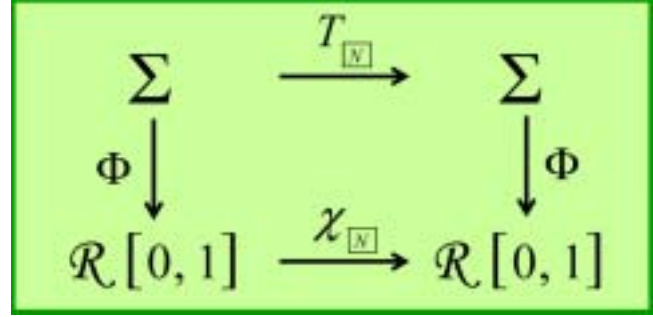


Fig. 2. A commutative diagram establishing a one-to-one correspondence between $T_{\boxed{N}}$ and $\chi_{\boxed{N}}$.

henceforth called the *CA characteristic function* of \boxed{N} . The one-to-one correspondence between the *global map* $T_{\boxed{N}}$ and the *CA characteristic function* $\chi_{\boxed{N}}$ is depicted in the *diagram* shown in Fig. 2, where Φ denotes the transformation of the state $\bar{\mathbf{x}}$ into the *decimal* function defined in Eq. (13). This diagram is said to be *commutative* because

$$\Phi \circ T_{\boxed{N}} = \chi_{\boxed{N}} \circ \Phi \quad (20)$$

where “ \circ ” denotes the *composition* operation.

Observe that in the limit where $I \rightarrow \infty$, the state space Σ coincides with the collection of all bi-infinite strings extending from $-\infty$ to ∞ , and

$$\lim_{I \rightarrow \infty} \mathcal{R}[0, 1] = [0, 1] \quad (21)$$

In this general case, the CA characteristic function $\chi_{\boxed{N}}$ is defined on every point (i.e. *real number*) $\phi \in [0, 1]$, thereby including all *irrational* numbers as well [Niven, 1967].

2.2. Algorithm for plotting the graph of CA characteristic functions

Since the *domain* of the CA characteristic function $\chi_{\boxed{N}}$ of any local rule \boxed{N} (for finite I) consists of a subset of *rational* numbers in the unit interval $[0, 1]$, a computer program for constructing the *graph* of the characteristic function $\chi_{\boxed{N}}$ can be easily written as follow:

Step 1. Divide the unit interval $[0, 1]$ into a finite number of uniformly-spaced points, called a *linear grid*, of width $\Delta\phi$. For the examples in Sec. 2.3, we choose $\Delta\phi = 0.005$.

Step 2. For each grid point $\phi_j \in [0, 1]$, identify the corresponding *binary* string $\mathbf{s}_j \in \Sigma$.

Step 3. Determine the image $\mathbf{s}'_j \in \Sigma$ of \mathbf{s}_j under \boxed{N} , i.e. find $\mathbf{s}'_j = T_{\boxed{N}}(\mathbf{s}_j)$ via the *truth table* of \boxed{N} .

Step 4. Calculate the *decimal* equivalent of s'_j via Eq. (13).

Step 5. Plot a vertical line through the abscissa $\phi_{[N]} = \phi_j$ with height equal to s'_j .

Step 6. Repeat steps 1–5 over all $(1/\Delta\phi) + 1$ grid points. For the examples in Sec. 2.3, there are $(1/0.005) + 1 = 201$ grid points.

For reasons that will be clear later, it is sometimes more revealing to plot the τ th iterated value

$$s_j^\tau = T_{[N]}^\tau(s_j) \triangleq \underbrace{T_{[N]} \circ T_{[N]} \circ \cdots \circ T_{[N]}}_{\tau \text{ times}}(s_j) \quad (22)$$

of s_j , instead of $T_{[N]}(s_j)$, at each grid point $\phi_j \in [0, 1]$. For obvious reasons, such a function is called a *time- τ CA characteristic function* and will henceforth be denoted by $\chi_{[N]}^\tau$. Using this terminology, the *algorithm* presented above can be used to plot the *graph* of the “*time-1*” *CA characteristic function* $\chi_{[N]}^1$ of any local rule $[N]$. The same algorithm applies *mutatis mutandis*, for plotting the *graph* of the *time- τ characteristic function* $\chi_{[N]}^\tau$ as well.

To enhance readability, it is desirable to plot the $M \triangleq (1/\Delta\phi) + 1$ vertical lines of $\chi_{[N]}^\tau$ in alternating red and blue colors, henceforth referred to as red and blue ϕ -coordinates ϕ_{red} and ϕ_{blue} , respectively. The “tip” of each vertical line gives the value of $\chi_{[N]}^\tau$ corresponding to each ϕ coordinate. The system of red and blue lines is defined via the following simple algorithm.

For any I , partition all $(I+1)$ -bit binary strings into a *red group* and a *blue group*. All members of the red group have a “0” as their *rightmost* bit. The *blue group* then consists of all $(I+1)$ -bit binary strings with a “1” as their *rightmost* bit. Each group has therefore exactly *one half* of the total number ($M = 2^{I+1}$) of distinct strings, namely, 2^I .

Since the *end* (rightmost) bit of each $\phi_{\text{blue}} \in [0, 1]$ is equal to a “1”, by construction, it follows that the *largest* value of ϕ_{blue} is greater than the *largest* value of ϕ_{red} by exactly $1/2^{I+1}$. This means that the *rightmost* vertical line must have color blue, and tends to $\phi = 1$ as $I \rightarrow \infty$. The rightmost blue line is, for plotting purpose, drawn through $\phi = 1$. We can then divide the interval $[0, 1]$ into $(1/\Delta\phi) + 1$ grid points, where $\Delta\phi$ is the prescribed resolution. All characteristic functions in Figs. 3–7 are drawn with $\Delta\phi = 0.005$, where a tiny red or blue *square* is drawn around the tip of each vertical line for ease of

identification. In other words, the distance between each red line and its adjacent blue line is equal to 0.005.

Although higher precision can be easily implemented by a computer, the limited printer resolution will cause adjacent red and blue lines to merge through ink diffusion for $\Delta\phi < 0.005$.

To construct Figs. 3–7, we chose $\Delta\phi = 0.005$, $\phi_{\text{start}} = 0.\underbrace{00 \cdots 00}_{65 \text{ "0"s}}1$, and $\phi_{\text{end}} = 0.\underbrace{11 \cdots 11}_{65 \text{ "1"s}}1$.

Our choice leads to exactly 100 *red vertical lines* (located at 0.005, 0.015, 0.025, ..., 0.995, $\Delta_{\text{red}} = 0.01$) with binary base-2 expansion $\phi_{\text{red}} = 0.\beta_1\beta_2\beta_3 \cdots \beta_{65}0$, $\beta_i \in \{0, 1\}$, which interleave with 101 *blue vertical lines* (located at 0.000, 0.01, 0.02, ..., 1.00, $\Delta_{\text{blue}} = 0.01$) with binary base-2 expansion $\phi_{\text{blue}} = 0.\beta'_1\beta'_2\beta'_3 \cdots \beta'_{65}1$, $\beta'_i \in \{0, 1\}$.

The 201 red and blue lines shown in the characteristic functions in Figs. 3–7 represent only their approximate positions on $[0, 1]$ because the resolution of their exact positions is determined by the value of I , which is chosen to be 65 in Figs. 3–7. This means that our state space Σ is “*coarse grain*” and contains only 2^{66} distinct 66-bit binary strings, each one representing a unique rational number on $[0, 1]$, of which only 201 are actually drawn in these figures to avoid clutter. Since an arbitrary rational number on $[0, 1]$ requires an *arbitrarily* large (though finite) value of I for an exact base-2 expansion (i.e. $I \rightarrow \infty$ in Eq. (13)), a *fine grain characteristic function* $\chi_{[N]}^\tau$ which includes all possible rational numbers $\phi \in [0, 1]$ in its domain would be impractical to plot on paper, or even store on any computer memory. However, the characteristic functions (calculated with $I = 65$) shown in Figs. 3 to 7 are adequate for most purposes. Increasing the value of I is equivalent to “sandwiching” more vertical lines in between the existing lines drawn in these figures.

2.3. A glimpse of some time- τ characteristic functions $\chi_{[N]}^\tau$

Let us take a glance at some representative examples of CA characteristic functions. For brevity, we will henceforth refer to “*time-1*” CA characteristic functions simply as “characteristic functions”.

Example 1. $\chi_{[128]}^1$

The graph of the characteristic function $\chi_{[128]}^1$ of $[128]$ is shown in Fig. 3(a). This is among the

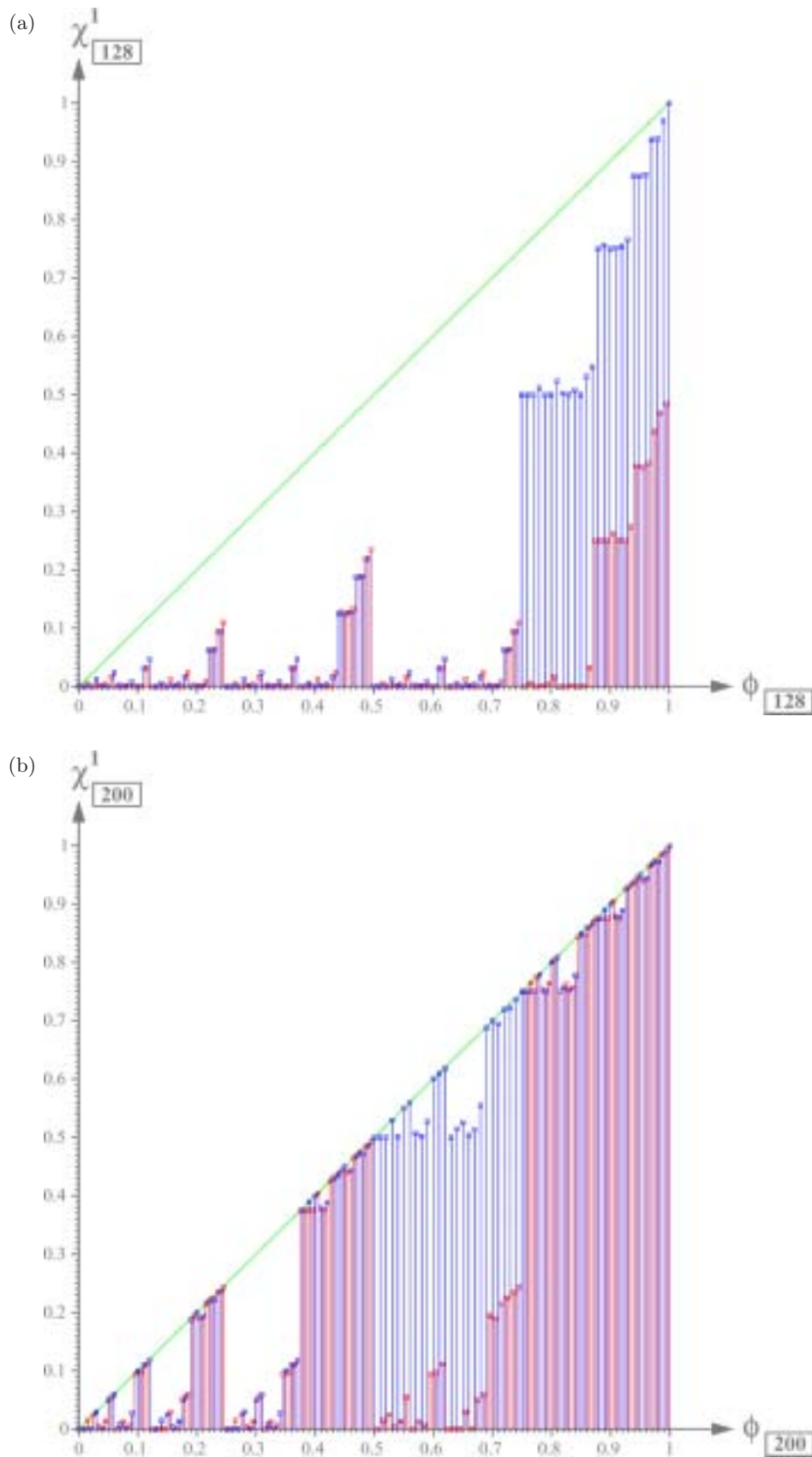


Fig. 3. Time-1 CA characteristic functions χ^1_{128} and χ^1_{200} for local rules 128 and 200 , respectively. Although only 201 points (enclosed by tiny squares) are shown, the abscissa (ϕ coordinate) of each point is calculated with a 66-bit string resolution.

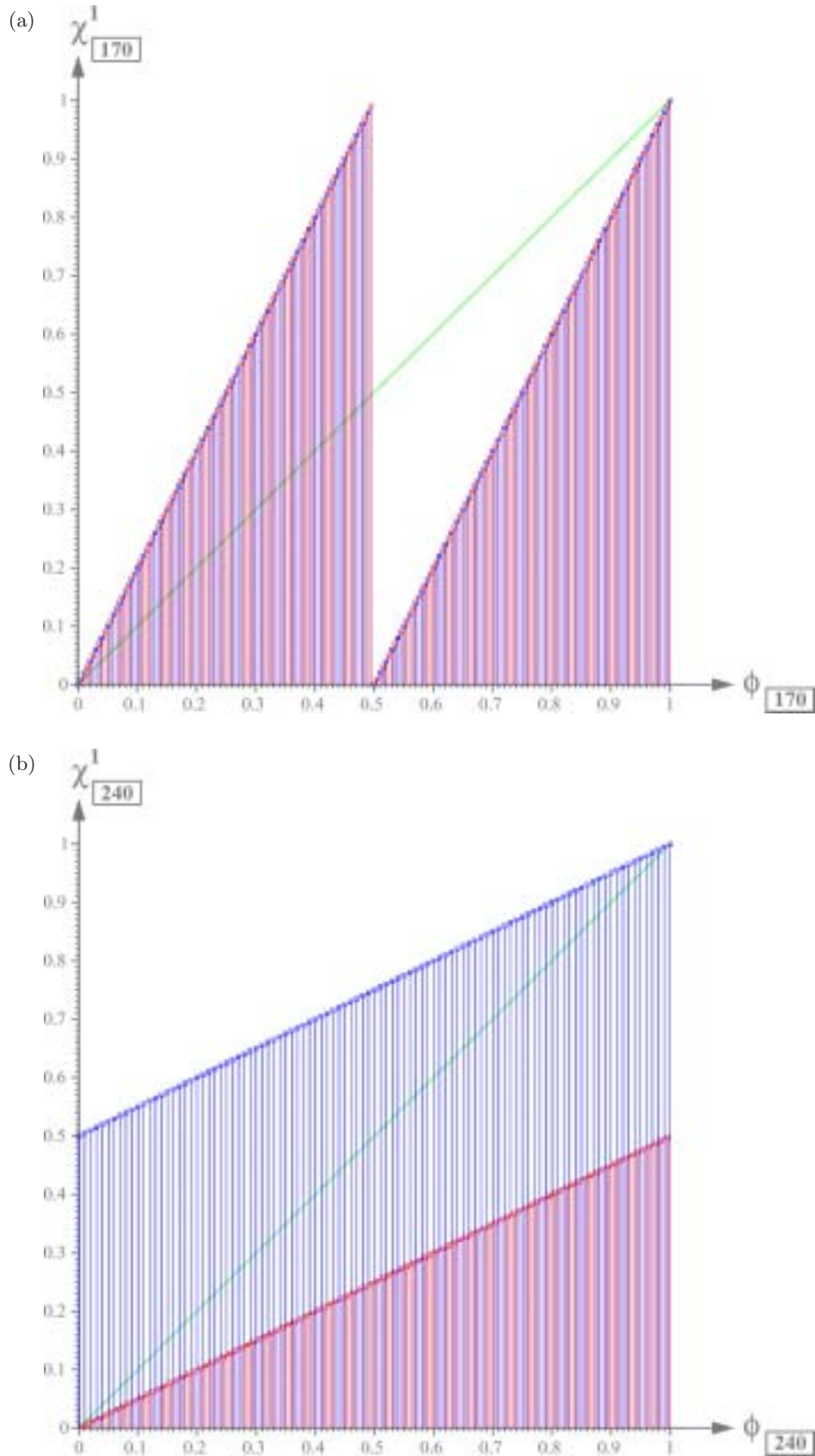


Fig. 4. Time-1 CA characteristic functions χ^1_{170} and χ^1_{240} for local rules 170 and 240 , respectively. Although only 201 points (enclosed by tiny squares) are shown, the abscissa (ϕ coordinate) of each point is calculated with a 66-bit string resolution.

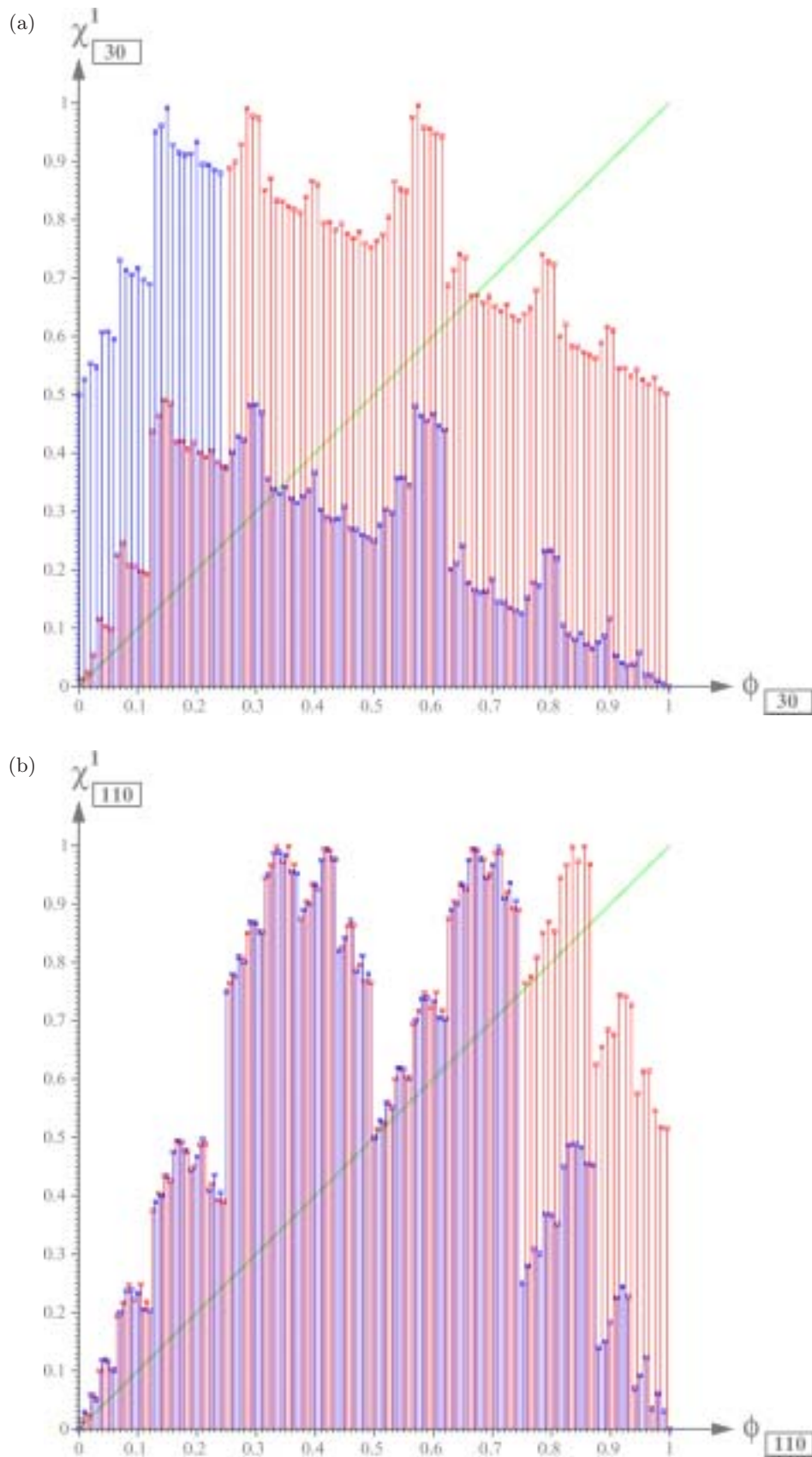


Fig. 5. Time-1 CA characteristic functions χ^1_{30} and χ^1_{110} for local rules 30 and 110, respectively. Although only 201 points (enclosed by tiny squares) are shown, the abscissa (ϕ coordinate) of each point is calculated with a 66-bit string resolution.

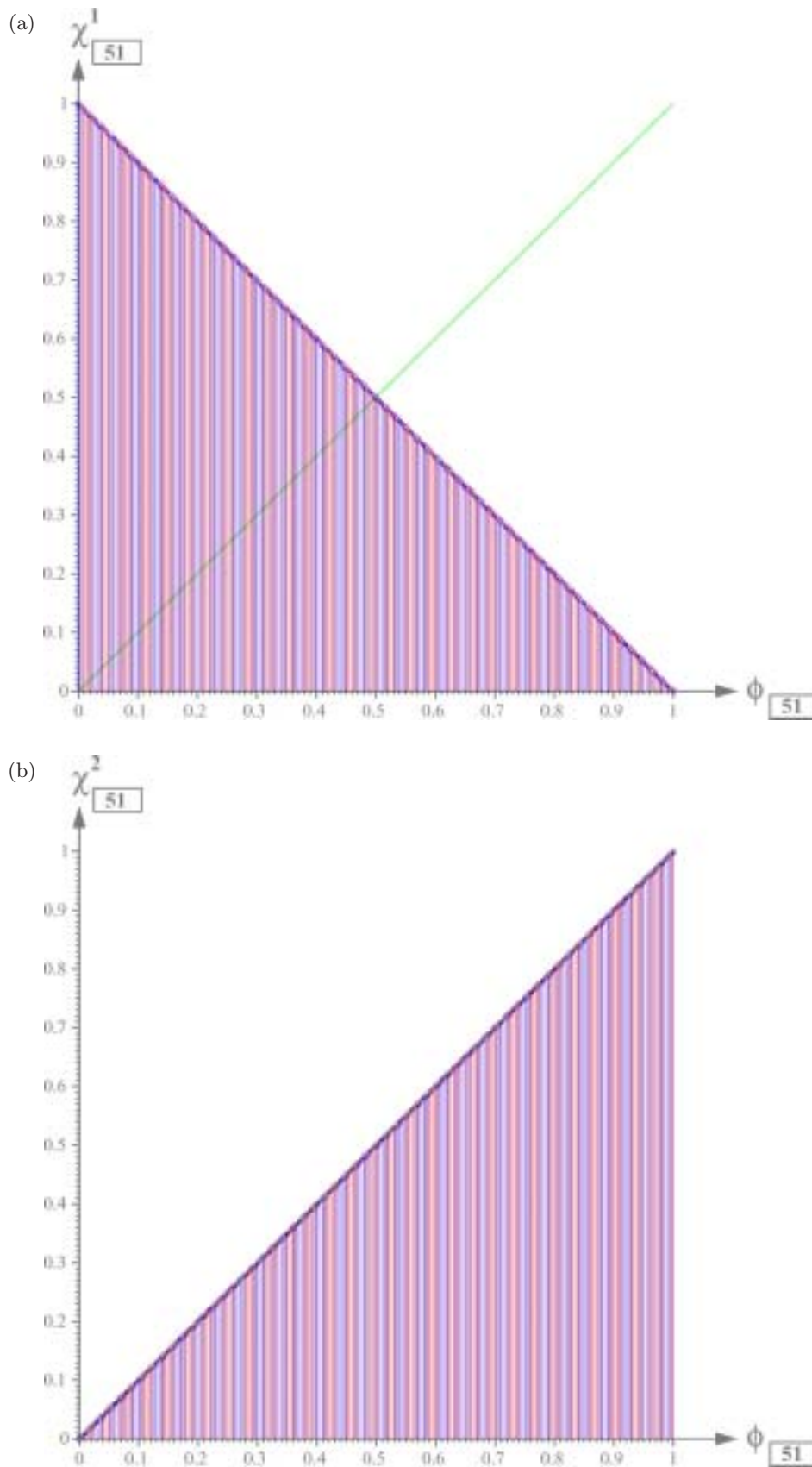


Fig. 6. Time-1 CA characteristic functions χ_{51}^1 and time-2 CA characteristic function χ_{51}^2 for local rule 51. Although only 201 points (enclosed by tiny squares) are shown, the abscissa (ϕ coordinate) of each point is calculated with a 66-bit string resolution.

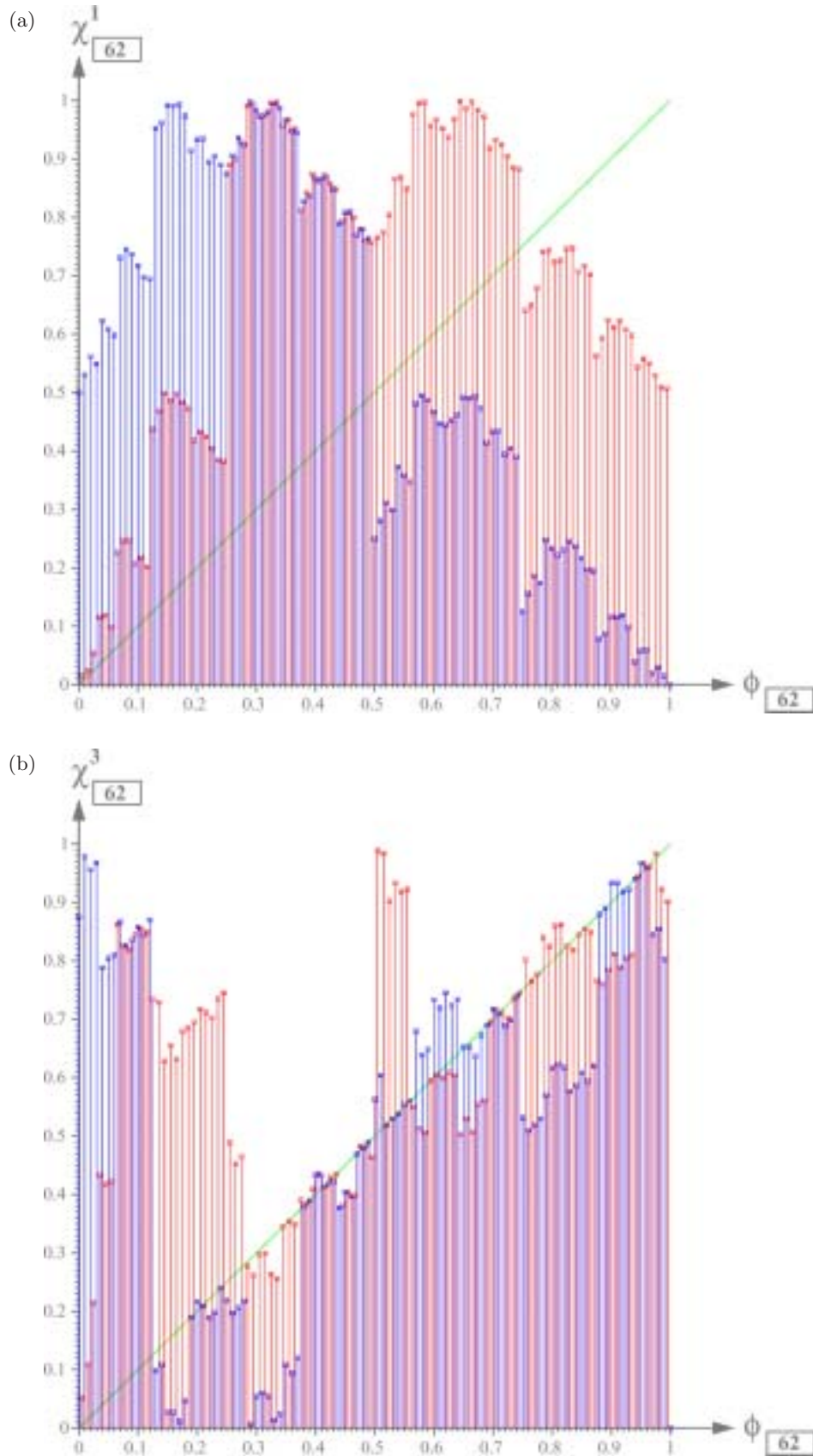


Fig. 7. Time-1 CA characteristic functions χ^1_{62} and time-3 CA characteristic function χ^3_{62} for local rule 62. Although only 201 points (enclosed by tiny squares) are shown, the abscissa (ϕ coordinate) of each point is calculated with a 66-bit string resolution.

simplest characteristic functions. Observe that no vertical lines intersect the *unit-slope* main diagonal except at $\phi_{\boxed{128}} = 0.\overline{00}$ and $\phi_{\boxed{128}} = 1.\overline{00}$ (where the *bar* over a sequence of binary bits denotes repetition of these bits *ad infinitum*). These two *period-1* fixed points give rise to a *homogeneous “0” dynamic pattern* $\mathcal{D}_{\boxed{128}}[0.\overline{00}]$ (homogeneous blue color) in the former, and a *homogeneous “1” dynamic pattern* $\mathcal{D}_{\boxed{128}}[1.\overline{00}]$ (homogeneous red color) in the latter. The *qualitative dynamics* of these two orbits, however, are dramatically different. The orbit from $\mathcal{D}_{\boxed{128}}[0.\overline{00}]$ is an *attractor* in the sense of *nonlinear dynamics* [Alligood *et al.*, 1996] because it has a nonempty *basin of attraction* \mathcal{B}_Λ , which in this case consists of all points in the closed-open unit interval $[0, 1)$.

The orbit from $\phi_{\boxed{128}} = 1.\overline{00}$ is an example of both an *invariant orbit*, and a *Garden of Eden*, to be defined in Sec. 3.

Example 2. $\chi_{\boxed{200}}^1$

The graph of the characteristic function $\chi_{\boxed{200}}^1$ of $\boxed{200}$ is shown in Fig. 3(b). In this case, observe that there are many vertical lines which terminate exactly on the main diagonal. There are therefore many *period-1 fixed points* which imply the presence of many *period-1 attractors*. This is characteristic of local rules belonging to Wolfram's *class 1* rules [Wolfram, 2002]. We will return to this class of attractors in Sec. 3.

Example 3. $\chi_{\boxed{170}}^1$

The graph of the characteristic function $\chi_{\boxed{170}}^1$ of $\boxed{170}$ is shown in Fig. 4(a). Note that there are no period-1 fixed points except at $\phi_{\boxed{170}} = 0.\overline{00}$ and $\phi_{\boxed{170}} = 1.\overline{00}$. Observe also the vertices of all vertical lines fall on one of two parallel lines with slope = 2. This is an example, *par excellence*, of the classic *Bernoulli shift* [Nagashima & Baba, 1999], a subject to be discussed at length in Sec. 5.

Example 4. $\chi_{\boxed{240}}^1$

The graph of the characteristic function $\chi_{\boxed{240}}^1$ of $\boxed{240}$ is shown in Fig. 4(b). There are no period-1 fixed points except at $\phi_{\boxed{240}} = 0.\overline{00}$ and $\phi_{\boxed{240}} = 1.\overline{00}$.² The “double-valued” appearance is only illusory because all red vertical lines terminate on the lower straight lines of slope = 1/2, and all

blue vertical lines terminate on the upper parallel straight lines. Since the blue and red vertical lines interleave but do not intersect each other, $\chi_{\boxed{240}}^1$ is a well-defined single-valued function. In fact, a careful examination of $\chi_{\boxed{170}}^1$ and $\chi_{\boxed{240}}^1$ in Fig. 4 will reveal that these two piecewise-linear functions are *inverse* of each other. Subsets of both characteristic functions in Fig. 4 are typical of Wolfram's *class 2* rules.

Example 5. $\chi_{\boxed{30}}^1$

The graph of the characteristic function $\chi_{\boxed{30}}^1$ of $\boxed{30}$ is shown in Fig. 5(a). This complicated characteristic is typical of all local rules belonging to Wolfram's *class 3* CA rules.

Example 6. $\chi_{\boxed{110}}^1$

The graph of the characteristic function $\chi_{\boxed{110}}^1$ of $\boxed{110}$ is shown in Fig. 5(b). This rather exotic characteristic exhibits many features typical of Wolfram's *class 4* rules.

Example 7. $\chi_{\boxed{51}}^1$ and $\chi_{\boxed{51}}^2$

The graphs of the “*time-1*” characteristic function $\chi_{\boxed{51}}^1$ and “*time-2*” characteristic function $\chi_{\boxed{51}}^2$ of $\boxed{51}$ are shown in Figs. 6(a) and 6(b), respectively. Observe that while there is only one period-1 fixed point in $\chi_{\boxed{51}}^1$, every vertical line terminates on the main diagonal of $\chi_{\boxed{51}}^2$. This implies that $\boxed{51}$ has a *dense* set of *period-2 invariant orbits*. Such local rules will be studied in Sec. 4.4.

Example 8. $\chi_{\boxed{62}}^1$ and $\chi_{\boxed{62}}^3$

The graphs of the “*time-1*” characteristic function $\chi_{\boxed{62}}^1$ and “*time-3*” characteristic function $\chi_{\boxed{62}}^3$ of $\boxed{62}$ are shown in Figs. 7(a) and 7(b), respectively. Observe that while there are no period-1 fixed points in $\chi_{\boxed{62}}^1$, there are many vertical lines which landed on the main diagonal of $\chi_{\boxed{62}}^3$. This implies that $\boxed{62}$ has many period-3 attractors. Such local rules will be studied in Sec. 4.3.

3. Transient Regimes and Attractors

For a CA with *finite* I , the state space contains exactly $n_\Sigma \triangleq 2^{I'}$ distinct states, where $I' = I + 1$. It follows that given any *initial state*

$$\mathbf{x}(0) = [x_0(0) \ x_1(0) \ \cdots \ x_{I-1}(0) \ x_I(0)] \quad (22)$$

²The leftmost vertical line should actually be drawn at $\phi = \varepsilon \approx 0$. Printer resolution precludes our showing the correct value $\chi_{\boxed{240}}^1(0.\overline{00}) = 0.\overline{00}$.

the *dynamic pattern* $\mathcal{D}_{\lfloor N \rfloor}[\mathbf{x}(0)]$ evolving from the initial state $\mathbf{x}(0)$ under *any* local rule $\lfloor N \rfloor$ must eventually repeat itself with a *minimum period* T_{Λ} , where the

$$\text{Attractor period} \quad T_{\Lambda} \leq 2^{I+1} \quad (23)$$

depends *only* on the local rule $\lfloor N \rfloor$, and is independent of the initial state $\mathbf{x}(0)$, assuming $\mathbf{x}(0)$ belongs to the *basin of attraction* of a period- T_{Λ} attractor Λ to be defined below.

Definition 1. Transient Regime and Transient Duration: Given any local rule $\lfloor N \rfloor$, and any *initial configuration* $\mathbf{x}(0)$, let T_{δ} be the *smallest* non-negative integer such that

$$\mathbf{x}(T_{\delta} + T_{\Lambda}) = \mathbf{x}(T_{\delta}) \quad (24)$$

Since $\mathbf{x}(t)$, $t = 0, 1, 2, \dots, T_{\delta} - 1$, will never recur again for all $t \geq T_{\delta}$, the first T_{δ} consecutive rows of

the dynamic pattern $\mathcal{D}_{\lfloor N \rfloor}[\mathbf{x}(0)]$ is called the *transient regime* originating from the initial state $\mathbf{x}(0)$ and the time $(T_{\delta} - 1)$ is called the *transient duration*.

Definition 2. Period- T_{Λ} Attractor: If $T_{\delta} > 1$, then the T_{Λ} consecutive rows of $\mathcal{D}_{\lfloor N \rfloor}[\mathbf{x}(0)]$ denoted by

$$\begin{aligned} \Lambda_{\lfloor N \rfloor}(\mathbf{x}(0)) \triangleq & \mathbf{x}(T_{\delta}) \cup \mathbf{x}(T_{\delta} + 1) \cdots \\ & \cup \mathbf{x}(T_{\delta} + (T_{\Lambda} - 1)) \end{aligned} \quad (25)$$

is called a **period- T_{Λ} attractor** of the local rule $\lfloor N \rfloor$ originating from the *initial configuration* $\mathbf{x}(0)$. The set \mathcal{B}_{Λ} of all *initial states* $\mathbf{x}(0)$ which tend to the *attractor* Λ is called the *basin of attraction* of Λ .

To illustrate the above definitions, consider first the *dynamic pattern* $\mathcal{D}_{\lfloor 62 \rfloor}[\mathbf{x}_a(0)]$ shown in Fig. 8(a). For the initial configuration \mathbf{x}_a (row 0 in Fig. 8(a)), we find $T_{\delta} = 51$ and $T_{\Lambda} = 3$. Hence, the *transient*

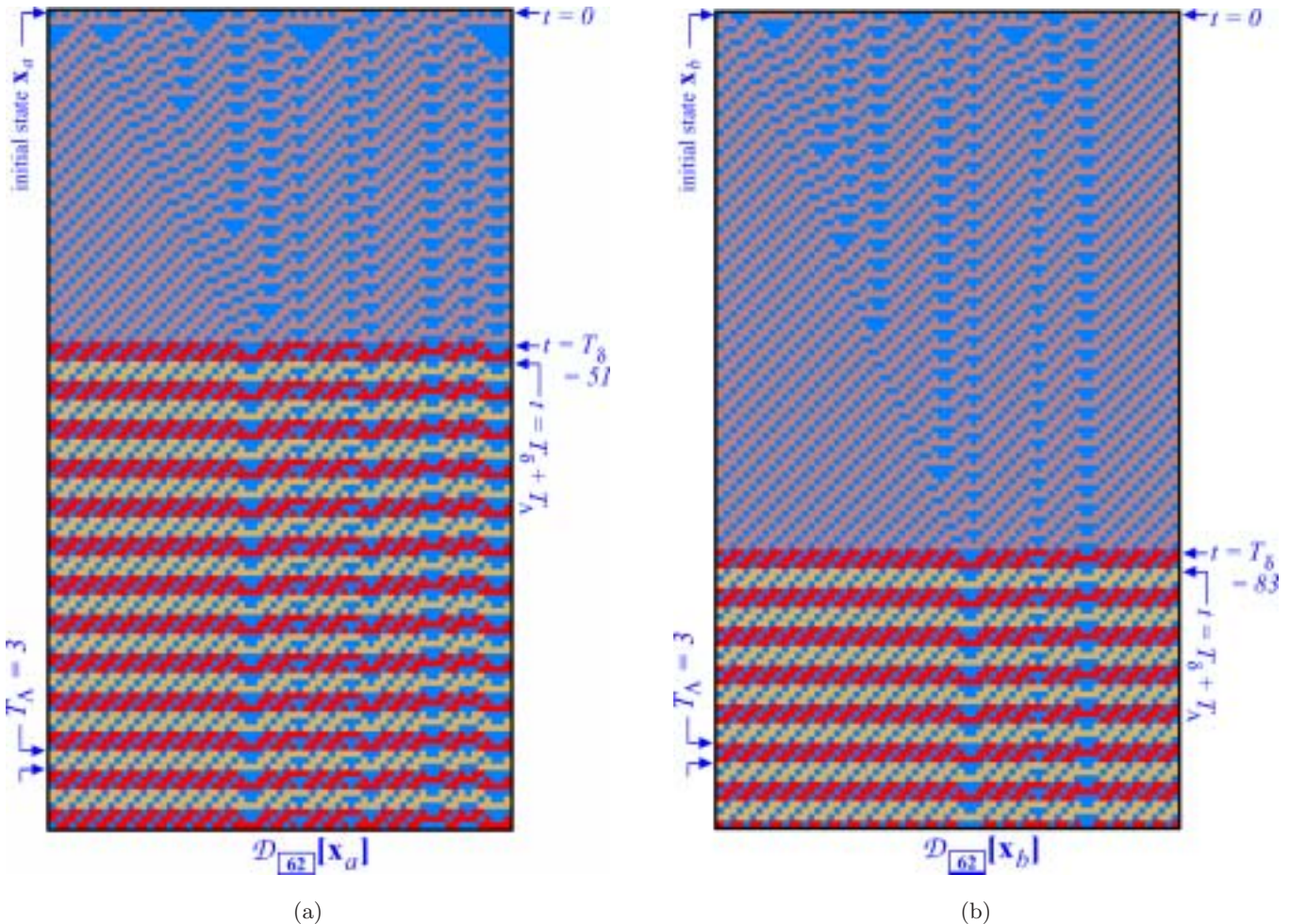


Fig. 8. Illustrations of the transient regime and transient duration of rule [62] originating from two different initial configurations \mathbf{x}_a and \mathbf{x}_b .

regime originating from \mathbf{x}_a of the dynamic pattern $\mathcal{D}_{[62]}[\mathbf{x}_a]$ consists of the first 51 rows in Fig. 8(a). The *period-3* orbit is clearly seen by the alternating color backgrounds. For the *dynamic pattern* $\mathcal{D}_{[62]}[\mathbf{x}_b]$ shown in Fig. 8(b), observe that the initial configuration \mathbf{x}_b (row 0 in Fig. 8(b)) gives rise to a longer *transient duration* $T_\delta = 83$.

However, since \mathbf{x}_a and \mathbf{x}_b in Fig. 8 were chosen to belong to the *basin of attraction* of Λ , the period T_Λ of the periodic orbit in Figs. 8(a) and 8(b) must be the same, namely, $T_\Lambda = 3$, as can be easily verified by inspection of the dynamic pattern in Fig. 8.

For some local rules, the period T_Λ can be much larger than the transient duration, as depicted in the two dynamic patterns $\mathcal{D}_{[99]}[\mathbf{x}_a]$ and $\mathcal{D}_{[99]}[\mathbf{x}_b]$ in Figs. 9(a) and 9(b) for local rule $[N] = [99]$. Observe that $T_\delta = 14$ and $T_\Lambda = 71$ for $\mathcal{D}_{[99]}[\mathbf{x}_a]$. Similarly, $T_\delta = 43$ and $T_\Lambda = 71$ for $\mathcal{D}_{[99]}[\mathbf{x}_b]$.

In fact, there are local rules such as $[110]$ and $[30]$, and their global equivalence classes, where T_Λ can tend to infinity as $T \rightarrow \infty$ (for $I = \infty$). In such cases, it is no longer useful to talk about a transient regime and we will simply refer to the entire dynamic pattern $\mathcal{D}_{[N]}[\mathbf{x}(0)]$ as an *orbit* originating from $\mathbf{x}(0)$.

The “basin of attraction” \mathcal{B}_Λ of an attractor Λ must contain, by definition, at least one point not belonging to Λ . It is possible, however, for some periodic orbits to have no basin of attraction.

Definition 3. Invariant Orbits: An orbit Γ whose basin of attraction is the empty set is called an *invariant orbit*.

It follows from Definition 3 that an invariant orbit must have a zero transient duration, i.e. $T_\delta = 1$.

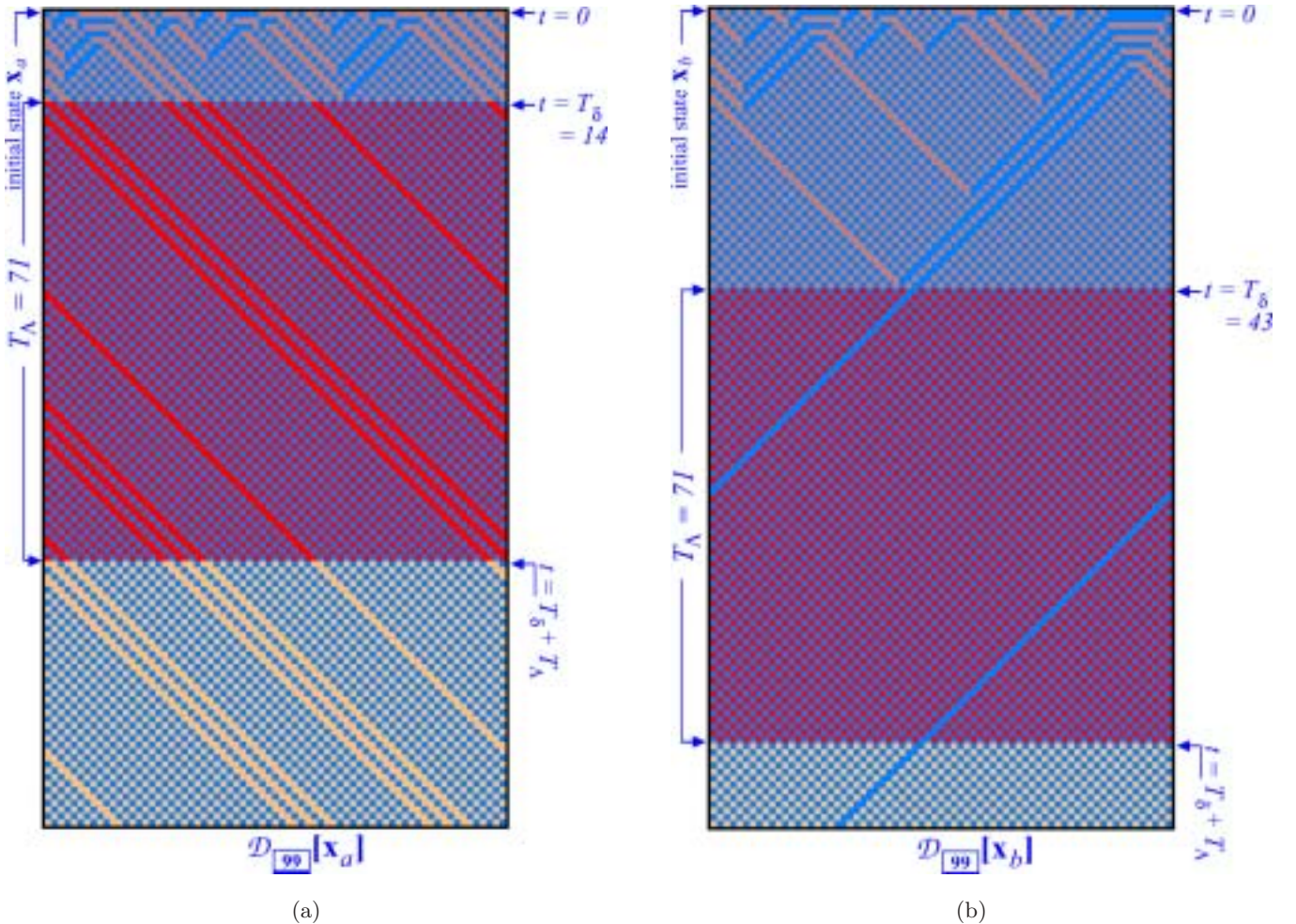


Fig. 9. Illustrations of the transient regime and transient duration of rule $[99]$ originating from two different initial configurations \mathbf{x}_a and \mathbf{x}_b .

Proposition 1. *Local Equivalent Class \mathcal{S}_4^1 is Invariant: The orbits of all six rules $\{\boxed{15}, \boxed{51}, \boxed{85}, \boxed{170}, \boxed{204}, \boxed{240}\}$ belonging to the local equivalence class \mathcal{S}_4^1 [Chua et al., 2003] are invariant.*

Proof. We will see in Table 2 and Sec. 5.4 that, for finite I , every point in Fig. 4(a) is a point on a *periodic orbit* of $\boxed{170}$ whose dynamics consist of shifting each initial string by one pixel to the left. Consequently, there is no transient regime in this case and hence all orbits of $\boxed{170}$ are *invariant orbits*. Since the shifting operation is preserved under the rotational transformations of the *local equivalence class* \mathcal{S}_4^1 listed in Table 25(o) of [Chua et al., 2003], it follows that all orbits of $\boxed{15}$, $\boxed{51}$, $\boxed{85}$, $\boxed{204}$, and $\boxed{240}$ are invariant as well. ■

It has been verified by exhaustive computer simulation that only the six rules belonging to \mathcal{S}_4^1 are endowed with only invariant orbits. In general, invariant orbits have noninvariant neighboring orbits. We have seen earlier a special case of an invariant orbit consisting of only a single point; namely, $\phi_{\boxed{128}} = 1.\overline{00}$ in Fig. 3(a). Observe that in addition to having no basin of attraction, $\phi_{\boxed{128}} = 1.\overline{00}$ has no preimage (predecessor). Such special initial configuration is called a *garden of Eden* [Moore, 1962].

Observe that no garden of Eden can be a *periodic* orbit with a period $T_\Lambda > 1$, otherwise any point on the orbit is a predecessor of its next iterate. A period-1 garden of Eden is therefore a truly unique specie worthy of its own name, henceforth dubbed an *isle of Eden*. Indeed, we can generalize this unique phenomenon, which does not exist in continuous dynamical systems (such as ODE), to define a “*period-k*” *isle of Eden* from the k th iterated characteristic function χ_N^k of \boxed{N} . A gallery of *period-k isles of Eden* of all one-dimensional cellular automata will be presented in Part V of this tutorial series.

3.1. Mapping CA attractors onto time- τ maps

Since *invariant orbits* are not attractors, they are *not robust* in the sense that precisely specified initial states must be used to observe them. Since one of the most fundamental problems in nonlinear dynamics is to analyze and predict their long-term behaviors as $t \rightarrow \infty$, we will develop some novel and effective techniques for analyzing and

predicting global *qualitative* behaviors of *robust* CA attractors.

In general, each CA local rule \boxed{N} can exhibit many distinct attractors Λ_i , $i = 1, 2, \dots, \Omega$, as demonstrated in Figs. 3–7. Each attractor represents a distinct *operating mode* and must be analyzed as a separate *dynamical* system. In order to exploit the lateral symmetry exhibited by many bilateral pairs N and $N^\dagger \triangleq T^\dagger[N]$ of local rules, where T^\dagger denotes the *left-right transformation* operation defined in [Chua et al., 2004], it is more revealing to represent and examine each attractor from two spatial directions, namely, a *forward* (left \rightarrow right) direction and a *backward* (right \rightarrow left) direction.

Since each CA attractor Λ is periodic (for finite I) with some period T_Λ , it is usually represented by displaying T_Λ consecutive binary bit strings $\mathbf{s}_1, \mathbf{s}_2, \dots, \mathbf{s}_{T_\Lambda}$, as illustrated in Figs. 8 and 9. In order to exploit the analytical tools from nonlinear dynamics [Alligood et al., 1996; Shilnikov et al., 1998], it is essential that we transcribe these rather unwieldy *pictorial* data into an equivalent nonlinear *time series*. Such a one-to-one transcription is precisely defined by Eqs. (13) and (17) via the commutative diagram shown in Fig. 2. Hence, each *forward Boolean string* $\vec{\mathbf{x}}$ is mapped bijectively onto a *real number* $\phi \in [0, 1]$ via Eqs. (12) and (13). Similarly, each *backward Boolean string* $\overleftarrow{\mathbf{x}}(0)$ is mapped bijectively onto a *real number* $\phi^\dagger \in [0, 1]$ via Eqs. (16) and (17). Each “*period- T_Λ* ” attractor Λ defined by a pattern made of T_Λ consecutive Boolean strings is therefore mapped onto a *forward time series*

$$\varphi = [\phi_0, \phi_1, \phi_2, \dots, \phi_{T_\Lambda}], \quad \phi_i \in [0, 1], \quad (26)$$

henceforth called a *forward orbit*, and a *backward time series*

$$\varphi^\dagger = [\phi_0^\dagger, \phi_1^\dagger, \phi_2^\dagger, \dots, \phi_{T_\Lambda}^\dagger], \quad \phi_i^\dagger \in [0, 1], \quad (27)$$

henceforth called a *backward orbit*, where the *length* of each time series (resp. *period* of each orbit) is equal to T_Λ .

It follows from the definition of the *period* of an attractor that $T_\Lambda = 1$ for all “*period-1*” attractors in Fig. 3(b), $T_\Lambda = 2$ for all “*period-2*” attractors in Fig. 6(b), and $T_\Lambda = 3$ for all “*period-3*” attractors in Fig. 7(b). Attractors associated with local rules belonging to Wolfram’s Classes 3 and 4 can have an extremely large period T_Λ , a number greater than the number of elementary particles in the universe even for a relatively small $I = 100$.

From a computational perspective, such time series is effectively infinite in length.

The qualitative dynamics associated with an attractor can often be uncovered and understood by plotting the following two *attractor-induced time- τ maps* [Alligood *et al.*, 1996] associated with the *forward time series* φ and the *backward time series* φ^\dagger , respectively:

$$\boxed{\begin{array}{c} \text{Forward time-}\tau \text{ map} \\ \rho_\tau[N] : \phi_{n-\tau} \mapsto \phi_n \end{array}} \quad (28)$$

$$\boxed{\begin{array}{c} \text{Backward time-}\tau \text{ map} \\ \rho_\tau^\dagger[N] : \phi_{n-\tau}^\dagger \mapsto \phi_n^\dagger \end{array}} \quad (29)$$

For each local rule $[N]$, the *forward time- τ map* ρ_τ and the *backward time- τ map* ρ_τ^\dagger are defined explicitly via the *time- τ characteristic function* $\chi_{[N]}^\tau$ as follow:

$$\boxed{\rho_\tau(\phi_{n-\tau}) = \chi_{[N]}^\tau(\phi_{n-\tau})} \quad (30)$$

$$\boxed{\rho_\tau^\dagger(\phi_{n-\tau}^\dagger) = \chi_{[N]}^\tau(\phi_{n-\tau}^\dagger)} \quad (31)$$

Explicit coordinates $(\phi_{n-\tau}, \phi_n)$ and $(\phi_{n-\tau}^\dagger, \phi_n^\dagger)$ for plotting each point of the *forward time- τ map* $\rho_\tau[N]$ and the *backward time- τ map* $\rho_\tau^\dagger[N]$, are listed in Table 1 for $\tau = 1, 2$, and 3.

When $\tau = 1$, the resulting *time-1 maps* [Alligood *et al.*, 1996; Hirsch & Smale, 1974] $\rho_1[N]$ and $\rho_1^\dagger[N]$ are sometimes called *first-return maps* in the literature because they behave like Poincare return maps [Poincare, 1897]. Figure 10 shows the Poincare first-return map interpretation of four *forward time-1 maps* $\rho_1[200]$, $\rho_1[51]$, $\rho_1[62]$, and $\rho_1[170]$ of CA rules [200], [51], [62], and [170], respectively. In each case, the Poincare cross-section is the same *unit square* $[0, 1] \times [0, 1]$ we have encountered earlier in our definition of the CA *characteristic function* $\chi_{[N]}^1$ in Eq. (19). Only one out of many attractors is shown for each *time-1 map* in Fig. 10.

In Fig. 10(a), only one *period-1 attractor* of rule [200] is shown (labeled as point ①). The *domain* of the *time-1 map* $\rho_1[200]$ in this trivial case consists of only the single point $\{\textcircled{1}\}$, and all iterates

map trivially onto the fixed point ①. One can interpret point ① as the point where a planet intersects an imaginary Poincare cross-section once every revolution.

Figure 10(b) shows a *period-2 attractor* (out of many others) of local rule [51]. The orbit of the circulating planet intersects the Poincare cross-section at two points. The domain of the *time-1 map* $\rho_1[51]$ is $\{\textcircled{1}, \textcircled{2}\}$ where $\rho_1(\textcircled{1}) \mapsto \textcircled{2}$ and $\rho_1(\textcircled{2}) \mapsto \textcircled{1}$.

Figure 10(c) shows a *period-3 attractor* of local rule [62]. The circulating orbit is seen to intersect the Poincare cross-section at three points. The domain of the *time-1 map* $\rho_1[62]$ consists of $\{\textcircled{1}, \textcircled{2}, \textcircled{3}\}$ where $\rho_1(\textcircled{1}) \mapsto \textcircled{2}$, $\rho_1(\textcircled{2}) \mapsto \textcircled{3}$, and $\rho_1(\textcircled{3}) \mapsto \textcircled{1}$.

Figure 10(d) shows a *Bernoulli σ_1 -shift attractor* (to be discussed in depth in Sec. 5) of local rule [170] where the domain of the *time-1 map* $\rho_1[170]$ consists of *all points* on the two parallel lines with slope equal to 2 for the case $I = \infty$. For finite $I > 60$, the attractor consists of *almost* all points on these two lines separated by tiny gaps $\Delta < 10^{-18}$ and is therefore not discernible. The domain in the case $I = \infty$ consists of the entire unit interval $[0, 1]$. Only a few iterates $(\textcircled{1}, \textcircled{2}, \textcircled{3}, \dots, \textcircled{6})$ are shown to avoid clutter. One can associate the complicated orbit in Fig. 10(d) with the trajectory of a comet, which in this case would visit almost all points on these two parallel lines, as originally envisioned by Poincare.

In so far as the qualitative dynamics is concerned, it suffices to examine the evolution of the *time-1 map* induced by the orbit in Fig. 10. To illustrate this important insight discovered by Poincare, let us examine the *forward time-1 map* of a period-3 attractor of [62] consisting of points ①, ②, ③ in Fig. 11(a), as well as the associated *backward time-1 map* in Fig. 11(b) consisting of points ①', ②' and ③'.

In order to illustrate what we mean by the fundamental principle which asserts that CA rules belonging to the same *global equivalence class* ε_m^k [Chua *et al.*, 2004] must have identical qualitative dynamics, we also show the forward time-1 map for [118] in Fig. 11(c), and the backward time-1 map for [118] in Fig. 11(d), where [118] and [62] belong to same equivalence class ε_{22}^2 derived in [Chua *et al.*, 2004]. Since [118] and [62] are related by a *left-right transformation* operator \mathbf{T}^\dagger , i.e. $T^\dagger[62] = [118]$, it follows from the theory of global equivalence class developed in [Chua *et al.*, 2004], that the two rules [62] and [118] have identical qualitative behaviors.

Table 1. Explicit coordinates $(\phi_{n-\tau}, \phi_n)$ for defining time- τ maps for $\tau = 1, 2, 3$.

Forward Time-1 map		Backward Time-1 map	
ϕ_{n-1}	$\phi_n = \chi_{[N]}^1(\phi_{n-1})$	ϕ_{n-1}^\dagger	$\phi_n^\dagger = \chi_{[N]}^1(\phi_{n-1}^\dagger)$
ϕ_0	$\phi_1 = \chi_{[N]}^1(\phi_0)$	ϕ_0^\dagger	$\phi_1^\dagger = \chi_{[N]}^1(\phi_0^\dagger)$
ϕ_1	$\phi_2 = \chi_{[N]}^1(\phi_1)$	ϕ_1^\dagger	$\phi_2^\dagger = \chi_{[N]}^1(\phi_1^\dagger)$
\vdots	\vdots	\vdots	\vdots
ϕ_{I_N-1}	$\phi_{I_N} = \chi_{[N]}^1(\phi_{I_N-1})$	$\phi_{I_N-1}^\dagger$	$\phi_{I_N}^\dagger = \chi_{[N]}^1(\phi_{I_N-1}^\dagger)$
Forward Time-2 map		Backward Time-2 map	
ϕ_{n-2}	$\phi_n = \chi_{[N]}^2(\phi_{n-2})$	ϕ_{n-2}^\dagger	$\phi_n^\dagger = \chi_{[N]}^2(\phi_{n-2}^\dagger)$
ϕ_{-1}	$\phi_1 = \chi_{[N]}^2(\phi_{-1})$	ϕ_{-1}^\dagger	$\phi_1^\dagger = \chi_{[N]}^2(\phi_{-1}^\dagger)$
ϕ_0	$\phi_2 = \chi_{[N]}^2(\phi_0)$	ϕ_0^\dagger	$\phi_2^\dagger = \chi_{[N]}^2(\phi_0^\dagger)$
ϕ_1	$\phi_3 = \chi_{[N]}^2(\phi_1)$	ϕ_1^\dagger	$\phi_3^\dagger = \chi_{[N]}^2(\phi_1^\dagger)$
\vdots	\vdots	\vdots	\vdots
ϕ_{I_N-2}	$\phi_{I_N} = \chi_{[N]}^2(\phi_{I_N-2})$	$\phi_{I_N-2}^\dagger$	$\phi_{I_N}^\dagger = \chi_{[N]}^2(\phi_{I_N-2}^\dagger)$
Forward Time-3 map		Backward Time-3 map	
ϕ_{n-3}	$\phi_n = \chi_{[N]}^3(\phi_{n-3})$	ϕ_{n-3}^\dagger	$\phi_n^\dagger = \chi_{[N]}^3(\phi_{n-3}^\dagger)$
ϕ_{-2}	$\phi_1 = \chi_{[N]}^3(\phi_{-2})$	ϕ_{-2}^\dagger	$\phi_1^\dagger = \chi_{[N]}^3(\phi_{-2}^\dagger)$
ϕ_{-1}	$\phi_2 = \chi_{[N]}^3(\phi_{-1})$	ϕ_{-1}^\dagger	$\phi_2^\dagger = \chi_{[N]}^3(\phi_{-1}^\dagger)$
ϕ_0	$\phi_3 = \chi_{[N]}^3(\phi_0)$	ϕ_0^\dagger	$\phi_3^\dagger = \chi_{[N]}^3(\phi_0^\dagger)$
ϕ_1	$\phi_4 = \chi_{[N]}^3(\phi_1)$	ϕ_1^\dagger	$\phi_4^\dagger = \chi_{[N]}^3(\phi_1^\dagger)$
\vdots	\vdots	\vdots	\vdots
ϕ_{I_N-3}	$\phi_{I_N} = \chi_{[N]}^3(\phi_{I_N-3})$	$\phi_{I_N-3}^\dagger$	$\phi_{I_N}^\dagger = \chi_{[N]}^3(\phi_{I_N-3}^\dagger)$

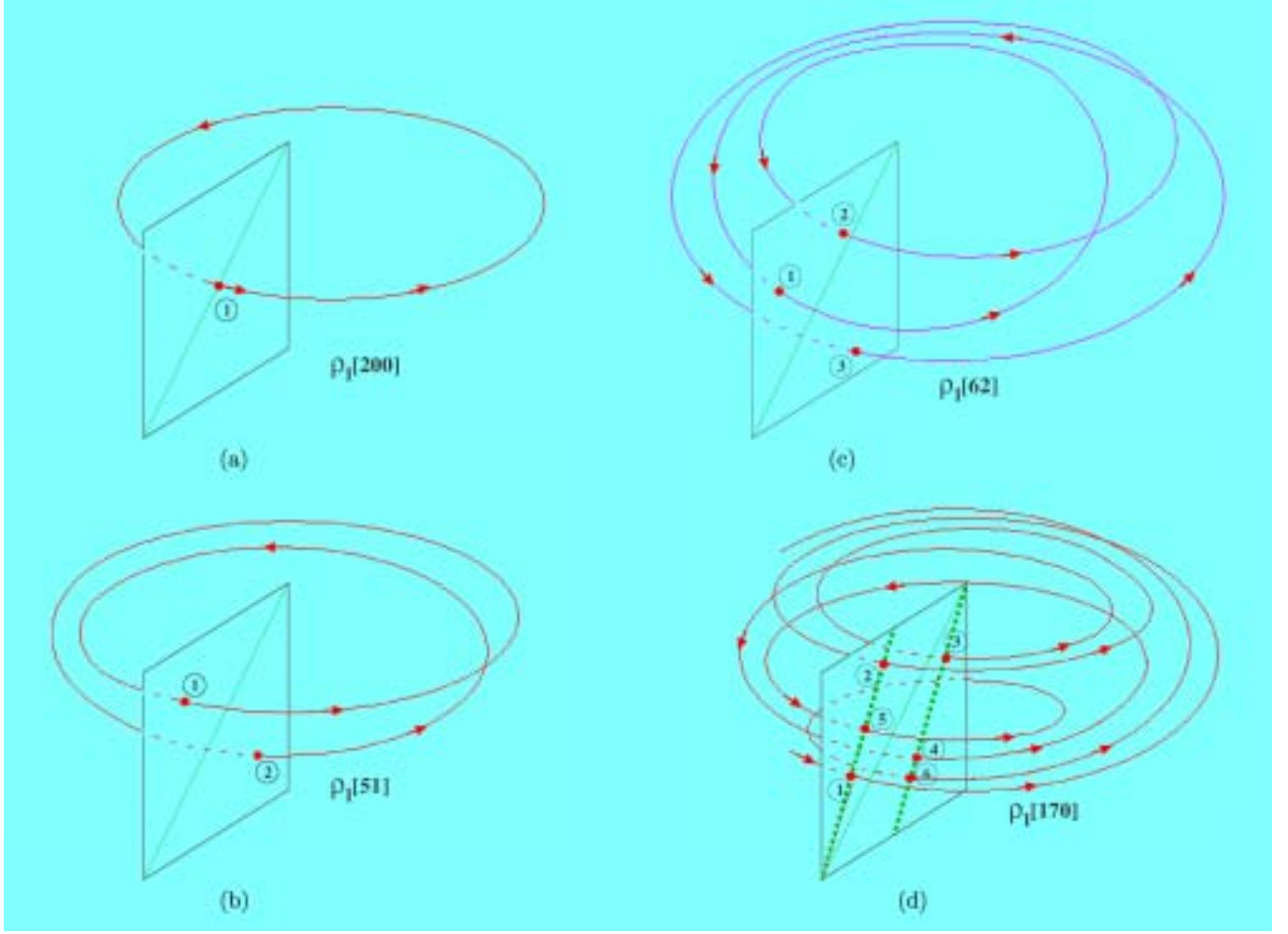


Fig. 10. Poincare return map interpretation of four *forward time-1 maps*. (a) Period-1 map $\rho_1[200]$. (b) Period-2 map $\rho_1[51]$. (c) Period-3 map $\rho_1[62]$. (d) Bernoulli σ_1 -shift map $\rho_1[170]$.

In particular, they have, *qualitatively*, the same transient regimes, the same attractors, and the same invariant orbits, *modulo* a bijection. Moreover, their dynamics must also be mapped onto each other, as depicted by the diagram shown in Fig. 11. This well-known geometrical construction is called a *Lameray diagram* [Shilnikov *et al.*, 1998], named after the French mathematician Lameray who first discovered its pedagogical value in the eighteenth century. It is also called a *cobweb diagram* [Alligood *et al.*, 1996] because it resembles the web spun by a spider.

Important Observation

Every Point on the *forward time-1 map* $\rho_1 : \phi_{n-1} \mapsto \phi_n$, or the *backward time-1 map* $\rho_1^\dagger : \phi_n^\dagger \mapsto \phi_{n-1}^\dagger$, of any CA rule \boxed{N} is a point on the characteristic function $\chi_{\boxed{N}}^1$.

In other words, the CA *characteristic function* $\chi_{\boxed{N}}^1$ is a *complete* and *global* representation of \boxed{N} . It is complete because it contains all information needed to derive the dynamic evolutions from *any* initial state by simply drawing a Lameray (cobweb) diagram directly on $\chi_{\boxed{N}}^1$! It is global because each point on $\chi_{\boxed{N}}^1$ codes for an entire configuration of length $I + 1$, and not just for one pixel if the local rule were used instead. Clearly, the points defining the *time-1 maps* $\rho_1[N]$ and $\rho_1^\dagger[N]$ are subsets of the points defining the characteristic function $\chi_{\boxed{N}}^1$.

It follows from the above observation that every point on a *time- τ map* of \boxed{N} is a point on the time- τ characteristic function $\chi_{\boxed{N}}^\tau$.

Remarks

1. If we imagine the three points on the time-1 map $\rho_1[62]$ in Fig. 11(a) as points on a *unimodal function* (e.g. logistic map) [Alligood

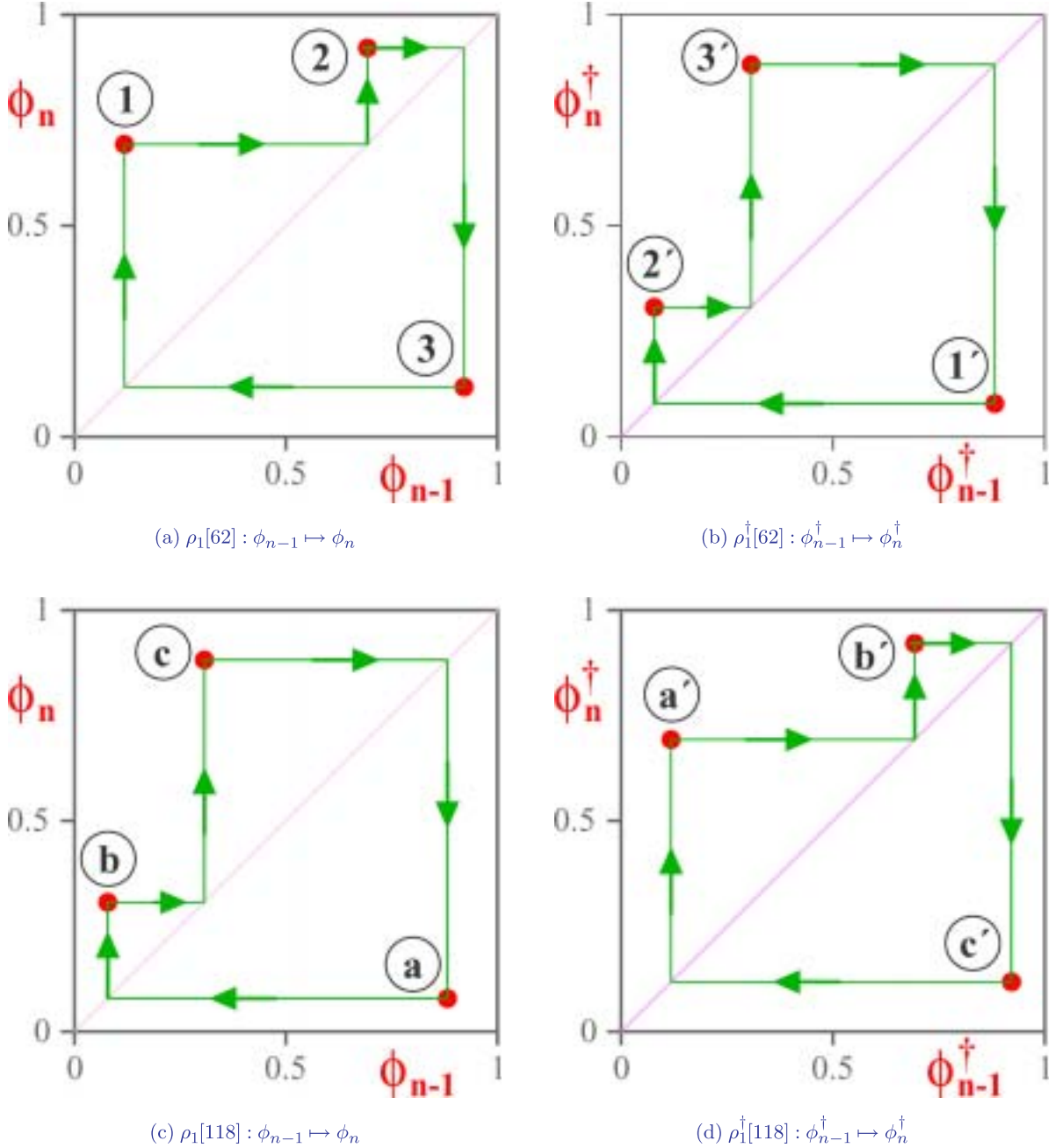


Fig. 11. Cobweb diagram showing the evolution of $\boxed{62}$ and $\boxed{118}$ from any state of a *period-3* attractor in *forward time* (a and c), and *backward time* (b and d). Points \textcircled{k} and $\textcircled{k'}$ denotes corresponding *instants of time*.

- et al.*, 1996], then we can associate this particular period-3 attractor of $\boxed{62}$ as a period-3 point of a *continuous map* $f : [0, 1] \rightarrow [0, 1]$ which we know is *chaotic* because “period-3 *implies chaos*” [Alligood *et al.*, 1996].
- It follows from *Remark 1* above that *every* forward and backward *time-1* map exhibited in Table 2 of Sec. 3.2 can be interpreted as a period- T_Λ attractor of a *continuous map* $f : [0, 1] \rightarrow [0, 1]$ over the unit interval $[0, 1]$.

- It follows from *Remark 2* above that for every CA rule \boxed{N} , $N = 0, 1, 2, \dots, 255$, and finite I , we can construct a *continuous one-dimensional map* $f_{\boxed{N}} : [0, 1] \rightarrow [0, 1]$ which has a period- T_Λ point coinciding with a period- T_Λ attractor, or invariant orbit, of rule \boxed{N} .
- It follows from *Remark 3* above that since *all* attractors, or *invariant orbits*, of a CA rule \boxed{N} are *disjoint sets of points* over $[0, 1]$, we can always construct a *polynomial* $\mathcal{P}_{\boxed{N}}(x)$, $x \in [0, 1]$,

which passes through all of these points. In fact, we can invoke the canonical representation from [Chua & Kang, 1977] to derive an *explicit* equation $\mathcal{P}_{\overline{N}}(x)$ involving the *absolute value function* as the only nonlinearity, such that $\mathcal{P}_{\overline{N}}(x)$ passes through the union of *all* points associated with *all* attractors $\Lambda_i, i = 1, 2, \dots, \Omega$ of \overline{N} . The continuous real-valued function $\mathcal{P}_{\overline{N}}(x) : [0, 1] \rightarrow [0, 1]$, henceforth called a “*Rule \overline{N} induced function*,” contains *each* attractor, $\Lambda_i, i = 1, 2, \dots, \Omega$, of \overline{N} as a period- T_{Λ_i} point. Since $\mathcal{P}_{\overline{N}}(x)$ can be constructed to include also attractors not observed from \overline{N} , it clearly has much richer nonlinear dynamics. Hence, for finite I , all attractors and invariant orbits of each of the 256 CA rules can be imbedded into a single *continuous real-valued function* over the unit interval $[0, 1]$.

3.2. A gallery of time-1 maps and power spectrum

The qualitative dynamics and long-term asymptotic behaviors of each *attractor* of a local rule \overline{N} can often be predicted from one or more of its *time- τ maps* $\rho_\tau[\overline{N}]$, $\tau = 1, 2, \dots$. In fact, a total of 224 out of 256 local rules have attractors that resemble those shown in Fig. 10, or their “*compositions*”. For an in-depth study of some of these rules in Sec. 5, and in Part V, as well as for future reference, a gallery of the *forward time-1 map* $\rho_1[\overline{N}]$ and the *backward time-1 map* $\rho_1^\dagger[\overline{N}]$ of up to three distinct attractors are exhibited in Table 2. For local rules with several qualitatively different attractors, their time-1 maps are printed in different colors. Unlike in Figs. 10 and 11, the points are not labeled to avoid clutter.

For each rule \overline{N} in Table 2, the *forward time-1 map* $\rho_1[\overline{N}]$ is printed in the *left* column and the *backward time-1 map* $\rho_1^\dagger[\overline{N}]$ is printed in the *right* column. All points with the same color (red, blue, or green) pertain to an attractor of the same color.

The *power spectrum* of the *forward time series* φ of Eq. (26) associated with the *red “forward” time-1 map* is calculated using the Mathcad software and printed in the *middle* column.³ We will see in Sec. 6 that the power spectrum reveals additional valuable and insightful information which cannot be extracted from time- τ maps.

Table 2 contains 256 three-component frames, henceforth referred to in this paper as CA *attractor vignettes*, corresponding to the 256 local rules. Each *vignette* \overline{N} provides a signature of the type of attractors inhabiting a CA local rule N . Except for the six local rules $\overline{15}$, $\overline{51}$, $\overline{85}$, $\overline{170}$, $\overline{204}$, and $\overline{240}$ (to be discussed in Sec. 4.4), whose dynamic patterns are *invariant orbits*, all other vignettes contain information on “robust” CA *attractors*.

The simplest vignette shows the *time-1 map* (in red) of only one attractor (e.g. vignette $\overline{2}$). In this case, the power spectrum pertains to the forward time-1 map $\rho_1[2]$ depicted in the left column. We will show in Sec. 6 that some spectrum harbors *additional* albeit *nonrobust dynamic modes*.

Vignette $\overline{11}$ of Table 2 shows two time-1 maps (colored in red and blue, respectively) corresponding to two distinct types of attractors, called *Bernoulli attractors*, to be analyzed in Sec. 5. In this case, the power spectrum pertains to the *red forward* time-1 map $\rho_1[11]$ depicted in the left column.

Vignette $\overline{25}$ shows three time-1 maps (colored in red, blue, and green, respectively) corresponding to three distinct types of attractors to be analyzed in Sec. 5. In this case, the power spectrum, as always, pertains to the *red forward* time-1 map $\rho_1[25]$ depicted in the left column.

An exception to our 3-color code applies to *time-1 maps* of rules with a continuum of period-1 and period-2 attractors. Since such attractors are qualitatively similar, only a *dull blue* color is used to indicate various *clusters* of *period-1* and *period-2* points. In addition, the location of *two* typical period-1 points are identified as solid dots (painted in light red and light blue color) in both forward and backward time-1 maps of such *period-1 attractors* (e.g. $\rho_1[4]$ and $\rho_1^\dagger[4]$ for $N = 4$). Note that the background color of the power spectrum of all period-1 time-1 maps are painted *yellow* with only a bold *red* line emerging at $f = 1$ signifying the absence of any other frequency components.

Similarly, two typical pairs of solid points are painted red and blue at the precise locations where they are located in both forward and backward *time-1 maps* of *period-2 attractors* for those rules harboring a continuum of period-2 attractors (e.g. $N = 5, 51$, etc). All other period-2 points form clusters and are painted in *dull blue* color. The power spectrum of all period-2 time-1 maps consists of a bold red line located at $f = 1/2$.

³The *power spectrum* of the corresponding *backward time-1 map* is *qualitatively identical* and is therefore redundant.

Table 2. Gallery of *forward time-1 maps* $\rho_1[N]$ and *backward time-1 maps* $\rho_1^\dagger[N]$ for attractor Λ_1 (red), Λ_2 (blue), and Λ_3 (green).

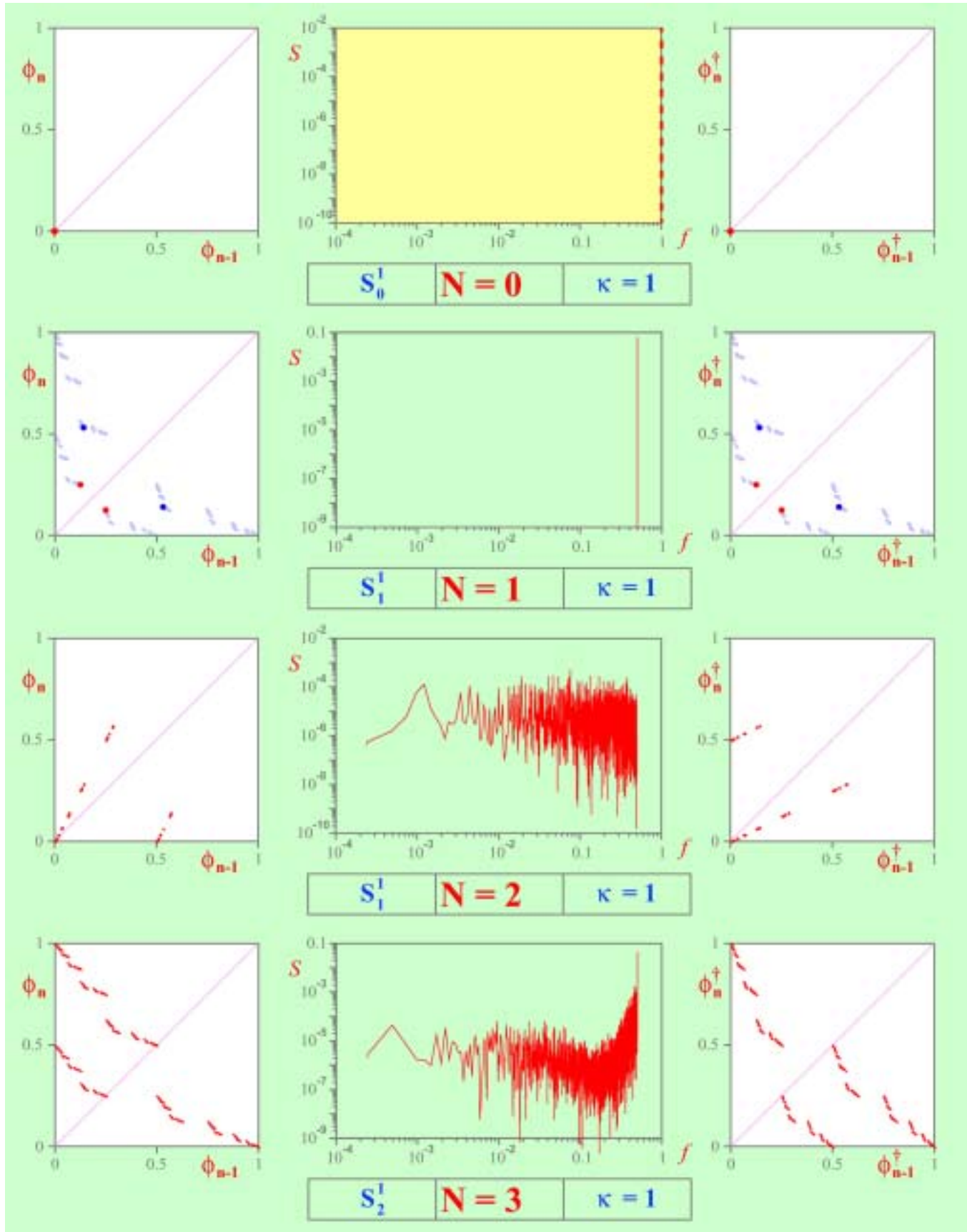


Table 2. (Continued)

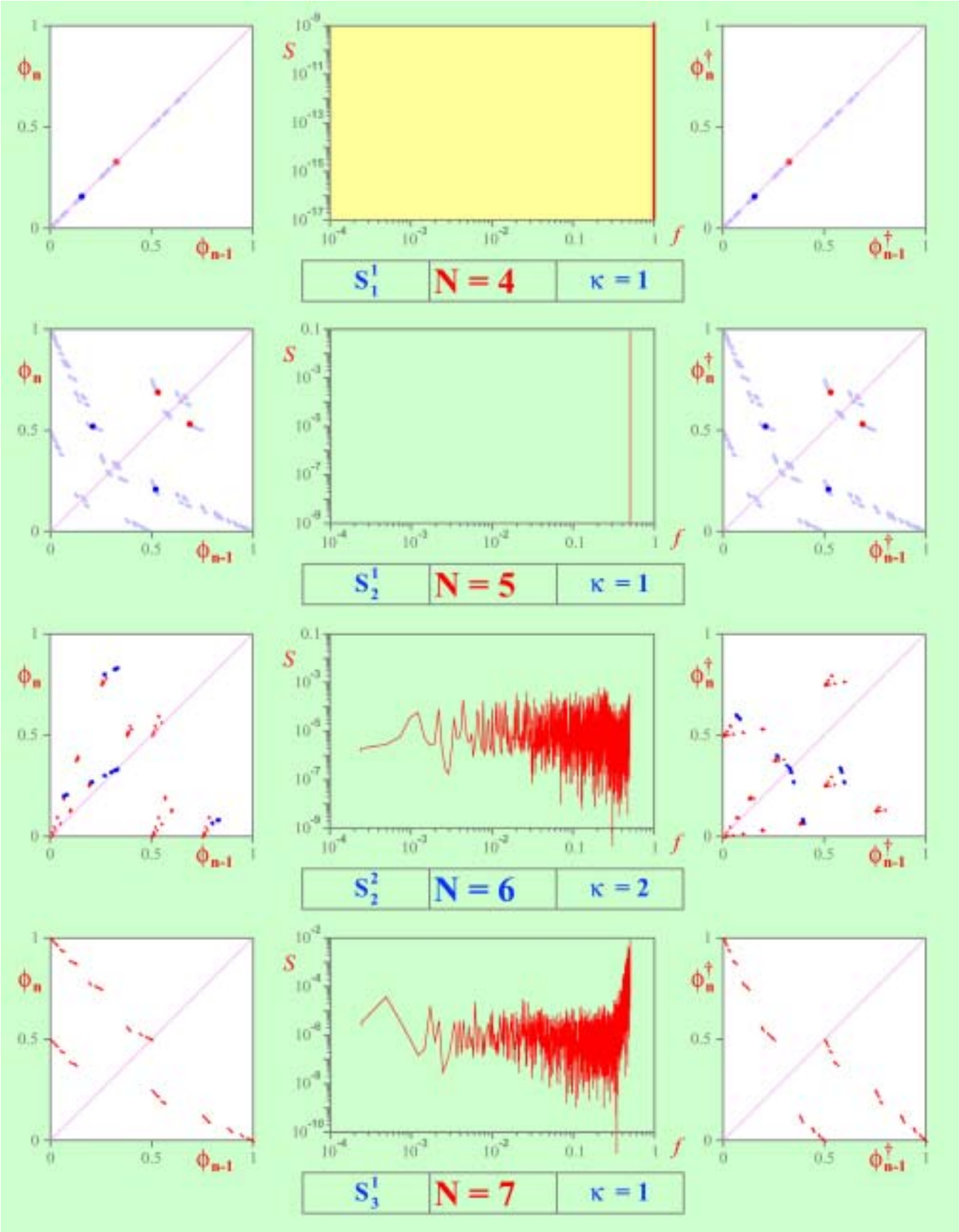


Table 2. (Continued)

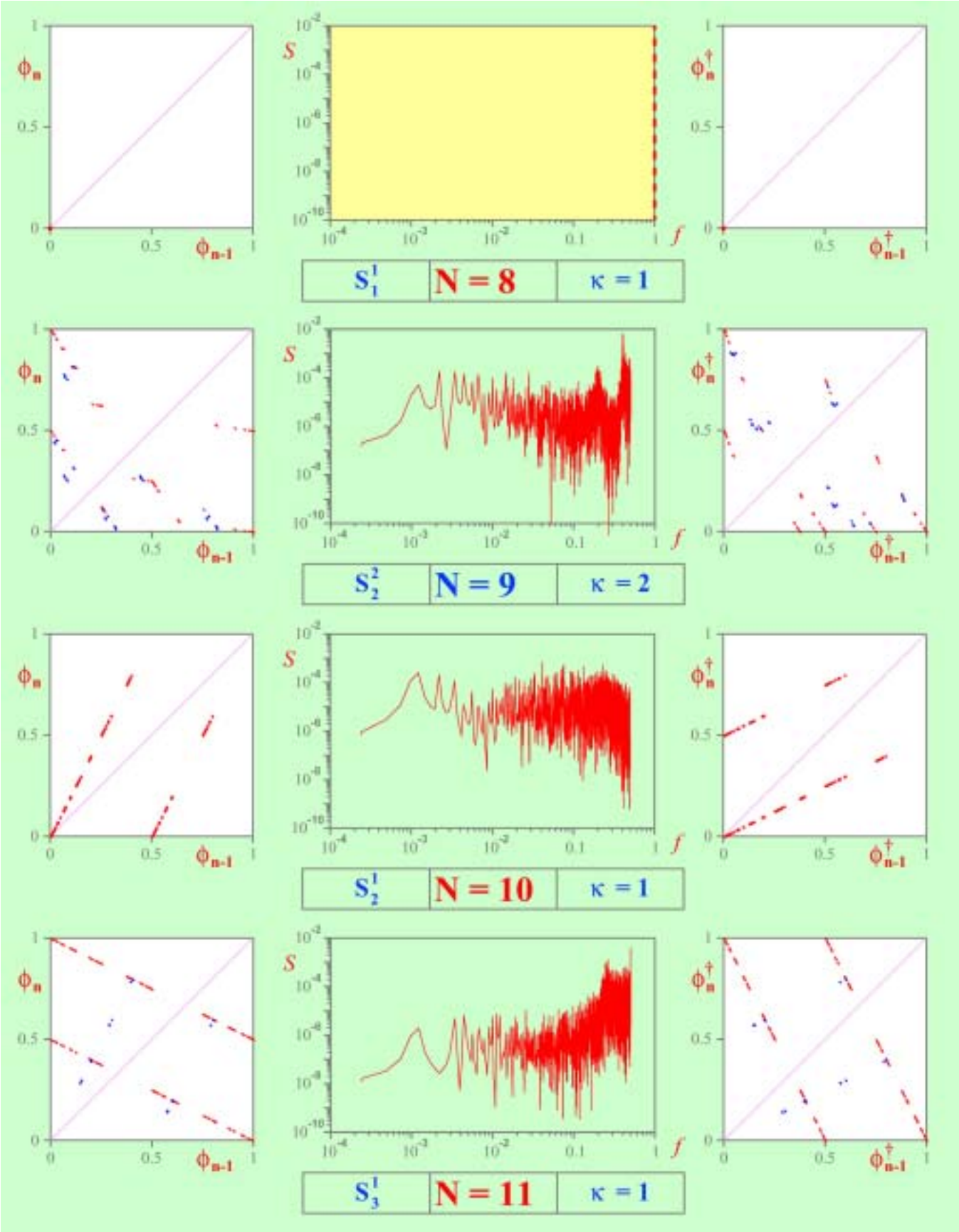


Table 2. (Continued)

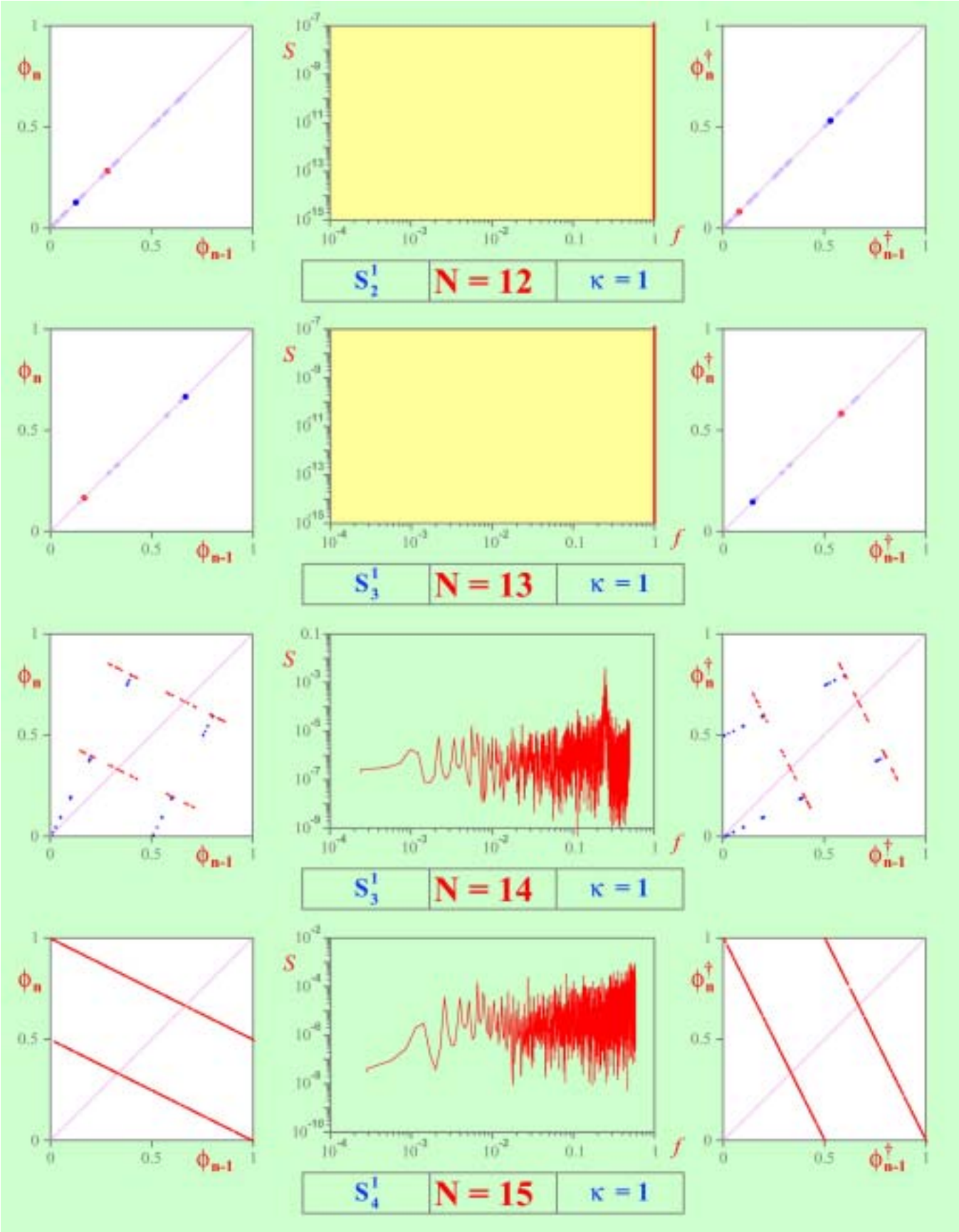


Table 2. (Continued)

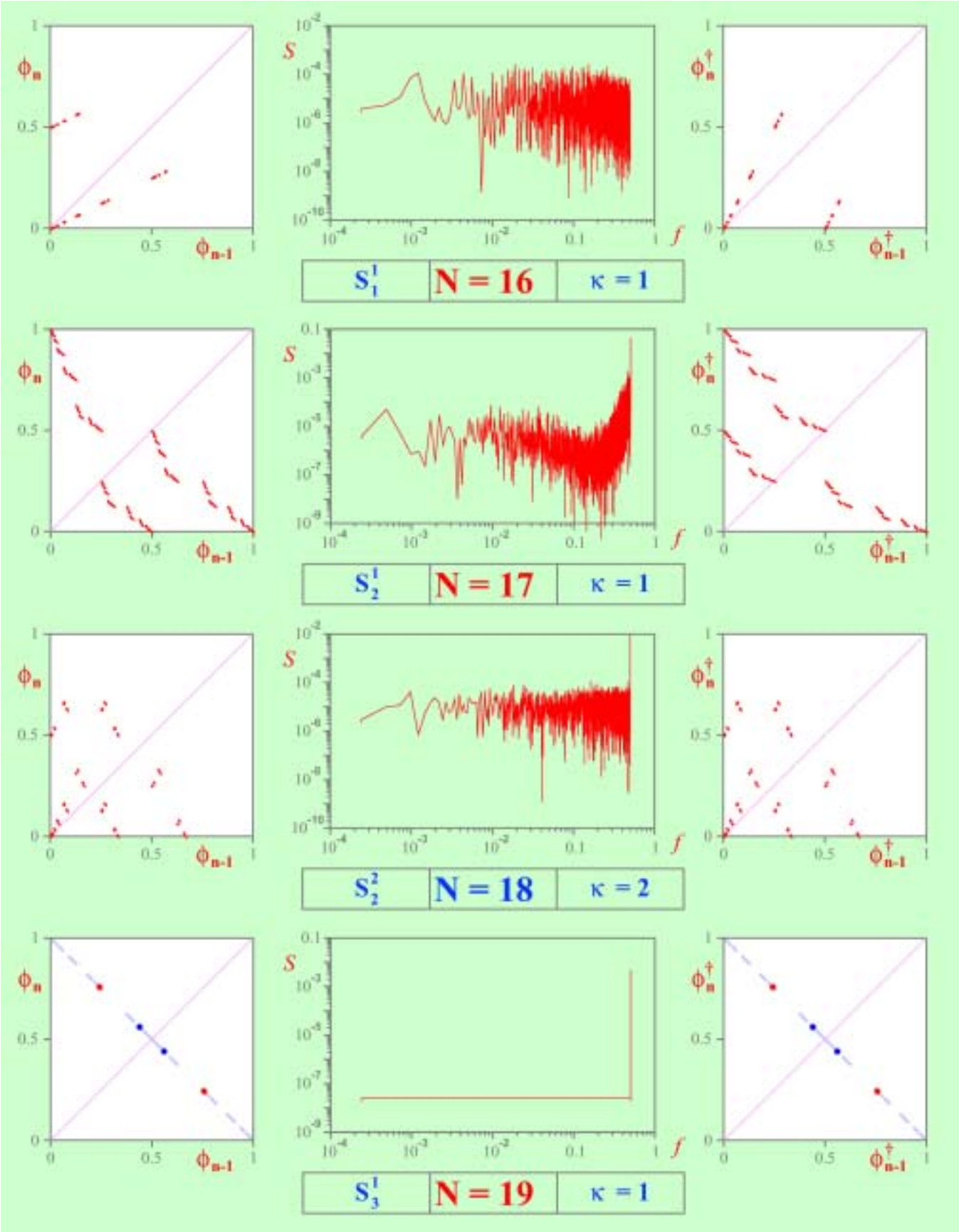


Table 2. (Continued)

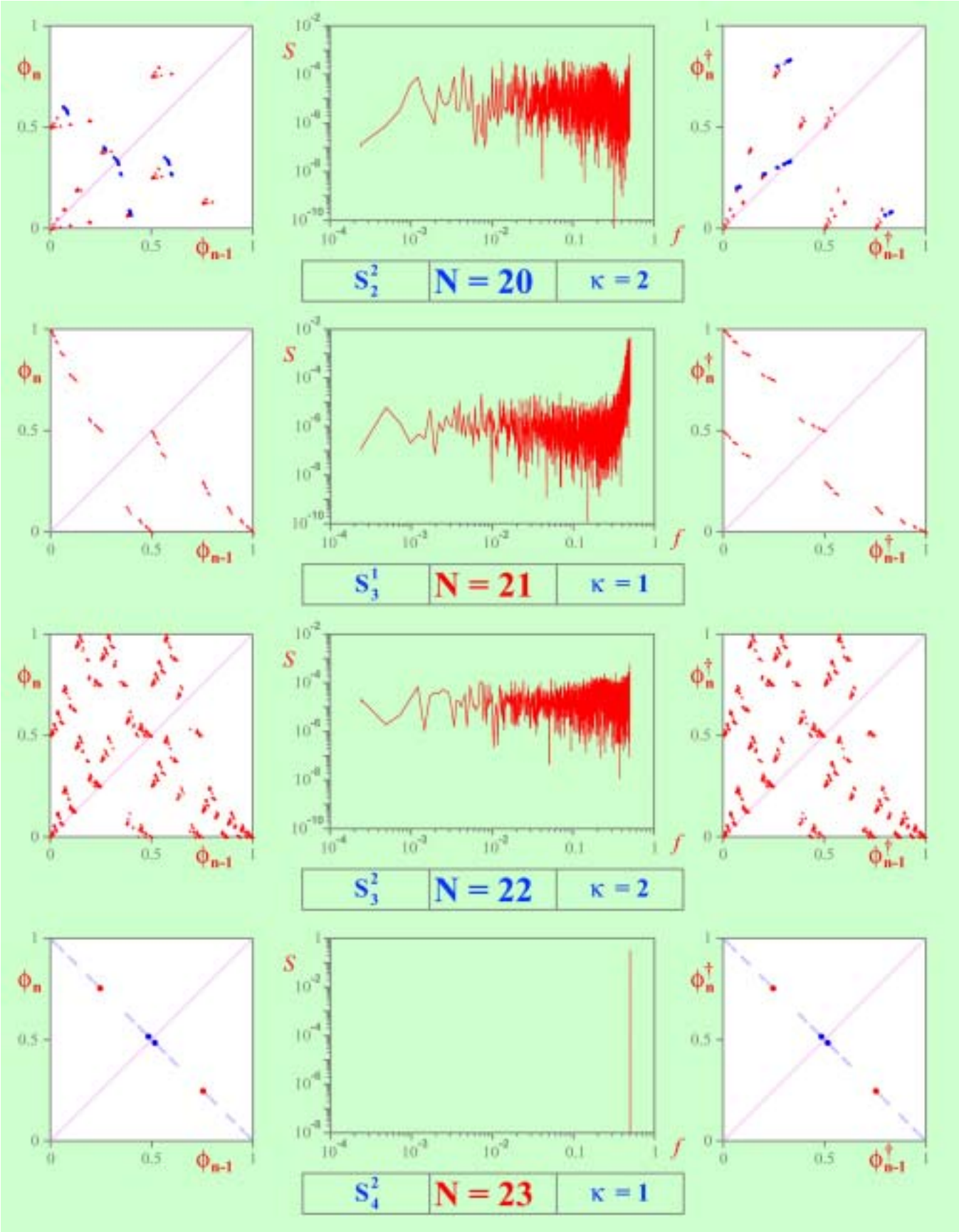


Table 2. (Continued)

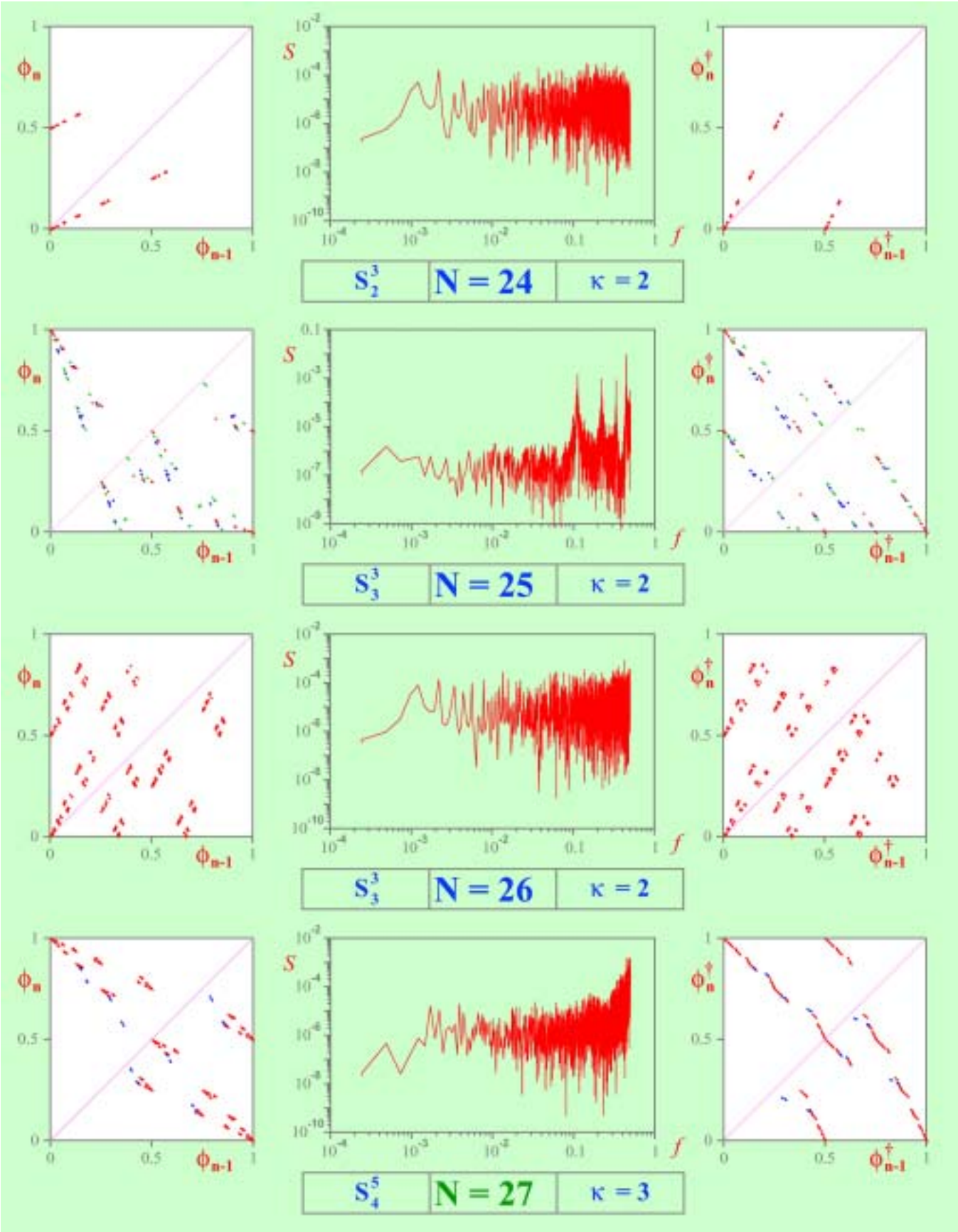


Table 2. (Continued)

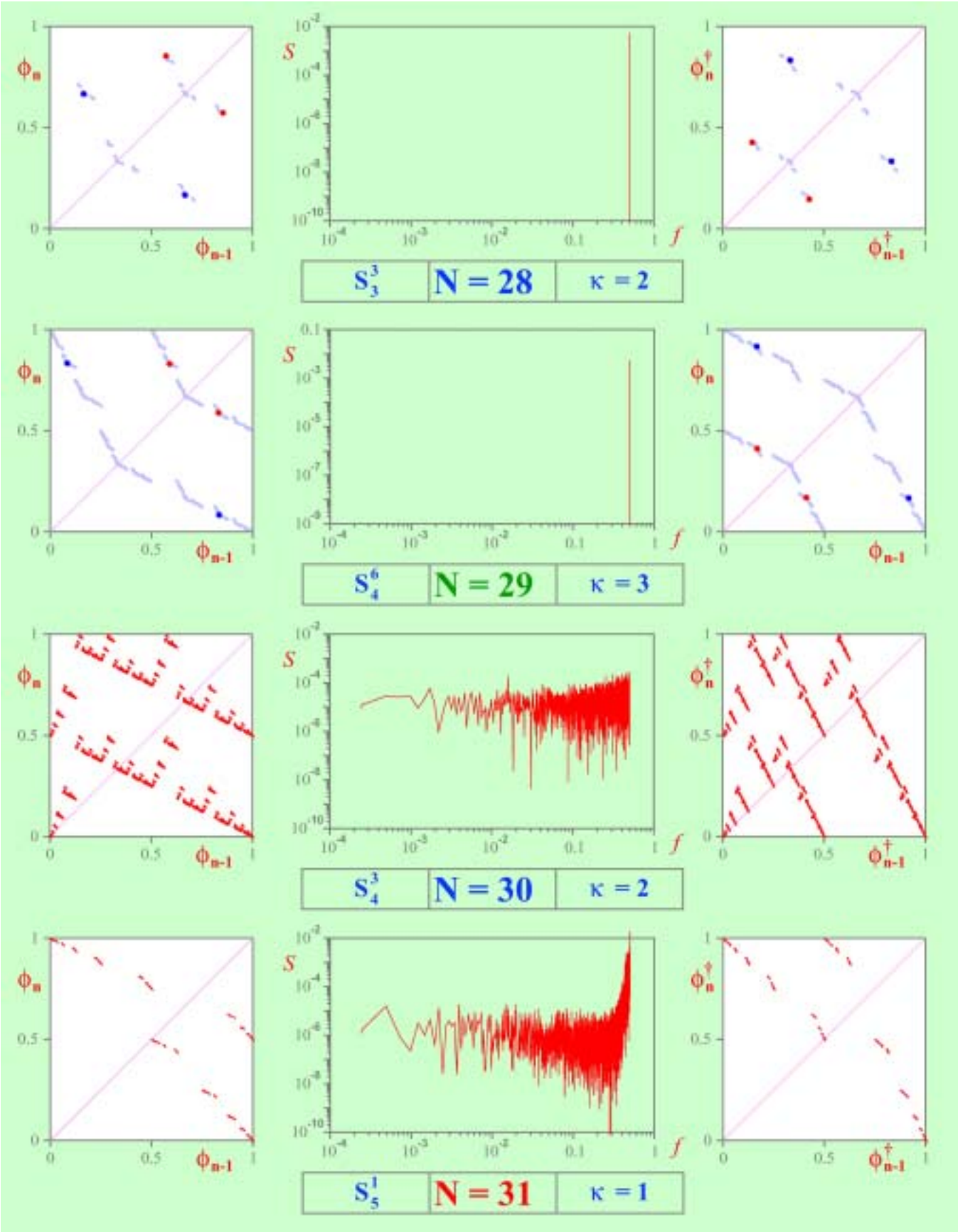


Table 2. (Continued)

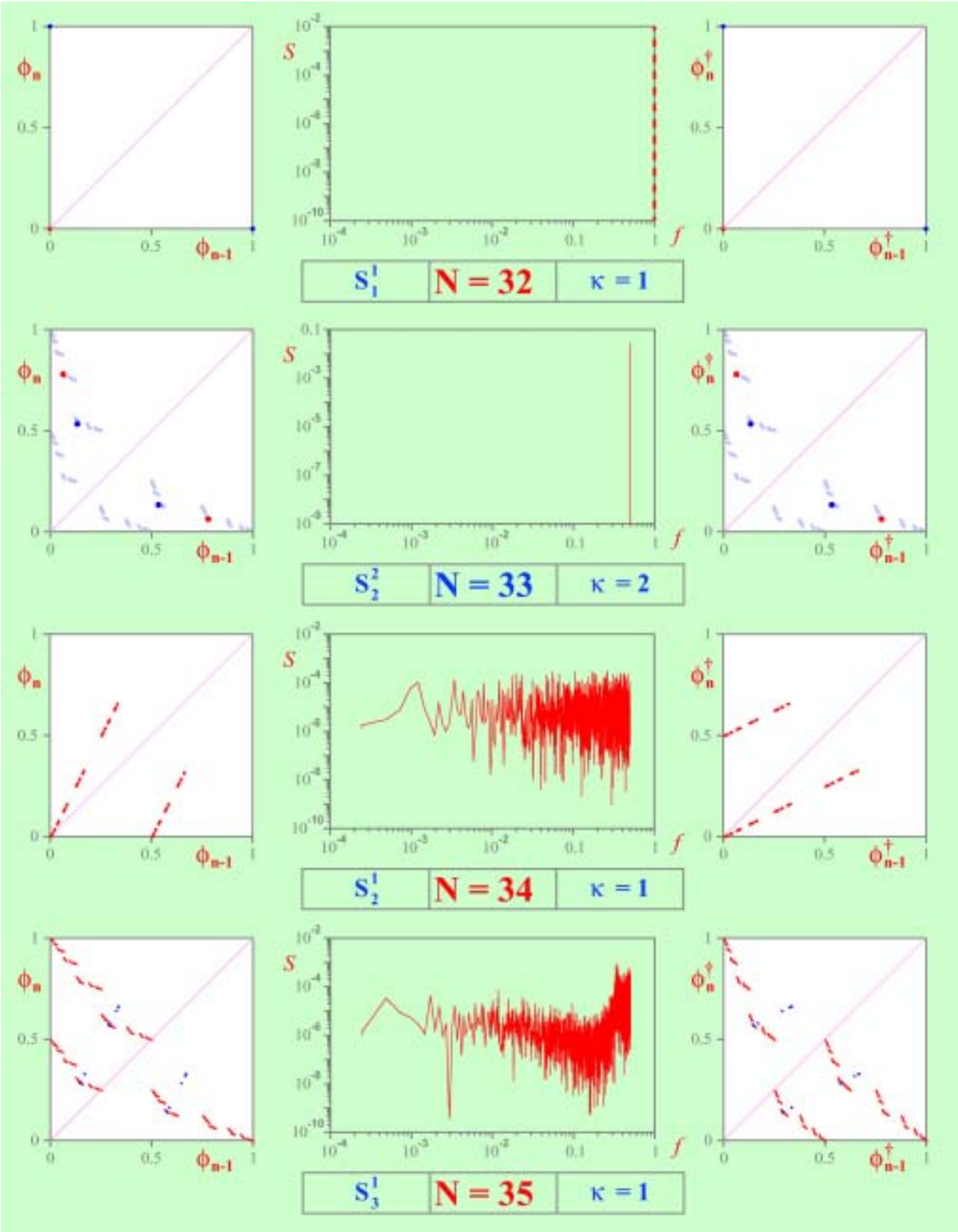


Table 2. (Continued)

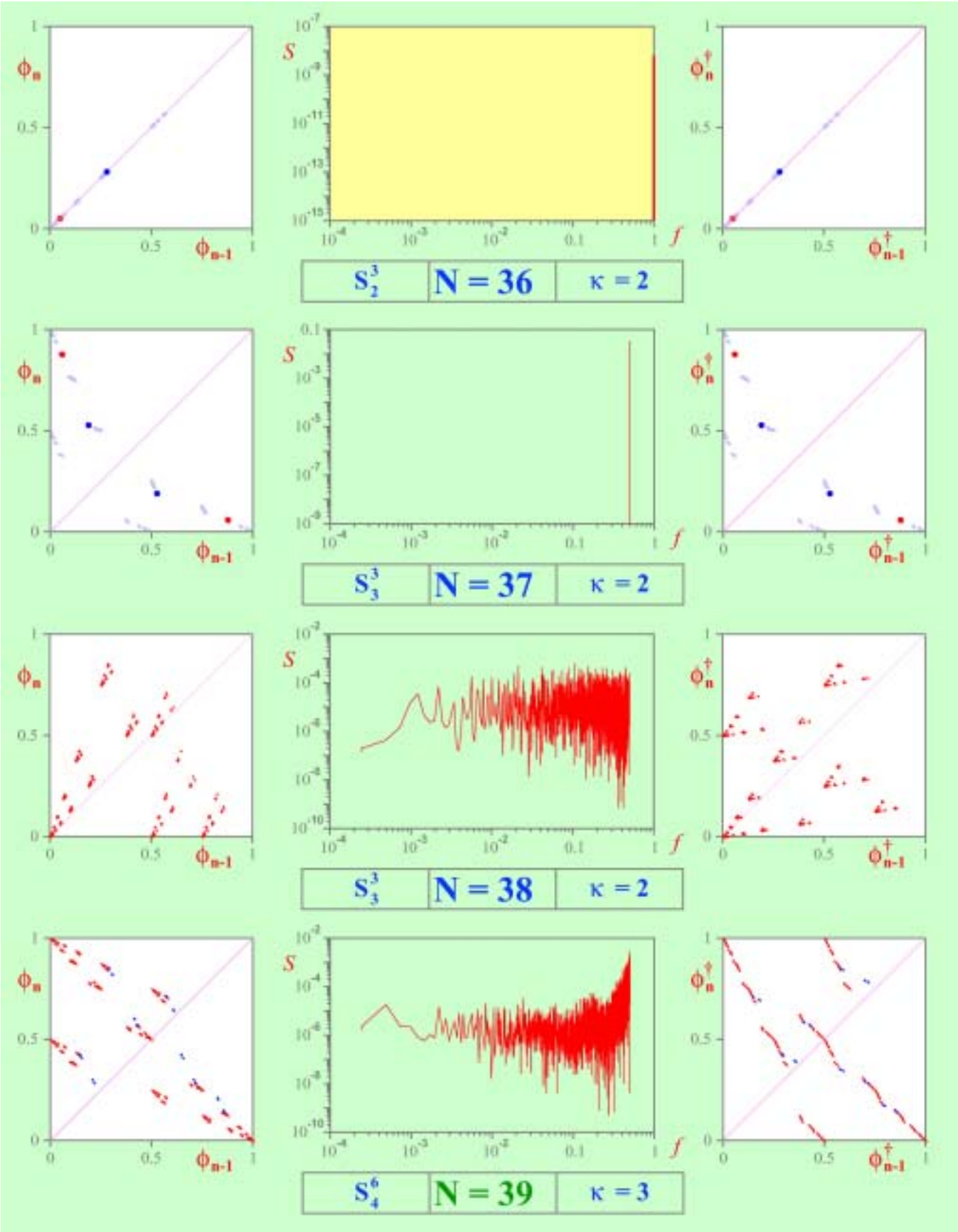


Table 2. (Continued)

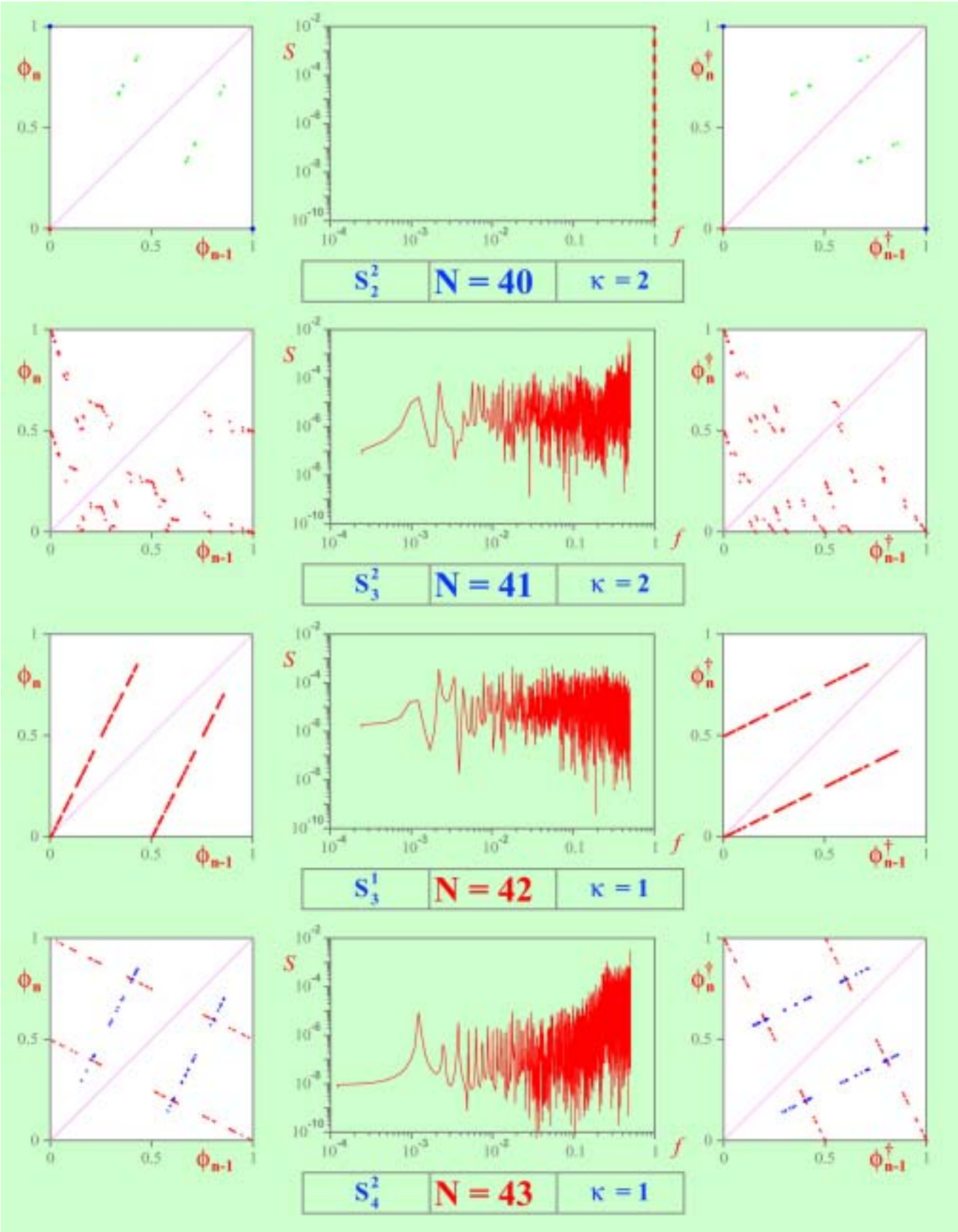


Table 2. (Continued)

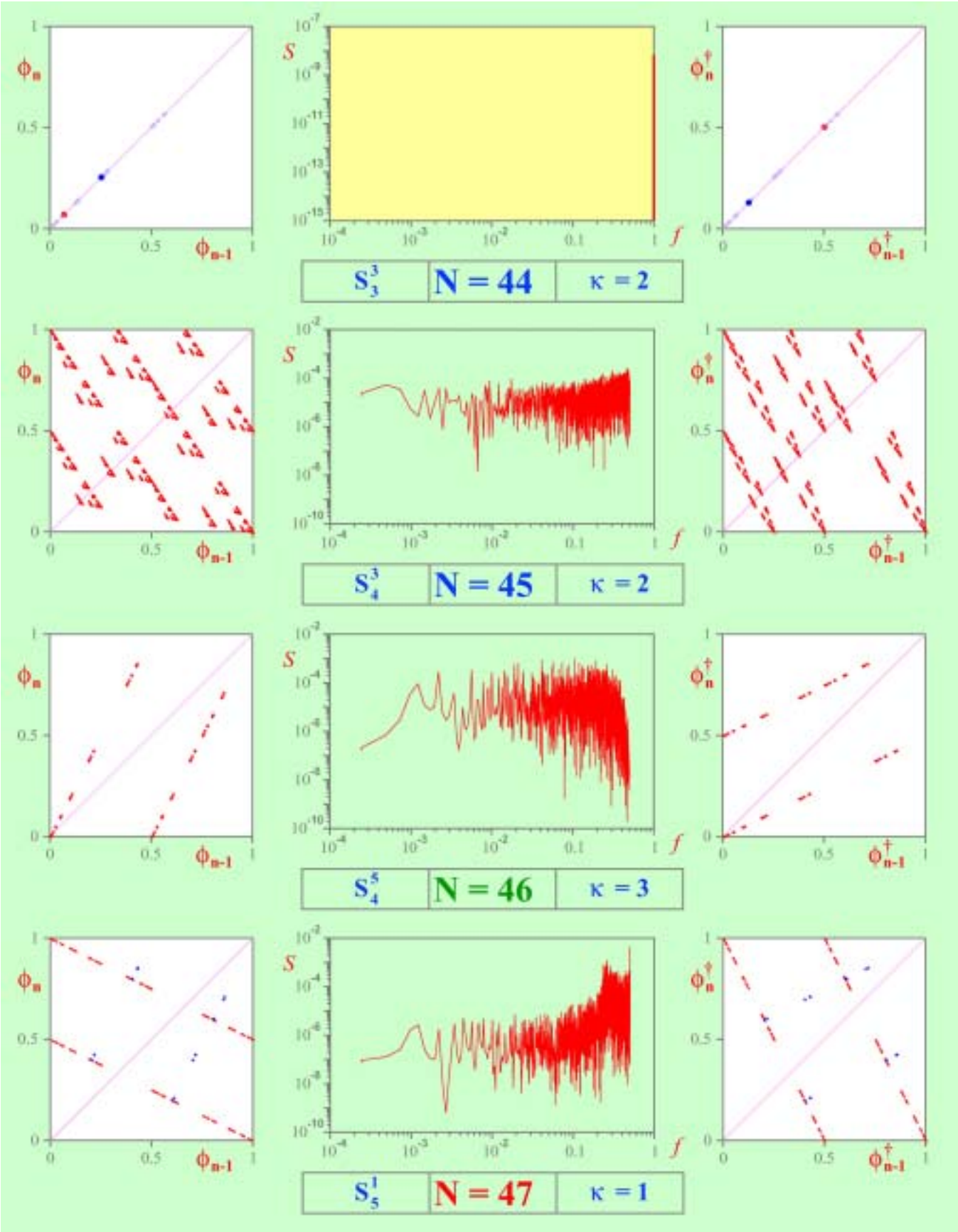


Table 2. (Continued)

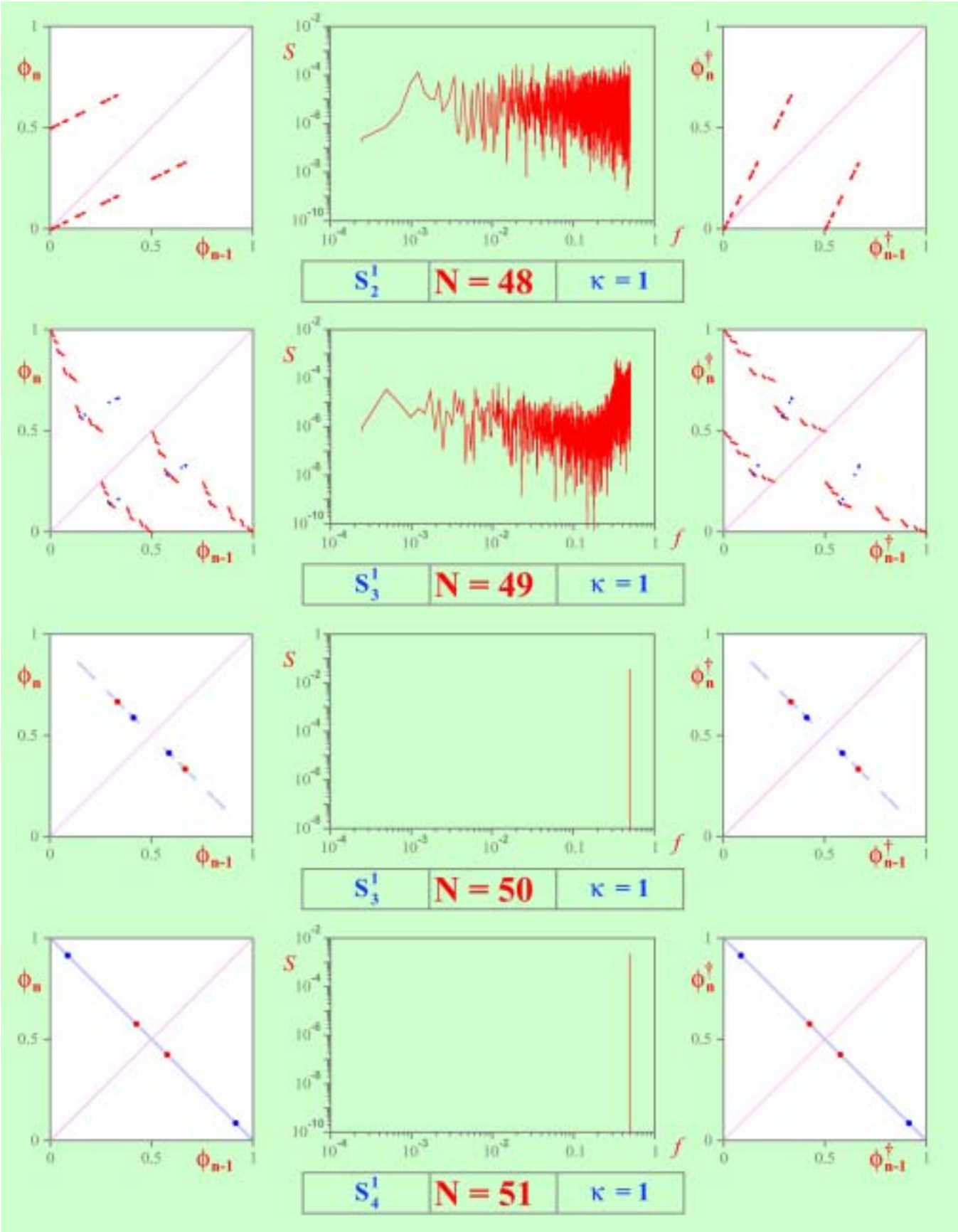


Table 2. (Continued)

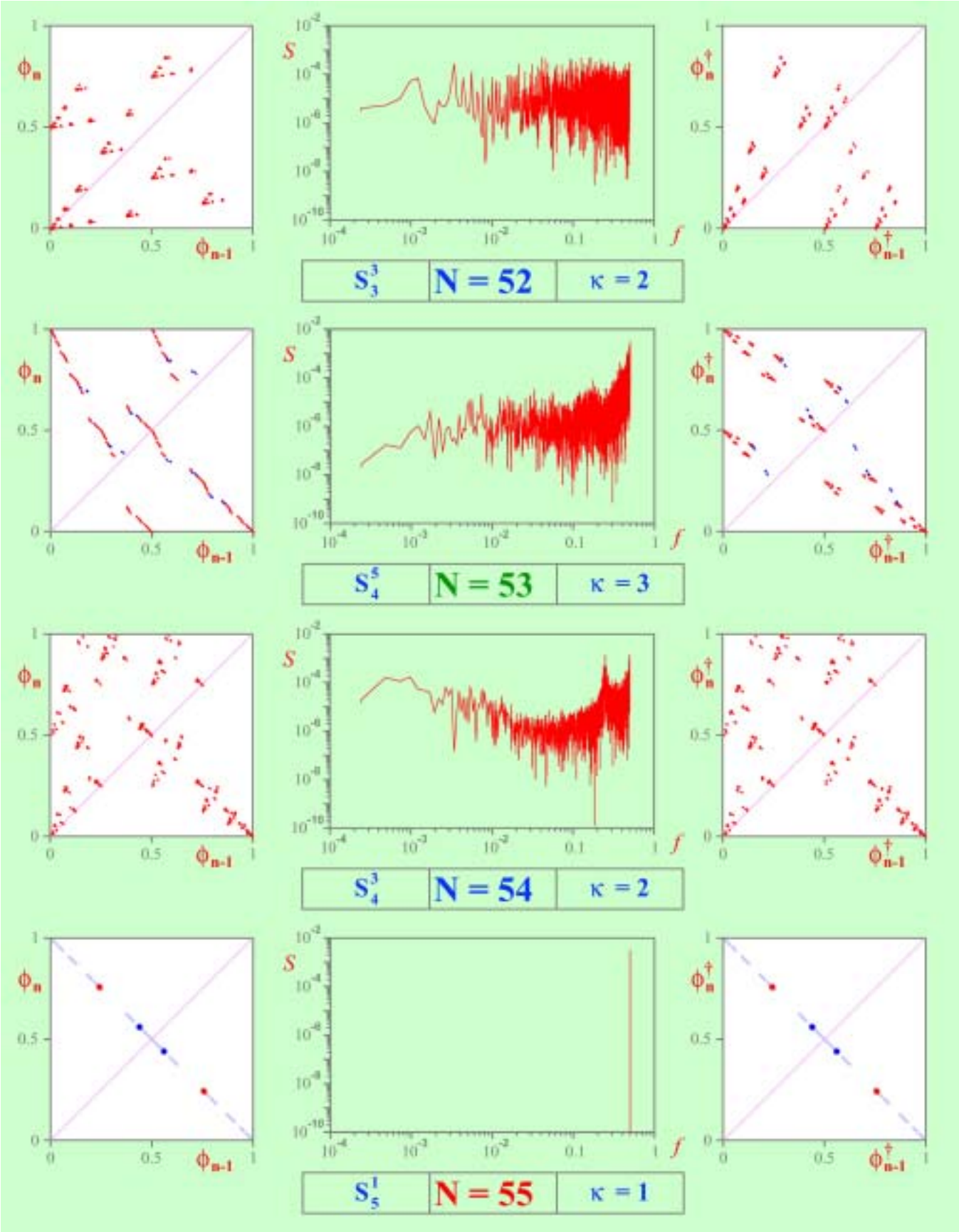


Table 2. (Continued)

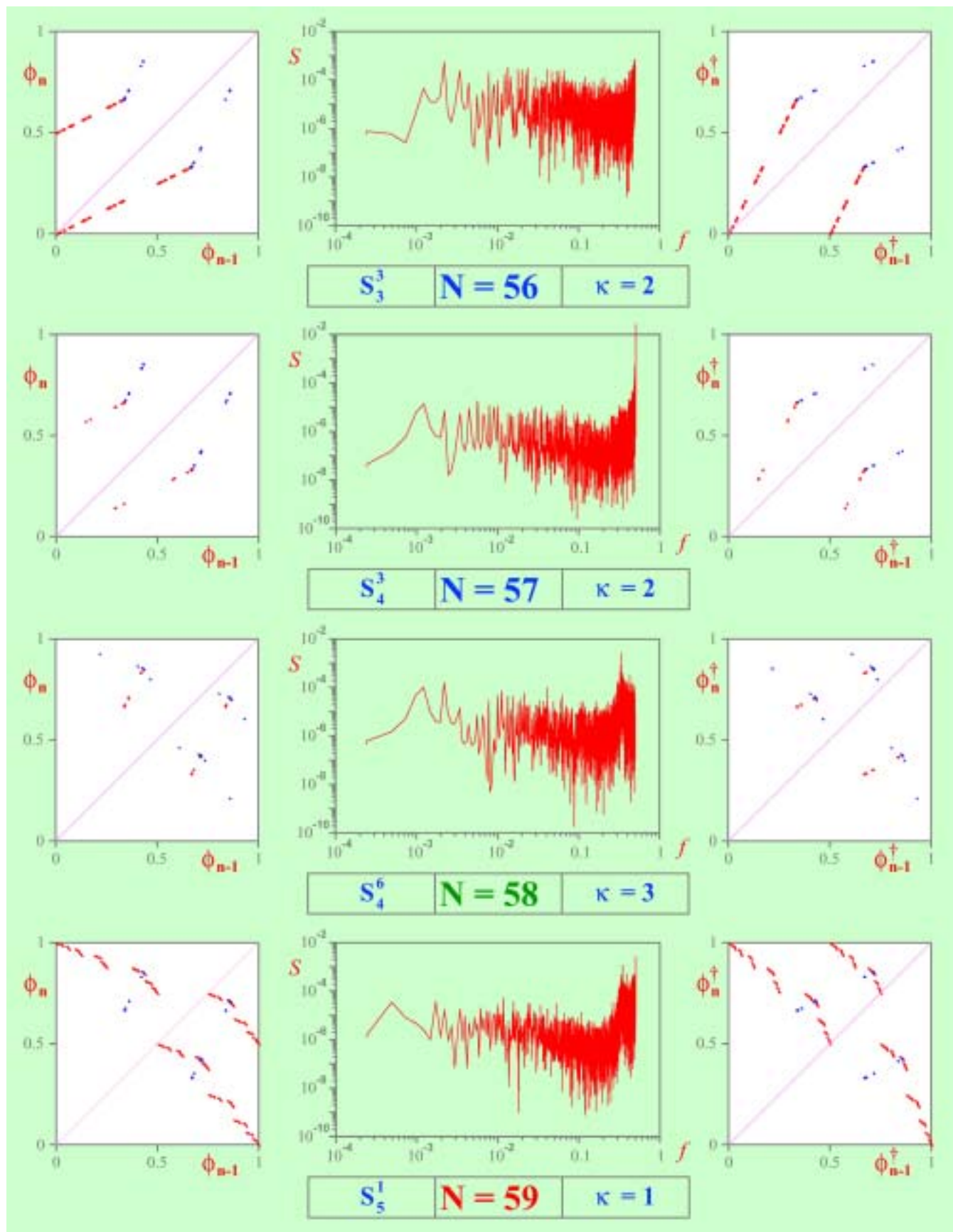


Table 2. (Continued)

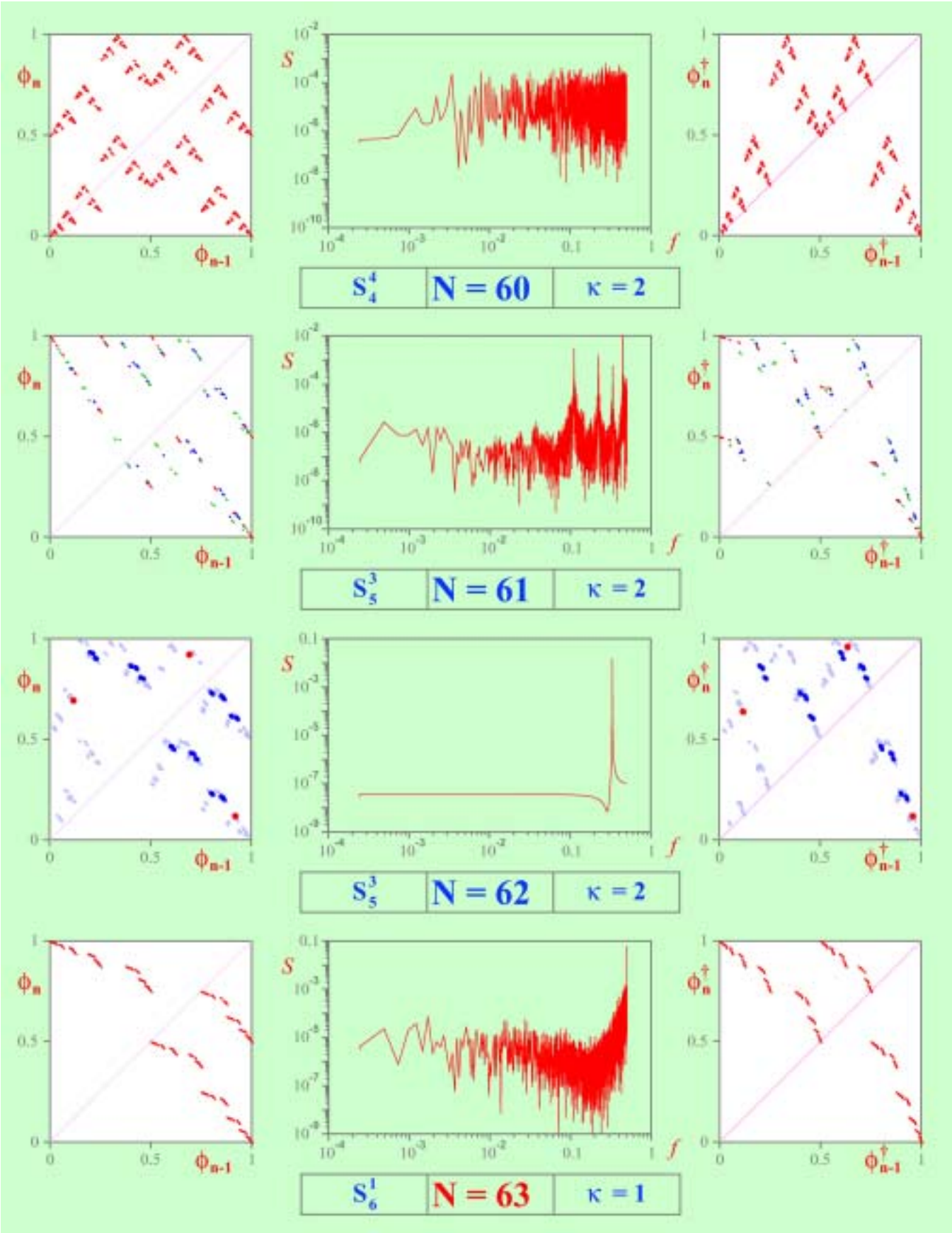


Table 2. (Continued)

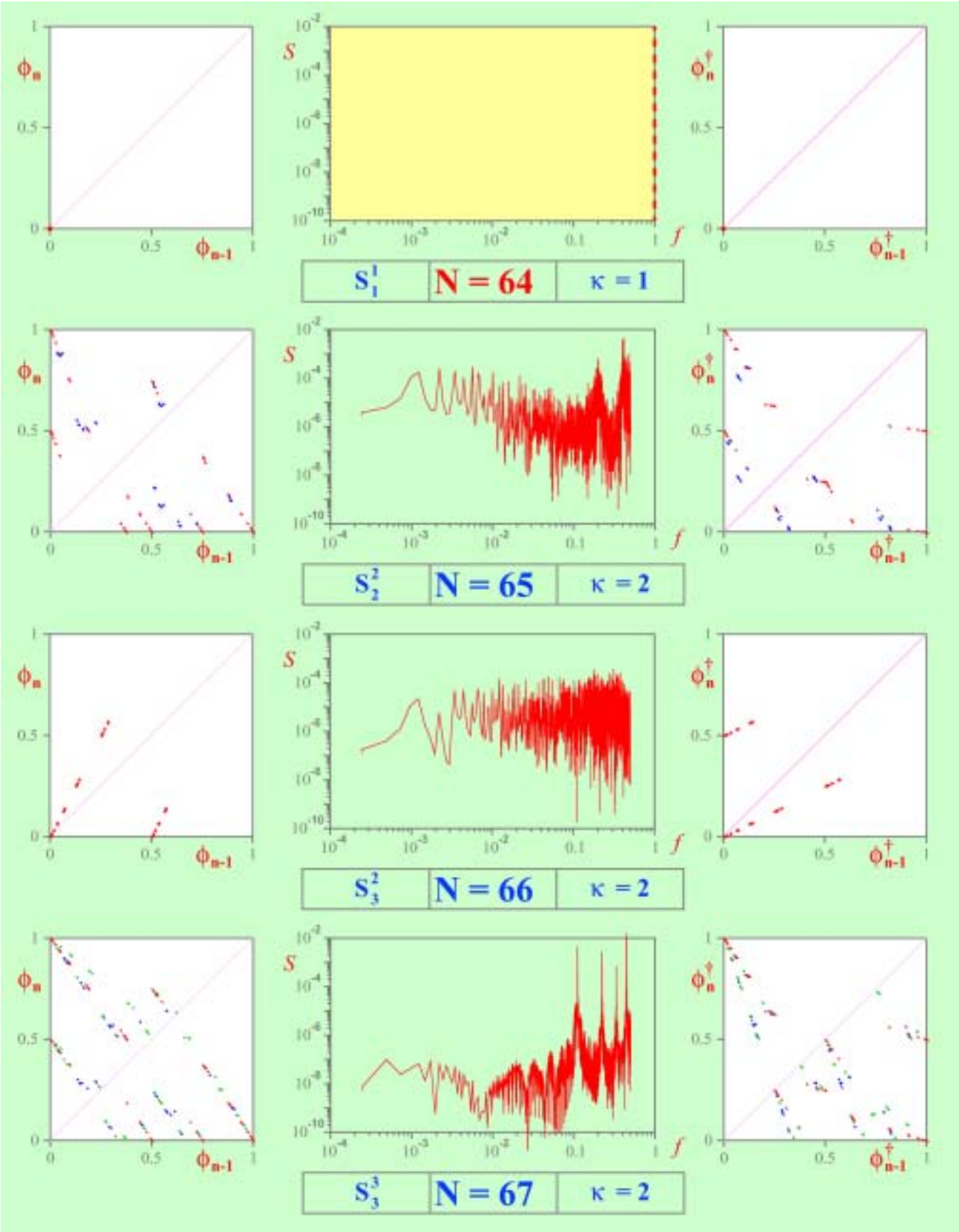


Table 2. (Continued)

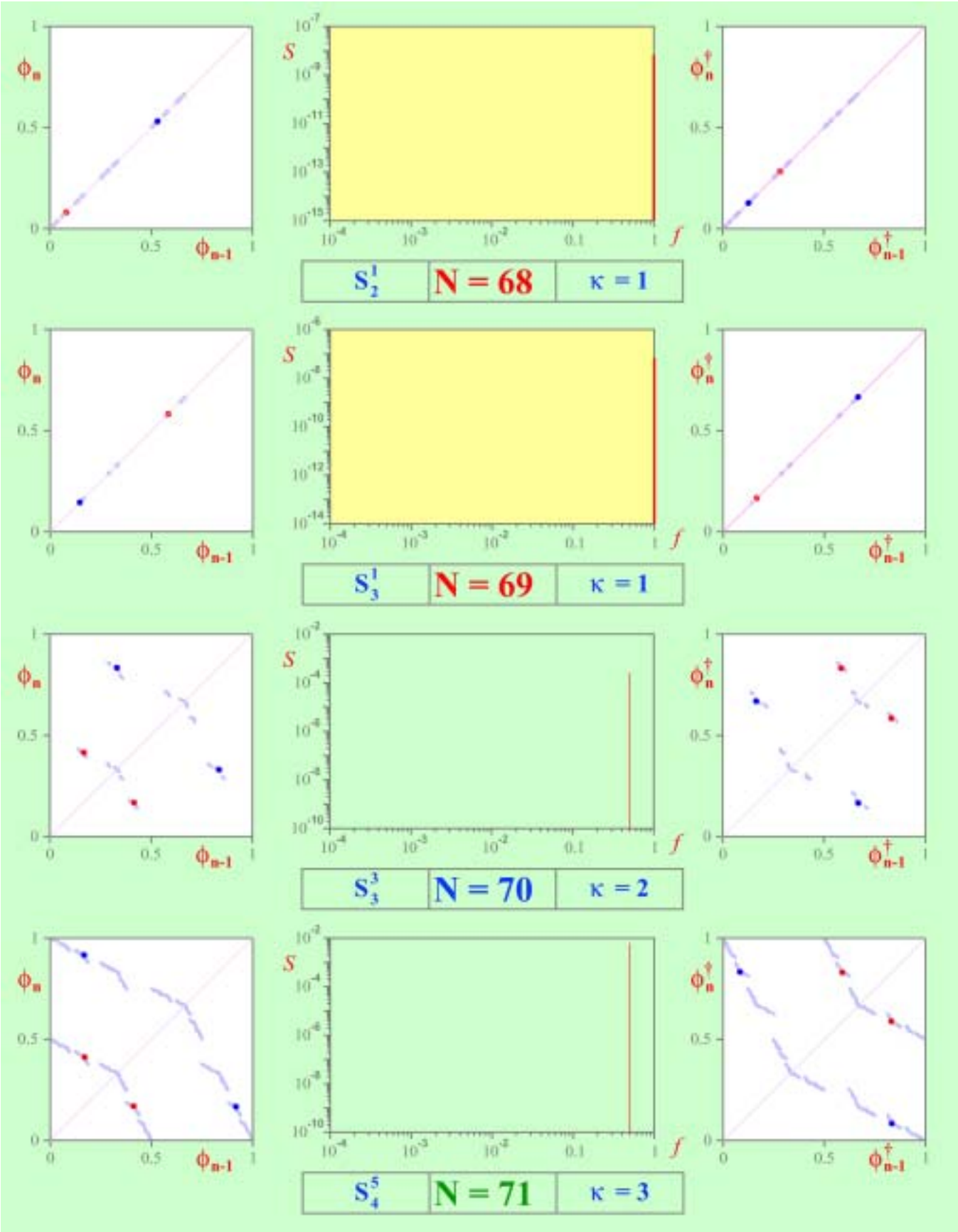


Table 2. (Continued)

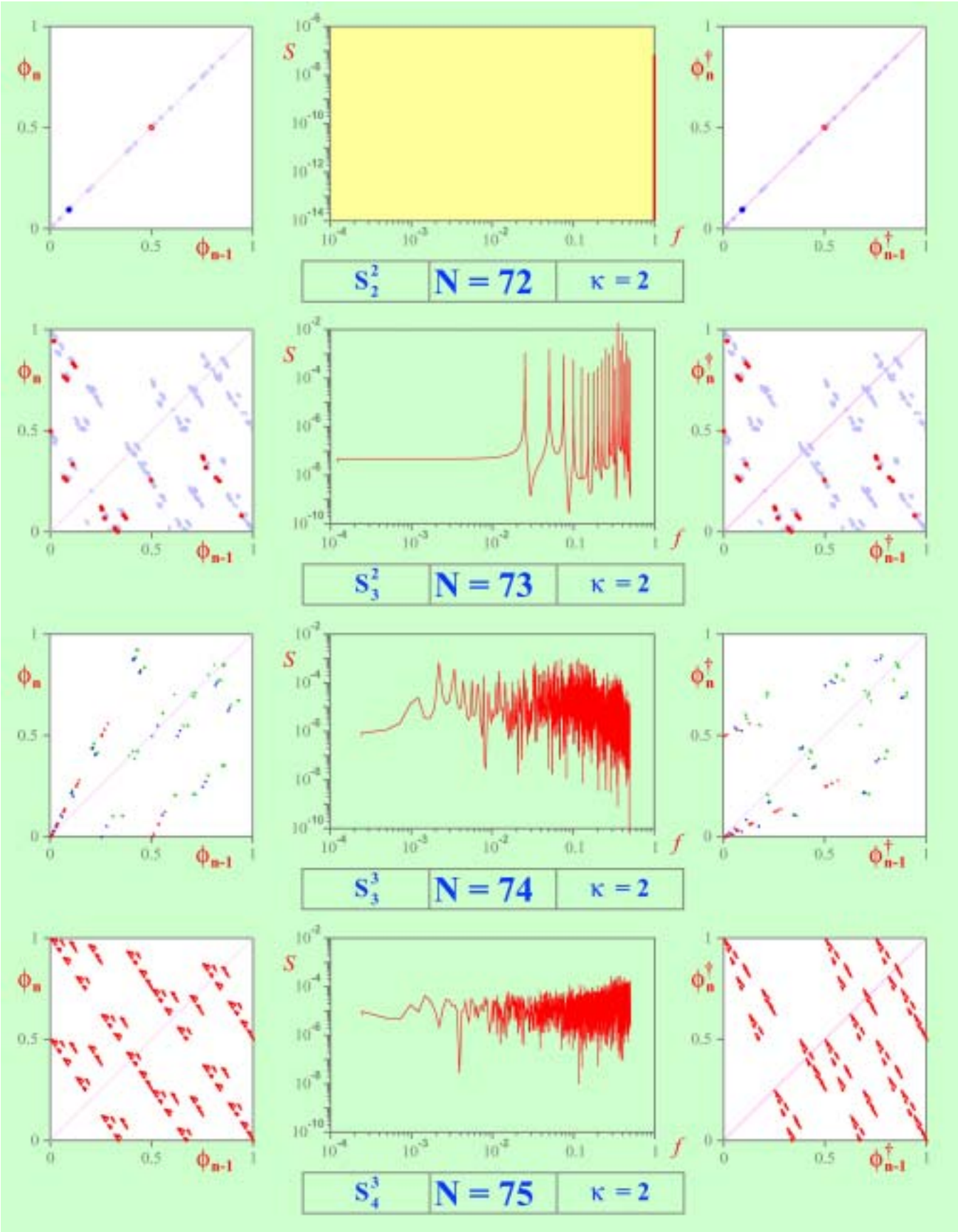


Table 2. (Continued)

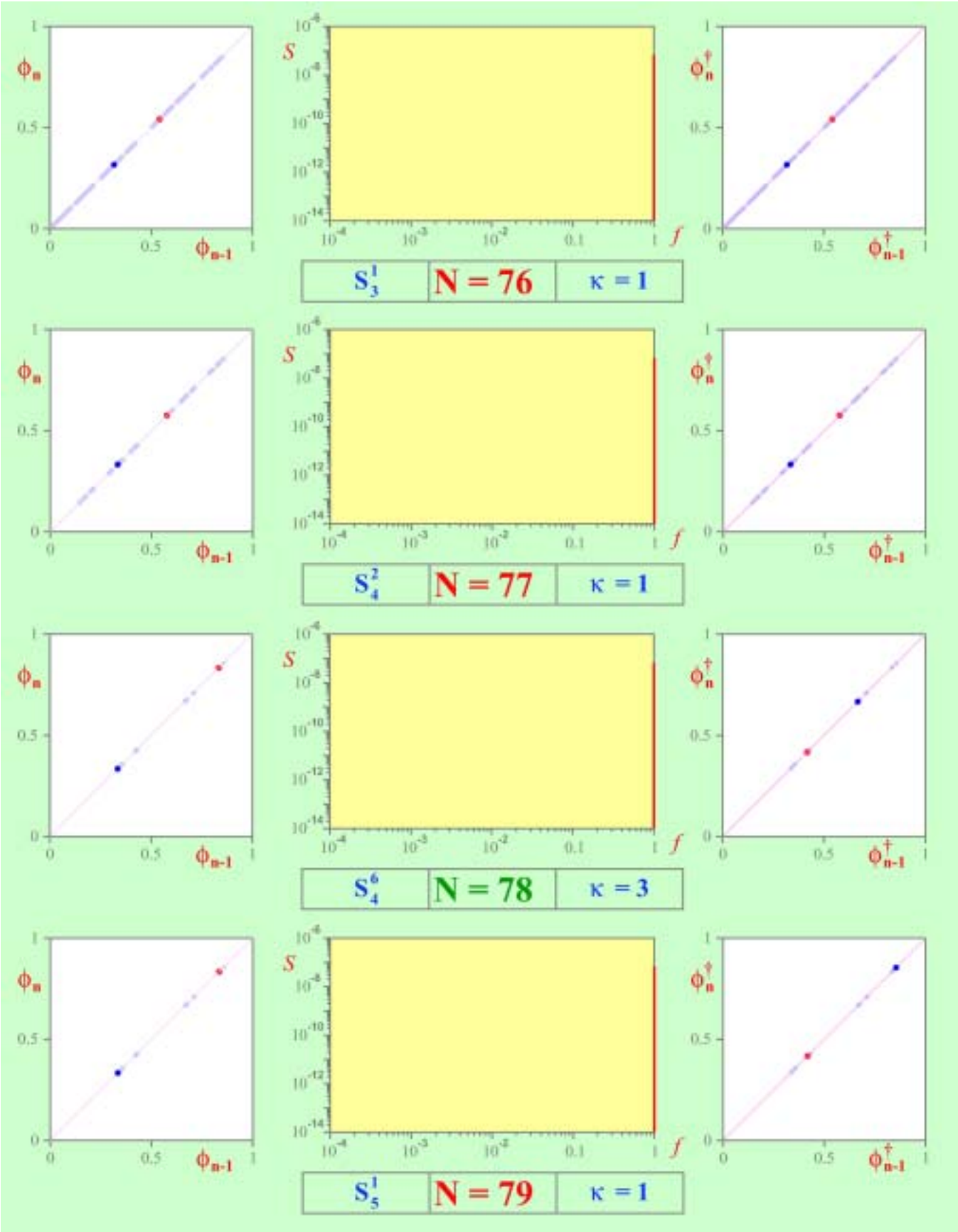


Table 2. (Continued)

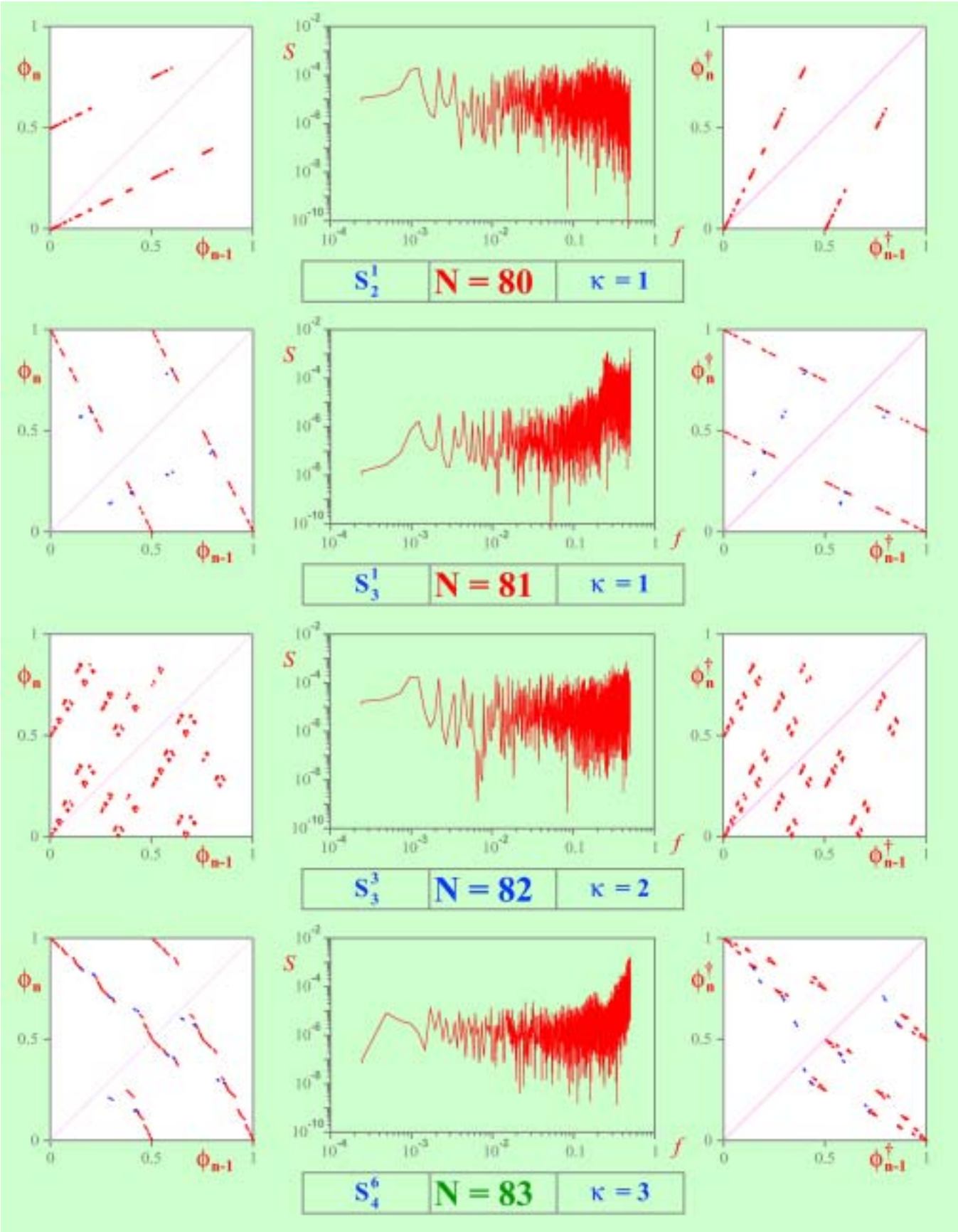


Table 2. (Continued)

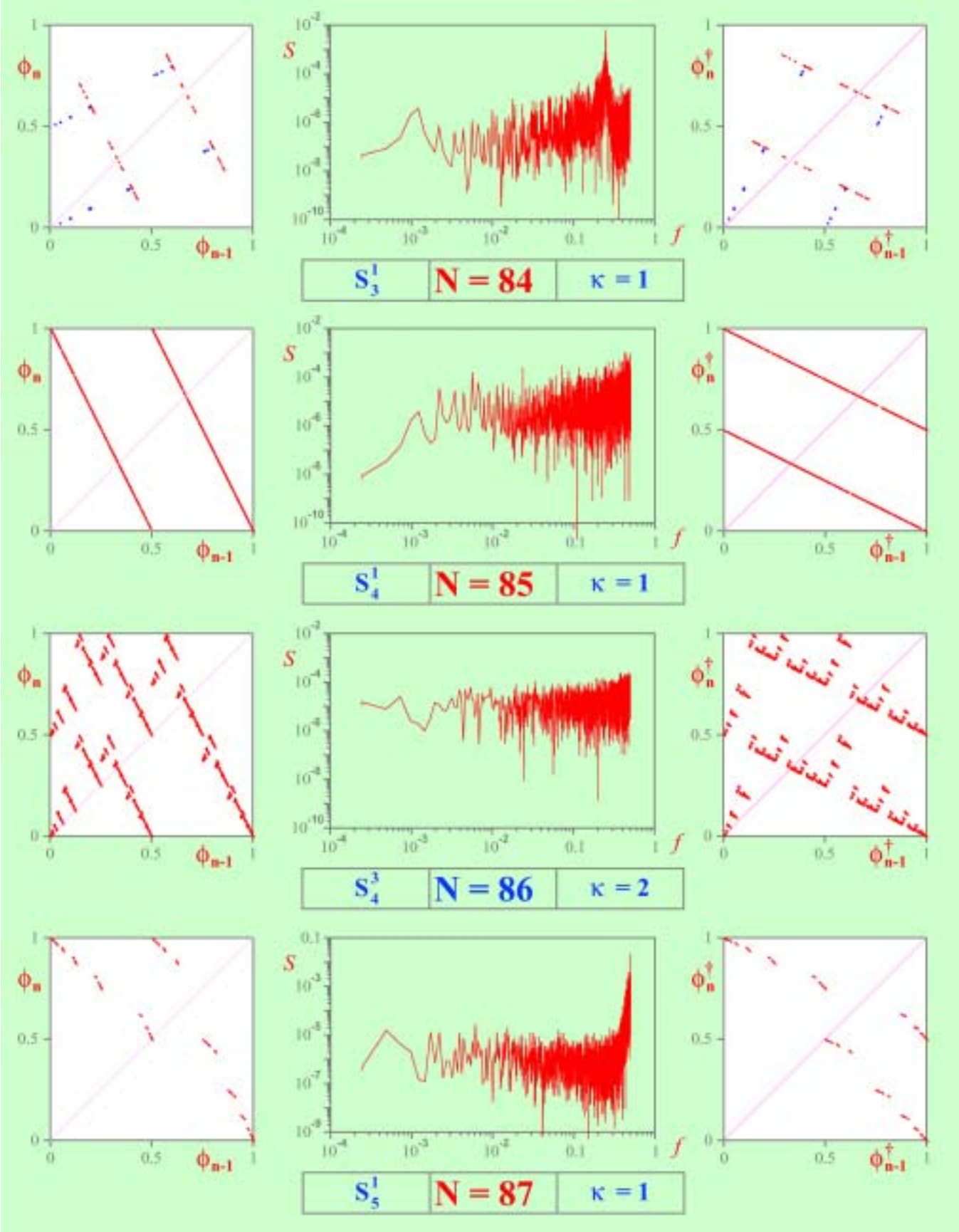


Table 2. (Continued)

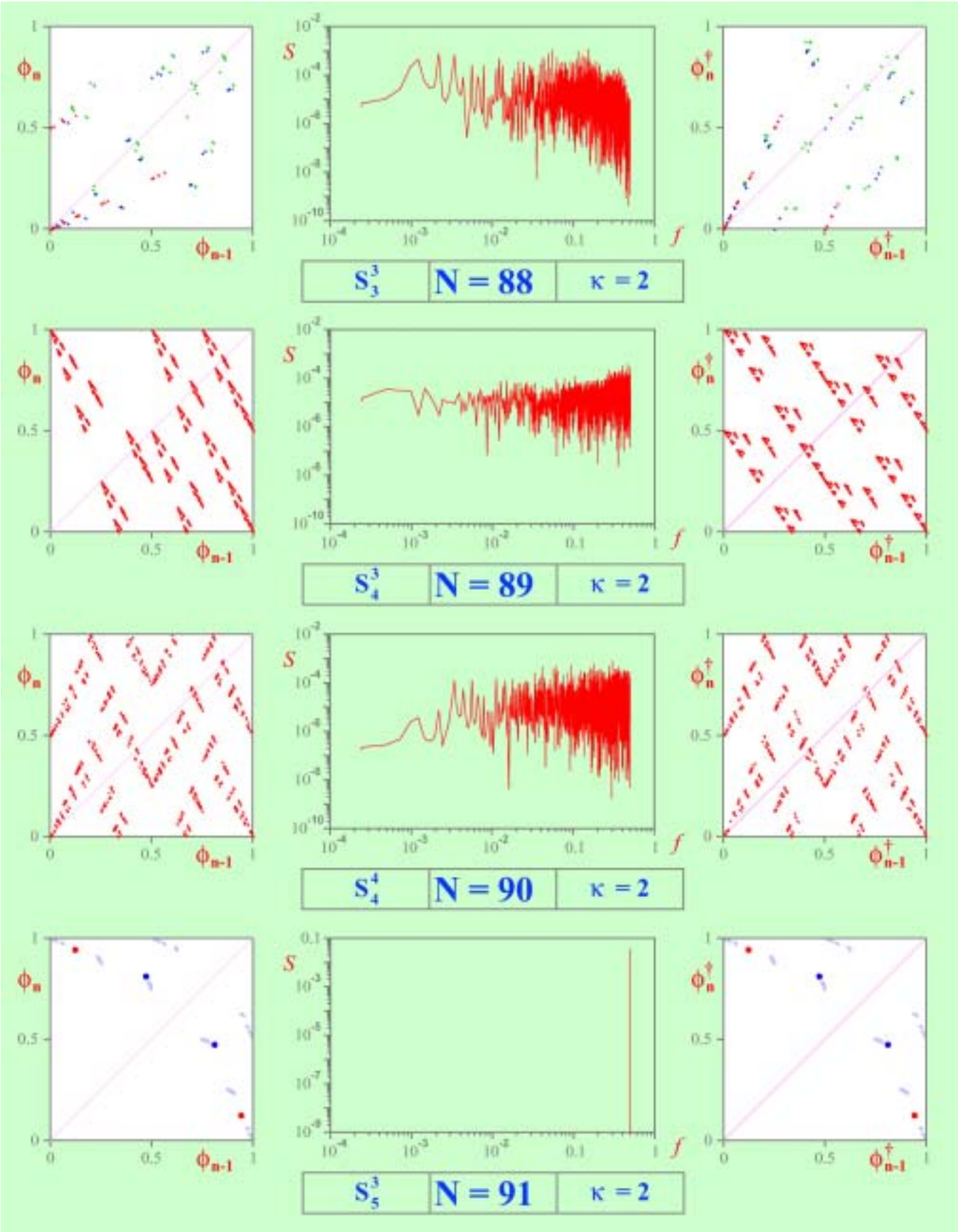


Table 2. (Continued)

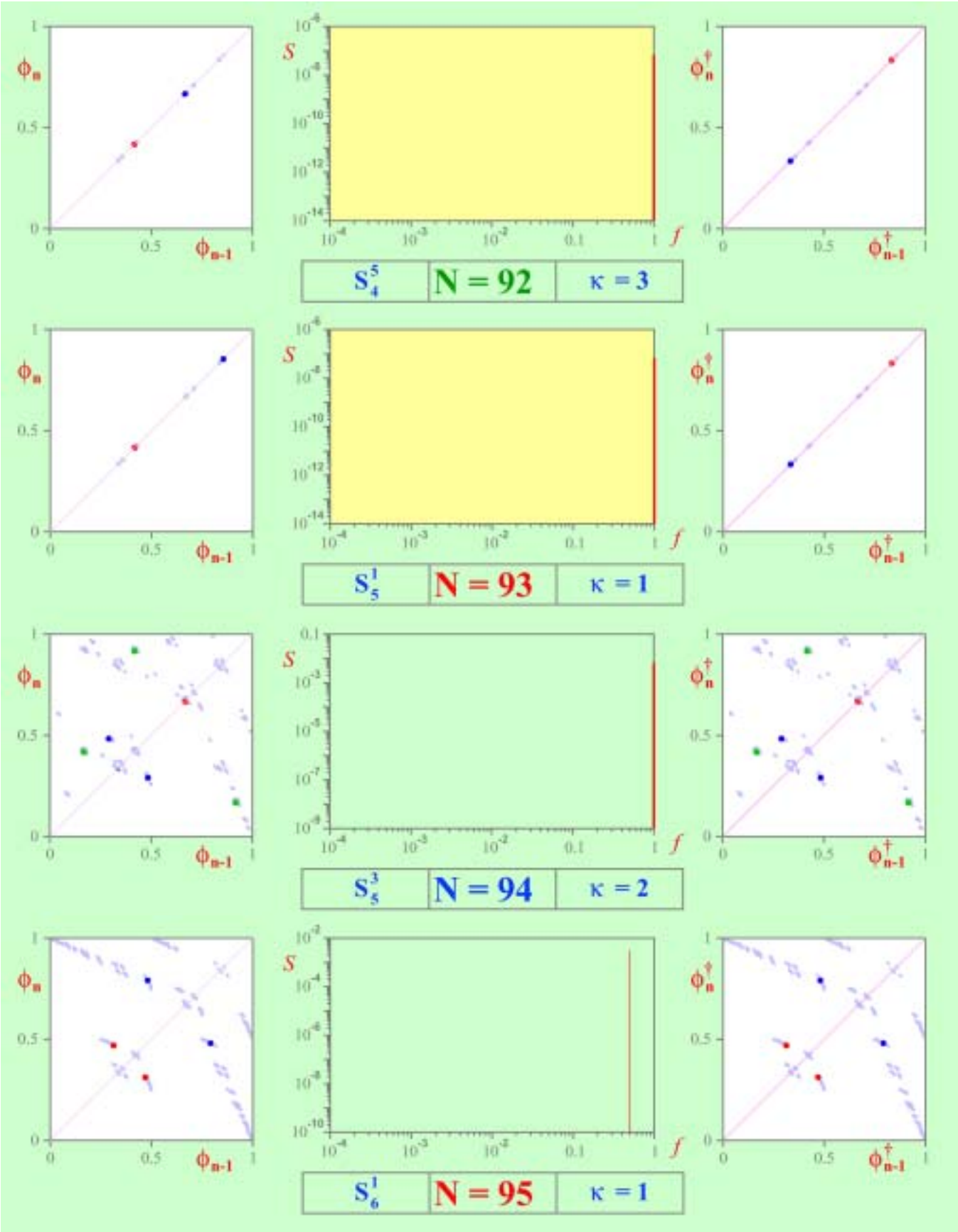


Table 2. (Continued)

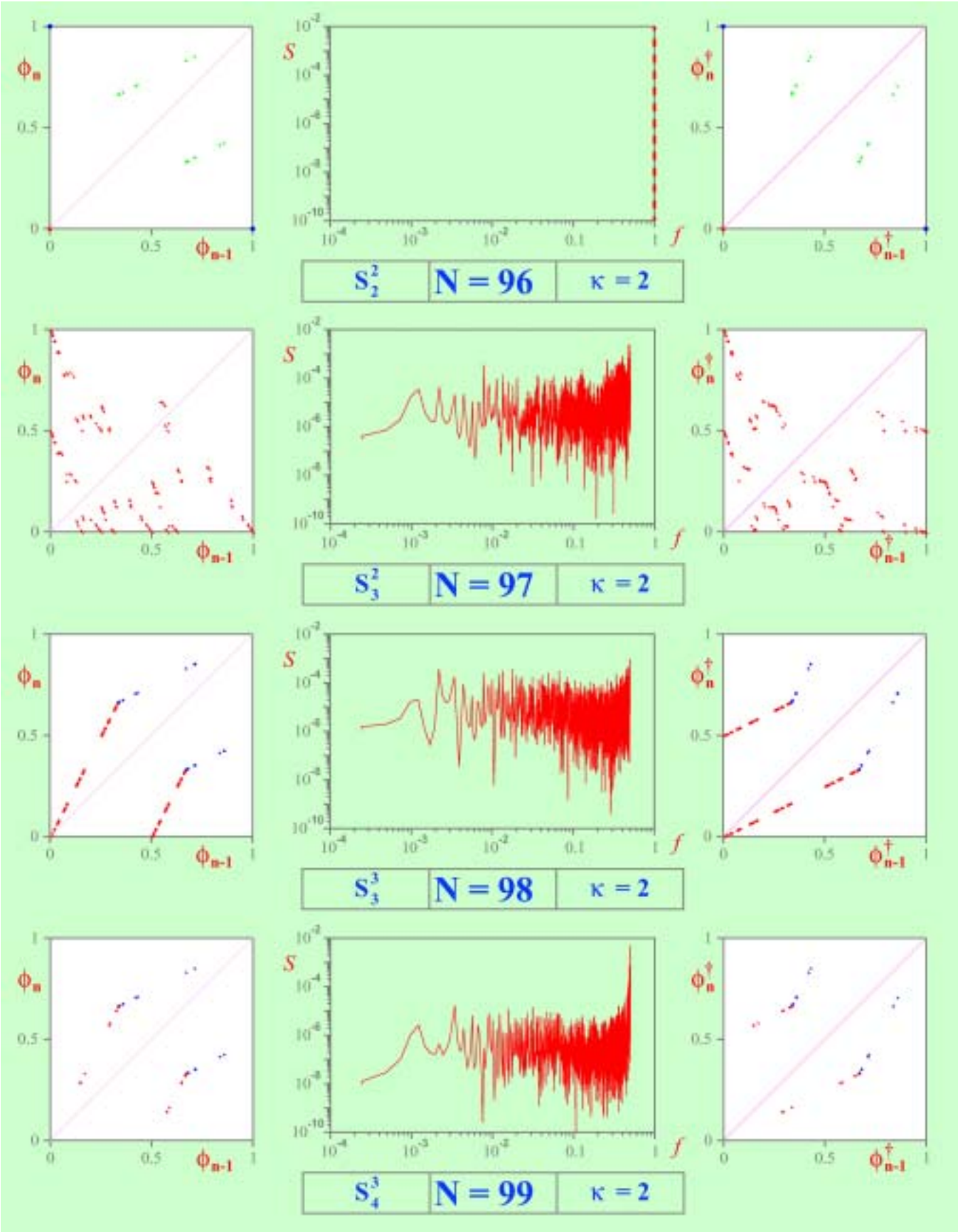


Table 2. (Continued)

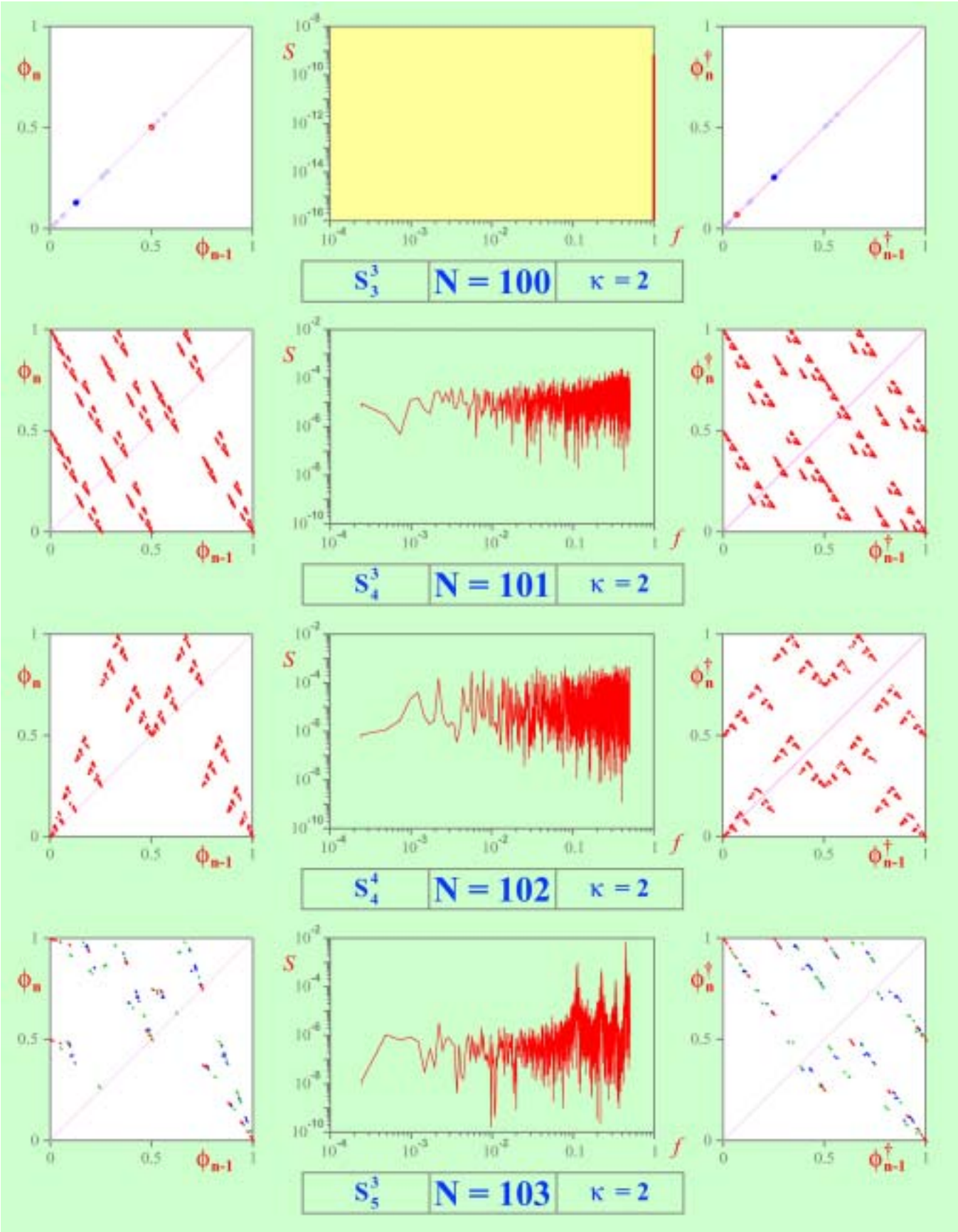


Table 2. (Continued)

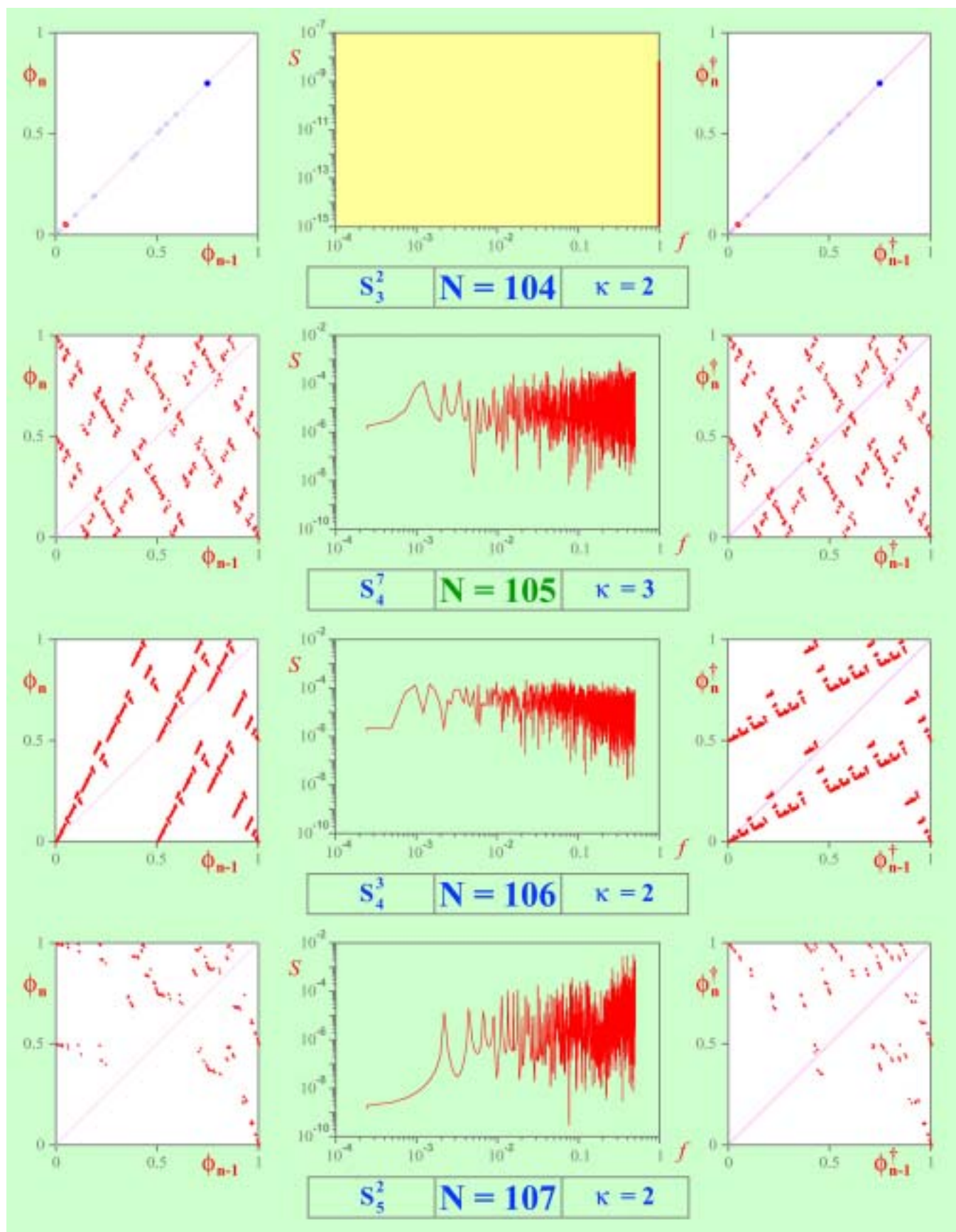


Table 2. (Continued)

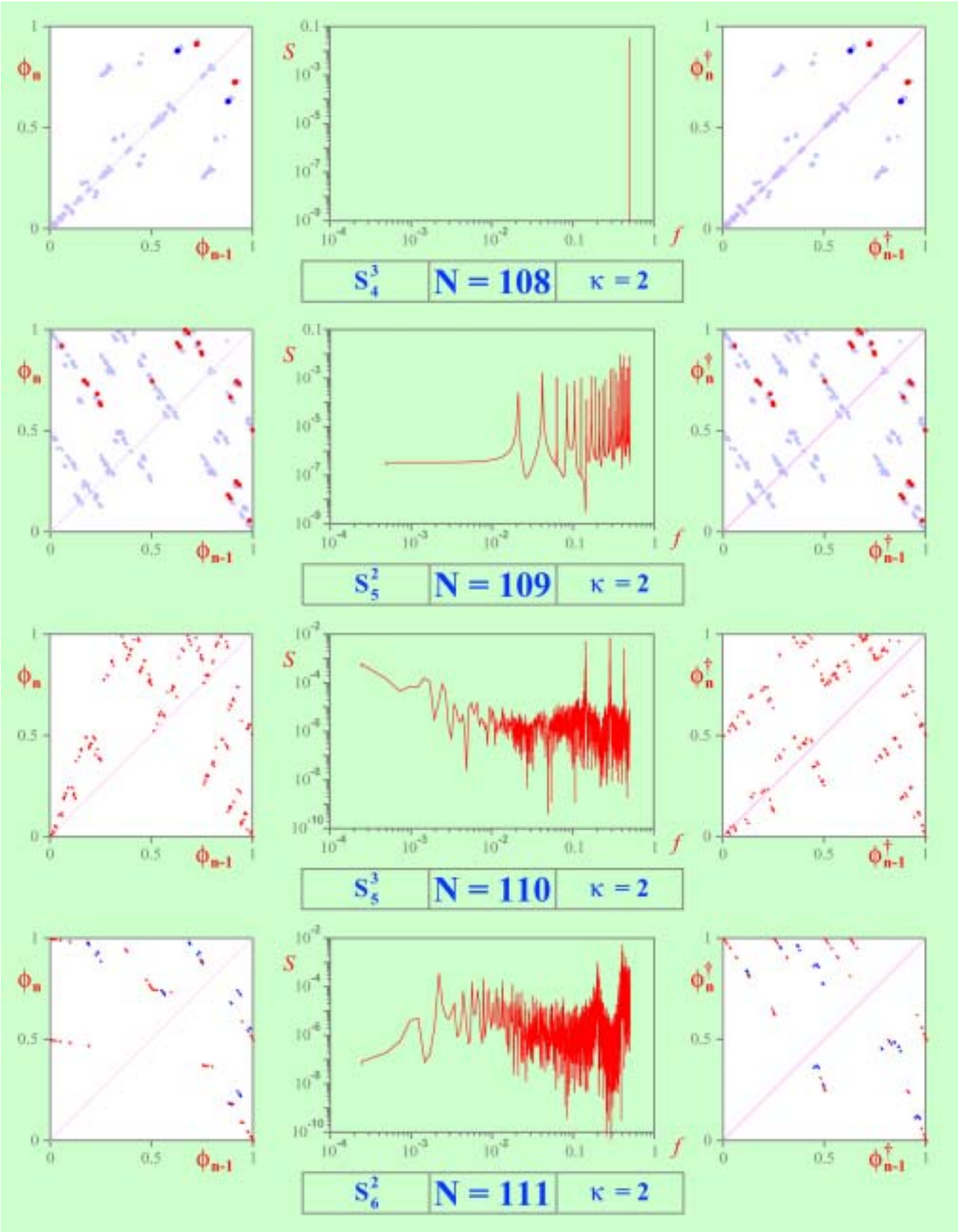


Table 2. (Continued)

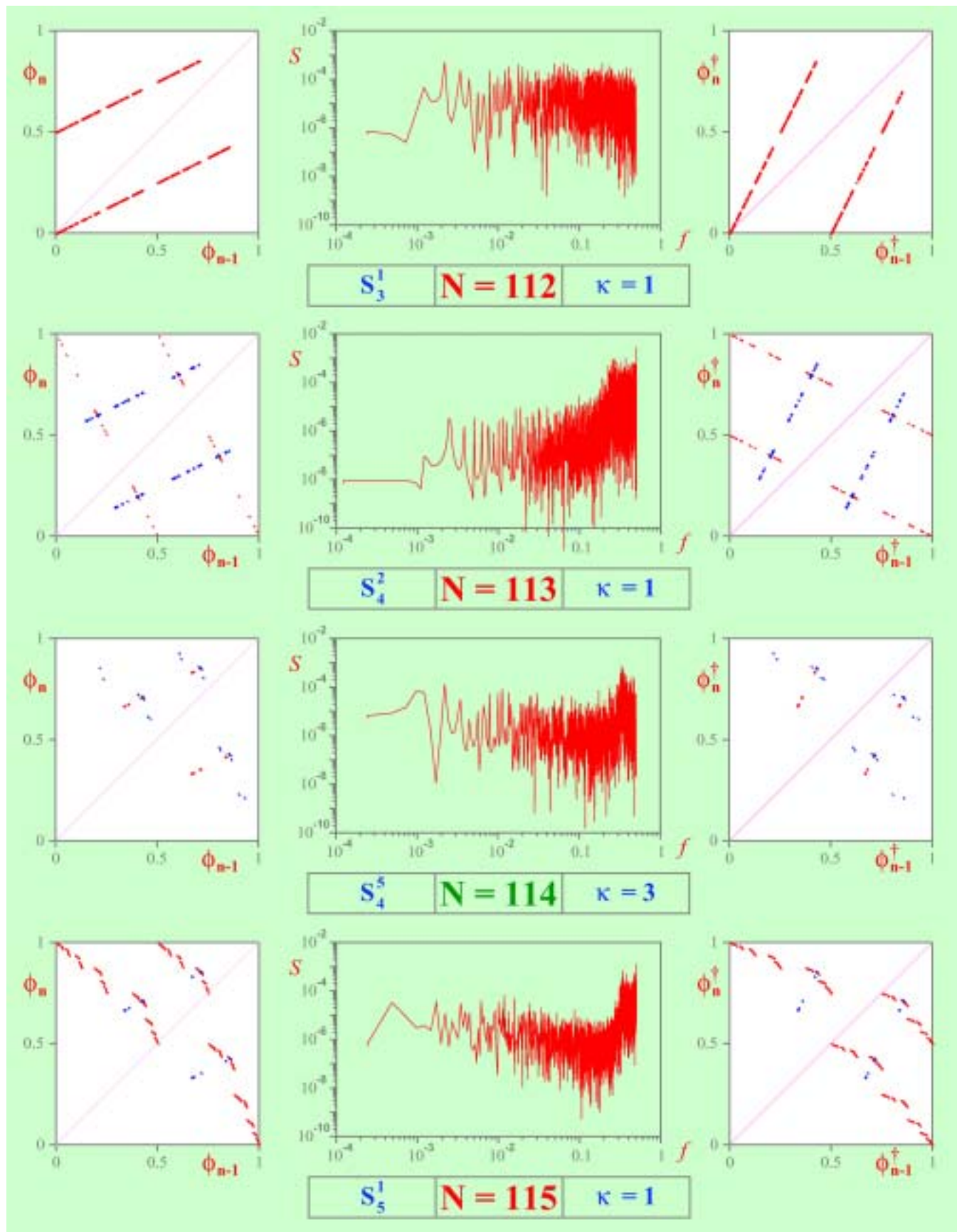


Table 2. (Continued)

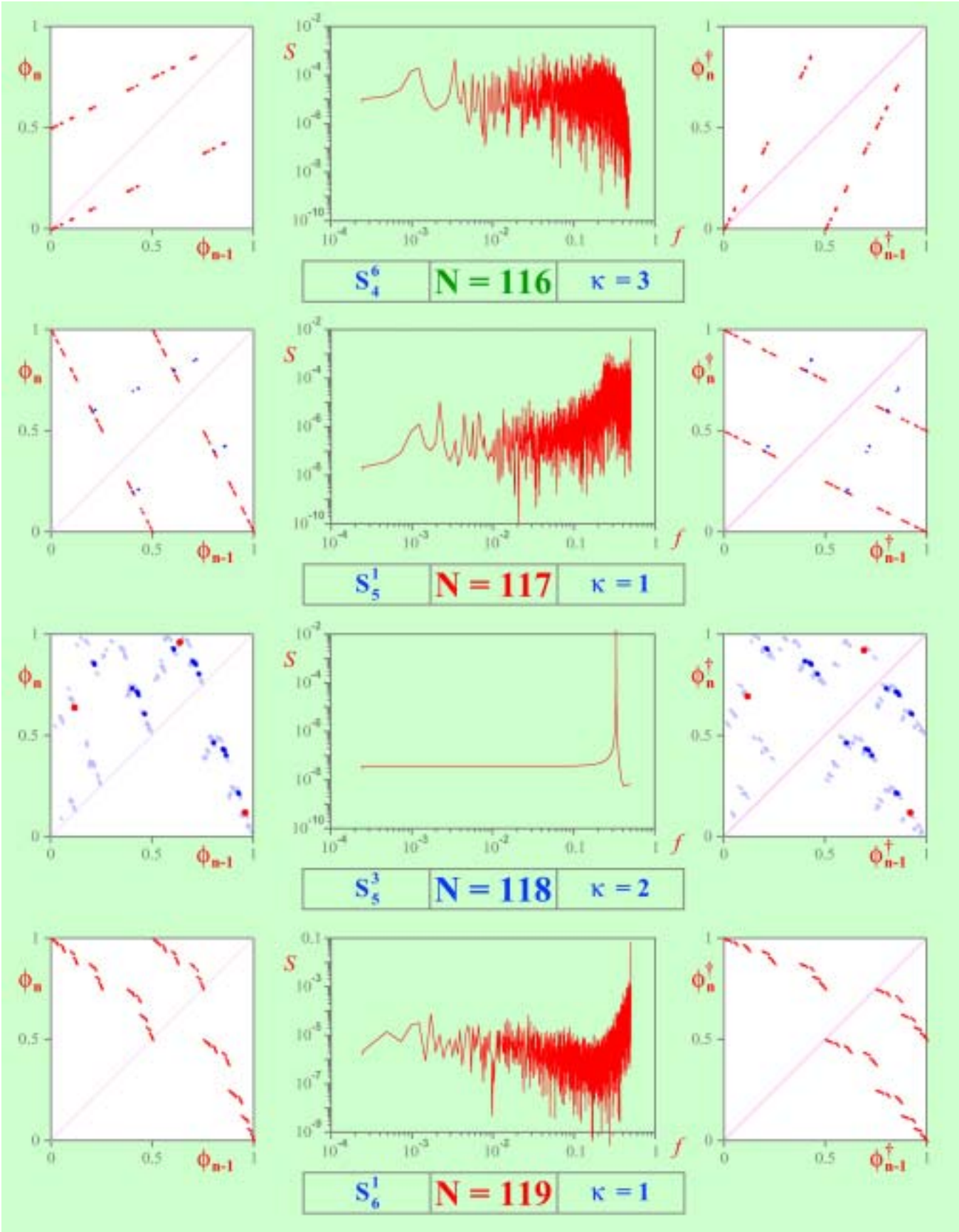


Table 2. (Continued)

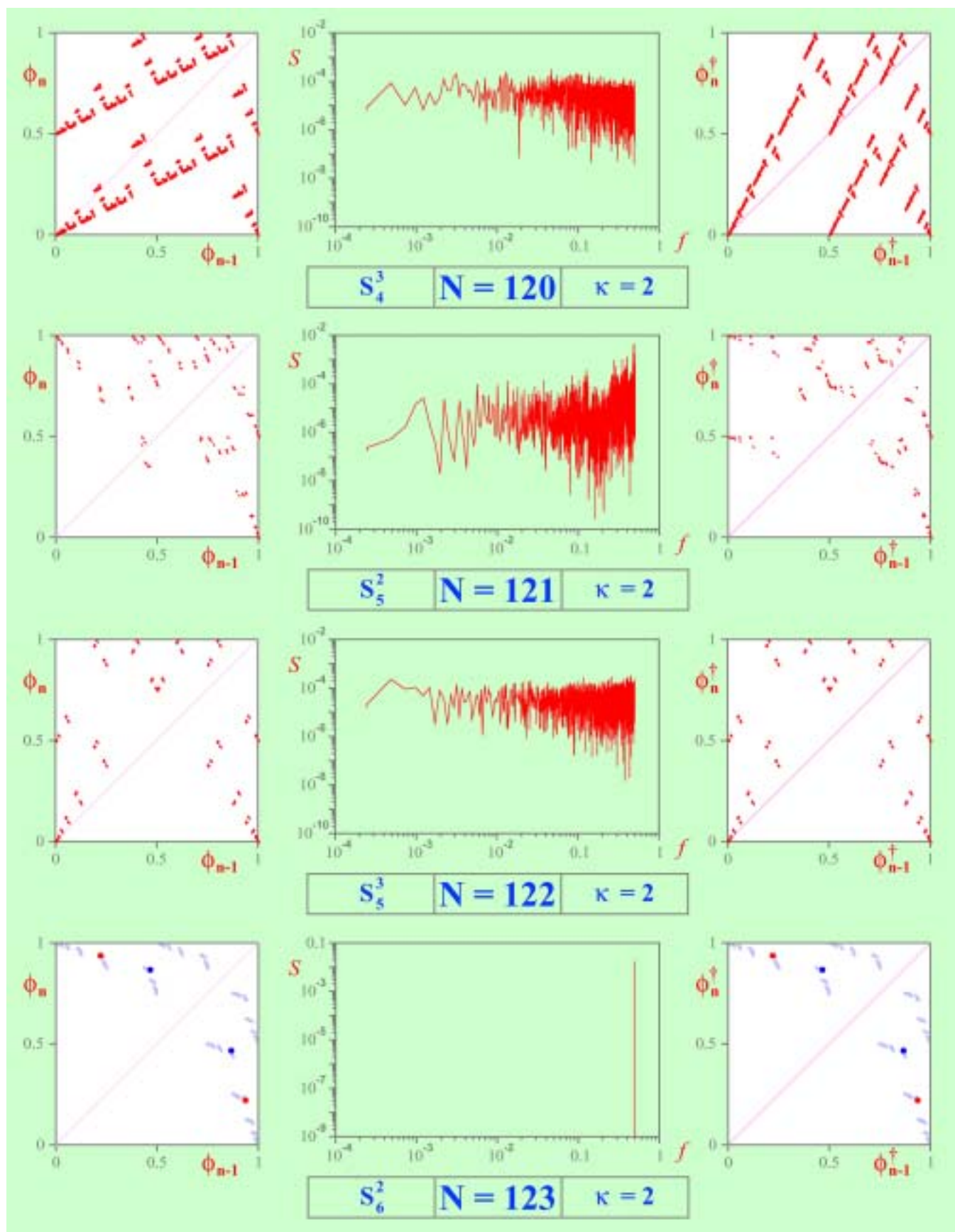


Table 2. (Continued)

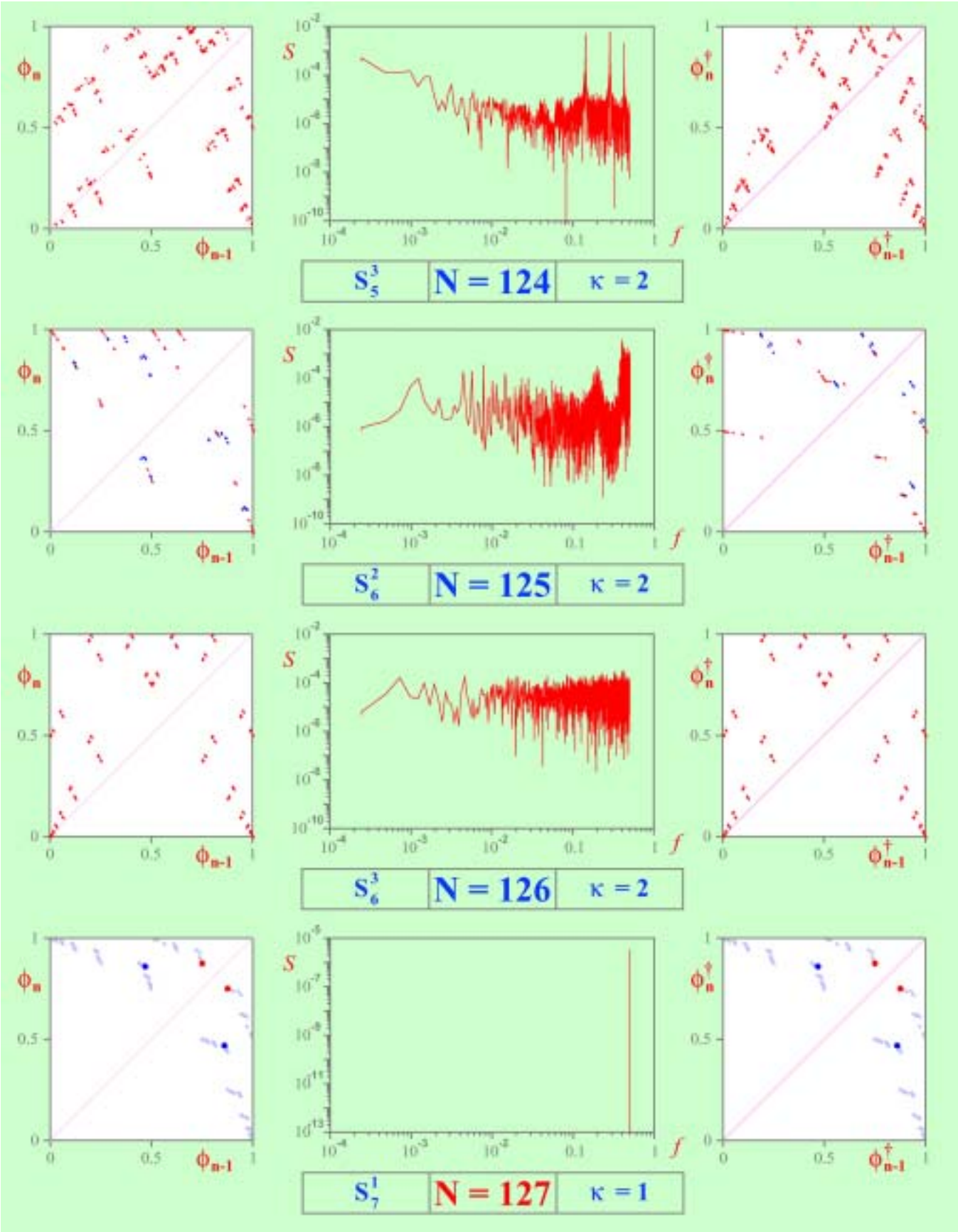


Table 2. (Continued)

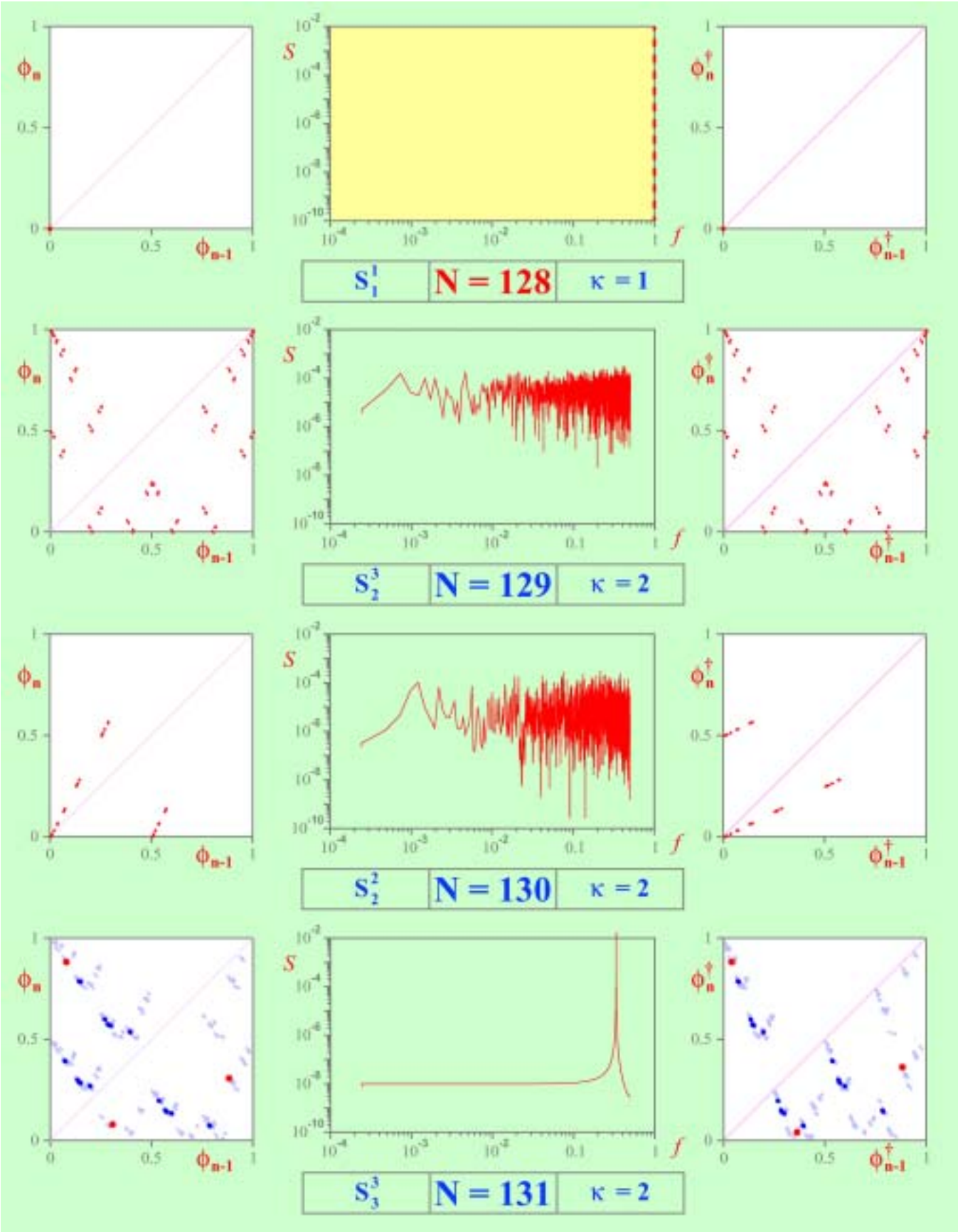


Table 2. (Continued)

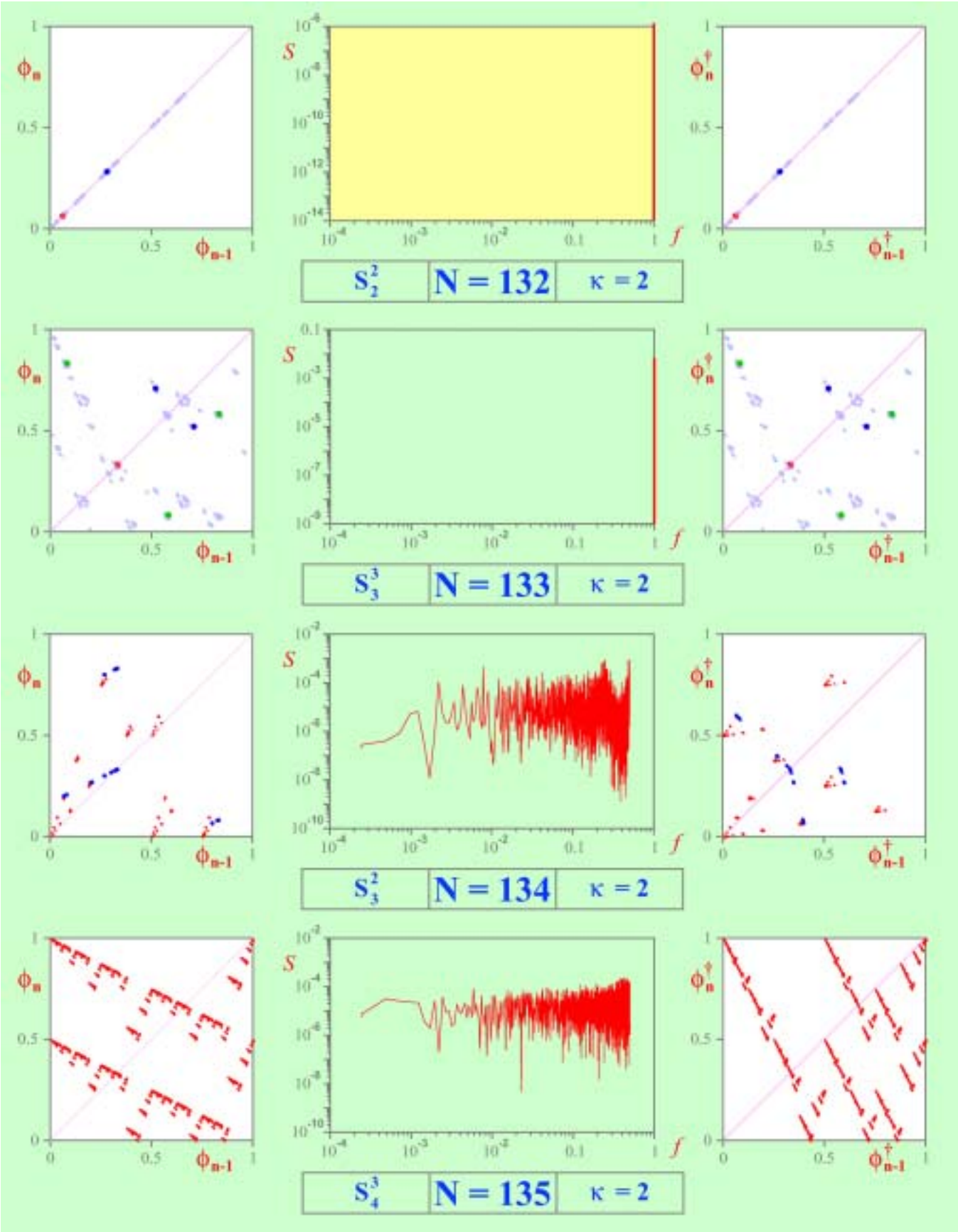


Table 2. (Continued)

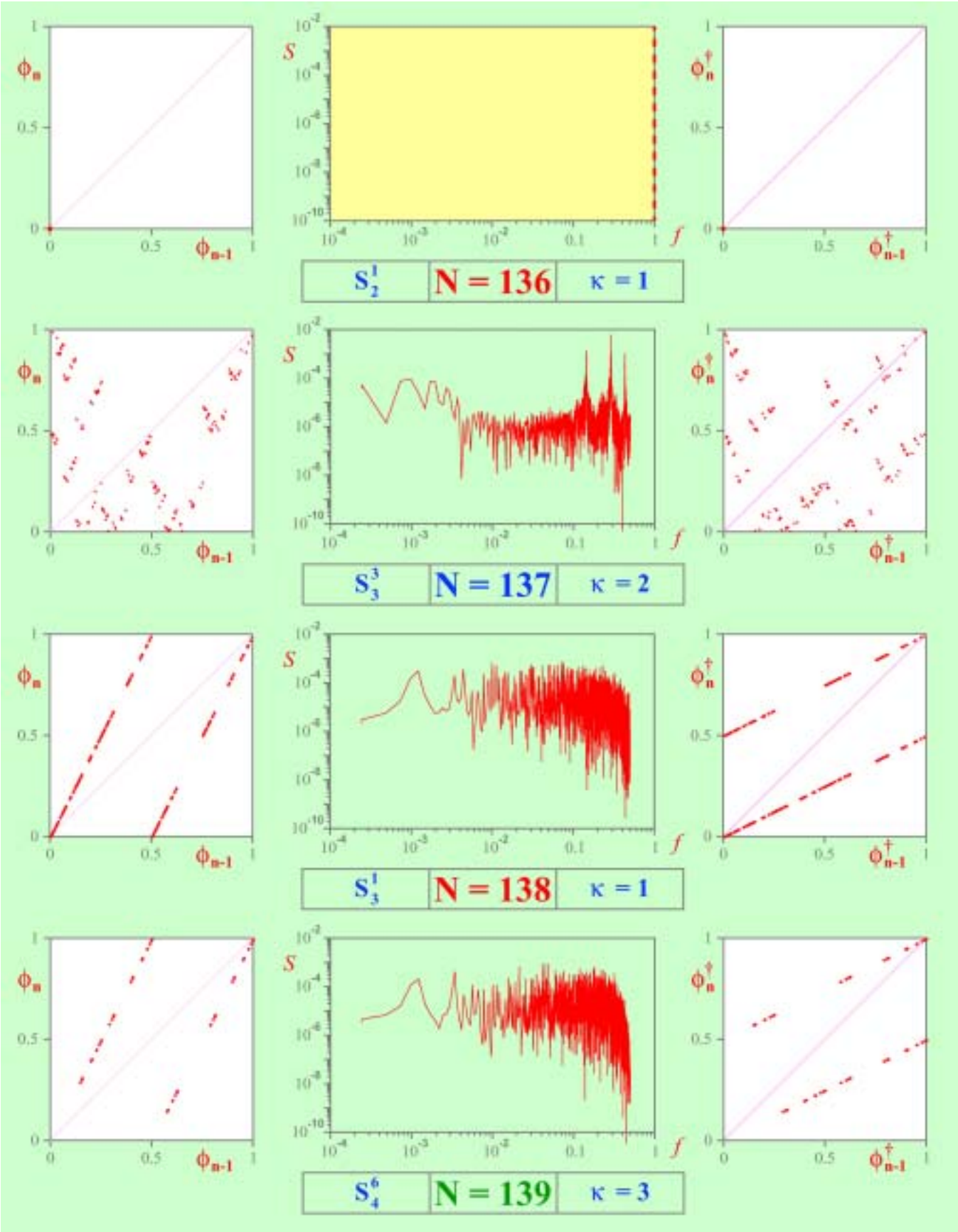


Table 2. (Continued)

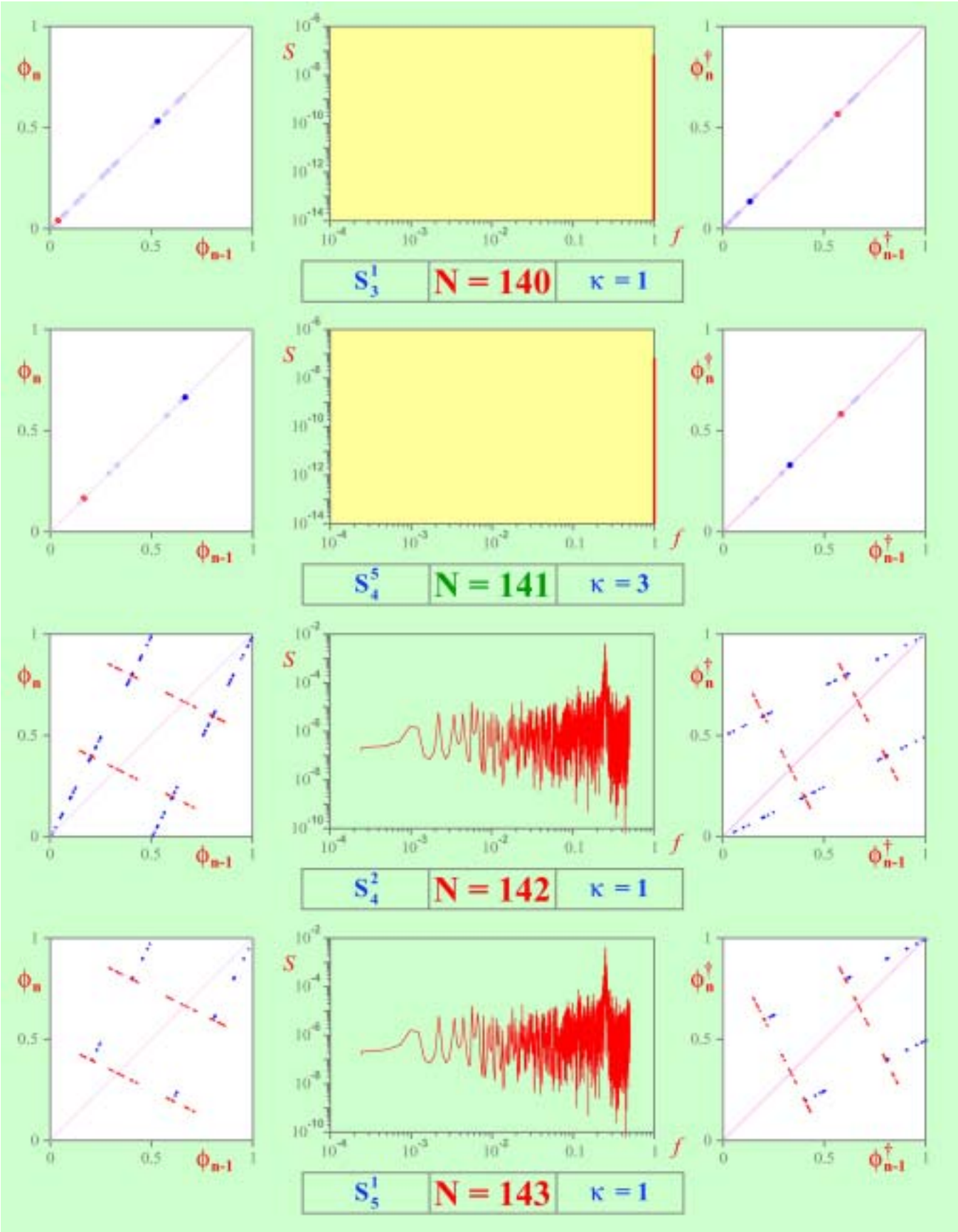


Table 2. (Continued)

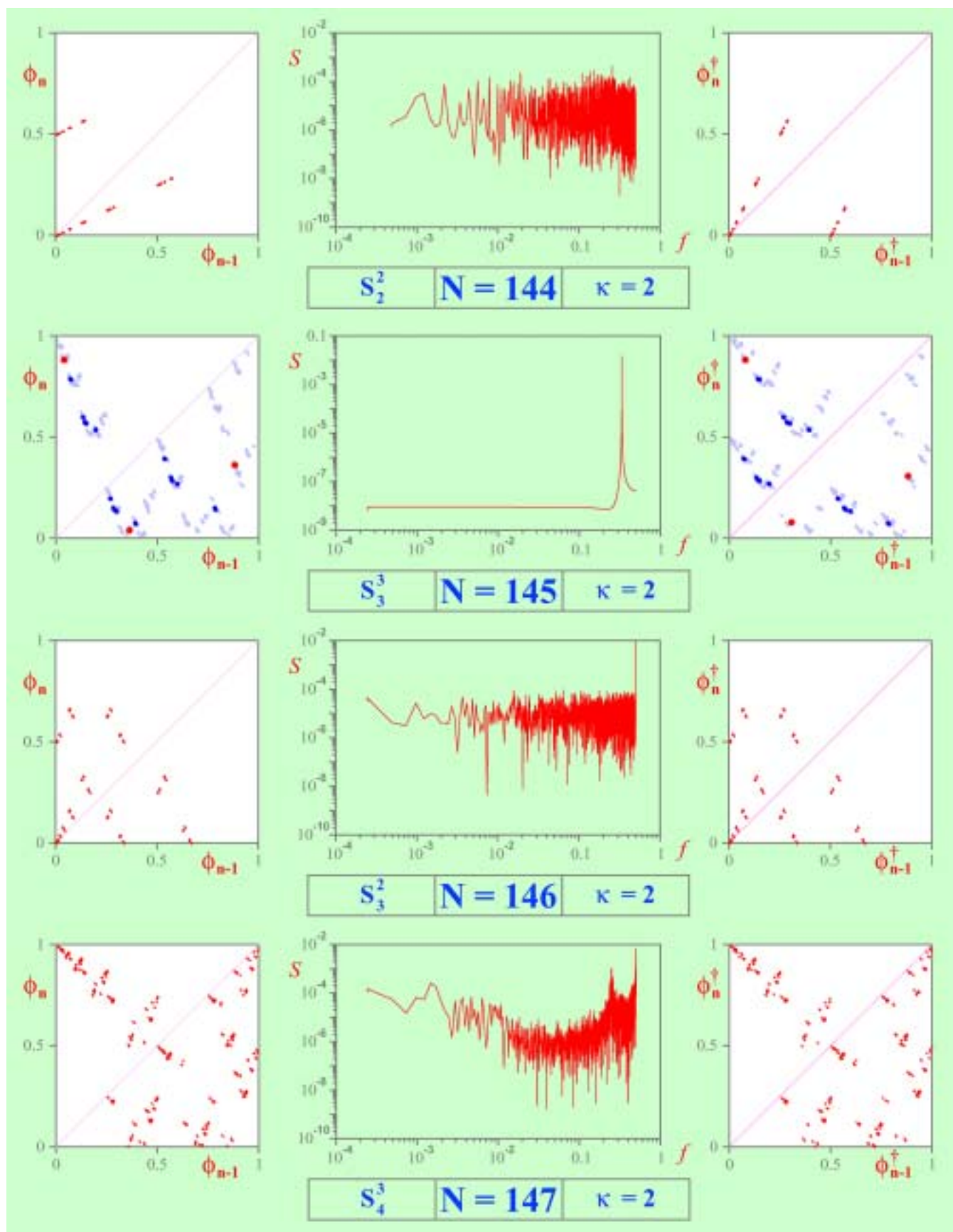


Table 2. (Continued)

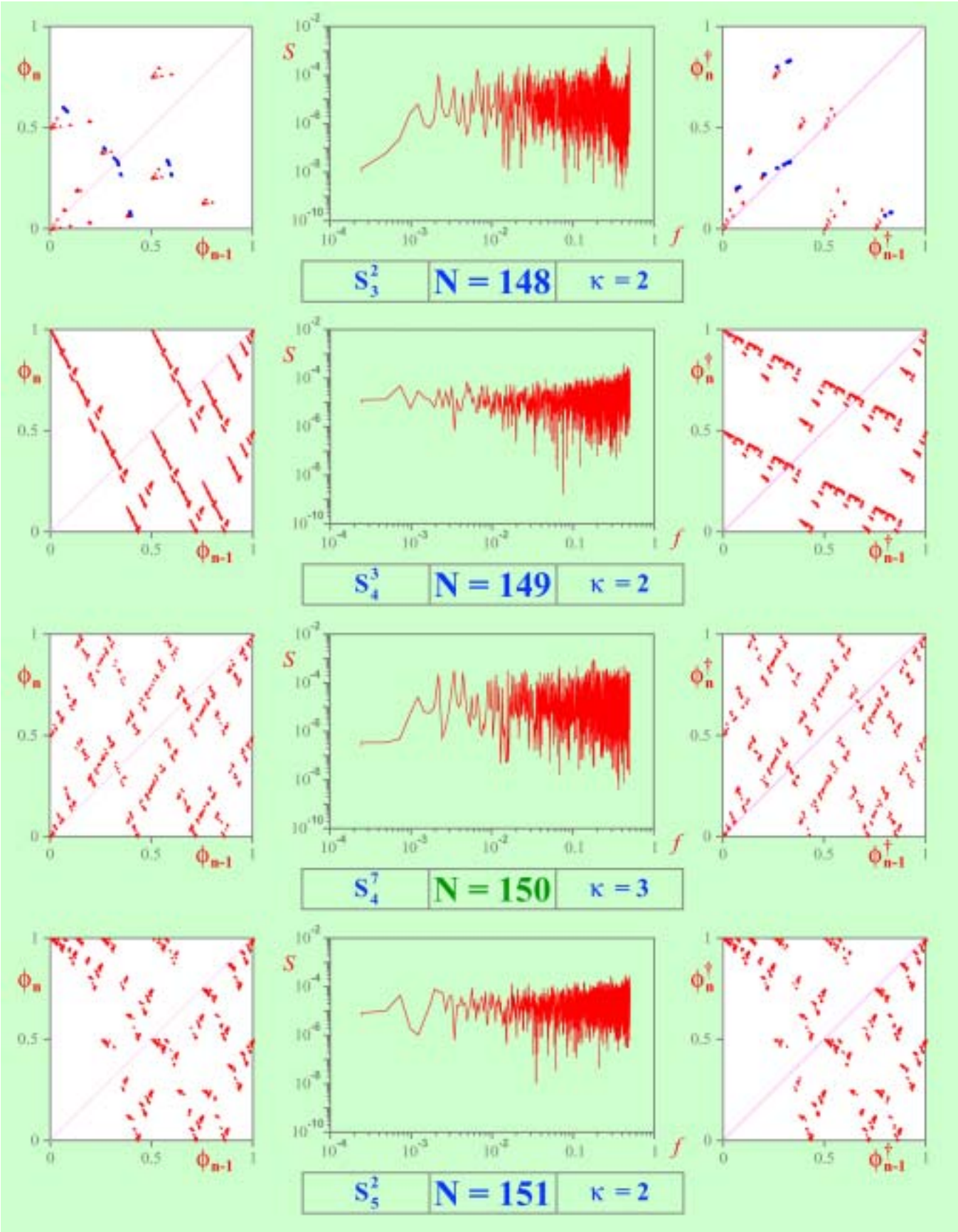


Table 2. (Continued)

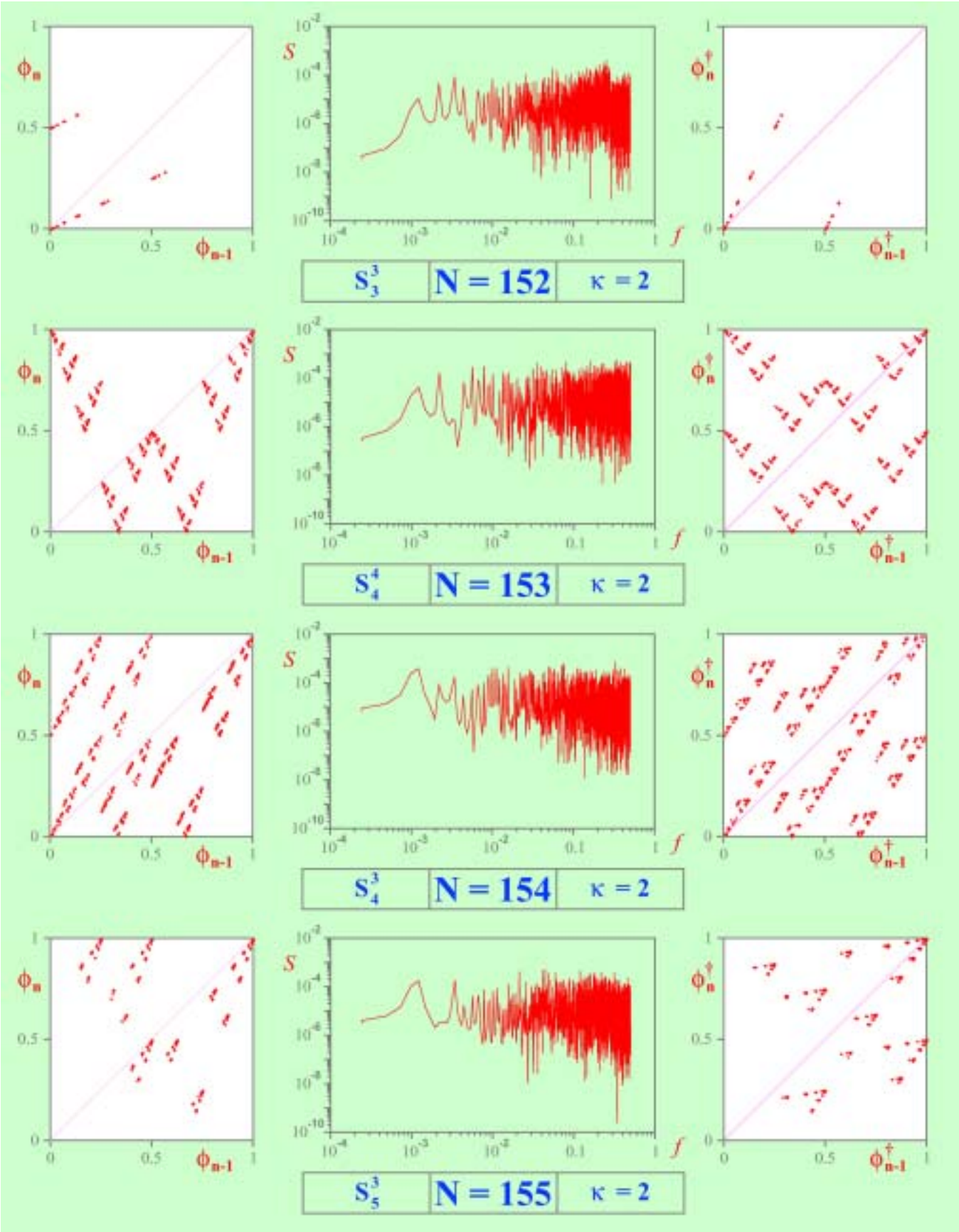


Table 2. (Continued)

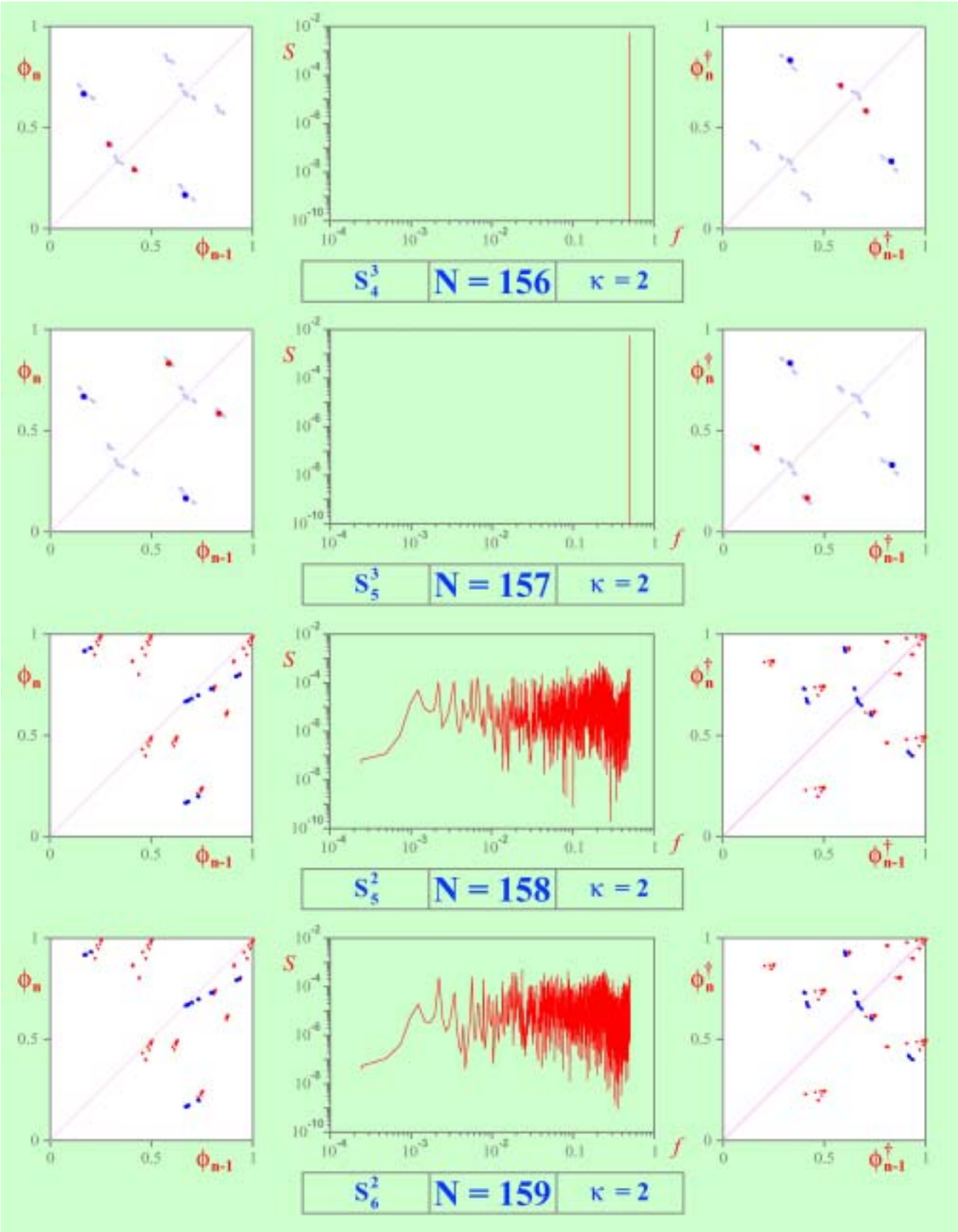


Table 2. (Continued)

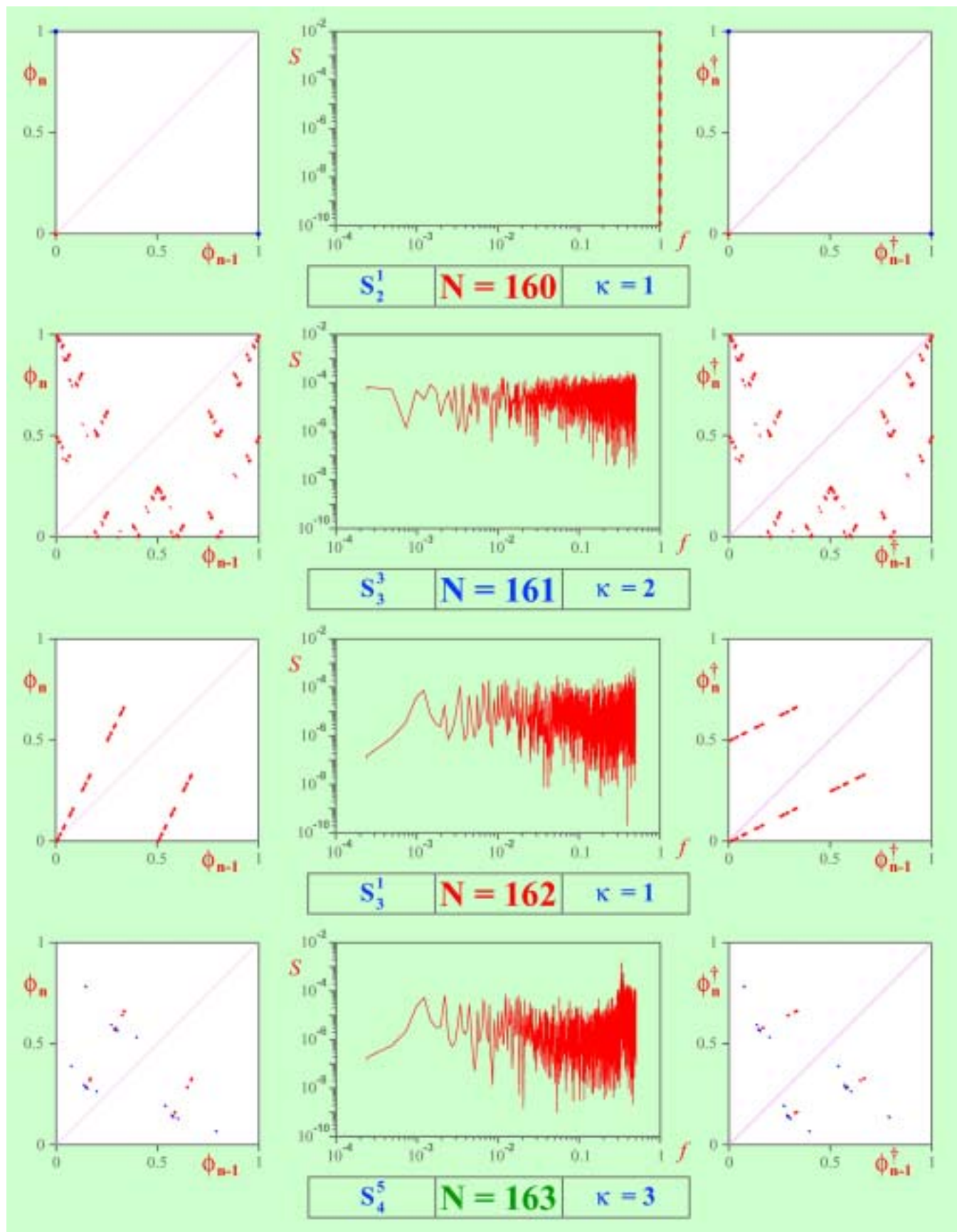


Table 2. (Continued)

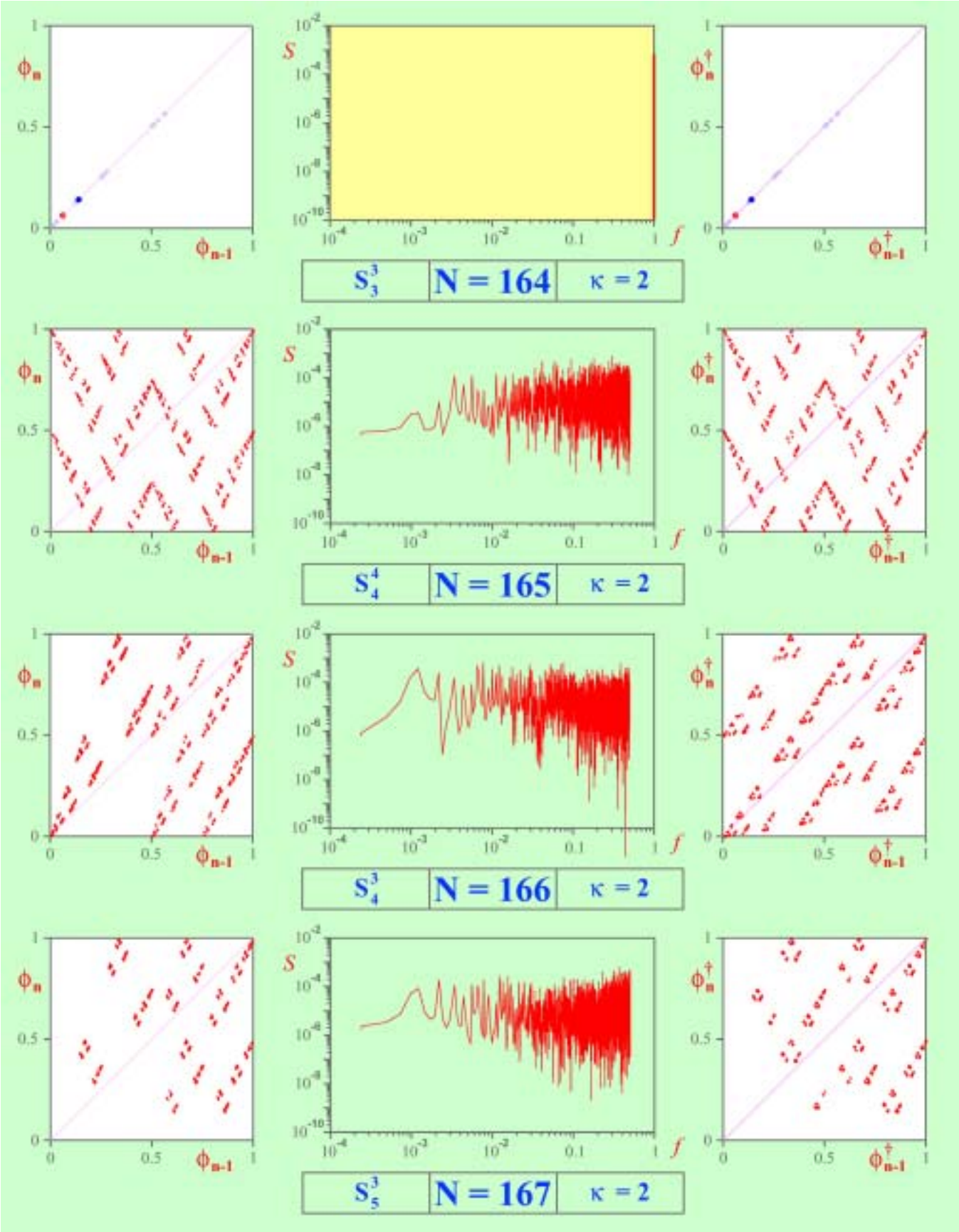


Table 2. (Continued)

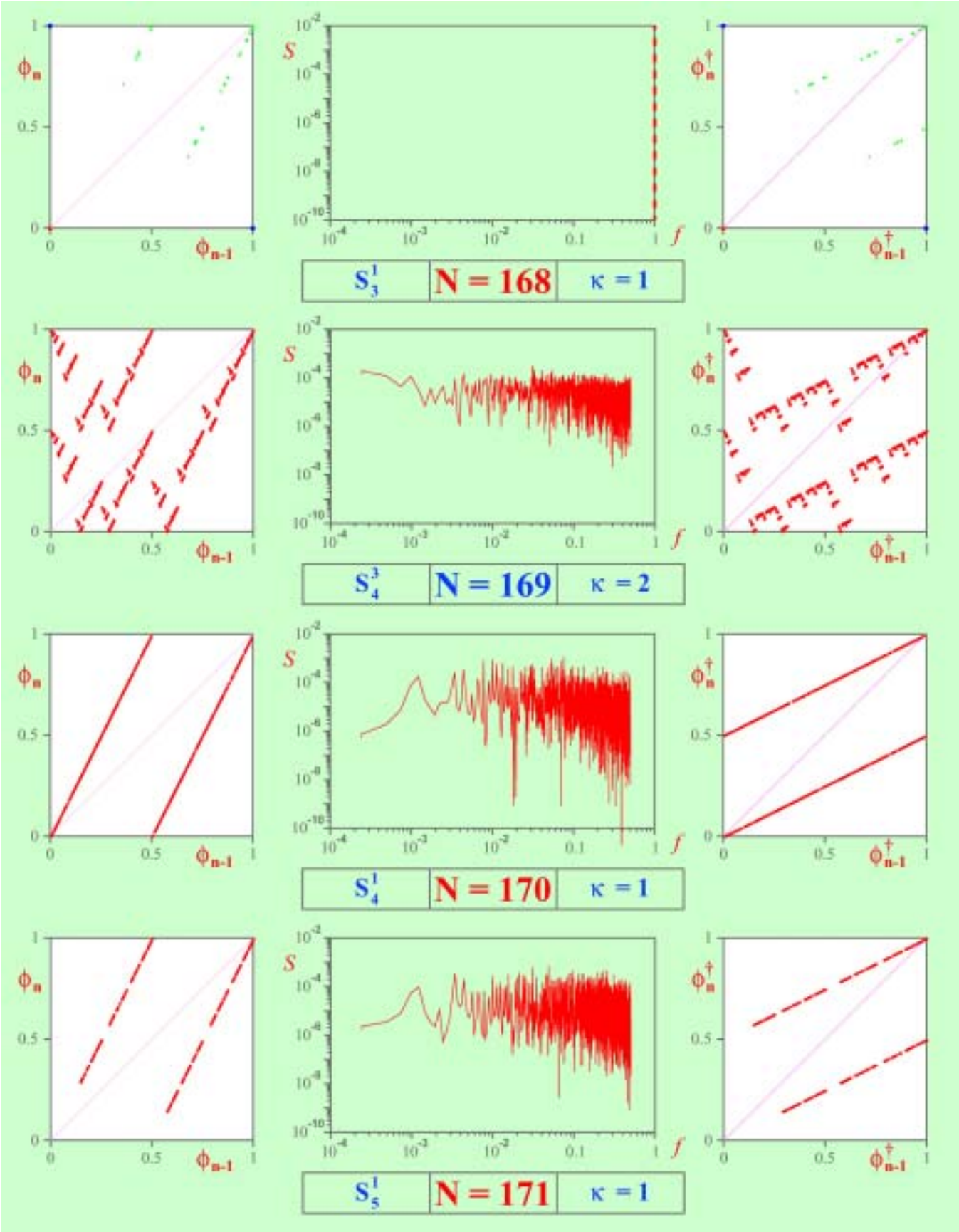


Table 2. (Continued)

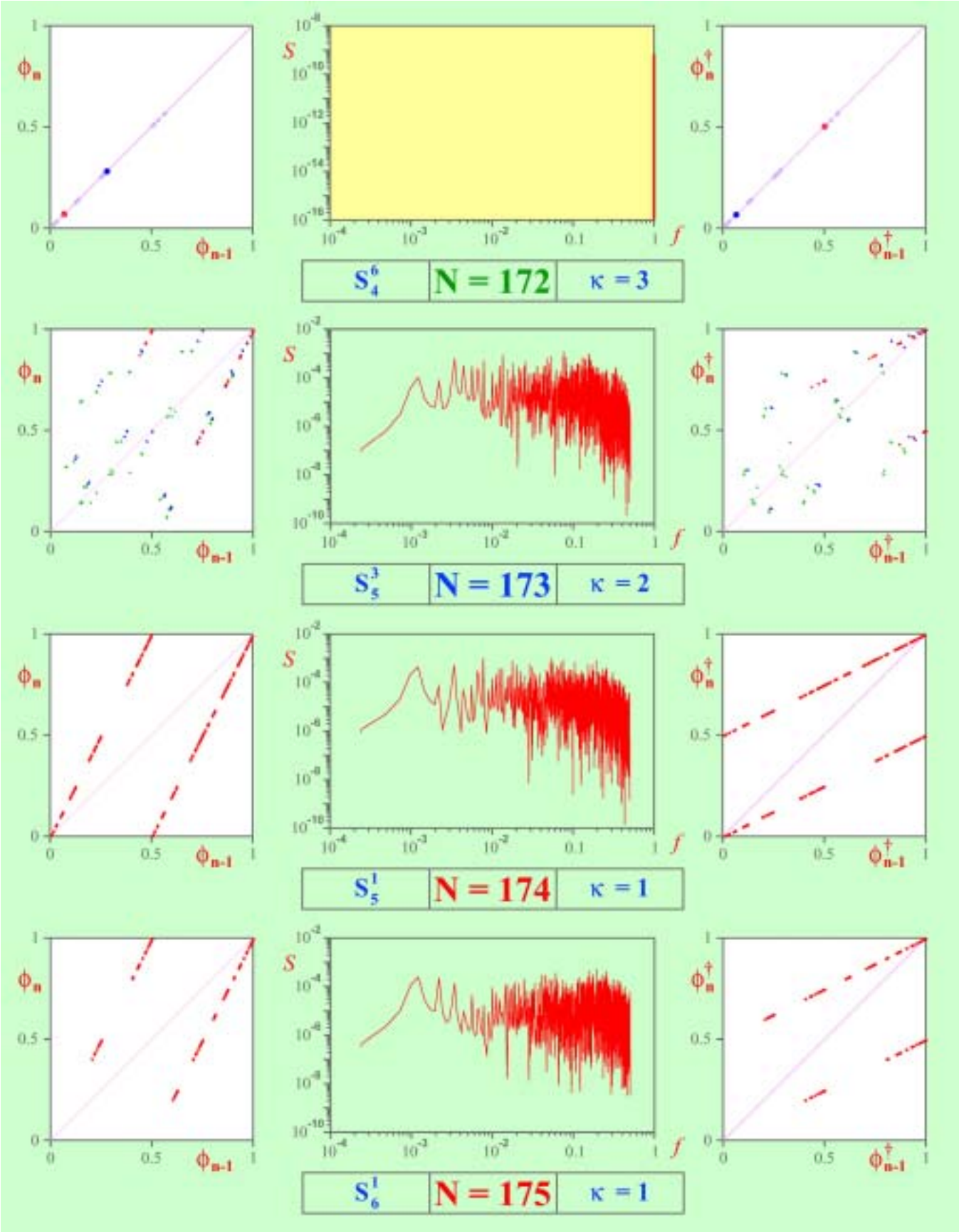


Table 2. (Continued)

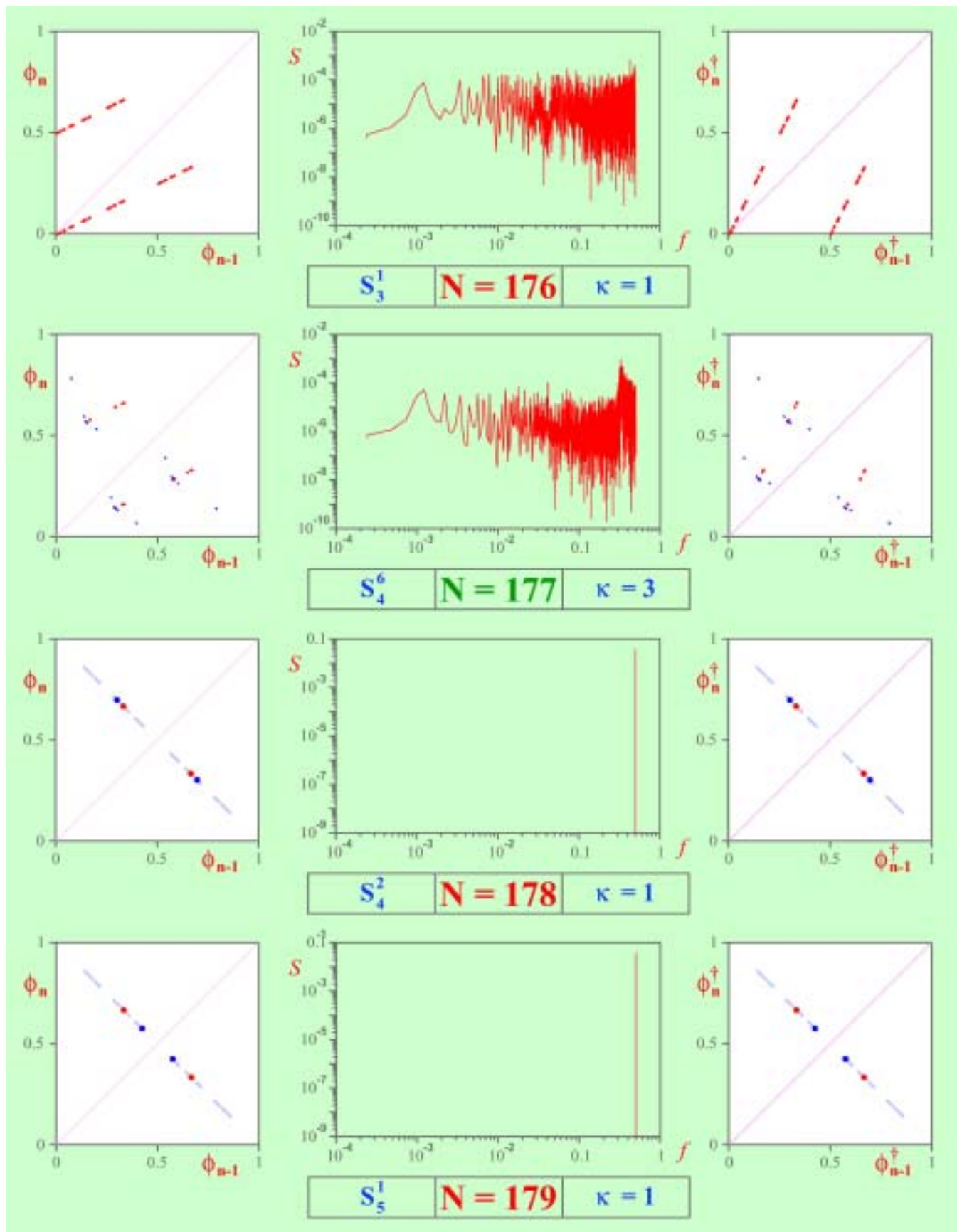


Table 2. (Continued)

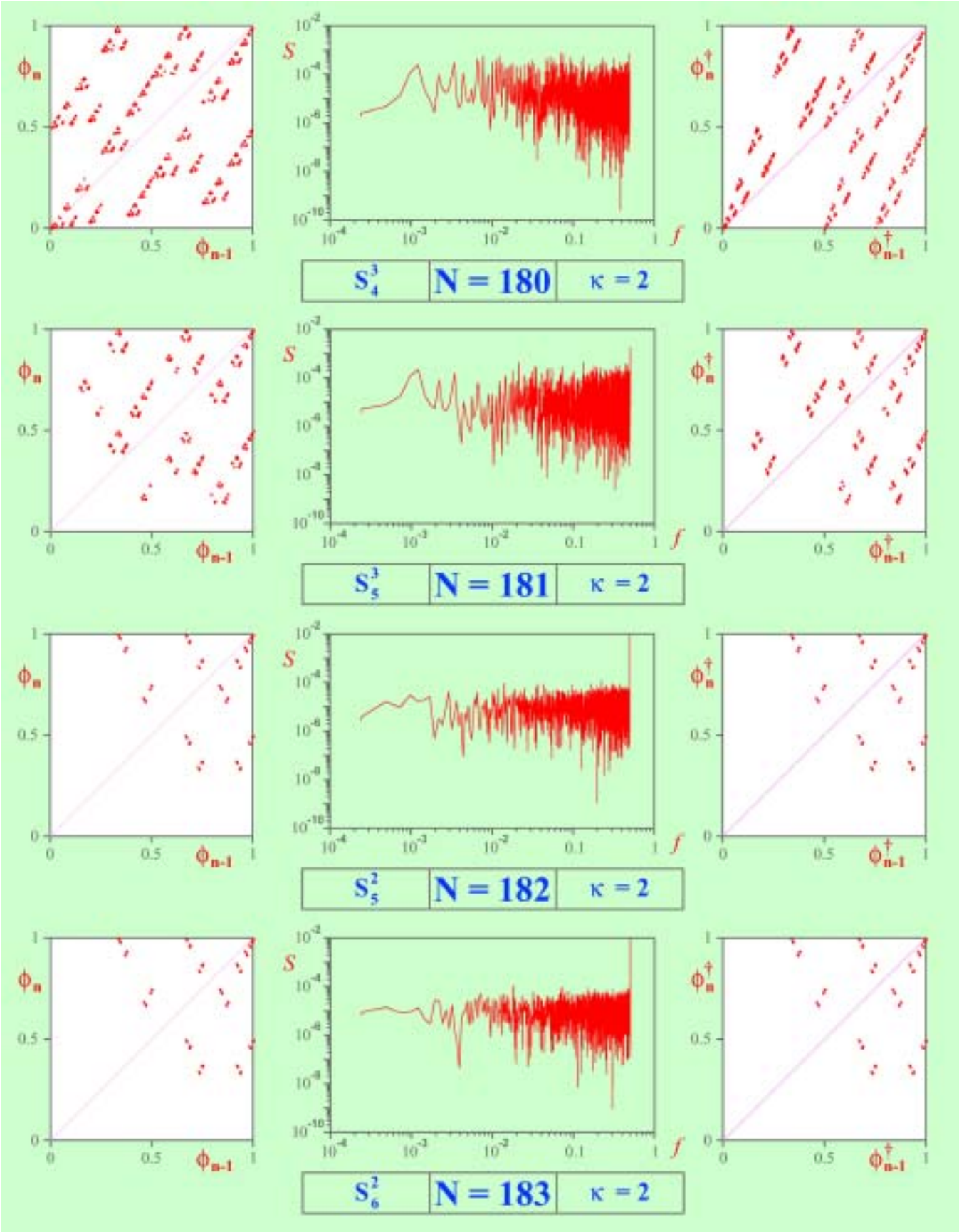


Table 2. (Continued)

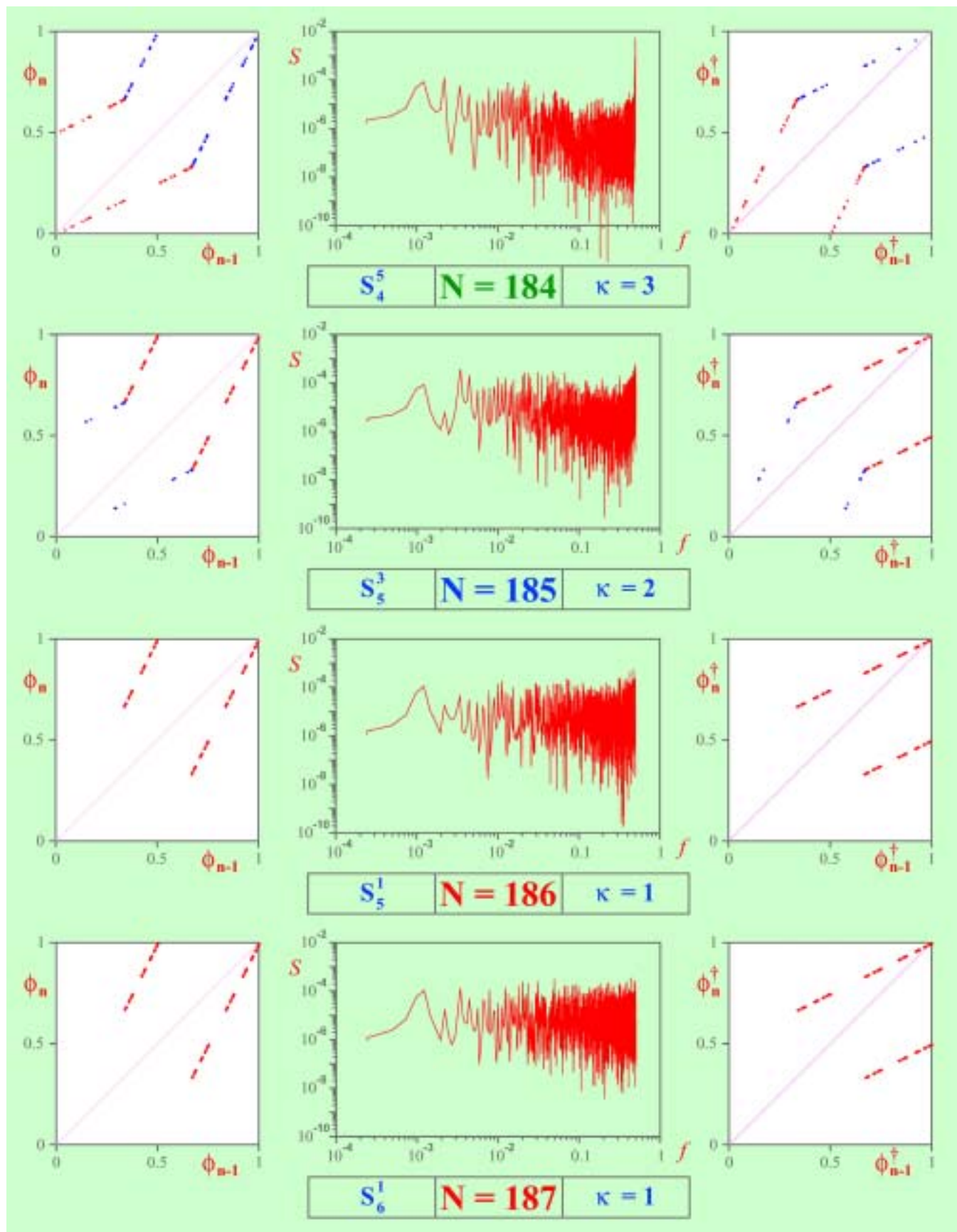


Table 2. (Continued)

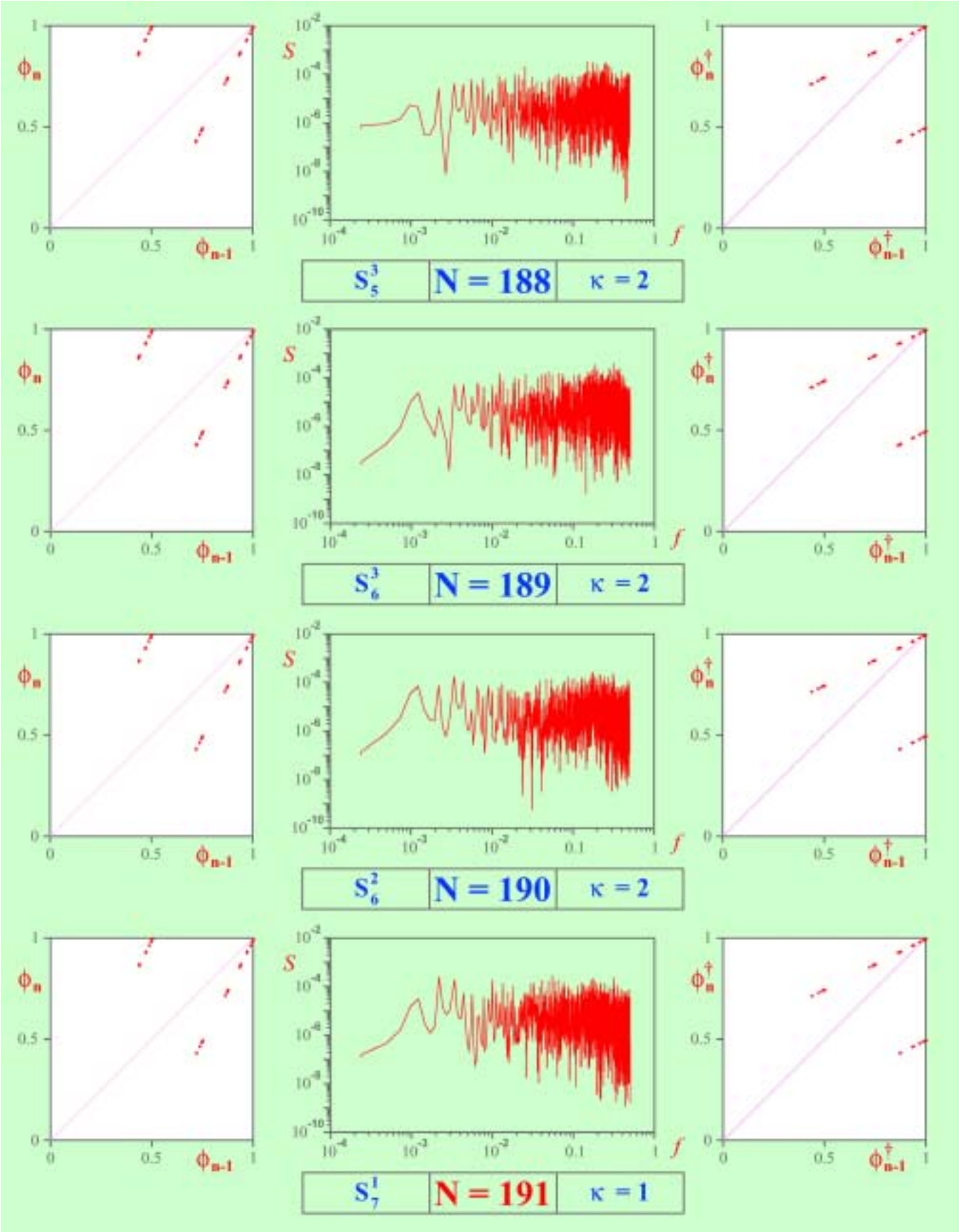


Table 2. (Continued)

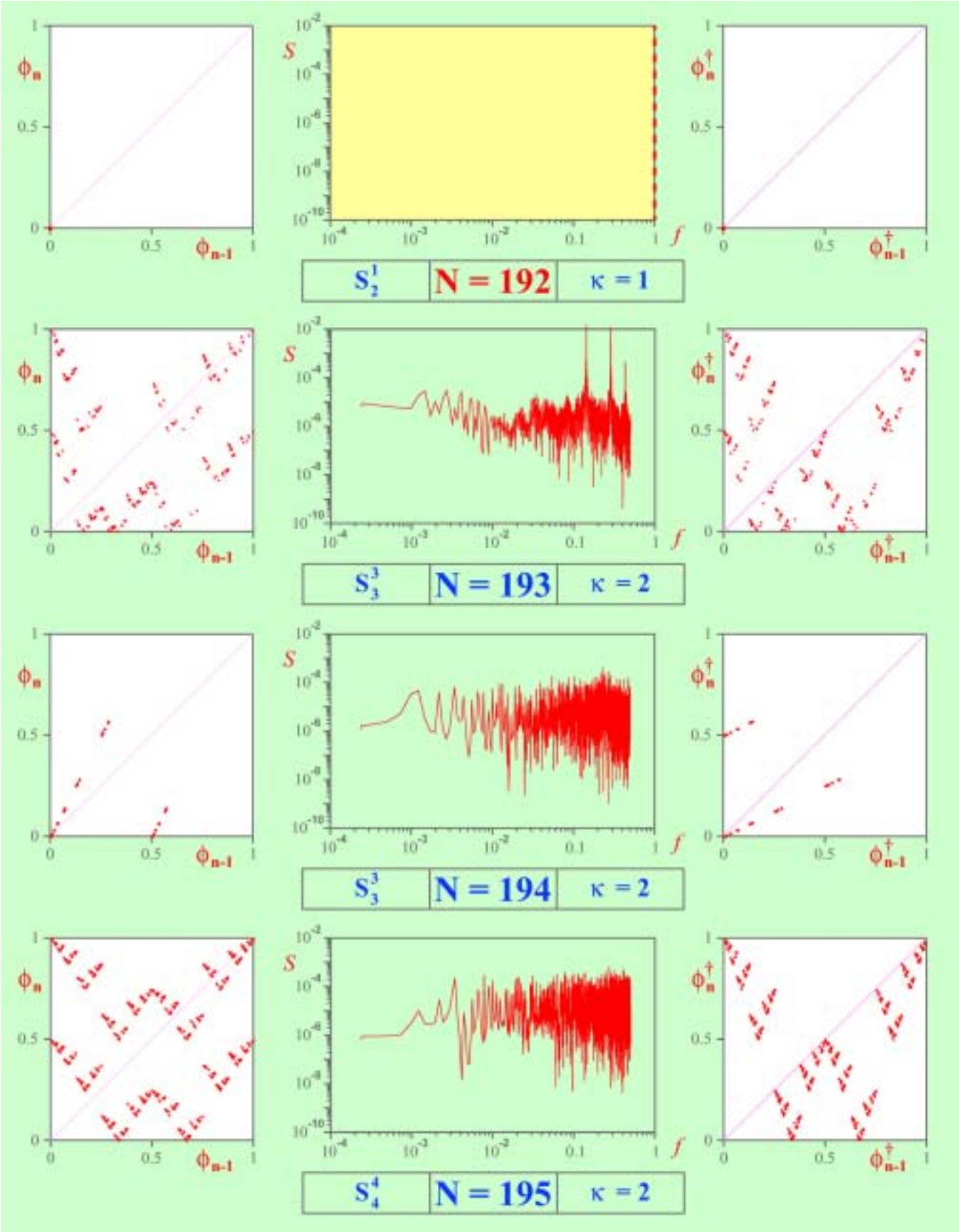


Table 2. (Continued)

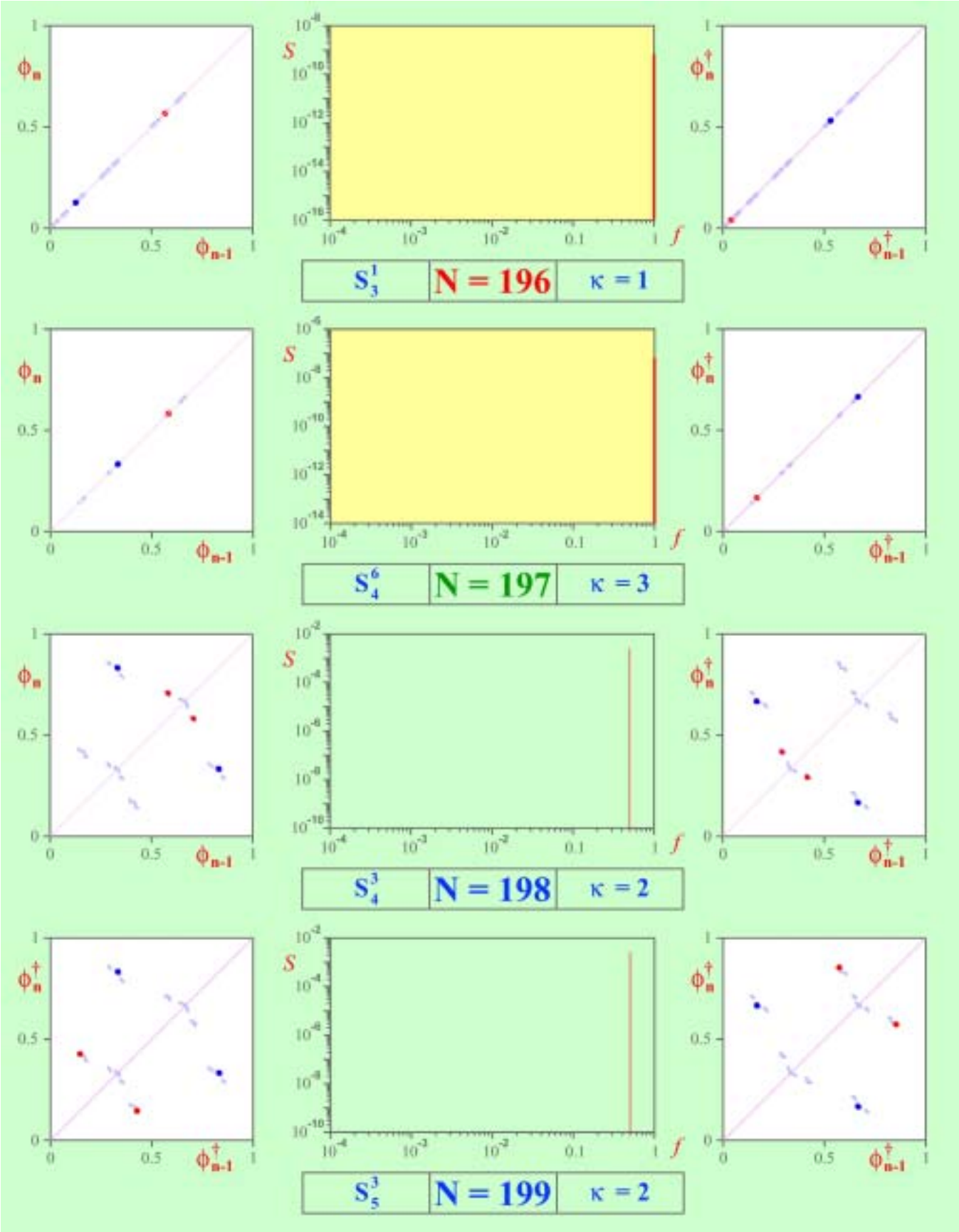


Table 2. (Continued)

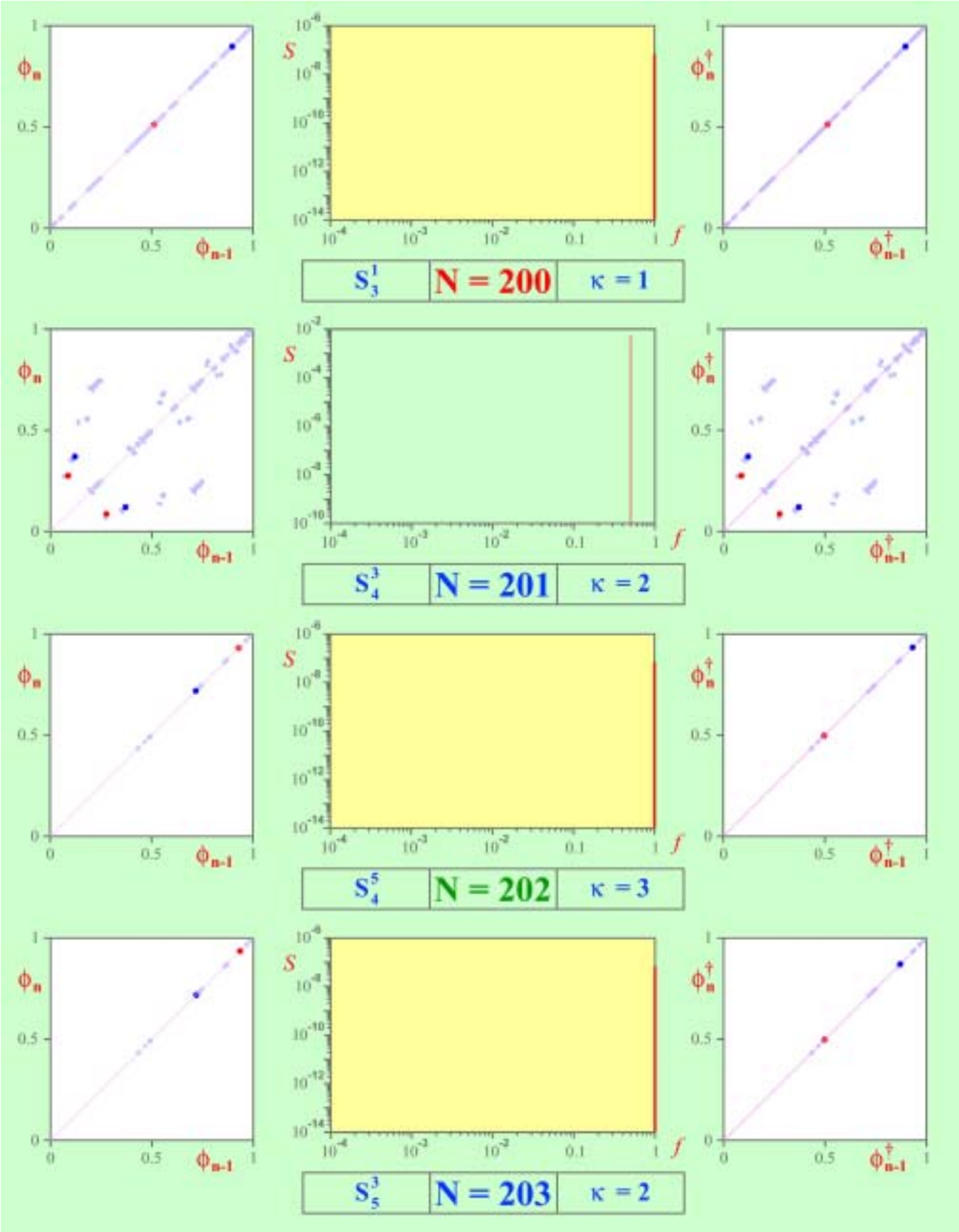


Table 2. (Continued)

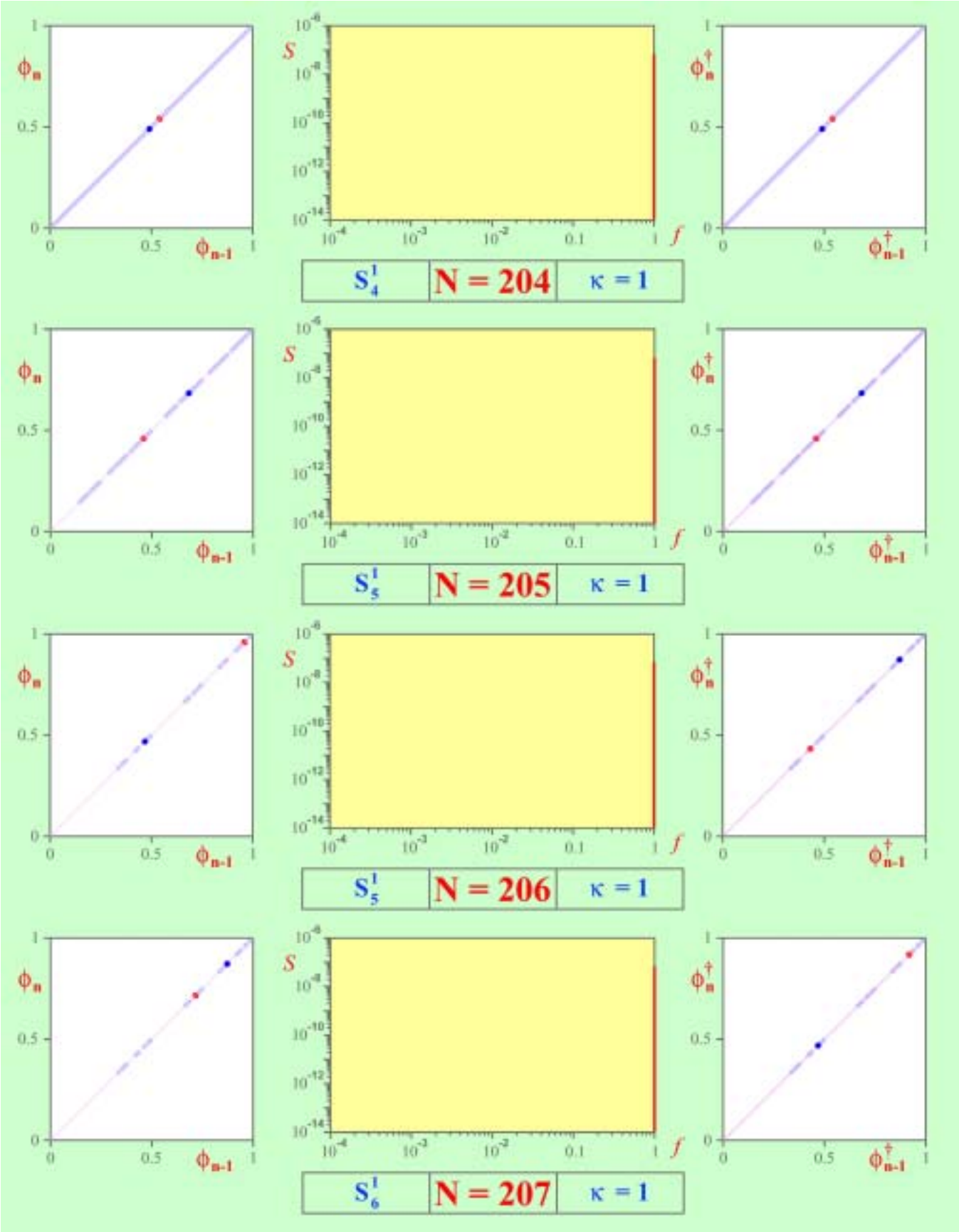


Table 2. (Continued)

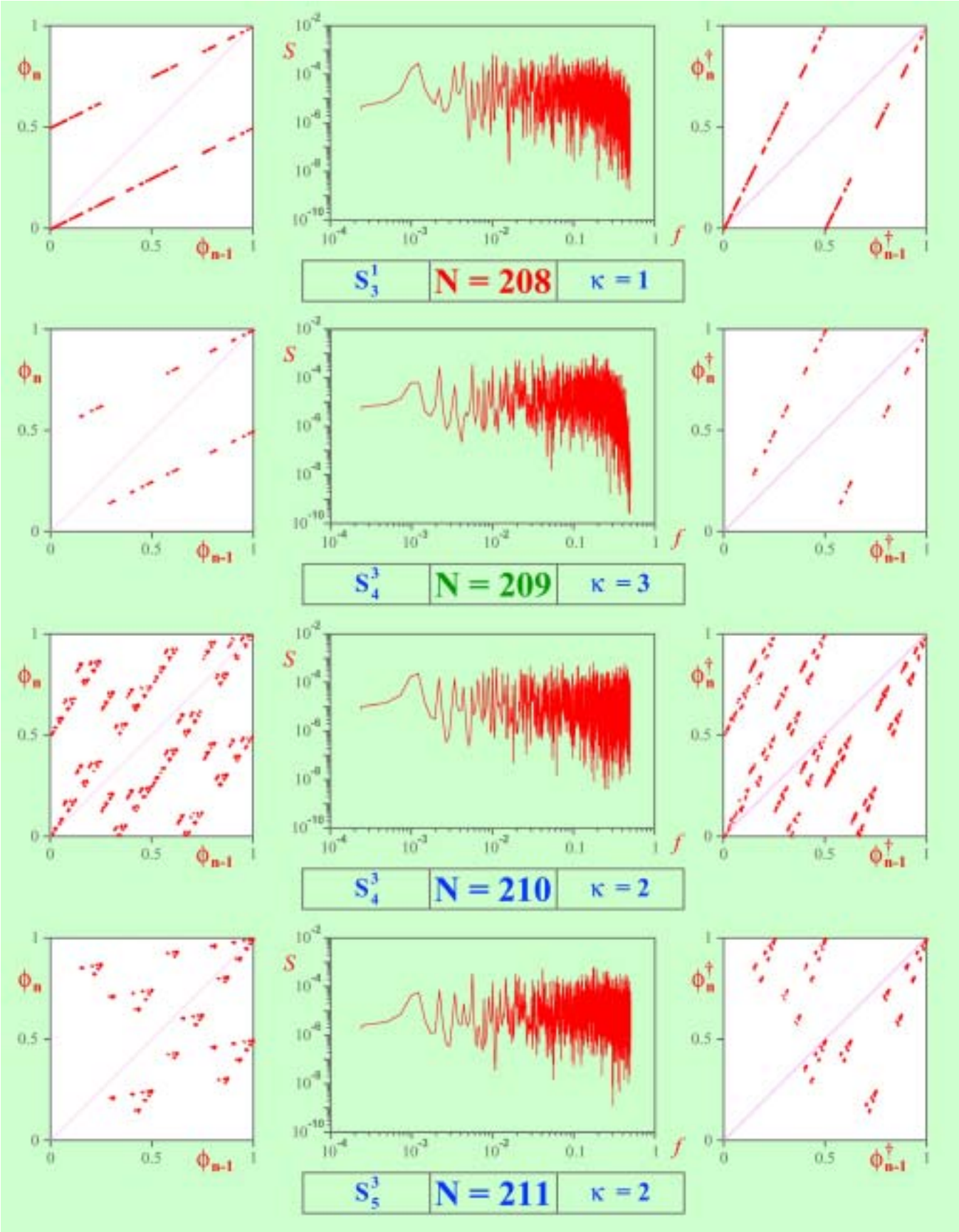


Table 2. (Continued)

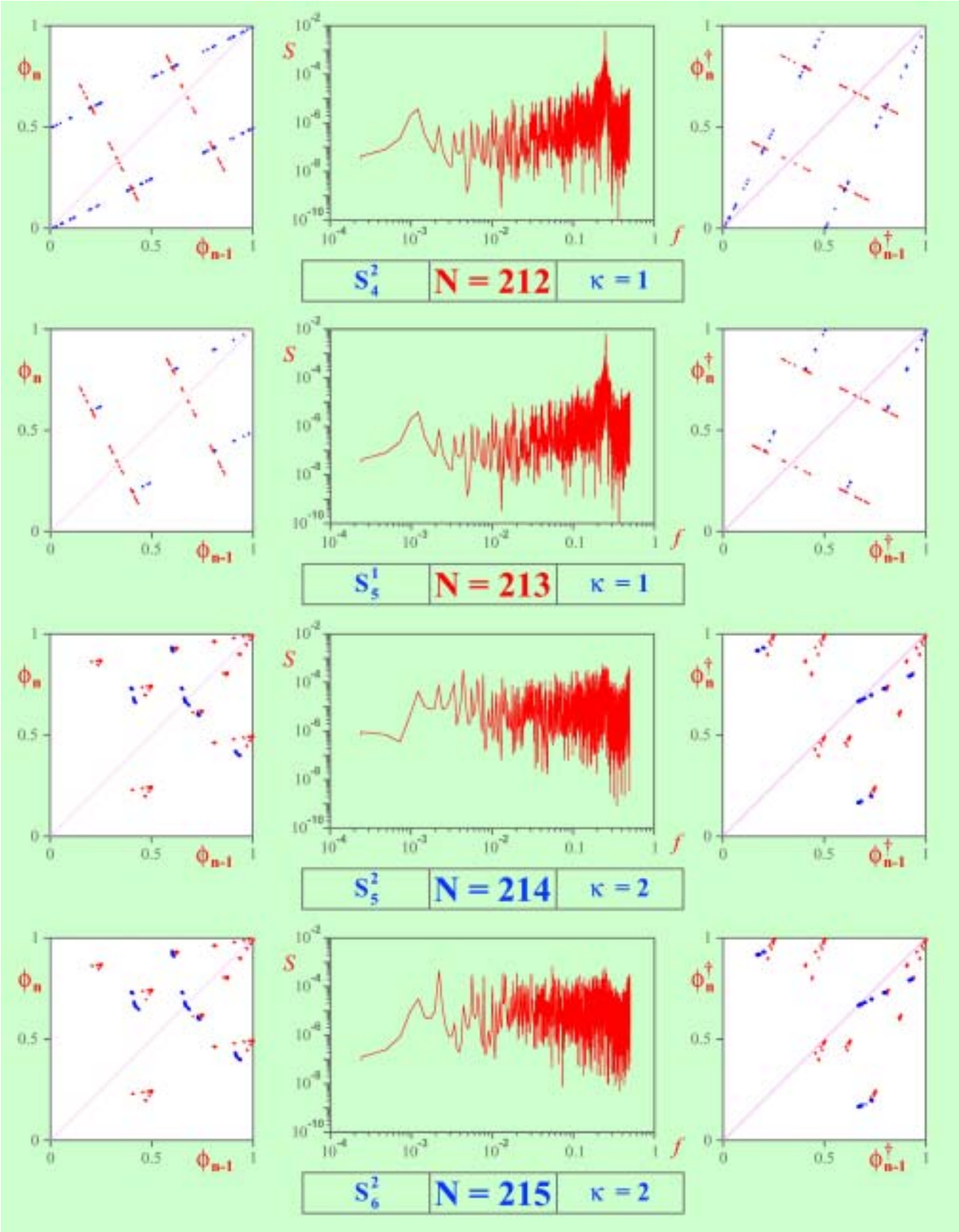


Table 2. (Continued)

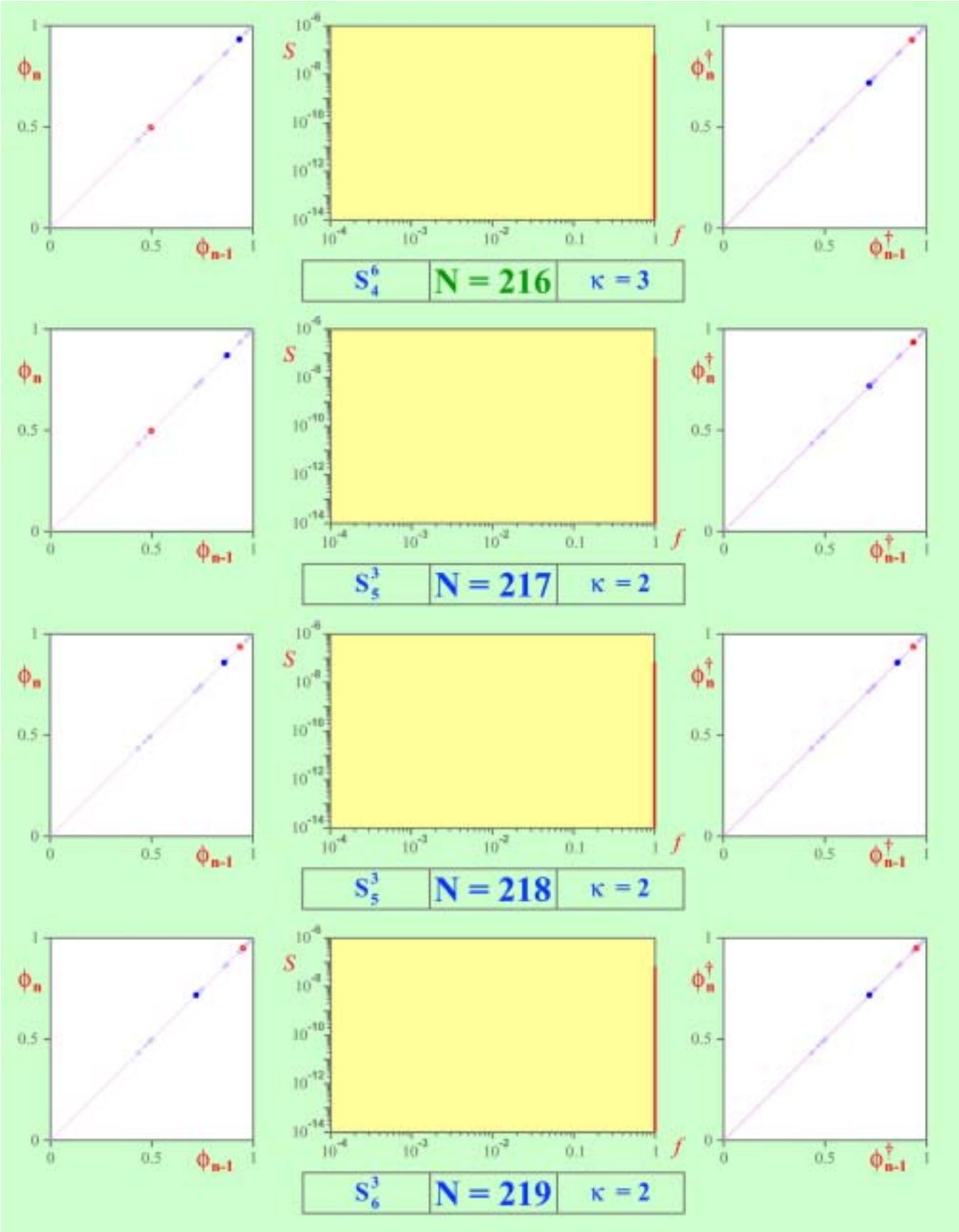


Table 2. (Continued)

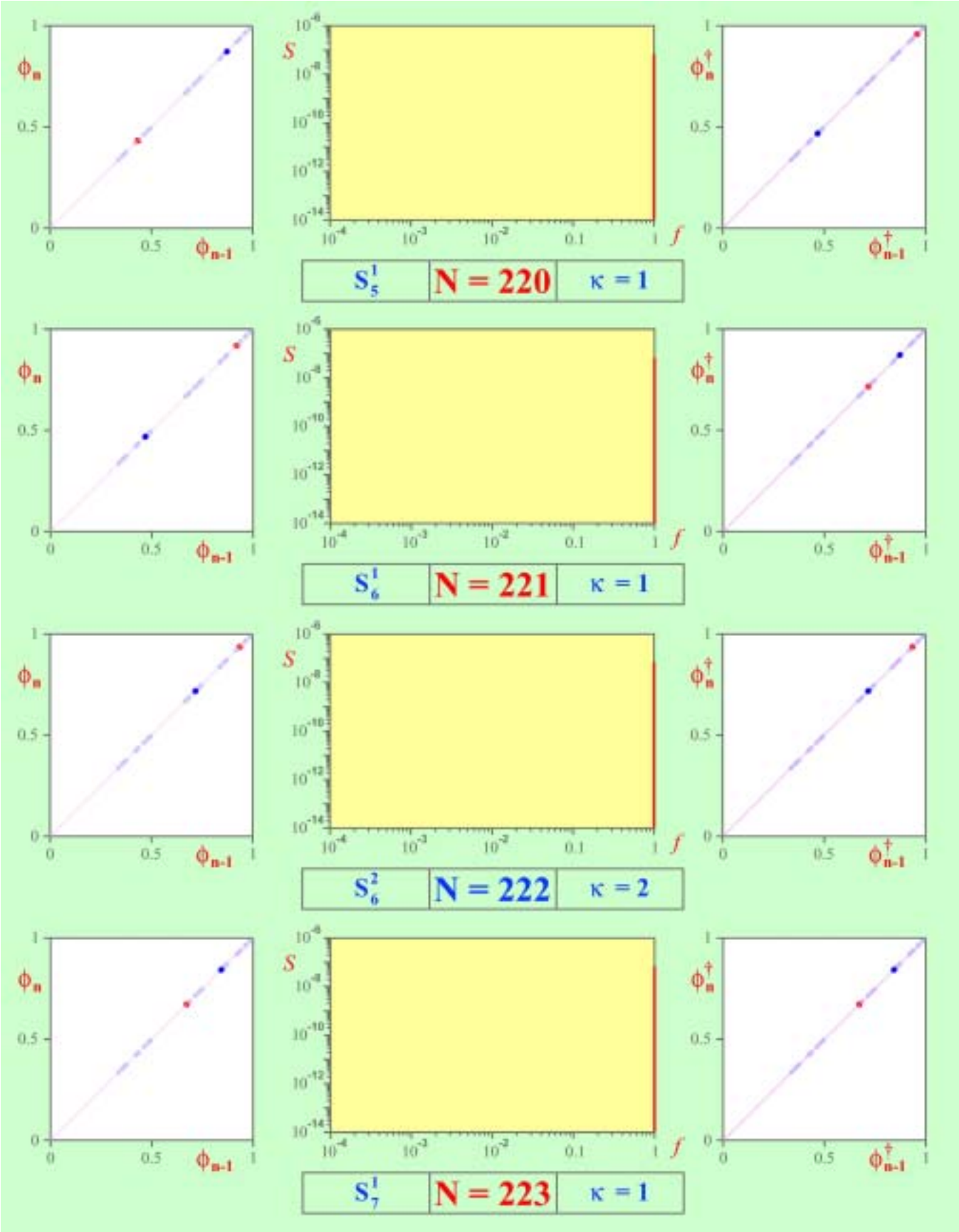


Table 2. (Continued)

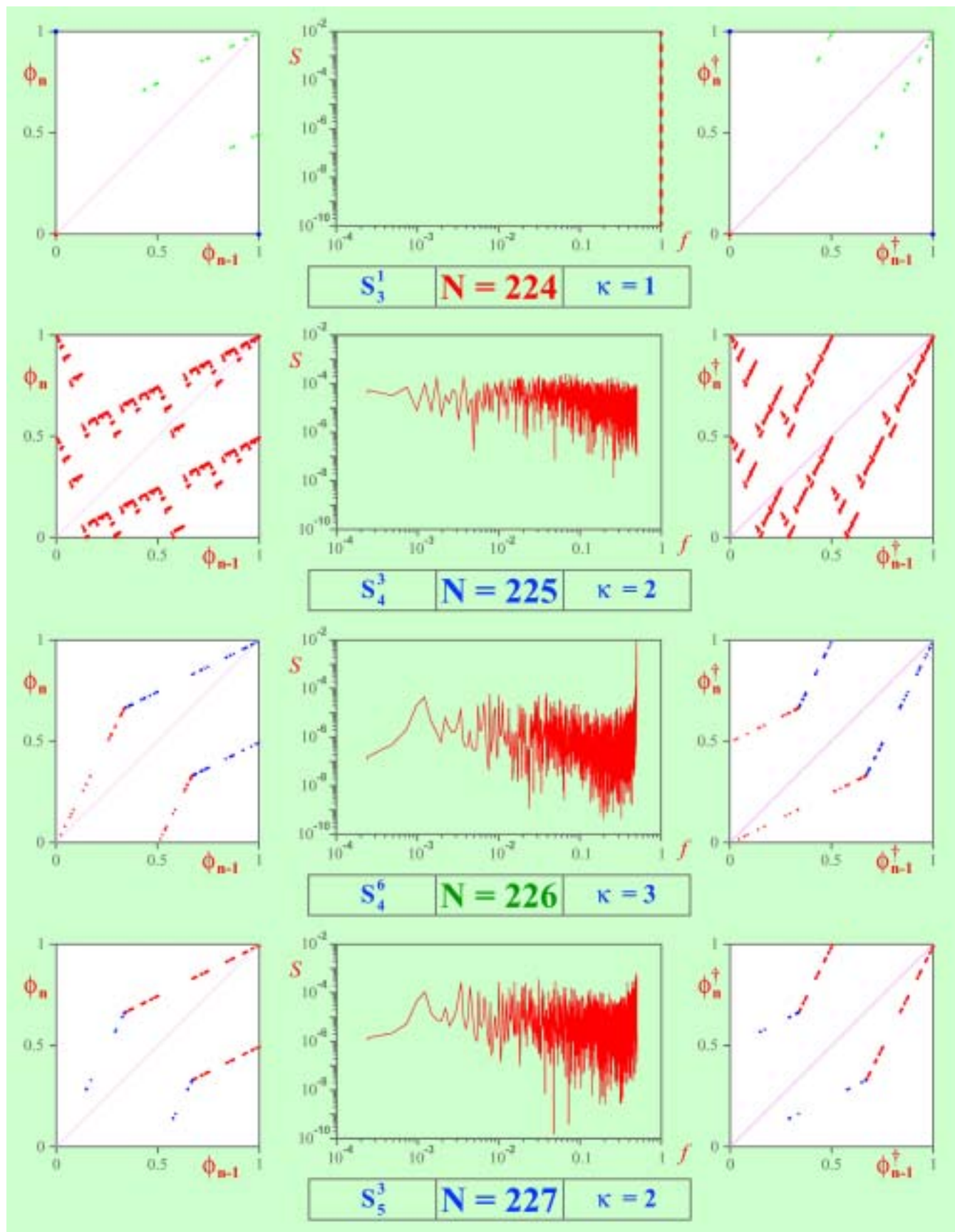


Table 2. (Continued)

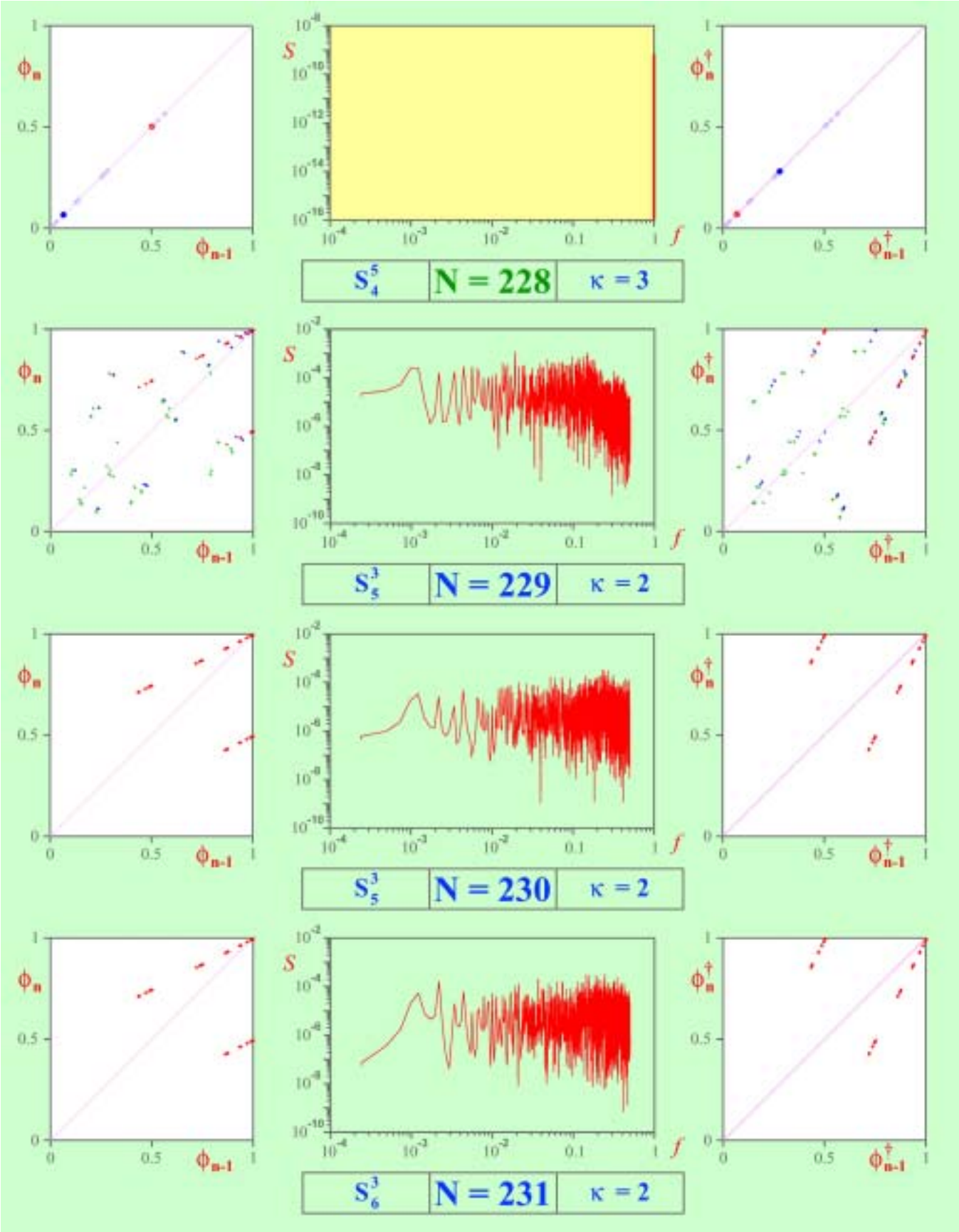


Table 2. (Continued)

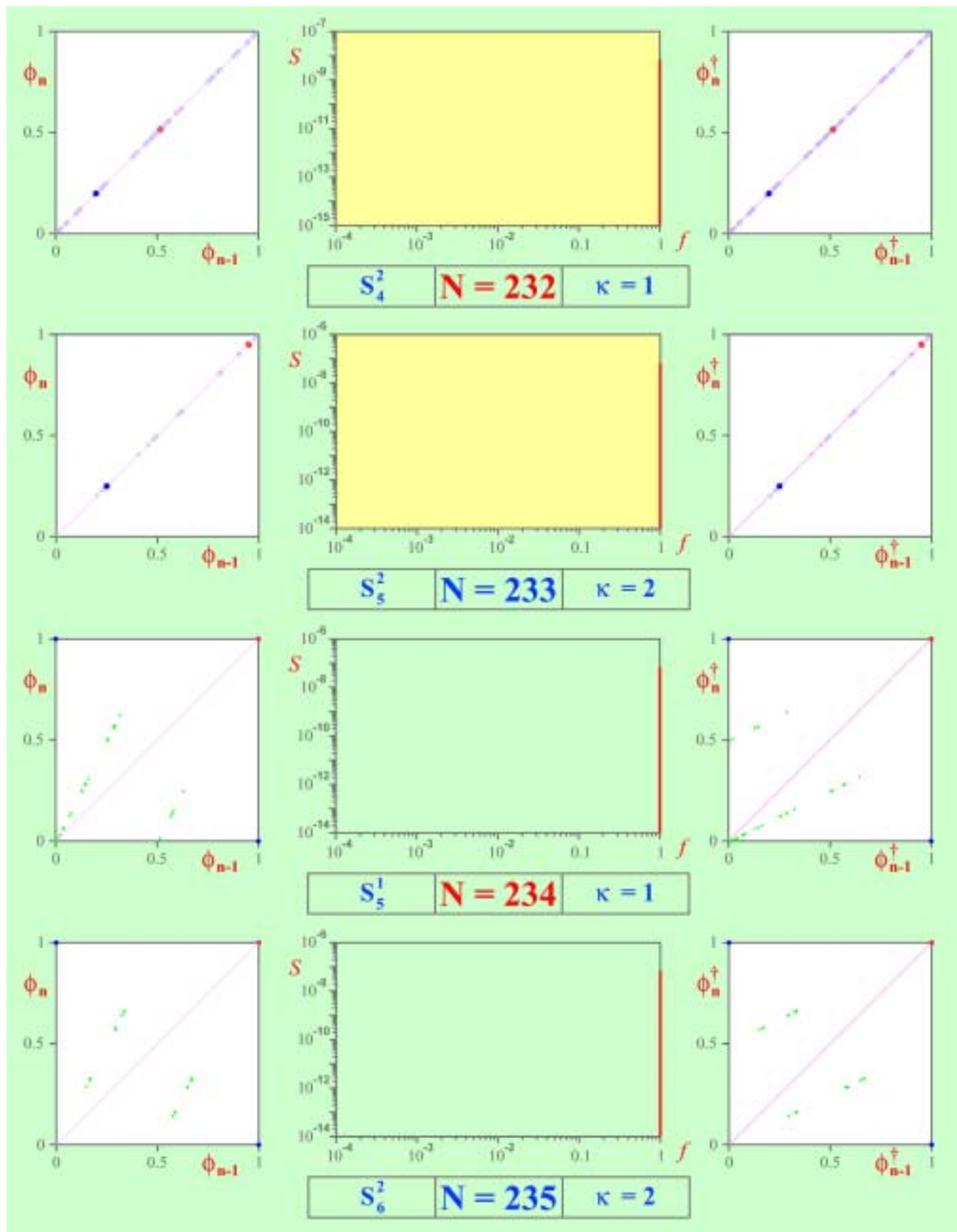


Table 2. (Continued)

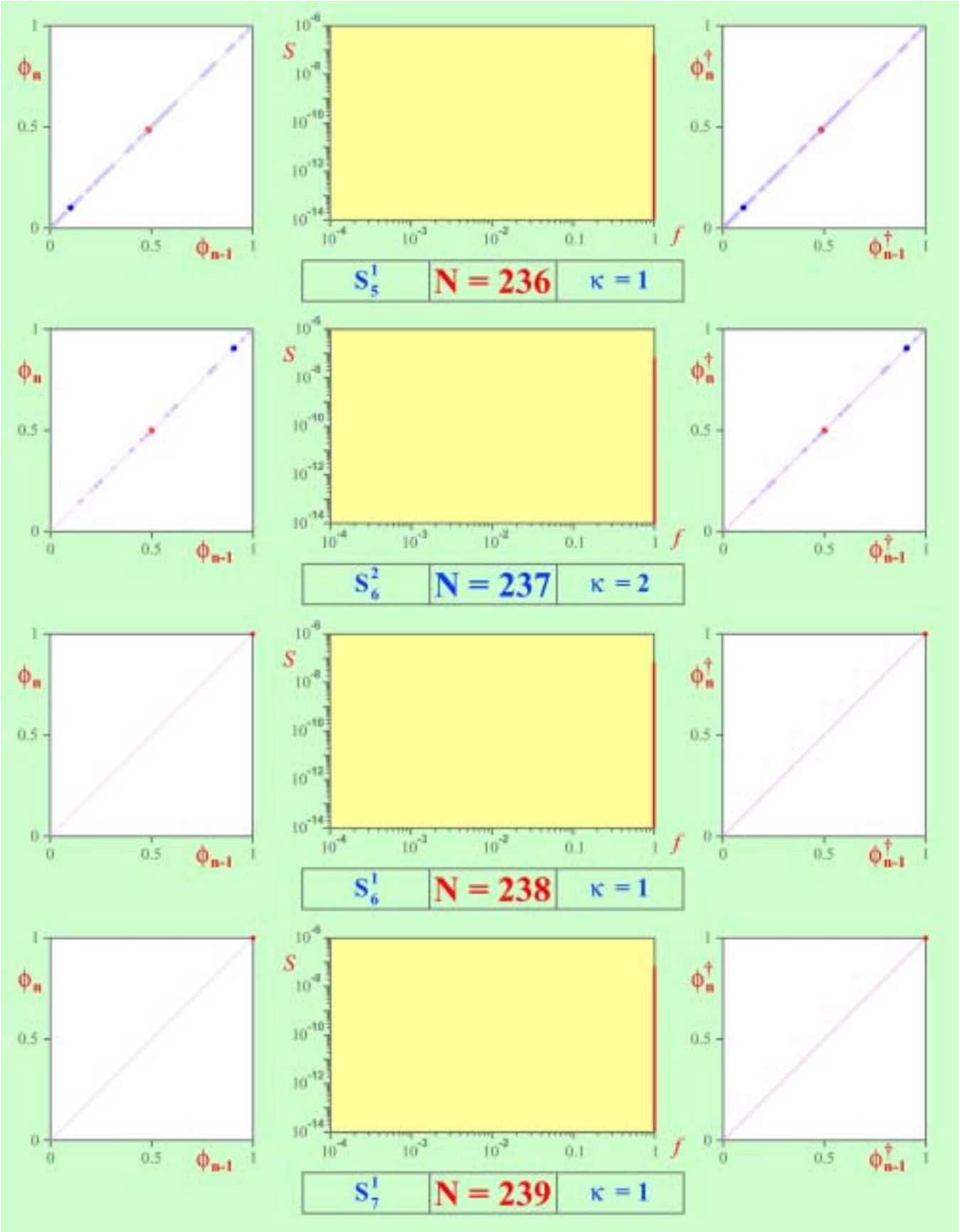


Table 2. (Continued)

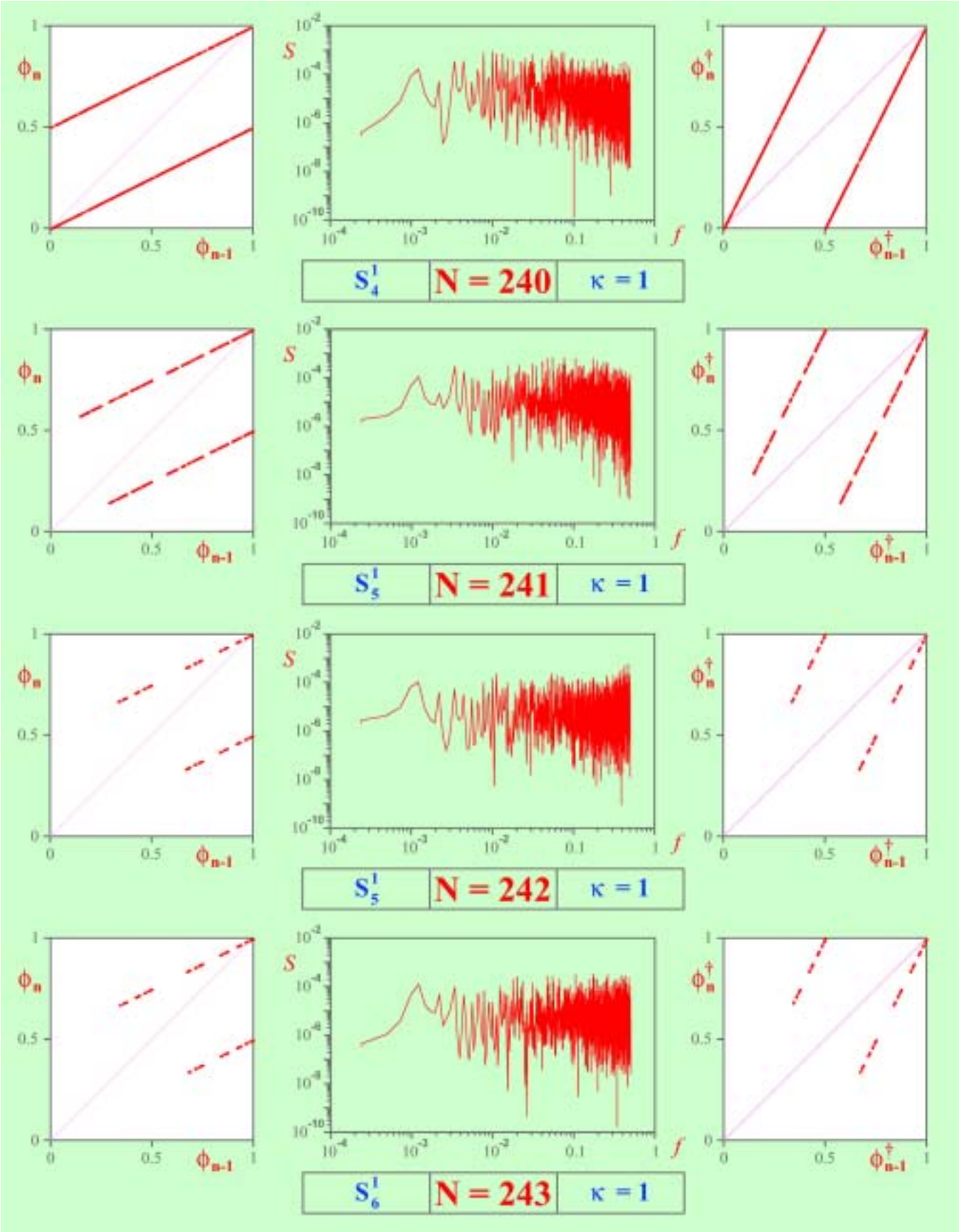


Table 2. (Continued)

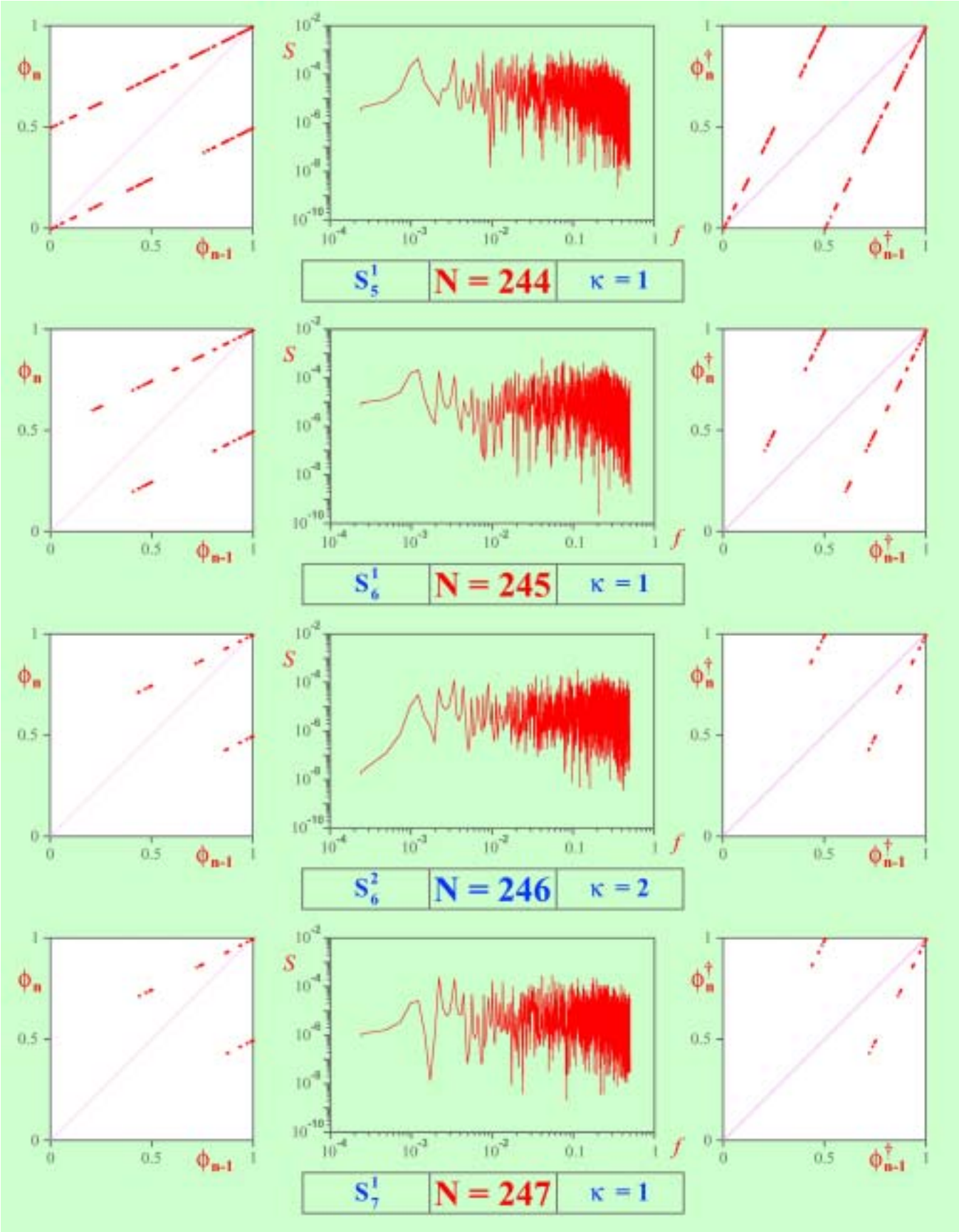


Table 2. (Continued)

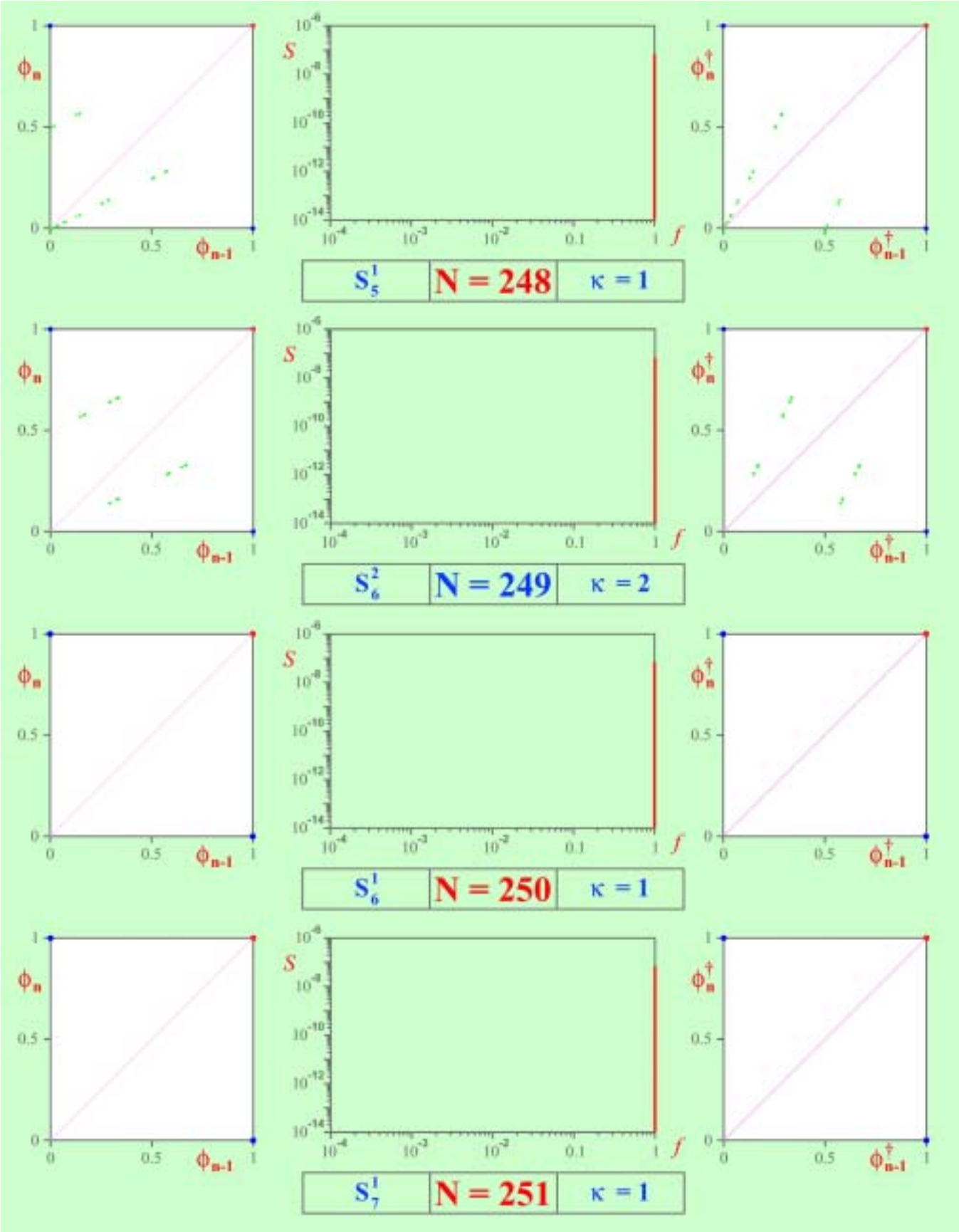
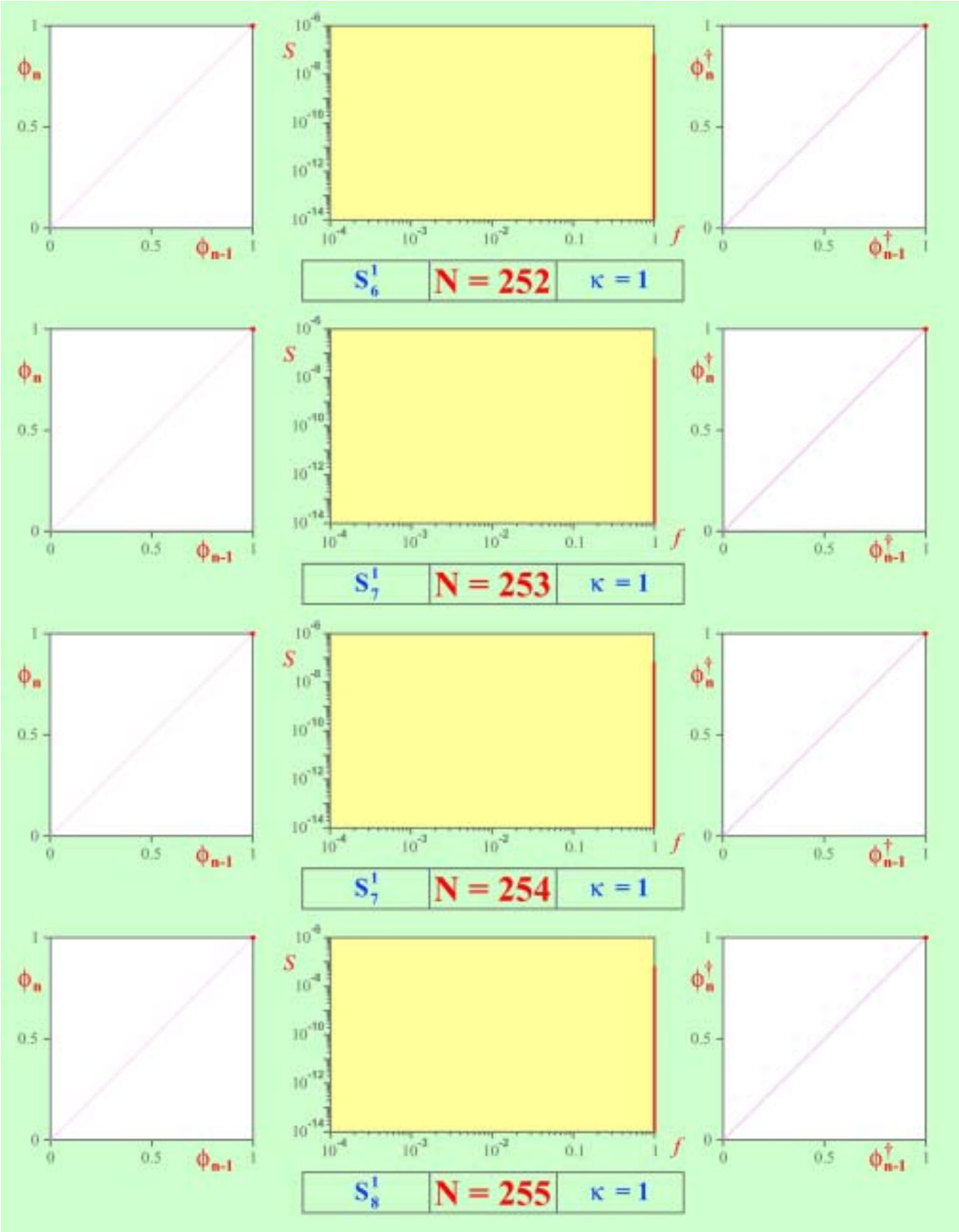


Table 2. (Continued)



All power spectra in Table 2 are calculated with $I = 450$. In some more intricate cases, such as $\boxed{110}$, $\boxed{54}$, etc., a larger value of $I \geq 900$ is used. An $(I + 1)$ -bit random bit string generated by a Borland Delphi random function software is used as our initial configuration (i.e. *initial state*). This bit string is not repeatable in view of its random nature. Since a sufficiently long random bit-string should in principle contain *all possible* combinations distributed over different portions of the string, we can expect that most of the robust modes of each local rule \boxed{N} will emerge in the subsequent iterations. Indeed, *all vignettes in Table 2 are repeatable with different random bit strings*.

In the case where there are *multiple* attractors with widely-separated basins of attractions we must repeat our simulations with different carefully chosen initial states. We usually choose initial configurations containing various periodic subconfigurations of different periods. It is important that such choices do not provoke the nonlinear dynamics from escaping into another basin of attraction. To enhance our chances of uncovering most of the robust modes, we usually found it useful to randomize the periodicity and relative positions of the various subconfigurations.

To obtain a reliable power spectrum at very low-frequency ranges, we have significantly extended our simulation time for some rules, such as $\boxed{110}$, $\boxed{137}$, etc., in order to obtain a sufficiently long time series of length up to $n = 2^{16} = 65536$. Such lengthy simulations also call for a corresponding increase in I because $f = 1/(I + 1)$ represents the lowest observable frequency component. For rules in Table 2 which exhibit a $1/f$ -spectrum, namely, the four universal computing rules $\boxed{110}$, $\boxed{124}$, $\boxed{137}$, and $\boxed{193}$ [Chua et al., 2004] discussed in Sec. 6.2, the determination of their low-frequency spectra in Table 2 requires an immense amount of simulation times.

3.3. Three general properties of time-1 maps

Following are some fundamental relationships exhibited by *time-1 maps* between various local rules. Let $N^\dagger \triangleq T^\dagger[N]$ denote the local rule obtained by applying the *left-right transformation* operator \mathbf{T}^\dagger to N [Chua et al., 2004]. We will henceforth call N^\dagger the *lateral twin* of N , and vice versa.

The twin rules (N, N^\dagger) , $N = 0, 1, 2, \dots, 255$, are *globally equivalent* and listed in Table 1 of [Chua et al., 2004]. It is therefore not surprising that their *forward* and *backward time-1 maps* are related.

Time-1 map Property 1: Dual mapping Correspondence

- (1) The *forward time-1 map* $\rho_1[N]$ of N is identical to the *backward time-1 map* $\rho_1^\dagger[N^\dagger]$ of N^\dagger :

$$\rho_1[N] = \rho_1^\dagger[N^\dagger] \quad (32)$$

- (2) The *forward time-1 map* $\rho_1[N^\dagger]$ of N^\dagger is identical to the *backward time-1 map* $\rho_1^\dagger[N]$ of N :

$$\rho_1[N^\dagger] = \rho_1^\dagger[N] \quad (33)$$

The proof follows from Eqs. (13), (17), (28) and (29).

As an example, compare vignette $\boxed{110}$ and its lateral twin vignette $\boxed{124}$ in Table 2. Observe the left frame of vignette $\boxed{110}$ and the right frame of vignette $\boxed{124}$ are identical. Similarly, the left frame of vignette $\boxed{124}$ and the right frame of vignette $\boxed{110}$ are also identical.

It is instructive for the reader to verify the *Dual mapping Correspondence* by comparing the twin vignettes of all rules in Table 2, thereby obtaining a “constructive”, *albeit* less rigorous, proof.

If \boxed{N} is *bilateral* in the sense that $N^\dagger \triangleq T^\dagger[N] = N$, i.e. N is a fixed point of the left-right transformation \mathbf{T}^\dagger , then we have the following Corollary:

Time-1 map Property 2: Bilateral mapping invariance

The *forward time-1 map* $\rho_1[N]$ and the *backward time-1 map* $\rho_1^\dagger[N]$ of any *bilateral* CA rule \boxed{N} are identical.

There are 64 bilateral CA rules. They are listed in Table 8 of [Chua et al., 2004]. For all of these rules, their vignettes in Table 2 have identical left and right frames (e.g. $\boxed{0}$, $\boxed{1}$, $\boxed{4}$, $\boxed{5}$, $\boxed{18}$, $\boxed{19}$, etc.).

Time-1 map Property 3: π -rotation mapping symmetry⁴

1. The *forward time-1 map* $\rho_1[N]$ of N and the *forward time-1 map* $\rho_1[\bar{N}]$ of $\bar{N} \triangleq \bar{T}[N]$

⁴Time-1 map property 3 is true for all rules except $\{\boxed{57}, \boxed{99}, \boxed{184}, \boxed{226}\}$.

are related by a 180° rotation about the center.⁵

2. The *backward time-1 map* $\rho_1^\dagger[N]$ of N and the *backward time-1 map* $\rho_1^\dagger[\overline{N}]$ of $\overline{N} \triangleq \overline{T}[N]$ are related by a 180° rotation about the center.

Remarks

1. The *time-1 map property 3* can be verified by inspection of Table 2.
2. The above three properties are stated for *time-1 maps* for simplicity. The same properties hold also for *time- τ maps* for all τ .
3. We have verified, by computer simulations, that the above three properties are *consistent* with *all time-1 maps* listed in Table 2. It is truly remarkable that such consistency is achieved by using only one *random configuration* “*probing*” string for each attractor.
4. Our computer simulation results have provided a resounding validation of Wiener’s brilliant insight of using *random signals* as *probes* for *nonlinear system characterizations* [Wiener, 1958].

3.4. Invertible time- τ maps

Since the *period* T_Λ of any attractor of \boxed{N} is the *smallest* integer where the orbit repeats itself, no two points in the *domain* of the functions $\rho_\tau[N]$ and $\rho_\tau^\dagger[N]$ can map to the same point, it follows that both maps $\rho_\tau[N]$ and $\rho_\tau^\dagger[N]$ are *bijective*, and hence have a well-defined *single-valued inverse map* $[\rho_\tau[N]]^{-1}$ and $[\rho_\tau^\dagger[N]]^{-1}$, respectively.

More than half (146 out of 256) of all one-dimensional CA rules exhibit the following important mathematical property which makes the nonlinear dynamics of these rules tractable.

Definition 3. Invertible Time- τ map ($I = \infty$): The *forward time- τ map* $\rho_\tau[N] : [0, 1] \rightarrow [0, 1]$ defined in Eq. (29) (for $\tau = 1$) is said to be *invertible* over $[0, 1]$ iff

$$\rho_\tau[N] = [\rho_\tau^\dagger[N]]^{-1} \quad (34)$$

Similarly, the *backward time- τ map* $\rho_\tau^\dagger[N] : [0, 1] \rightarrow [0, 1]$ defined in Eq. (30) (for $\tau = 1$) is said to be *invertible* over $[0, 1]$ iff

$$\rho_\tau^\dagger[N] = [\rho_\tau[N]]^{-1} \quad (35)$$

Remarks

1. It is important to keep in mind that each time- τ map is associated with *one, and only one*, attractor. We will see in Example 3 below that time- τ maps corresponding to different attractors of the same rule \boxed{N} may exhibit different invertibility property.
2. For *finite* I , the *domain* of the functions $\rho_\tau[N]$ and $\rho_\tau^\dagger[N]$ in Definition 3 must be restricted to a subset of all rational numbers on $[0, 1]$.

Geometrical Interpretation of Invertible time-1 maps

For $\tau = 1$, the two conditions (34) and (35) are equivalent to the condition that the set of points, henceforth called the *graphs* of $\rho_1[N]$, and $\rho_1^\dagger[N]$, in the left and right frames of vignette \boxed{N} , are *mirror images* (i.e. reflection) of each other relative to the main diagonal.

Example 1. Consider vignette $\boxed{3}$ of Table 2. Its left and right frames have only one color (red). Hence $\boxed{3}$ has only one robust attractor.⁶ Since the *graph* of $\rho_1[3]$ on the left and the *graph* of $\rho_1^\dagger[3]$ on the right of vignette $\boxed{3}$ are *reflections* of each other about the main diagonal, the *time-1 maps* $\rho_1[3]$ and $\rho_1^\dagger[3]$ are *invertible*.

Example 2. Consider vignette $\boxed{11}$. The two colors in the left and right frames imply that $\boxed{11}$ has at least two robust attractors. But since both graphs of the same color are mirror images about the diagonal, both pairs of *time-1 maps* of $\boxed{11}$ are invertible.

Example 3. Consider vignette $\boxed{110}$. The red color graphs on the left and the right sides of vignette $\boxed{110}$ are clearly *not* mirror images of each other. Hence, the *forward time-1 map* $\rho_1[110]$ and the *backward time-1 map* $\rho_1^\dagger[110]$ are *not invertible*.

⁵The symbol \overline{T} denotes the *global complementation operator* defined in [Chua et al., 2004]. Indeed, the two *forward time-1 maps* $\{\rho_1[N], \rho_1[\overline{N}]\}$ form a two-element Abelian group whose group multiplication operation consists of a 180° rotation about the center. Similar property applies to the two *backward time-1 maps* $\{\rho_1^\dagger[N], \rho_1^\dagger[\overline{N}]\}$. Both are examples of the abstract element group C_2 .

⁶For each vignette in Table 2, we have shown only *time-1 maps* of robust *attractor prototypes*. Many rules have attractors that can only be observed with specially chosen initial configurations.

Example 4. Finally, consider vignette [62]. There are at least two attractors. The graphs of the red color *time-1 maps* $\rho_1[62]$ and $\rho_1^\dagger[62]$ consisting of only three red dots⁷ are not mirror symmetric about the main diagonal. It follows that the red color *forward and backward time-1 maps* of [62] are *not* invertible. In contrast, the blue color *time-1 maps* $\rho_1[62]$ and $\rho_1^\dagger[62]$ consisting of a large ensemble of points exhibit reflection (mirror) symmetry about the diagonal and hence the two blue color time-1 maps of [62] are invertible.

Remarks

1. A *forward time-1 map* $\rho_1[N]$ is *invertible* if, and only if, its associated *backward time-1 map* $\rho_1^\dagger[N]$ is *invertible*.
2. Since the “composition” between two *invertible* functions is also an *invertible* function, it follows that if a *forward time-1 map* $\rho_1[N]$, or a *backward time-1 map* $\rho_1^\dagger[N]$, is *invertible*, then so are their associated time- τ maps $\rho_\tau[N]$ and $\rho_\tau^\dagger[N]$, for any integer τ .

4. Period- k Time-1 Maps: $k = 1, 2, 3$

In this section we organize local rules into three separate groups based on the global qualitative behaviors of their *time-1 maps*, which were derived from *random* initial configurations. Each *time-1 map* is the outcome of a *single random* initial state. Unlike the 256 dynamic patterns presented in [Wolfram, 2002] and [Chua et al., 2003], which have no *predictive* ability because the “probing” input signal consists of only a single *red* center pixel, the *time-1 maps* in Table 2 can be used, *with complete confidence*, to *predict* the long-term behaviors due to *any* initial configurations. *Time-1 maps* are, *qualitatively*, reminiscent of the classic *Green’s function* from theoretical physics, the *impulse response* from linear circuit and system theory [Chua et al., 1987] and the Brownian motion response *a la* Wiener [Wiener, 1958], where in all cases, a *single* testing signal is enough to predict the response to *any* initial configurations.

4.1. Period-1 rules

Our research on *time-1 maps* of period-1 attractors has found that there are a total of 93 (out of 256) one-dimensional CA rules from Table 2 with robust *period-1 modes* in the sense that almost all random initial states will converge to a *period-1 configuration*; namely, a fixed point. These 93 rules can be logically partitioned into four distinct families whose members are listed in Tables 3 and 4, respectively. These rules are organized in accordance with the theory of *global equivalence class* ε_m^κ developed in [Chua et al., 2004].⁸ Since all members of a given equivalence class ε_m^κ have identical global dynamical behaviors, it suffices to examine and analyze in depth only one member of each class. Since Table 3 contains 45 rules which exhibit *invertible* time-1 maps, we will henceforth refer to these rules as *invertible rules* for simplicity. These rules are *invertible* because their *forward time-1 maps* $\rho_1[N]$ and *backward time-1 maps* $\rho_1^\dagger[N]$ are identical with respect to both color and position, along the main diagonal, and hence they satisfy Definition 3 in a trivial way. Observe that since there are only 20 global equivalence classes in Table 3, only 20 out of the 45 invertible rules have qualitatively distinct global dynamical response to arbitrary initial states, including transient, attractor, and invariant orbit regimes, and their respective basins of attraction (for attractors).

Table 4 contains 24 *noninvertible* period-1 rules from Table 2. Since they can be partitioned into six global equivalence classes, only six representative *noninvertible period-1 rules* warrant an in-depth analysis. Observe that the rules in Table 4 are *noninvertible* because each fixed point of $\rho_1[N]$ in the left frame of vignette [N] does not map into the same point in $\rho_1^\dagger[N]$ in the right frame of vignette [N]. For example, the red fixed point in the left frame of vignette [12] and its corresponding fixed-point in the right frame of vignette [12] are two different points, and hence are not mirror images of each other, relative to the main diagonal.

A careful examination of the vignettes in Table 2 corresponding to the 45 *time-1 maps* from Table 3 reveals that there are 12 rules from Table 3 which must tend to a homogeneous “0” (colored

⁷Note that the *domain* of the two red color *time-1 maps* $\rho_1[62]$ and $\rho_1^\dagger[62]$ consists of only three *rational* numbers, obtained by projecting the three red points onto $[0, 1]$.

⁸Throughout this paper, each rule N is coded in *red*, *blue* or *green* color, in accordance with the *complexity index* [Chua et al., 2002] $\kappa = 1, 2$, or 3 , respectively.

Table 3. 45 Invertible *period-1* rules, among them only 29 are *bilateral*.

ε_m^κ	N	$T^\dagger[N]$	$\bar{T}[N]$	$T^*[N]$	κ
ε_1^1	0	0	255	255	1
ε_5^1	4	4	223	223	1
ε_8^1	8	64	239	253	1
ε_{17}^1	32	32	251	251	1
ε_{11}^2	36	36	219	219	2
ε_{14}^2	40	96	235	249	2
ε_{23}^2	72	72	237	237	2
ε_{24}^1	76	76	205	205	1
ε_{25}^1	77	77	77	77	1
ε_{27}^2	94	94	133	133	2
ε_{28}^2	104	104	233	233	2
ε_{26}^1	128	128	254	254	1
ε_{35}^2	132	132	222	222	2
ε_{27}^1	136	192	238	252	1
ε_{31}^1	160	160	250	250	1
ε_{41}^2	164	164	218	218	2
ε_{33}^1	168	224	234	248	1
ε_{37}^1	200	200	236	236	1
ε_{38}^1	204	204	204	204	1
ε_{39}^1	232	232	232	232	1

Table 4. 24 Noninvertible *period-1* rules.

ε_m^κ	N	$T^\dagger[N]$	$\overline{T}[N]$	$T^*[N]$	κ
ε_{11}^1	12	68	207	221	1
ε_{12}^1	13	69	79	93	1
ε_{16}^2	44	100	203	217	2
ε_5^3	78	92	141	197	3
ε_{29}^1	140	196	206	220	1
ε_8^3	172	228	202	216	3

blue in Fig. 12) attractor and another 12 rules which must tend to a homogeneous “1” (colored red in Fig. 13), for almost all initial states. These 24 *homogeneous* rules are collected in Tables 5

and 6, respectively. Since all *time-1 maps* in Table 5 consists of a *fixed point* at $\phi_n = 0.\overline{00}$, we can *predict* that all dynamic patterns from the 12 rules in Table 5 must tend to a homogeneous “0”

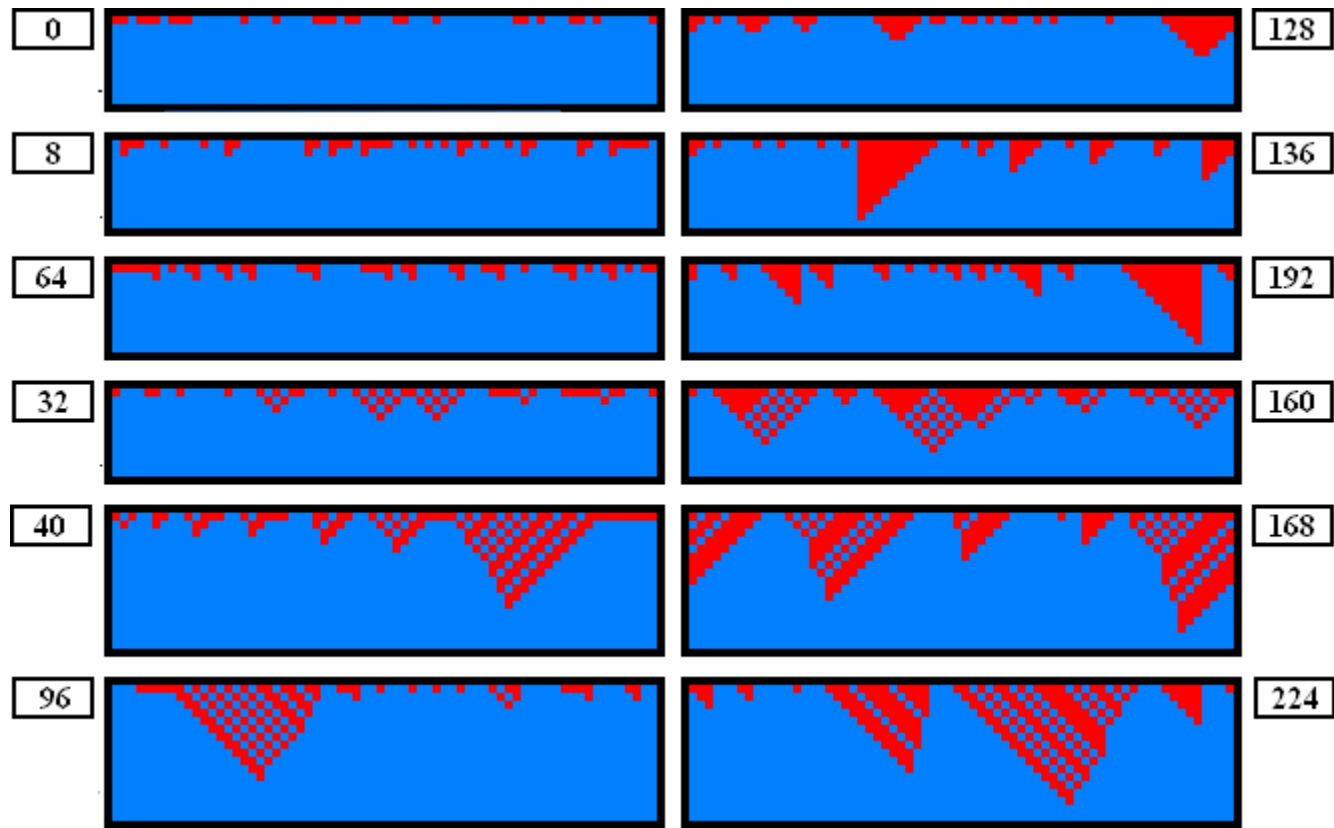


Fig. 12. All rules belonging to Table 5 tend to a homogeneous blue (“0”) state, regardless of the initial state, chosen randomly. Each pattern has 67 rows and 11 columns.

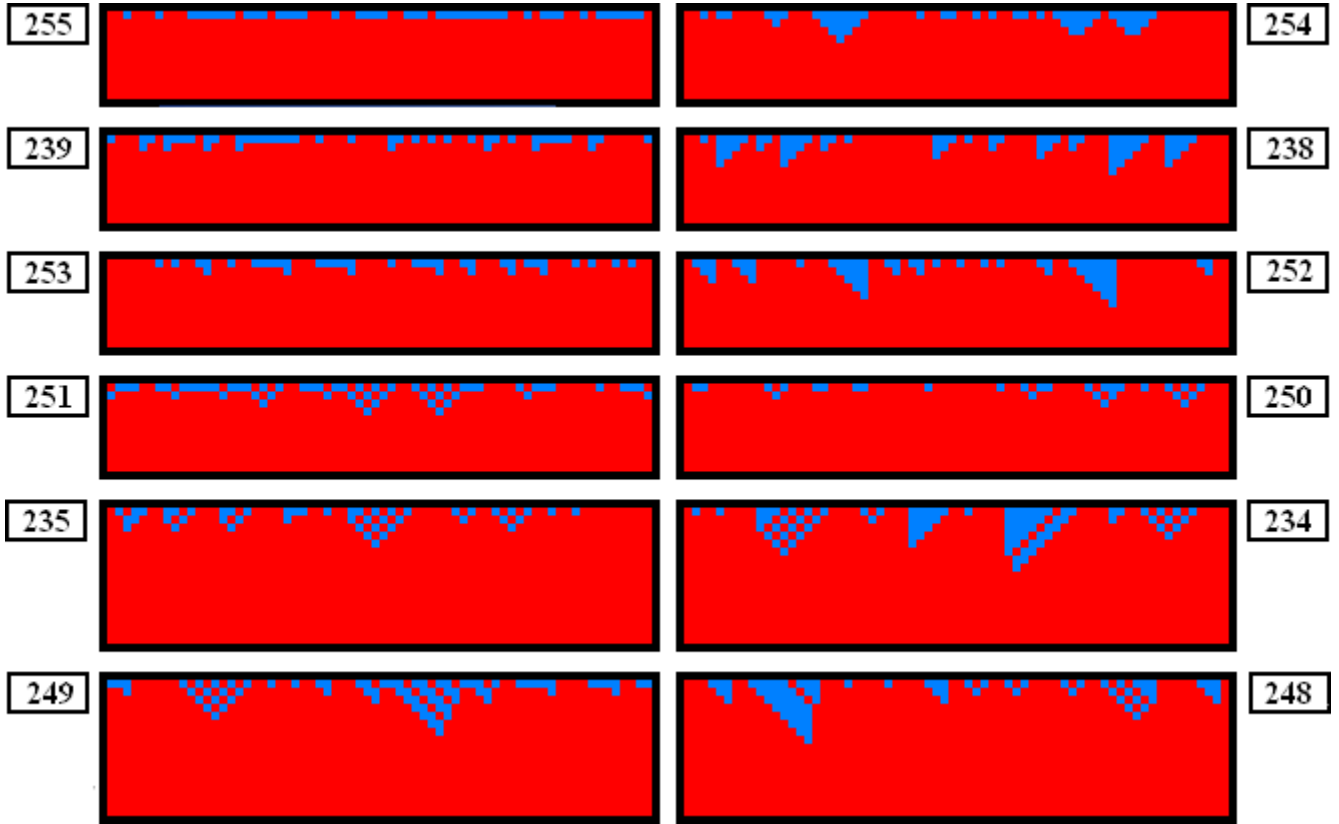


Fig. 13. All rules belonging to Table 6 tend to a homogeneous red (“1”) state, regardless of the initial state, chosen randomly. Each pattern has 67 rows and 11 columns.

Table 5. 12 Homogeneous “0” (blue) Rules. All are *invertible* but only four are *bilateral*.

ϵ_m^κ	N	$T^\dagger[N]$	κ
$\epsilon_{/}^1$	0	0	1
ϵ_8^1	8	64	1
ϵ_{17}^1	32	32	1
ϵ_{14}^2	40	96	2
ϵ_{26}^1	128	128	1
ϵ_{27}^1	136	192	1
ϵ_{31}^1	160	160	1
ϵ_{33}^1	168	224	1

Table 6. 12 Homogeneous “1” (red) Rules. All are *invertible* but only four are *bilateral*.

ϵ_m^κ	N	$T^\dagger[N]$	κ
$\epsilon_{/}^1$	255	255	1
ϵ_8^1	239	253	1
ϵ_{17}^1	251	251	1
ϵ_{14}^2	235	249	2
ϵ_{26}^1	254	254	1
ϵ_{27}^1	238	252	1
ϵ_{31}^1	250	250	1
ϵ_{33}^1	234	248	1

(blue) pattern after T_δ iterations. Simulating these 12 rules from a random initial state leads to the 12 dynamic patterns shown in Fig. 12, which confirm our prediction of a homogeneous blue steady state.

A similar analysis of the 12 rules in Table 6 shows a common fixed point at $\phi = 1.\overline{00}$, which implies a homogeneous “1” (red) steady state response, as confirmed by the simulation results shown in Fig. 13.

A comparison of Tables 3 and 5 shows that all *nonbilateral* (i.e. $N \neq N^\dagger$) period-1 rules from Table 3 are members of Tables 5 and 6, which can exhibit only trivial homogeneous “0” and “1”, respectively, patterns. Hence, *all invertible non-homogeneous period-1 rules are bilateral*. However, there are 16 *invertible but nonbilateral period-1 rules*; they all yield trivial homogeneous “0” or “1” patterns and are listed in Tables 5 and 6.

As an illustration, the dynamic patterns $\mathcal{D}_{\overline{N}}[\mathbf{x}(0)]$ of three *invertible* (and *bilateral*) *period-1 rules* selected from Table 3 are displayed in the left column of Fig. 14; namely, $N = \overline{4}$, $\overline{77}$, and $\overline{232}$. Observe that since $\overline{223}$ in Table 3 belongs to the same global equivalence class ε_5^1 as that of $\overline{4}$, it has the same qualitative behaviors as $\overline{4}$ [Chua et al., 2004], and need

not be examined. Three additional period-1 patterns chosen from three *noninvertible* and *nonbilateral* rules listed in Table 4 ($\overline{44}$, $\overline{78}$, and $\overline{172}$) are displayed in the right column of Fig. 14. By the same principle of global equivalence, we can predict that the three rules $\{\overline{100}$, $\overline{203}$, $\overline{217}\} \in \varepsilon_{16}^2$ must have the same qualitative behavior as $\overline{44}$. Similarly, the three rules $\{\overline{92}$, $\overline{141}$, $\overline{197}\} \in \varepsilon_5^3$ must have the same qualitative behaviors as $\overline{78}$, and the three rules $\{\overline{228}$, $\overline{202}$, $\overline{216}\} \in \varepsilon_8^3$ must have the same qualitative behaviors as $\overline{172}$.

Except for the 12 homogeneous “0” rules in Table 5 and the 12 homogeneous “1” rules in Table 6, all other *period-1 rules* in Tables 3 and 4 consist of *clusters* of period-1 points distributed over different locations on the main diagonal of the respective vignettes in Table 2. To demonstrate that the three *time-1 map properties* from Sec. 3.3 hold for *all* period-1 attractors, two typical period-1 points are highlighted as red and blue dots in each period-1 vignette in Table 2. Observe that the red and blue dots occupy identical positions in the left and the right frames of each vignette for all *bilateral* period-1 rules (e.g. $\overline{4}$, $\overline{36}$, $\overline{72}$, etc.), as predicted by the *bilateral*

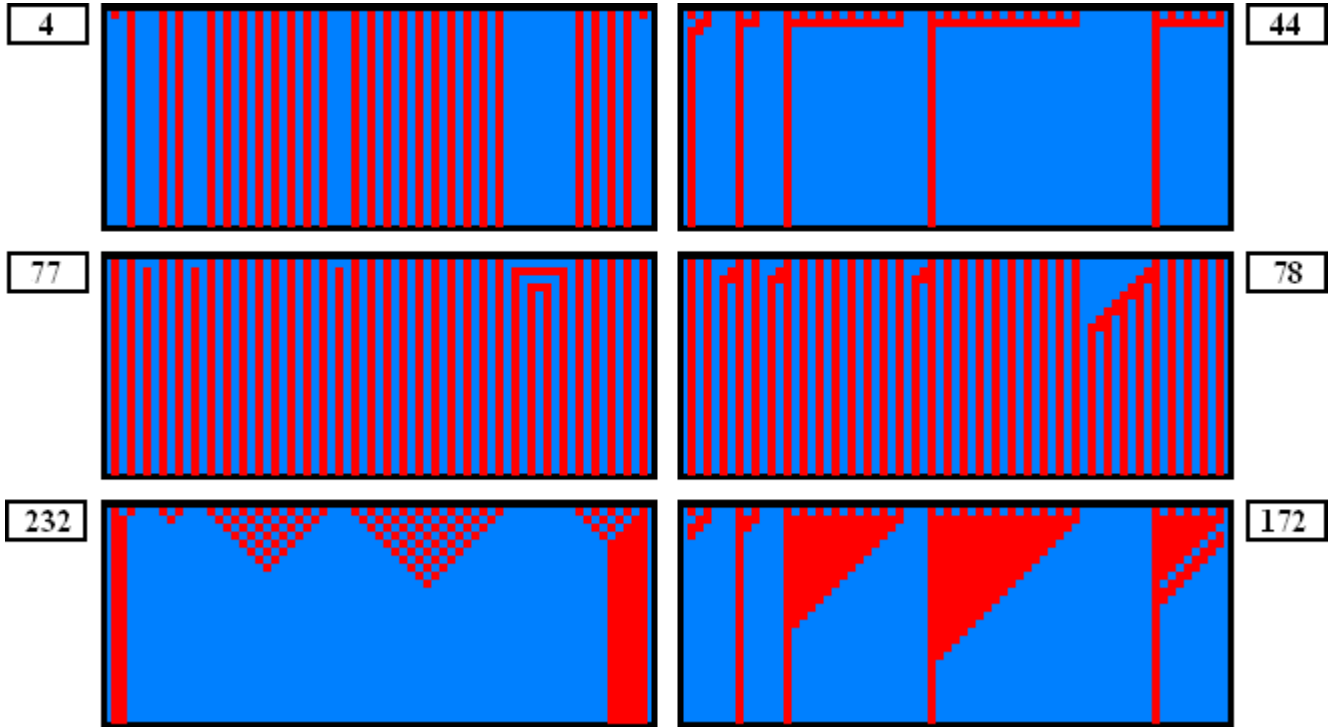


Fig. 14. Gallery of six period-1 dynamic patterns. The patterns on the left are invertible and bilateral. Those on the right are noninvertible and nonbilateral. Each pattern has 68 rows and 26 columns. The initial configurations (row 0) are chosen randomly.

mapping invariance. Clusters associated with *non-bilateral* period-1 rules in the left frame are different from those in the right frame of corresponding vignettes, (e.g. [12], [13], [44], etc.). However, the π -rotation mapping symmetry implies that the left frame of vignette \overline{N} must be identical to the right frame of vignette $\overline{T}[N]$, modulo 180° rotation about the center. Indeed, the left frame of vignette [12] and the right frame vignette $\overline{T}[12] = [207]$ are related by a 180° rotation, as predicted.

While there are many *nonhomogeneous* period-1 attractors, each represented by a point belonging to some dull blue cluster in Table 2, there is *only one attractor* (shown in red) in all, except eight (namely, [40], [96], [168], [224], [235], [249], [234], and [248]), *homogeneous* period-1 rules in Table 2. These eight exceptions, shown in blue, are endowed with a *second* attractor of a more complicated type (called a *Bernoulli* σ_1 -shift) to be discussed in Sec. 5.

Since there are a total of 69 period-1 CA rules (45 in Table 3 and 24 in Table 4), and since 24 among them (12 in Table 5 and 12 in Table 6) have only *one* period-1 attractors, namely, 12 *homogeneous* “0” attractors and 12 *homogeneous* “1” attractors, there are altogether 45 period-1 CA rules having many *distinct* period-1 points clustered in disconnected groups along the main diagonal in the left and right frames of their associated vignettes in Table 2 (printed in dull blue color). For finite I , these period-1 point are rational numbers on $(0, 1)$. Since rational numbers are *denumerable* [Niven, 1967], these period-1 points are sparsely distributed and almost every point on $(0, 1)$ are *not* period-1.

4.2. Period-2 rules

An examination of Table 2 shows that there are 17 *invertible* CA rules possessing *period-2* attractors. They are listed in Table 7, organized into 10 global equivalent classes. All 17 rules in Table 7 are *bilateral*, i.e. $N = N^\dagger$. In addition, there are eight *noninvertible* CA rules from three global equivalent classes possessing *period-2* attractors, as exhibited in Table 8. Observe that all of these rules are *non-bilateral*.

Each *period-2* attractor is manifested by two isolated points, symmetrically positioned with respect to the main diagonal in both *forward* and *backward time-1 maps* in Table 2. As in the period-1 case, in general there are many *distinct* period-2 attractors for each period-2 CA rule, and they tend

to be organized in various disconnected clusters; they are depicted in *dull blue* color in each period-2 vignette in Table 2. In addition, two prototype period-2 points are singled out and printed in *red* and *blue* colors, respectively, at their precise locations (within the resolution of the printer).

The 17 rules in Table 7 are invertible because corresponding points in their *forward* and *backward time-1 maps* in the corresponding left and right vignette frames in Table 2 are symmetric, with respect to both color and position, about the main diagonal.

Observe also that the left and right vignette frames in Table 2 of all 17 rules in Table 7 are identical, as predicted by the “*bilateral mapping invariance*” (*time-1 map property 2*).

The eight rules in Table 8 are noninvertible because their *forward* and *backward time-1 maps* are not symmetric with respect to the main diagonal. For example, the left and right frames of vignette [28] in Table 2 are not mirror symmetric with respect to the main diagonal. Observe, however, that the right frame of vignette [28] is identical to the left frame of vignette [70] ($[70] = T^\dagger[[28]]$) in Table 2, as predicted by the “*dual mapping Correspondence*” (*time-1 map property 1*). Similarly, the left frame of vignette [28] is identical to the right frame of vignette [70].

Observe next that the *left* frame of vignette [28] and the *left* frame of vignette [199] $= \overline{T}[[28]]$ are related by a 180° rotation about the center, as predicted by the “ π -rotation mapping symmetry” (*time-1 map property 3*). Similarly, the *right* frame of vignette [28] and the *right* frame of vignette [199] are related by a 180° rotation.

As an illustration, the dynamic patterns $D_{\overline{N}}[x(0)]$ of three *invertible* (and *bilateral*) *period-2* rules selected from Table 7 are displayed in the left column of Fig. 15, namely, $N = [33]$, [51], and [108]. Observe that since [123] in Table 7 belongs to the same global equivalence class ε_{10}^2 as that of [33], it has the same qualitative behaviors as [33]. Three additional period-2 patterns chosen from three *noninvertible* and *nonbilateral* rules listed in Table 8 ([28], [29], [198]) are displayed in the right column of Fig. 15. By the same principle of global equivalence, we can predict that the three rules $\{[70], [199], [157]\} \in \varepsilon_8^2$ must have the same qualitative behavior as [28]. Similarly, rule [71] $\in \varepsilon_2^3$ must have the same qualitative behaviors as [29], and rule [156] $\in \varepsilon_{40}^2$ must have the same qualitative behaviors as [198].

Table 7. 17 Invertible *period-2* rules (all are bilateral rules).

\mathcal{E}_m^κ	N	$T^\dagger[N]$	$\overline{T}[N]$	$T^*[N]$	κ
\mathcal{E}_2^1	1	1	127	127	1
\mathcal{E}_6^1	5	5	95	95	1
\mathcal{E}_{15}^1	19	19	55	55	1
\mathcal{E}_{16}^1	23	23	23	23	1
\mathcal{E}_{10}^2	33	33	123	123	2
\mathcal{E}_{12}^2	37	37	91	91	2
\mathcal{E}_{22}^1	50	50	179	179	1
\mathcal{E}_{23}^1	51	51	51	51	1
\mathcal{E}_{30}^2	108	108	201	201	2
\mathcal{E}_{35}^1	178	178	178	178	1

Table 8. 8 Noninvertible *period-2* rules (all are nonbilateral rules).

\mathcal{E}_m^κ	N	$T^\dagger[N]$	$\overline{T}[N]$	$T^*[N]$	κ
\mathcal{E}_8^2	28	70	199	157	2
\mathcal{E}_2^3	29	71	71	29	3
\mathcal{E}_{40}^2	156	198	198	156	2

Finally, we note from Table 2 that all eight *non-invertible* and *nonbilateral* period-2 rules in Table 8 possess an additional form of symmetry; namely, the *forward time-1 map* $\rho_1[N]$ is related to the *backward time-1 map* $\rho_1^\dagger[N]$ by a 180° rotation about the center. In other words, the left and right vignette frames of each rule in Table 8 are related by a 180° rotation about the origin. We will henceforth

call this rather rare property a *self π -rotation symmetry*.

4.3. Period-3 rules

A comprehensive examination of Table 2 shows that there are only four CA rules that possess robust period-3 attractors, namely, [62], [118], [131], and

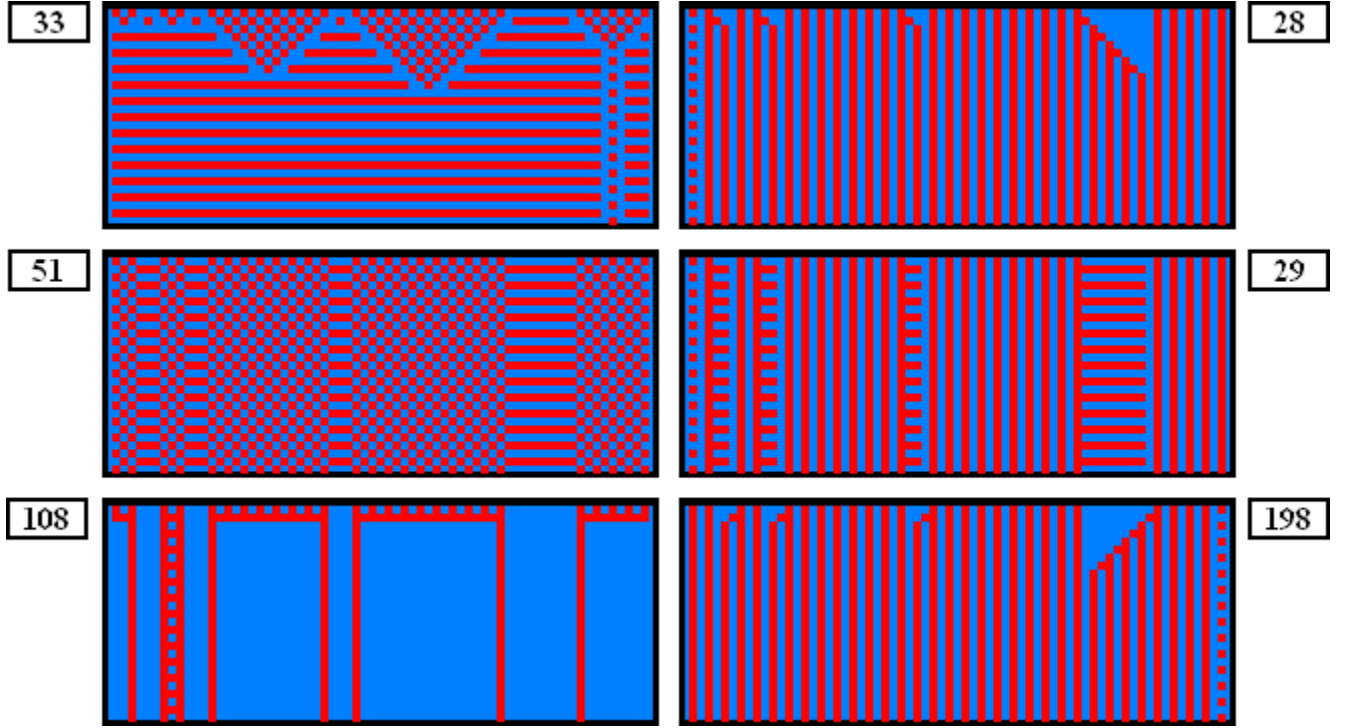


Fig. 15. Gallery of six period-2 dynamic patterns. The patterns on the left are invertible and bilateral. Those on the right are noninvertible and nonbilateral. Each pattern has 68 rows and 26 columns.

[145]. An examination of the vignettes of these four rules in Table 2 show that they are *nonbilateral* and *noninvertible*. Since all four rules belong to the same global equivalence class ε_{22}^2 , as depicted in Table 9, it follows that it suffices to conduct an in-depth analysis of only one of these four rules. Since we have already been exposed to [62] in Fig. 11, let us continue to use this rule for illustrations.

Figure 16 shows the dynamic pattern $\mathcal{D}_{\overline{\mathbf{v}}}[\mathbf{x}(0)]$ of [62], [118], [131], and [145] for different choices of initial states which give rise to qualitatively similar evolution patterns. Observe that each pattern converges to a *period-3* attractor after some transient time T_δ whose value depends on the initial states. The presence of a robust *period-3* mode in [62] can be predicted from the *power spectrum* of the *forward time series* φ (defined in Eq. (26)) where a sharp peak centered at $f = 1/3$ is clearly discernible.

In addition to the robust period-3 *time-1* maps depicted (in red) in vignettes [62], [118], [131], and [145], there is a second robust attractor, depicted in blue in Table 2 which can only be understood by examining its associated *time-2* map $\rho_2[62]$ to be discussed in Sec. 5.

Just like period-1 and period-2 rules, there are many other robust *period-3* attractors in [62], [118], [131], and [145]. They are distributed over the unit square as *dull blue* clusters.

Unlike the dynamics patterns associated with *period-1* and *period-2* rules where different subpatterns evolve independently from one another, and do not interact with one another, we see from [62] that several subpatterns can interact and compete in the sense that one subpattern usually emerges as the winner, after annihilating other competing subpatterns. Such interactions occur in the dynamics of

Table 9. 4 Noninvertible *period-3* rules (all are nonbilateral rules).

ε_m^k	N	$T^\dagger[N]$	$\overline{T}[N]$	$T^*[N]$	κ
ε_{22}^2	62	118	131	145	2

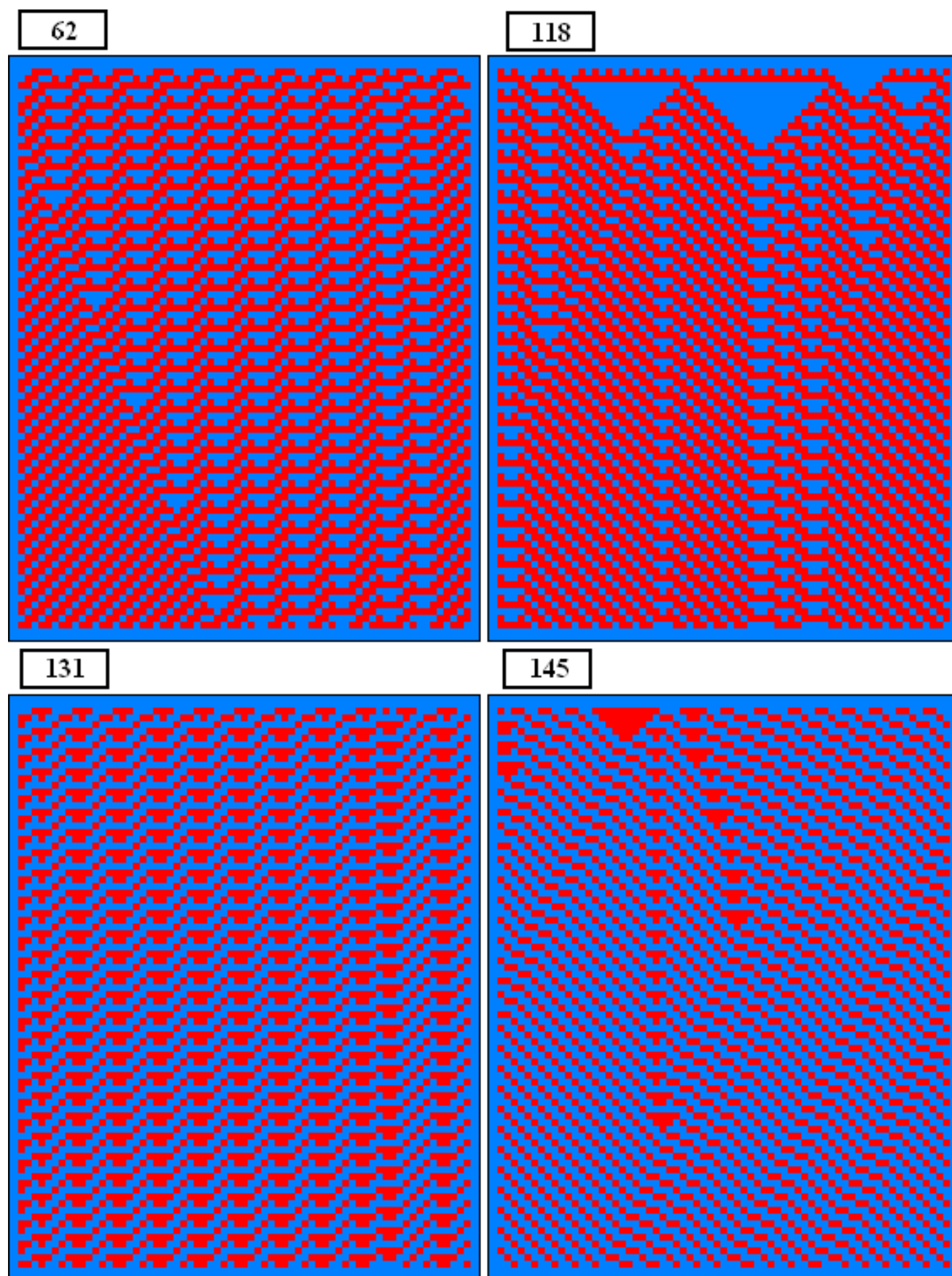


Fig. 16. Evolutions of four globally equivalent rules [62], [118], [131], and [145]. All patterns consist of 82 rows and 66 columns.

[62] because it can support subpatterns which propagate to the left, and to the right, thereby colliding with each other in due time.

4.4. Invariant orbits

For finite I , there can be only a finite number T_Λ of points on the forward and backward *time-1 maps* of any rule $[N]$. This implies that the *domain of time-1 maps* are generally extremely sparse even for rules with a very large period T_Λ . Geometrically this means that a vertical line drawn through an arbitrary point $\phi_{n-1} \in (0, 1)$ will almost never intersect the *time-1 map* of most rules. In other words, *one expects to see many gaps in most time-1 maps* in Table 2.

A careful examination of all 256 rules in Table 2 reveals that there are six, and only six rules, which have a *dense time-1 map*; namely, $\{[15], [51], [85], [170], [204], [240]\}$. Observe the graph of the *time-1 map* of these six rules project to almost all points on the unit interval $[0, 1]$. In the limit, these points actually tend to a continuum so that the *time-1 map* $\rho_1[N]$ coincides with the characteristic function $\chi_{[N]}^1$. In this case, *every point* $\phi_{n-1} \in [0, 1]$ is a *point on a periodic orbit* of $[N]$, and there are no *transient* regimes in these six rules. We have therefore the following

Proposition. *All dynamic patterns $D_{[N]}[x(0)]$ of the six rules $[15], [51], [85], [170], [204],$ and $[240]$, belonging to the local equivalence class S_4^1 are invariant orbits.*

5. Bernoulli σ_τ -Shift Rules

In addition to the 98 rules we have listed so far (45 *invertible period-1* rules in Table 3, 24 *noninvertible period-1* rules in Table 4, 17 *invertible period-2* rules in Table 7, eight *noninvertible period-2* rules in Table 8, and four *noninvertible period-3* rules in Table 9) where we can predict their global long-term dynamical behaviors, there are 112 additional rules whose attractors can be precisely *predicted* by invoking the remarkably simple *symbolic dynamics* exhibited by the well-known *Bernoulli shift map* [Tang *et al.*, 1983; Nogashima & Baba, 1999]. In particular, we will show in this section that the

evolution of each initial configuration of these 112 rules can be predicted by *shifting* it either to the left, or to the right, by 1, 2 or 3 pixels, and possibly followed by a complementation (i.e. change of color).

5.1. Gallery of Bernoulli σ_τ -shift rules

Among the 256 CA rules listed in Table 2, there are 112 rules, henceforth called “*Bernoulli σ_τ -Shift Rules*”, which have simple Bernoulli-shift dynamics. They are extracted from Table 2 and reorganized into three separate Tables. Table 10 contains 84 *invertible* Bernoulli σ_τ -shift rules, organized as members of 24 global equivalence classes ε_m^κ , and listed column 1. Observe that the second attractor (blue in Table 2) of the four period-3 rules $\{[62], [118], [131], [145]\}$ belonging to ε_{22}^2 are members of Table 10 and hence are also Bernoulli rules. The four members of each equivalence class are listed in columns 2–5. The *color* chosen for each rule in these columns follows the same code for the *complexity index* [Chua *et al.*, 2002]. The index κ for each class is listed in column 6. Since some rules in Table 10 have 2 Bernoulli⁹ attractors, this information is indicated by an “**X**” sign in columns 7 and 8, depending on whether the *forward time-1 map* $\rho_1[N](\phi_{n-1} \mapsto \phi_n)$, or the *forward time-2 map* $\rho_2[N](\phi_{n-2} \mapsto \phi_n)$ is required to represent the attractor in order to uncover its *Bernoulli-shift* attractor. The number of Bernoulli attractors for each rule $[N]$ is listed in column 9. The last column 10 provides an *index of table number* (13-1 to 13-9) where the characterizing features of each equivalence class belonging to Table 10 can be found.

Table 11 contains 20 *noninvertible* Bernoulli σ_τ -shift rules with two Bernoulli attractors, organized in the same format as Table 10. In this table, all rules have two Bernoulli attractors. The relevant Bernoulli σ_τ -shift maps in this table consist of either the *forward time-2 map* $\rho_2[N](\phi_{n-2} \mapsto \phi_n)$, or the *forward time-3 map* $\rho_3[N](\phi_{n-3} \mapsto \phi_n)$.

Table 12 contains eight *noninvertible* Bernoulli σ_τ -shift rules with three Bernoulli attractors displayed in a similar format except for two new columns replacing the former “attractor-number”

⁹To avoid clutter, we will henceforth refer to a Bernoulli σ_τ -shift map, rule, or attractor simply as a *Bernoulli map*, *Bernoulli rule* or *Bernoulli attractor*, respectively. We also abuse our language and use the same name “*Bernoulli attractor k* ”, $k = 1, 2, 3$, to mean the k th family of attractors which share the same *qualitative global dynamics*, such as “shift left by 2 pixels”.

Table 10. 84 Invertible *Bernoulli* σ_T -shift rules with one or two *Bernoulli* attractors.

ε_m^{κ}	N	$T^{\dagger}[N]$	$\overline{T}[N]$	$T^{\#}[N]$	κ	$\phi_{n-1} \mapsto \phi_n$	$\phi_{n-2} \mapsto \phi_n$	Number of attractors	Table index
ε_3^1	2	16	191	247	1	X		1	13-1
ε_4^1	3	17	63	119	1		X	1	13-8
ε_7^1	7	21	31	87	1		X	1	13-8
ε_9^1	10	80	175	245	1	X		1	13-1
ε_{10}^1	11	81	47	117	1	X X		2	13-3
ε_{13}^1	14	84	143	213	1	X X		2	13-4
ε_{14}^1	15	85	15	85	1	X		1	13-2
ε_5^2	24	66	231	189	2	X		1	13-1
ε_{18}^1	34	48	187	243	1	X		1	13-1
ε_{19}^1	35	49	59	115	1	X	X	2	13-7
ε_{20}^1	42	112	171	241	1	X		1	13-1
ε_{21}^1	43	113	43	113	1	X X		2	13-3
ε_3^3	46	116	139	209	3	X		1	13-1
ε_{19}^2	56	98	227	185	2	X X		2	13-5
ε_{20}^2	57	99	99	57	2	X X		2	13-5
ε_4^3	58	114	163	177	3	X	X	2	13-6
ε_{22}^2	62	118	131	145	2	X	X	2	13-9
ε_{34}^2	130	144	190	246	2	X		1	13-1
ε_{28}^1	138	208	174	244	1	X		1	13-1
ε_{30}^1	142	212	142	212	1	X X		2	13-4
ε_{38}^2	152	194	230	188	2	X		1	13-1
ε_{32}^1	162	176	186	242	1	X		1	13-1
ε_{34}^1	170	240	170	240	1	X		1	13-1
ε_9^3	184	226	226	184	3	X X		2	13-5

Table 11. 20 Noninvertible Bernoulli σ_τ -shift rules with two Bernoulli attractors.

\mathcal{E}_m^κ	N	$T^\dagger[N]$	$\bar{T}[N]$	$T^*[N]$	κ	$\phi_{n-2} \mapsto \phi_n$	$\phi_{n-3} \mapsto \phi_n$	Number of attractors	Table index
\mathcal{E}_1^2	6	20	159	215	2	X X		2	14-1
\mathcal{E}_2^2	9	65	111	125	2	X	X	2	14-2
\mathcal{E}_1^3	27	83	39	53	3	X X		2	14-3
\mathcal{E}_{13}^2	38	52	155	211	2	X X		2	14-4
\mathcal{E}_{36}^2	134	148	158	214	2	X X		2	14-5

Table 12. 8 Noninvertible Bernoulli σ_τ -shift rules with three Bernoulli attractors.

\mathcal{E}_m^κ	N	$T^\dagger[N]$	$\bar{T}[N]$	$T^*[N]$	κ	$\phi_{n-1} \mapsto \phi_n$	$\phi_{n-2} \mapsto \phi_n$	$\phi_{n-3} \mapsto \phi_n$	$\phi_{n-5} \mapsto \phi_n$	Table index
\mathcal{E}_6^2	25	67	103	61	2		X	X	X	15-1
\mathcal{E}_{23}^2	74	88	173	229	2	X	X	X		15-2

column due to space limitation. Observe that there are four distinct Bernoulli σ_τ -shift maps represented in Table 12, namely, the forward *time-1*, *time-2*, *time-3* and *time-5* maps $\rho_\tau(\phi_{n-\tau} \mapsto \phi_n)$, $\tau = 1, 2, 3, 5$.

In order to state the Bernoulli shifting algorithm in an unambiguous way, we have collected all those rules from Table 10 which evolve in accordance with the same *shifting mode* into the same group, and have identified each by a *shift-mode ID code* $\mathbf{B}_{[N]}[\alpha, \beta, \tau]$ in *column 1* of Table 13. All Bernoulli rules from Table 13 obeying the same ID code are listed in the rightmost *column 5* of Table 13. Since all rules having the same ID code $\mathbf{B}_{[N]}[\alpha, \beta, \tau]$ exhibit a qualitatively similar power spectrum, the spectrum of only the first member $[N]$ of each group is chosen as a *prototype*. For example, $N = [2]$ and $[16]$ in Table 13-1, $[11]$ in Table 13-3, $[14]$ in Table 13-4, ... and $[62]$ in Table 13-9. The power spectrum and the *forward time-1 map* $\rho_1[N](\phi_{n-1} \mapsto \phi_n)$ from vignette $[N]$ of Table 2 are reproduced in *columns 2 and 3*, respectively, of Table 13. In addition, the power spectrum from column 2 is partitioned into a *low* (red), *mid* (green), and *high* (blue) frequency range in *column 4*, where various characteristic features of rule

$[N]$ are identified and annotated. The bold color line segments shown in some of the annotated spectrum represent the *average* spectrum calculated over a narrow range via a least-square method.

For some rules, such as $[58]$, $[3]$, $[17]$, $[35]$, ..., etc., the *forward time-2 map* $\rho_2[N](\phi_{n-2} \mapsto \phi_n)$ is plotted in *column 3* instead of $\rho_1[N](\phi_{n-1} \mapsto \phi_n)$ because it is this map which reveals its Bernoulli character. Indeed, the forward *time-1* maps of these rules do *not* reveal any interesting features! The *hidden* Bernoulli character of these maps emerges, however, as soon as one glances at the $\tau = 2$ *characteristic function* $\chi_{[N]}^2$.

A careful analysis of the *forward time- τ maps* in *column 3* of Table 13 shows that all points (red dots) from the *time- τ map* (left frame) of vignette $[N]$ of Table 2 fall exactly on parallel *light blue* lines with a *slope*

$$\beta \in \left\{ \pm \frac{1}{8}, \pm \frac{1}{4}, \pm \frac{1}{2}, \pm 2, \pm 4, \pm 8 \right\} \quad (36)$$

For reasons that will soon be obvious, we will henceforth refer to the parallel *light blue* lines of each Bernoulli rule $[N]$ listed in Table 13 as the *Bernoulli σ_τ -shift map* of $[N]$, even though only a *subset* of

Table 13-1. $B_N[\alpha, \beta, \tau]$ characterization for 84 invertible Bernoulli rules with one or two Bernoulli attractors.

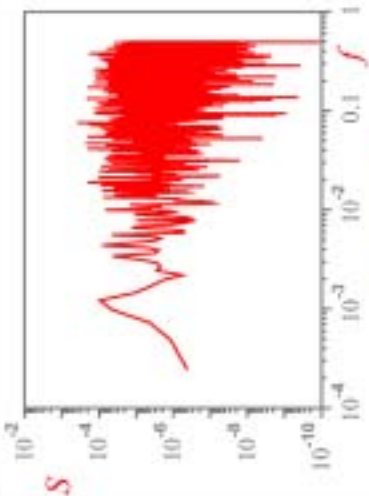
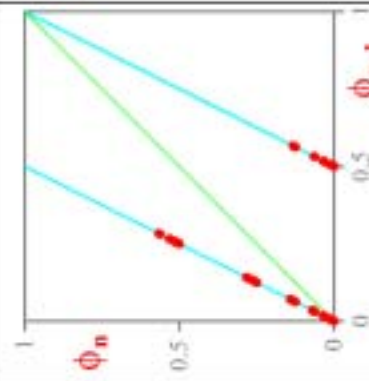
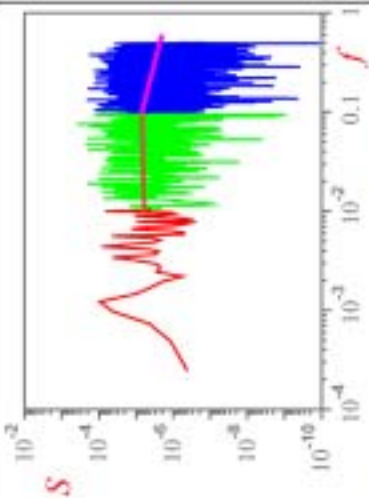
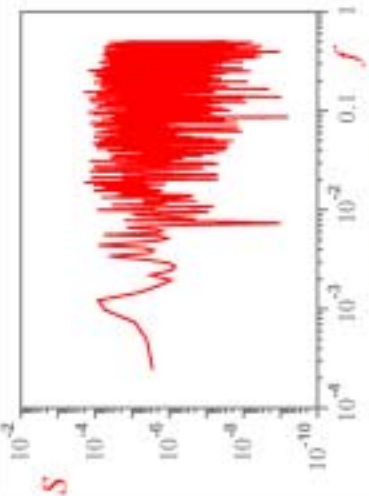
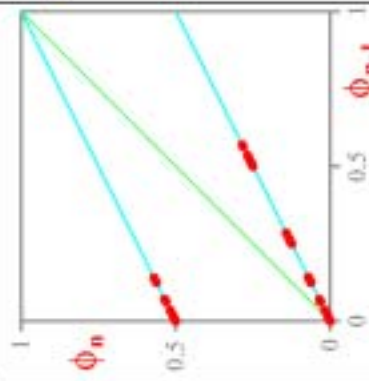
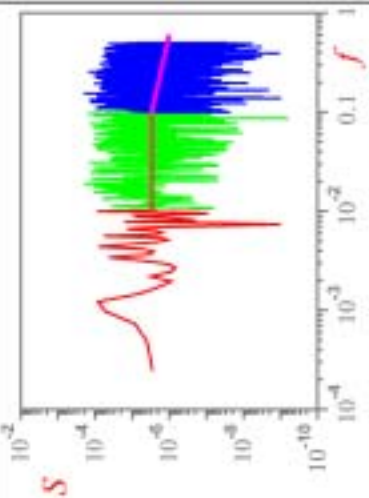
$B_N[\alpha, \beta, \tau]$	Power spectrum	Bernoulli σ_τ -shift map	Characteristic features	N
$B_2[1, 2, 1]$			 <p>Power approximately uniform over $0.01 < f < 0.1$ Power decreases for $f > 0.1$</p>	<div>2</div> <div>10</div> <div>34</div> <div>42</div> <div>46</div> <div>66</div> <div>130</div> <div>138</div> <div>139</div> <div>162</div> <div>170</div> <div>171</div> <div>174</div> <div>175</div> <div>186</div> <div>187</div> <div>188</div> <div>189</div> <div>190</div> <div>191</div> <div>194</div>
$B_{16}[1, 1/2, 1]$			 <p>Power approximately uniform over $0.01 < f < 0.1$ Power decreases for $f > 0.1$</p>	<div>16</div> <div>24</div> <div>48</div> <div>80</div> <div>112</div> <div>116</div> <div>144</div> <div>152</div> <div>176</div> <div>208</div> <div>209</div> <div>230</div> <div>231</div> <div>240</div> <div>241</div> <div>242</div> <div>243</div> <div>244</div> <div>245</div> <div>246</div> <div>247</div>

Table 13-2. (Continued)

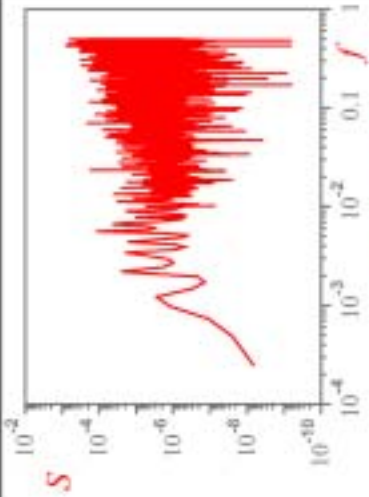
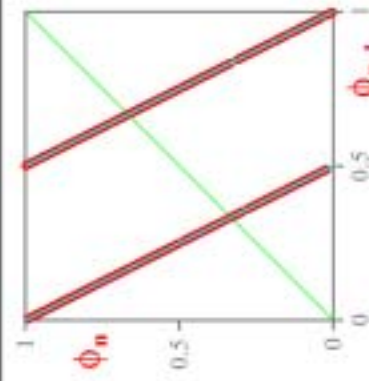
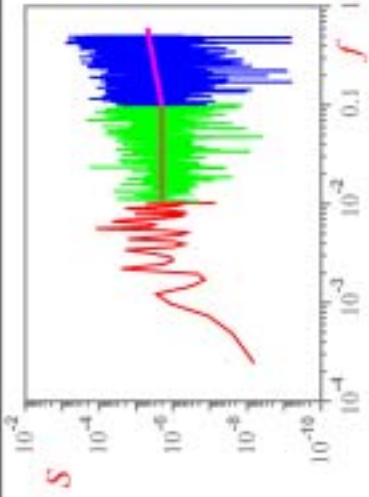
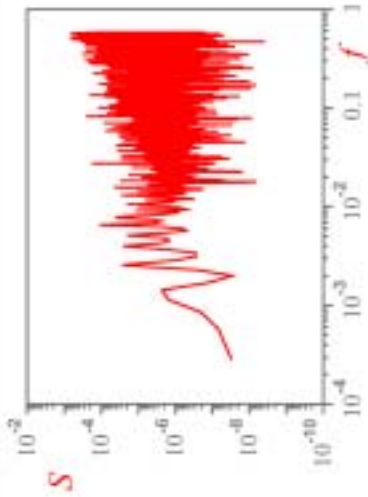
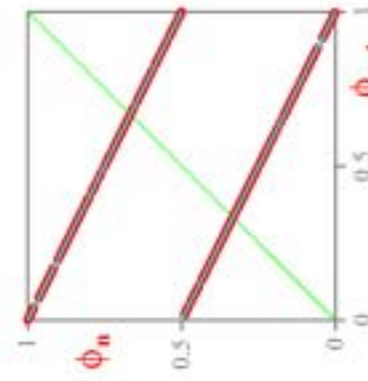
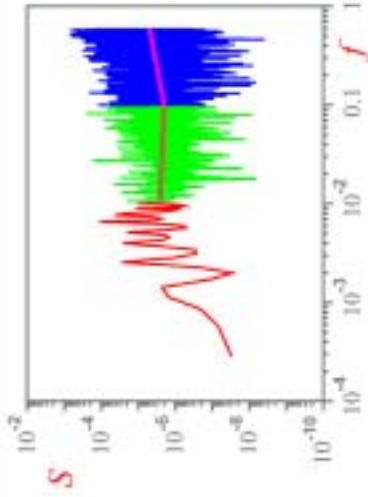
$B_N[\alpha, \beta, \tau]$	Power spectrum	Bernoulli σ_τ -shift map	Characteristic features	N
$B_{85}^{[85]}[1, -2, 1]$				85
$B_{15}^{[15]}[2, -1/2, 1]$				15

Table 13-3. (Continued)

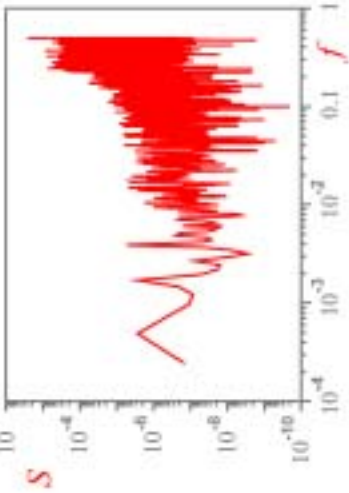
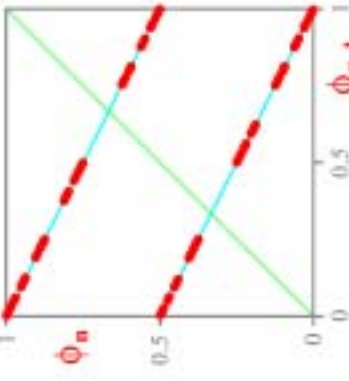
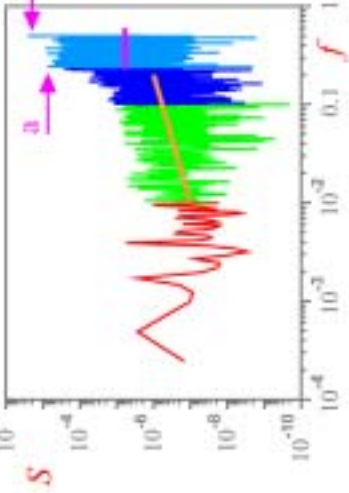
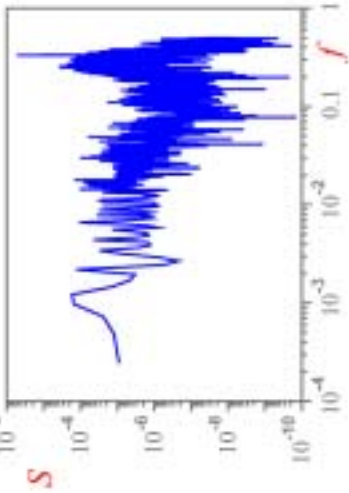
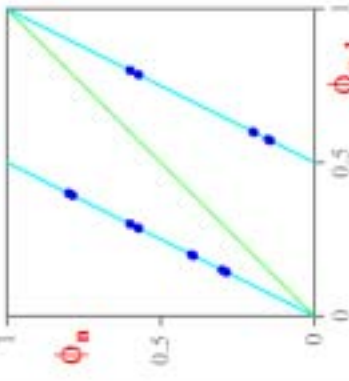
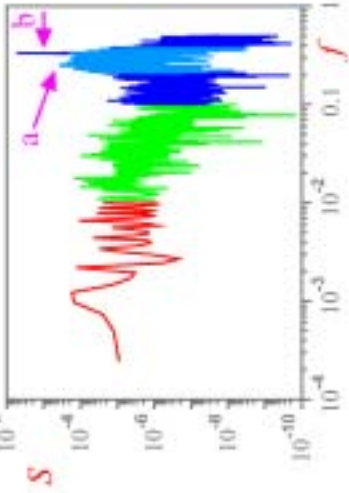
$B_N[\alpha, \beta, \tau]$	Power spectrum	Bernoulli σ_τ -shift map	Characteristic features	N
$B_{II}^{[1, -1/2, 1]}$	 <div>11</div>	 <div>Attractor 1 $\phi_{n-1} \mapsto \phi_n$</div>	 <p>Mild ascent over $0.01 < f < 0.2$. A plateau for $f > 0.2$. Broad peak at a ($f = 1/4$) and sharp peak at b ($f = 2/4$) imply period-4 mode.</p>	<div>11</div> <div>43</div> <div>47</div> <div>81</div> <div>113</div> <div>117</div>
$B_{II}^{[2, 2, 1]}$	 <div>11</div>	 <div>Attractor 2 $\phi_{n-1} \mapsto \phi_n$</div>	 <p>Power is not uniform for $f > 0.01$. A broad peak near a ($f = 1/4$) implies period-4 mode. Sharp peak at b ($f = 1/3$) implies period-3 mode.</p>	<div>11</div> <div>43</div> <div>47</div> <div>81</div> <div>113</div> <div>117</div>

Table 13-4. (Continued)

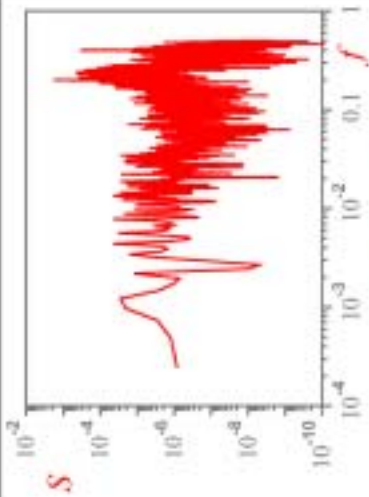
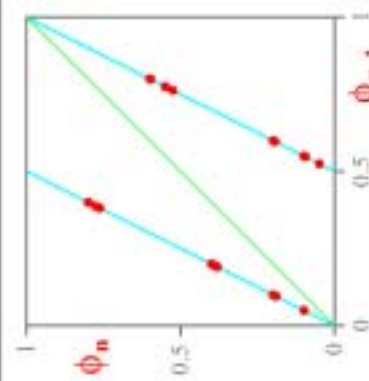
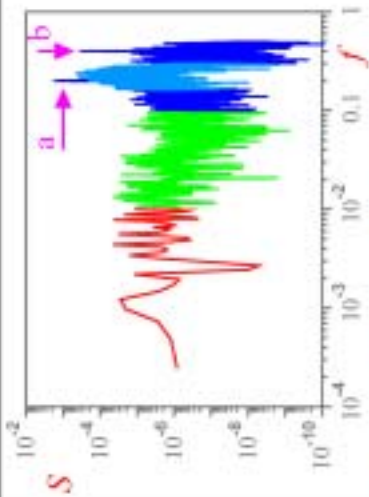
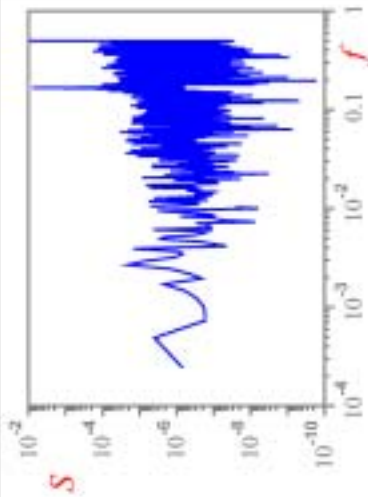
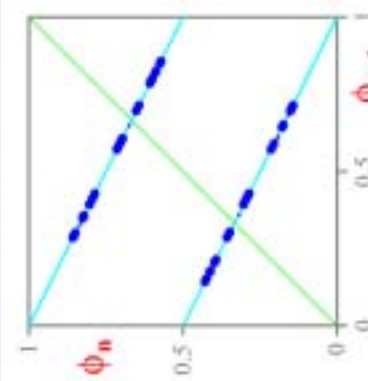
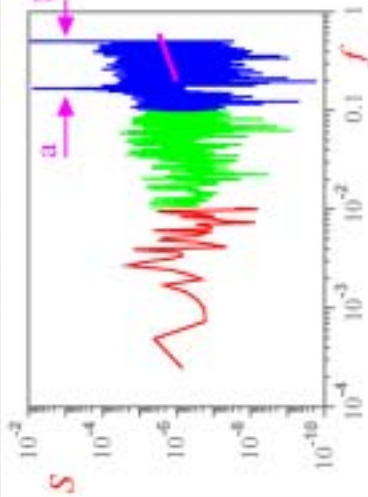
$B_N[\alpha, \beta, \tau]$	Power spectrum	Bernoulli σ_τ -shift map	Characteristic features	N
$B_{14}^{[14]}[1, 2, 1]$	 <div>14</div>	 <div>Attractor 1</div> $\phi_{n-1} \mapsto \phi_n$	 <p>Power is not uniform for $f > 0.01$. A broad peak near a ($f = 1/4$) implies period-4 mode. Sharp peaks at a ($f = 1/5$) and b ($f = 2/5$) imply period-5 mode.</p>	<div>14</div> <div>84</div> <div>142</div> <div>143</div> <div>212</div> <div>213</div>
$B_{14}^{[14]}[2, -1/2, 1]$	 <div>14</div>	 <div>Attractor 2</div> $\phi_{n-1} \mapsto \phi_n$	 <p>Power is not uniform for $f > 0.01$. A mild ascent for $f > 0.1$. Sharp peaks at a ($f = 1/6$) and b ($f = 3/6$) imply period-6 mode.</p>	<div>14</div> <div>84</div> <div>142</div> <div>143</div> <div>212</div> <div>213</div>

Table 13-5. (Continued)

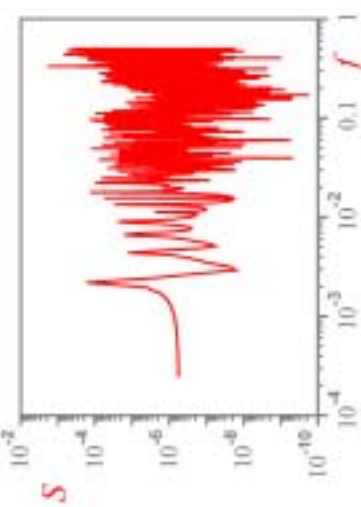
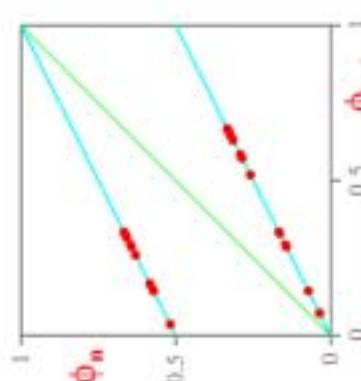
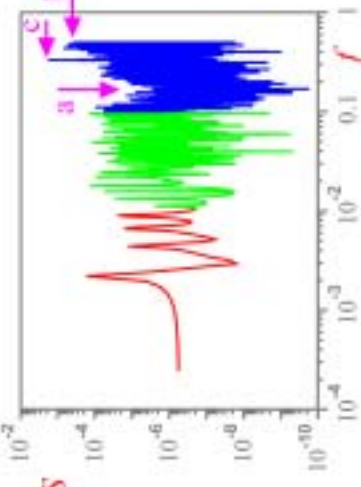
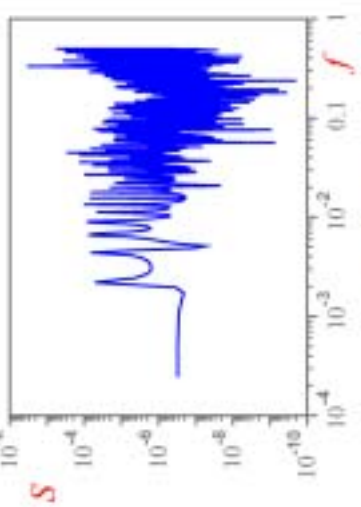
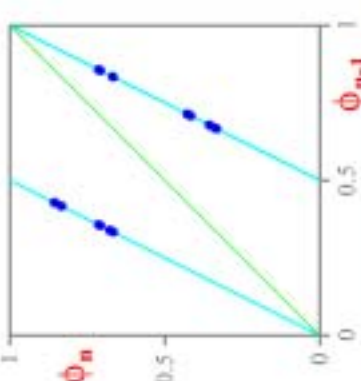
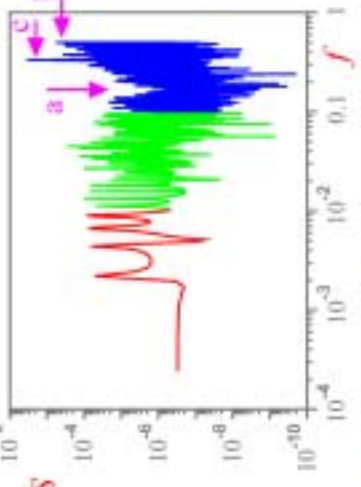
$B_N[\alpha, \beta, \tau]$	Power spectrum	Bernoulli σ_τ -shift map	Characteristic features	N
$B_{56}^{[1, 1/2, 1]}$	 <div>56</div>	 <div>Attractor 1</div> $\phi_{n-1} \mapsto \phi_n$	 <p>Power is not uniform for $f > 0.01$. There is a deep trough at a ($f = 1/6$). A broad peak at b ($f = 1/2$) implies period-2 mode. Sharp peak c ($f = 1/3$) implies period-3 mode.</p>	<div>56</div> <div>57</div> <div>98</div> <div>99</div> <div>184</div> <div>185</div> <div>226</div> <div>227</div>
$B_{56}^{[2, 2, 1]}$	 <div>56</div>	 <div>Attractor 2</div> $\phi_{n-1} \mapsto \phi_n$	 <p>Power is not uniform for $f > 0.01$. There is a deep trough at a ($f = 1/6$). A broad peak at b ($f = 1/2$) implies period-2 mode. Sharp peak c ($f = 1/3$) implies period-3 mode.</p>	<div>56</div> <div>57</div> <div>98</div> <div>99</div> <div>184</div> <div>185</div> <div>226</div> <div>227</div>

Table 13-6. (Continued)

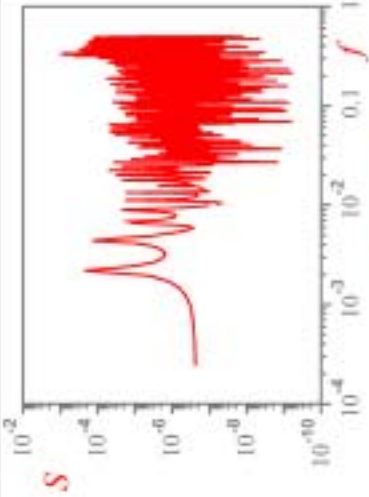
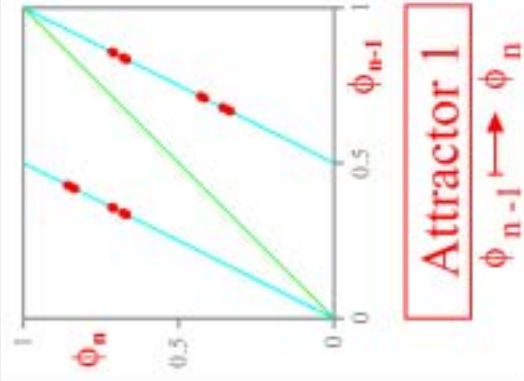
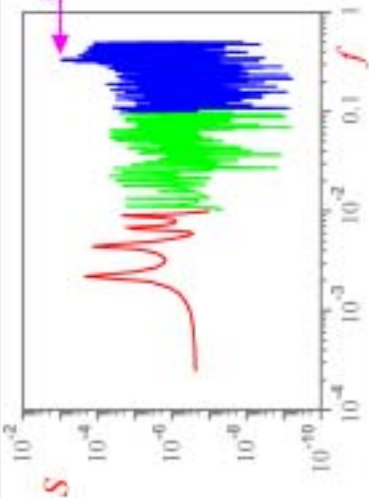
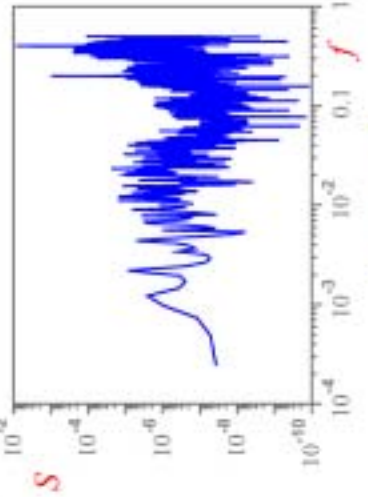
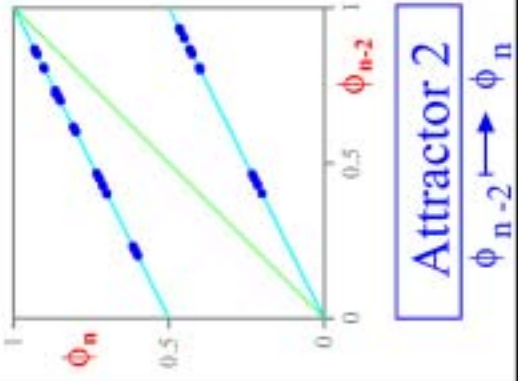
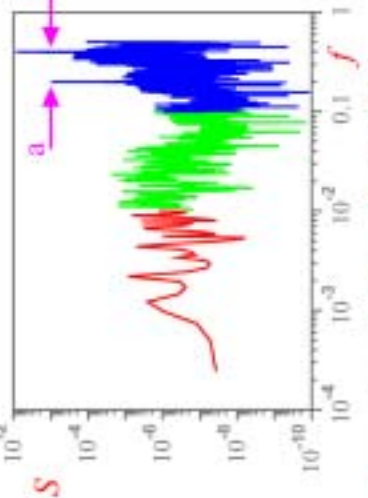
$B_N[\alpha, \beta, \tau]$	Power spectrum	Bernoulli σ_τ -shift map	Characteristic features	N
$B_{58}^{[1,2,1]}$	 58	 Attractor 1 $\phi_{n-1} \mapsto \phi_n$	 Power is not uniform for $f > 0.01$. Sharp peak a ($f = 1/3$) implies period-3 mode.	<div>58</div> <div>114</div> <div>163</div> <div>177</div>
$B_{58}^{[2,1/2,2]}$	 58	 Attractor 2 $\phi_{n-2} \mapsto \phi_n$	 Power is not uniform for $f > 0.01$. Sharp peaks a ($f = 1/5$) and b ($f = 2/5$) imply period-5 mode.	<div>58</div> <div>114</div> <div>163</div> <div>177</div>

Table 13-7. (Continued)

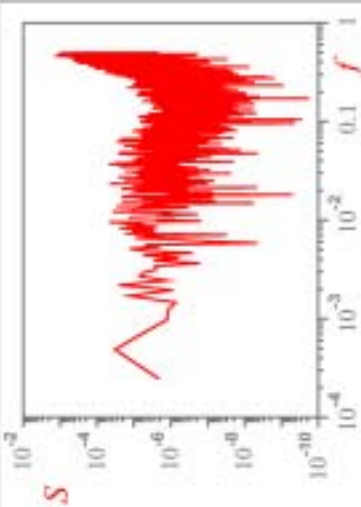
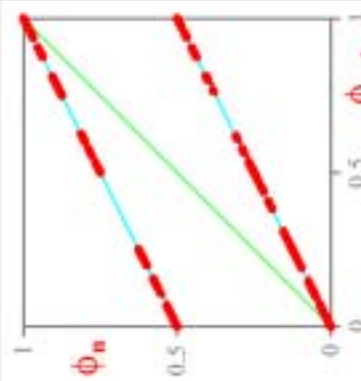
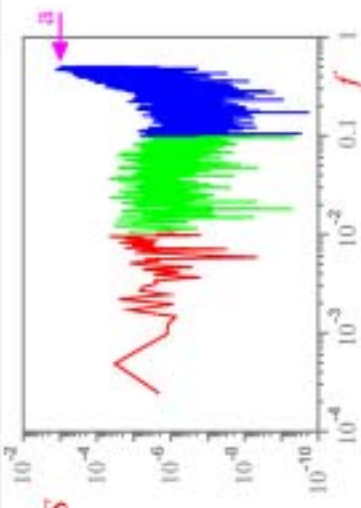
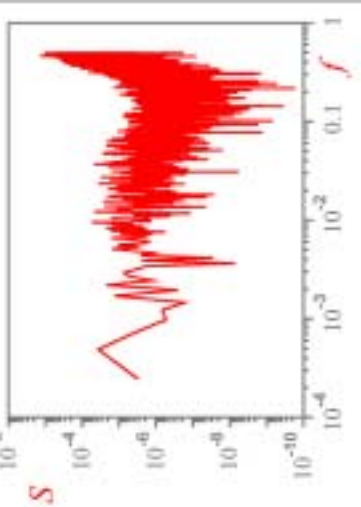
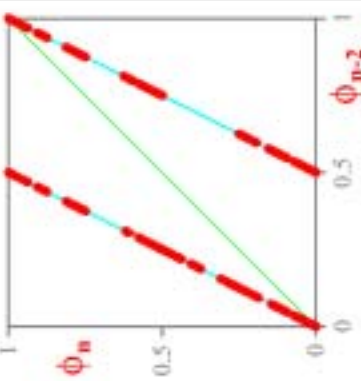
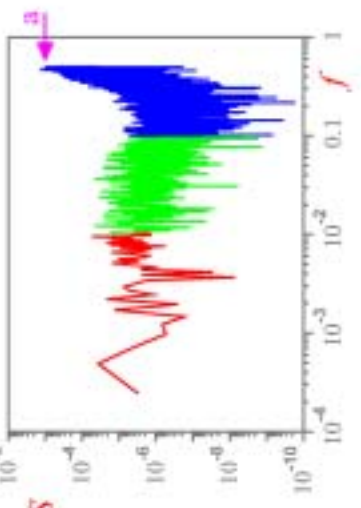
$B_N[\alpha, \beta, \tau]$	Power spectrum	Bernoulli σ_τ -shift map	Characteristic features	N
$B_3[1, 1/2, 2]$	 3	 Attractor 1 $\phi_{n-2} \mapsto \phi_n$	 Power is not uniform for $f > 0.01$. A broad peak at $(f = 1/2)$ implies period-2 mode.	3 7 31 63
$B_{17}[1, 2, 2]$	 17	 Attractor 1 $\phi_{n-2} \mapsto \phi_n$	 Power is not uniform for $f > 0.01$. A broad peak at $(f = 1/2)$ implies period-2 mode.	17 21 87 119

Table 13-8. (Continued)

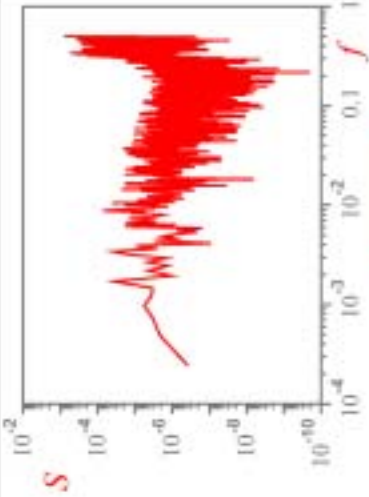
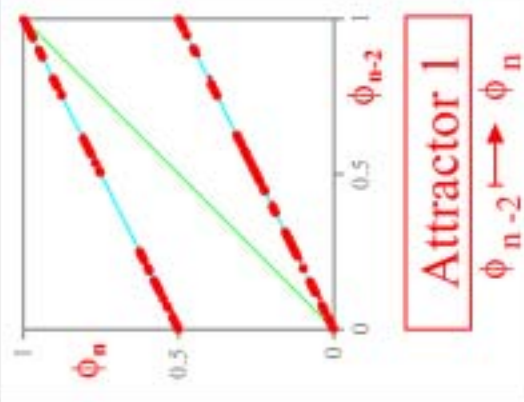
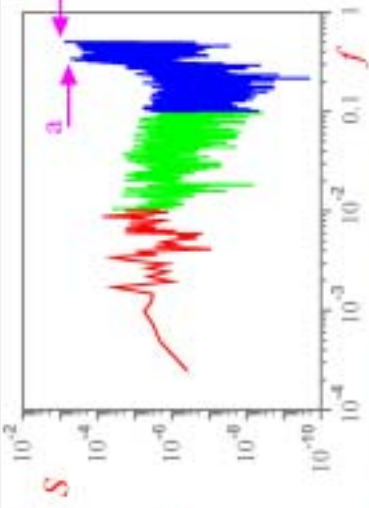
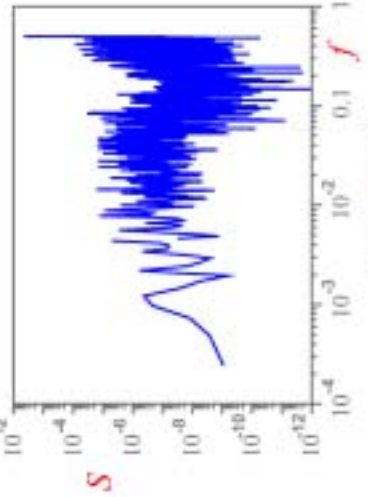
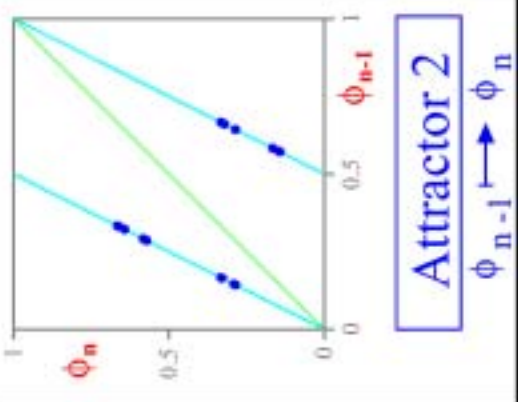
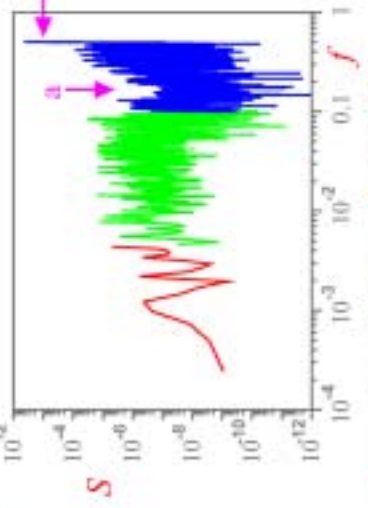
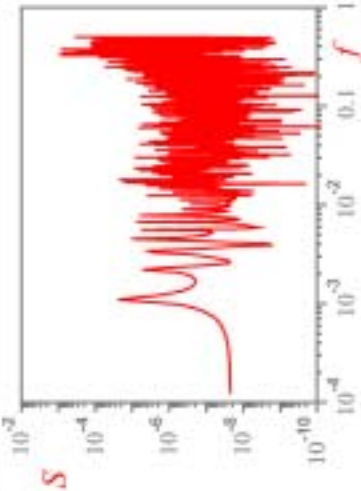
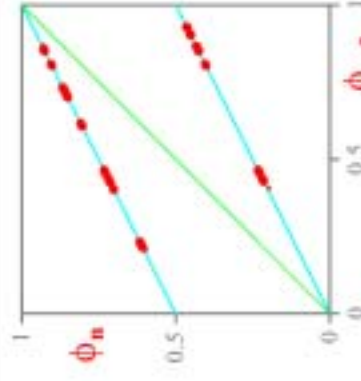
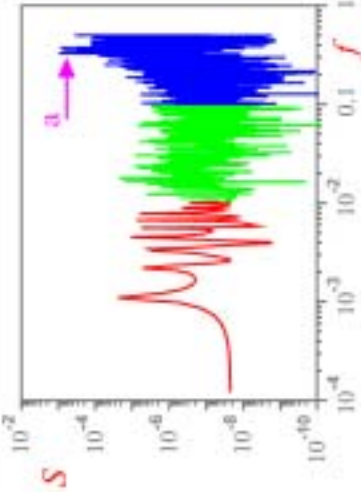
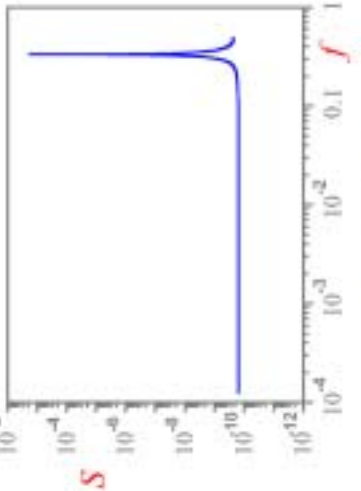
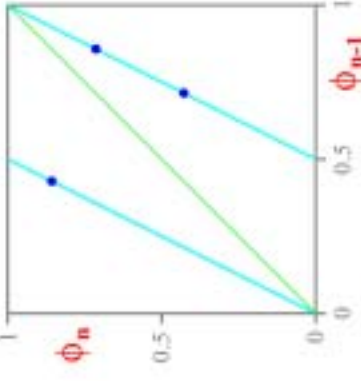
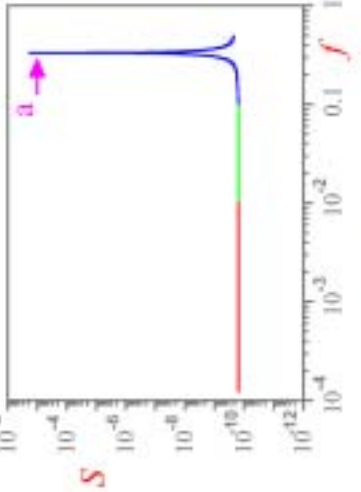
$B_N[\alpha, \beta, \tau]$	Power spectrum	Bernoulli σ_τ -shift map	Characteristic features	N
$B_{35}^{[35]}[1, 1/2, 2]$	 35	 Attractor 1 $\phi_{n-2} \mapsto \phi_n$	 Power is not uniform for $f > 0.01$. Sharp peaks a ($f = 1/3$) and b ($f = 1/2$) imply period-3 and period-2 modes.	<div>35</div> <div>49</div> <div>59</div> <div>115</div>
$B_{35}^{[35]}[2, 2, 1]$	 35	 Attractor 2 $\phi_{n-1} \mapsto \phi_n$	 Power is not uniform for $f > 0.01$. There is a deep trough at a ($f = 1/6$). Sharp peak a ($f = 1/2$) implies period-2 mode.	<div>35</div> <div>49</div> <div>59</div> <div>115</div>

Table 13-9. (Continued)

$B_N[\alpha, \beta, \tau]$	Power spectrum	Bernoulli σ_τ -shift map	Characteristic features	N
$B_{62}^{[1, 1/2, 2]}$	 <div>62</div>	 <div>Attractor 1</div> $\phi_{n-2} \mapsto \phi_n$	 Power is not uniform for $f > 0.01$. A broad peak a ($f = 1/3$) implies period-3 mode.	<div>62</div> <div>118</div> <div>131</div> <div>145</div>
$B_{62}^{[2, 2, 1]}$	 <div>62</div>	 <div>Attractor 2</div> $\phi_{n-1} \mapsto \phi_n$	 Power is zero for $f < 0.1$. Sharp peak a ($f = 1/3$) implies period-3 mode.	<div>62</div> <div>118</div> <div>131</div> <div>145</div>

these lines belongs to the *graph* of the corresponding *time- τ maps*. It is truly remarkable that the *forward time- τ map* of all Bernoulli rules in Table 13 is always a subset of a Bernoulli σ_τ -shift map with $\tau \in \{1, 2\}$. This amazing result can be confirmed by exhaustive computer simulations of all 256 CA rules.

A cursory examination of Table 13 shows that some rules \boxed{N} , such as $\boxed{11}$, $\boxed{14}$, $\boxed{56}$, etc., occur twice, one for each attractor in \boxed{N} . To distinguish between these two attractors, we introduce an integer $\alpha \in \{1, 2\}$, where $\alpha = 1$ if \boxed{N} has only one attractor, and $\alpha = 2$ if it has 2. Let us summarize the above coding scheme as follow:

The ID code $\mathbf{B}_{\boxed{N}}[\alpha, \beta, \tau]$ of each *Bernoulli shift mode* in Table 13 is uniquely identified by three parameters $\{\alpha, \beta, \tau\}$, where $\alpha \in \{1, 2\}$ denotes the number of attractors in \boxed{N} , β (defined in Eq. (36), denotes the *slope* of the Bernoulli σ_τ -shift map (parallel *light blue* lines), and τ denotes the relevant forward *time- τ map* shown in column 3.

Following exactly the same organization format, we reorganize the 20 *noninvertible* rules from Table 11 into Table 14. Since all rules from Table 11 have two attractors, $\alpha \in \{1, 2\}$ in Table 14. Observe, however, that unlike Table 13 where $\tau \in \{1, 2\}$, we now have $\tau \in \{2, 3\}$. In other words, the red points in column 3 are not merely copied from Table 2, but must now be calculated.

Finally, the eight *noninvertible* rules in Table 12 are reorganized into Table 15. Since all rules belonging to Table 12 have three attractors, we have $\alpha \in \{1, 2, 3\}$. As a departure from the previous format, a *new* column 5 is added in Table 15 displaying a typical dynamic pattern for each attractor in order to demonstrate that the attractors have *qualitatively* distinct characters, each one having a different basin of attraction. Observe also that $\tau \in \{2, 3, 5\}$ in Table 15.

5.2. Predicting the dynamic evolution from $\{\beta, \tau\}$

The dynamic evolution of any one of the 112 Bernoulli rules from Tables 10–12 can be predicted uniquely from only two parameters in view of the following theorem:

Theorem 1. σ_τ -Shift Theorem

Let $\mathbf{B}_{\boxed{N}}[\alpha, \beta, \tau]$ be the ID code of *Bernoulli rule* \boxed{N} . Let

$$\mathbf{s}^t \triangleq \{x_0^t \quad x_1^t \quad x_2^t \quad \cdots \quad x_I^t\} \quad (37)$$

denote any $(I+1)$ -bit *initial state* (configuration) and let

$$\mathbf{s}^{t+\tau} \triangleq \{x_0^{t+\tau} \quad x_1^{t+\tau} \quad x_2^{t+\tau} \quad \cdots \quad x_I^{t+\tau}\} \quad (38)$$

denote the *evolved state* of \boxed{N} at time $t + \tau$, $\tau = 1, 2, 3, \dots$. Then $\mathbf{s}^{t+\tau}$ can be derived from the following:

σ_τ -Shifting rule

Case 1.

$$\beta = 2^\sigma > 0, \quad \tau = n, \quad n = 1, 2, 3, \dots$$

(a) $\sigma = 1, 2, 3, \dots$

\mathbf{s}^{t+n} is obtained by shifting \mathbf{s}^t to the left by “ σ ” pixels.

(b) $\sigma = -1, -2, -3, \dots$

\mathbf{s}^{t+n} is obtained by shifting \mathbf{s}^t to the right by “ $|\sigma|$ ” pixels.

Case 2.

$$\beta = 2^\sigma < 0, \quad \tau = n, \quad n = 1, 2, 3, \dots$$

Same as **Case 1** but followed by *complementing* the color of all pixels.

Proof. Due to space limitation, the formal proof of this theorem will be given in Part V. ■

Applying the σ_τ -shifting rule from the above σ_τ -shifting rule theorem, we obtained the explicit σ_τ -shifting dynamics in Table 16 for each of the 112 Bernoulli rules from Tables 10–12. Each row in Table 16 spells out the precise instruction for predicting the first, second, third, or fifth iteration of any Bernoulli rule \boxed{N} (with ID code $\mathbf{B}_{\boxed{N}}[\alpha, \beta, \tau]$) (from any initial state (configuration) \mathbf{s}^t on any attractor) corresponding to $\tau = 1, 2, 3$, or 5, respectively. If \boxed{N} has more than one attractor, one row is devoted to each attractor and the appropriate row to pick depends on which basin of attraction does the *initial state* belong to. To *predict* the next

Table 14-1. $B_N[\alpha, \beta, \tau]$ characterization for 20 noninvertible Bernoulli rules with two *Bernoulli attractors*.

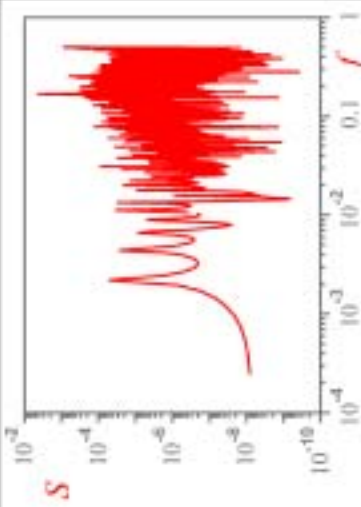
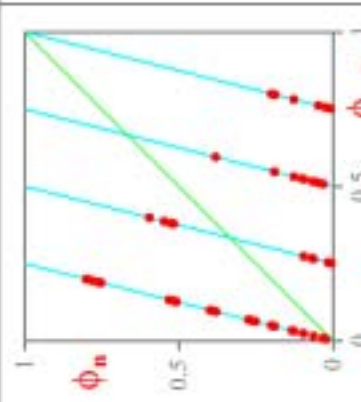
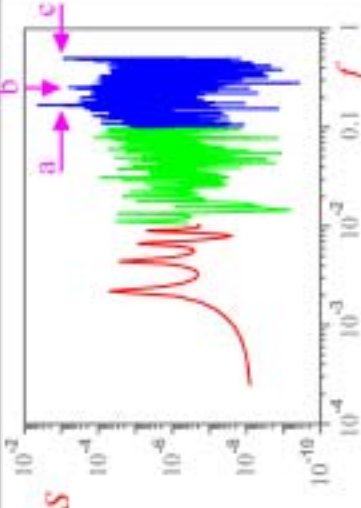
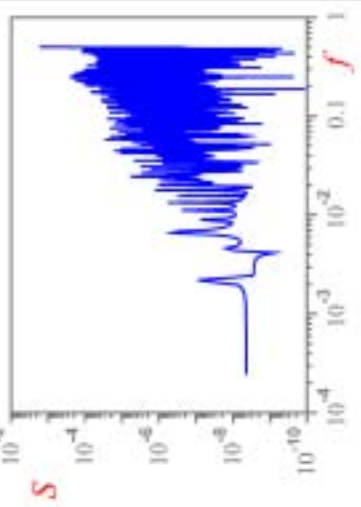
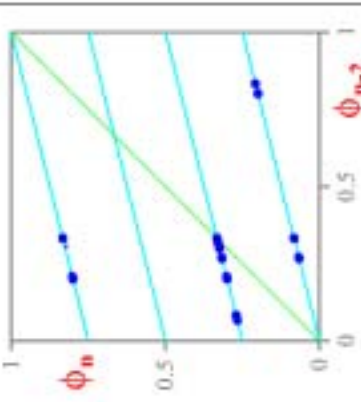
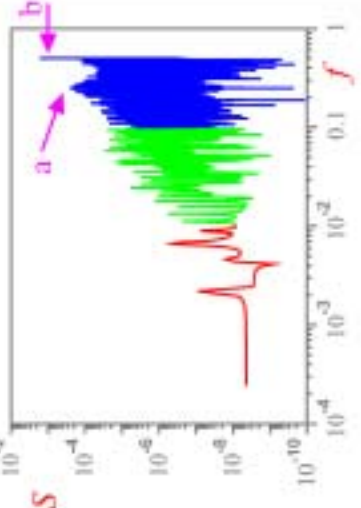
$B_N[\alpha, \beta, \tau]$	Power spectrum	Bernoulli σ_τ -shift map	Characteristic features	N
$B_6[1, 4, 2]$	 <div>6</div>	 <div>Attractor 1</div>	 <p>Power is not uniform for $f > 0.01$. Sharp peaks a ($f = 1/6$), b ($f = 1/4$), and c ($f = 1/2$) imply period-6, period-4, and period-2 modes.</p>	<div>6</div> <div>20</div> <div>159</div> <div>215</div>
$B_6[2, 1/4, 2]$	 <div>6</div>	 <div>Attractor 2</div>	 <p>Power is not uniform for $f > 0.01$. A broad peak a ($f = 1/4$) implies period-4 mode. A sharp peak b ($f = 1/2$) implies period-2 mode.</p>	<div>6</div> <div>20</div> <div>159</div> <div>215</div>

Table 14-2. (Continued)

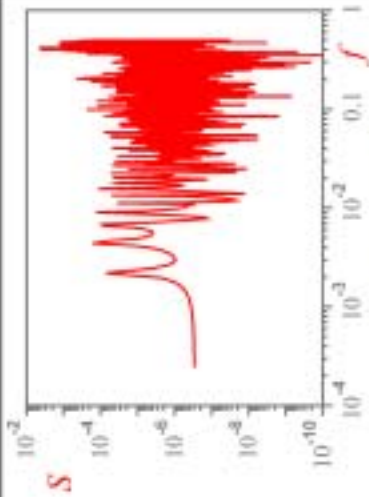
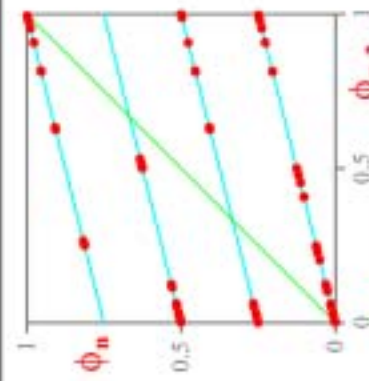
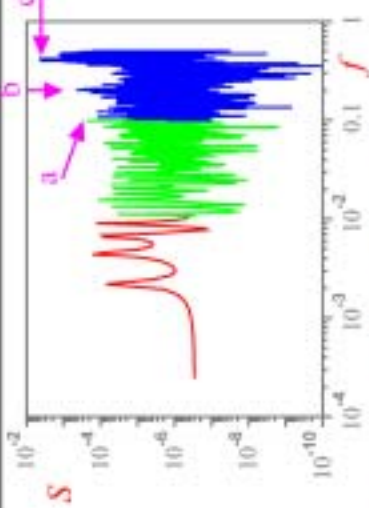
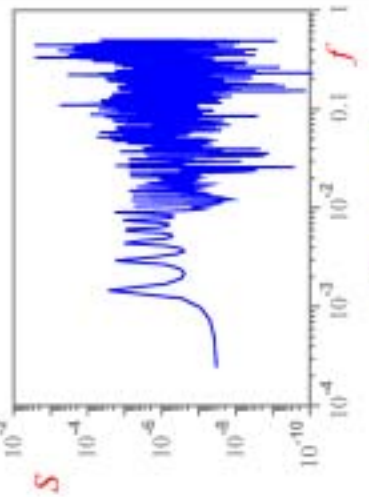
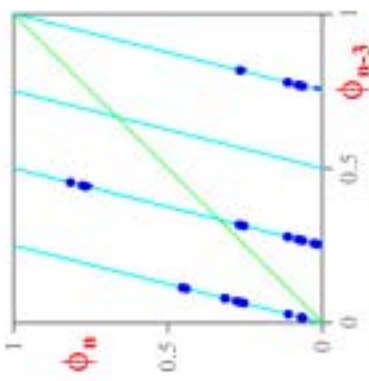
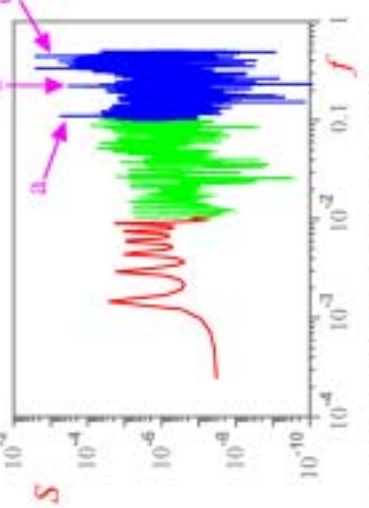
$B_N[\alpha, \beta, \tau]$	Power spectrum	Bernoulli σ_τ -shift map	Characteristic features	N
$B_9[1, 1/4, 2]$	 <div>9</div>	 <div>Attractor 1</div> $\phi_{n-2} \mapsto \phi_n$	 <p>Power is not uniform for $f > 0.01$. Broad peaks a ($f = 1/9$), b ($f = 1/5$), and c ($f = 2/5$) imply period-9, period-5 modes and 2nd harmonics.</p>	<div>9</div> <div>65</div> <div>111</div> <div>125</div>
$B_9[2, 4, 3]$	 <div>9</div>	 <div>Attractor 2</div> $\phi_{n-3} \mapsto \phi_n$	 <p>Power is not uniform for $f > 0.01$. Sharp peaks a ($f = 1/9$), b ($f = 1/5$), and c ($f = 2/5$) imply period-9, period-5 modes and 2nd harmonics.</p>	<div>9</div> <div>65</div> <div>111</div> <div>125</div>

Table 14-3. (Continued)

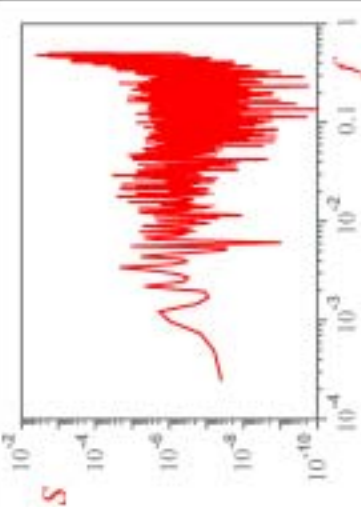
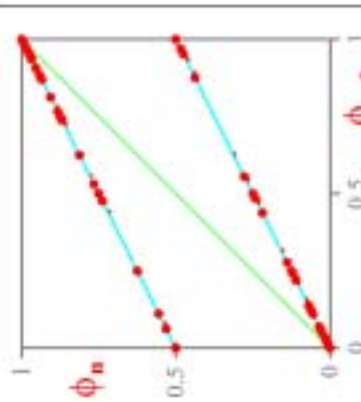
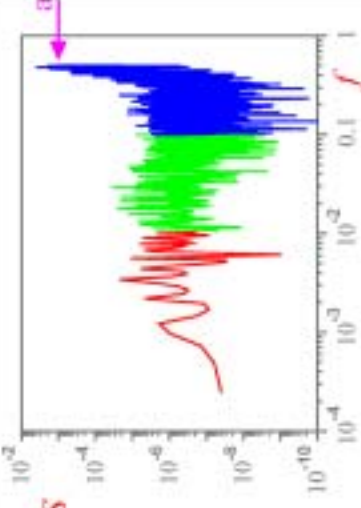
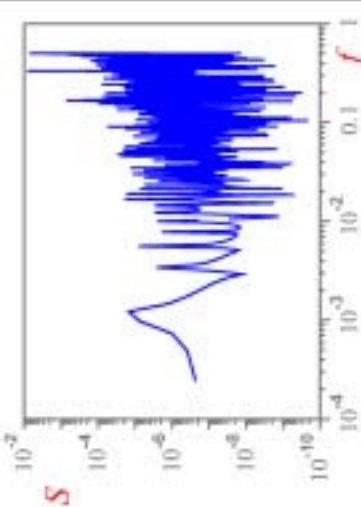
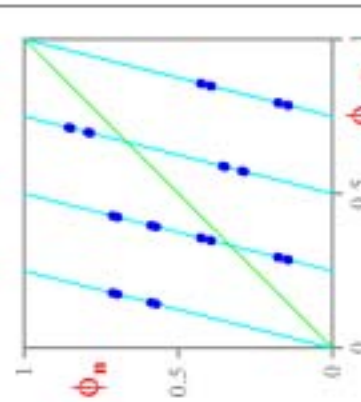
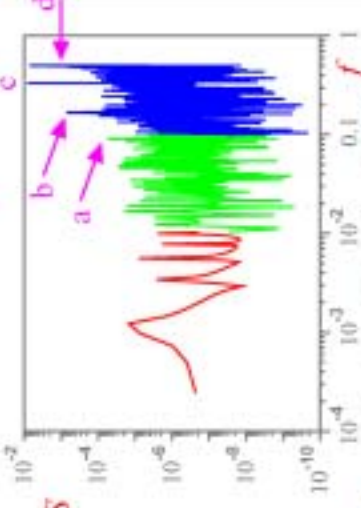
$B_N[\alpha, \beta, \tau]$	Power spectrum	Bernoulli σ_τ -shift map	Characteristic features	N
$B_{27}^{[27]}[1, 1/2, 2]$	 27	 Attractor 1 $\phi_{n-2} \mapsto \phi_n$	 Power is not uniform for $f > 0.01$. A broad peak a ($f = 1/2$) implies period-2 mode.	<div>27</div> <div>39</div> <div>53</div> <div>83</div>
$B_{27}^{[27]}[2, 4, 2]$	 27	 Attractor 2 $\phi_{n-2} \mapsto \phi_n$	 Power is not uniform for $f > 0.01$. Sharp peaks a ($f = 1/12$), b ($f = 1/6$), imply period-12 and period-6 modes. Peaks c ($f = 1/3$), d ($f = 1/2$) imply higher harmonics of the above modes.	<div>27</div> <div>39</div> <div>53</div> <div>83</div>

Table 14-4. (Continued)

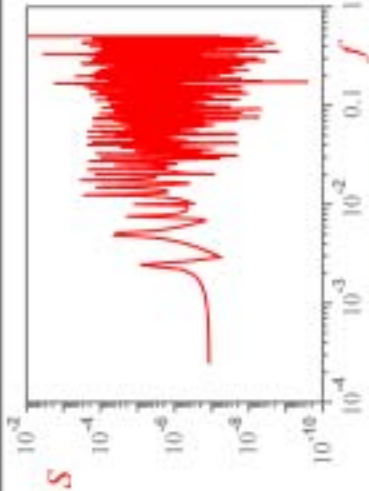
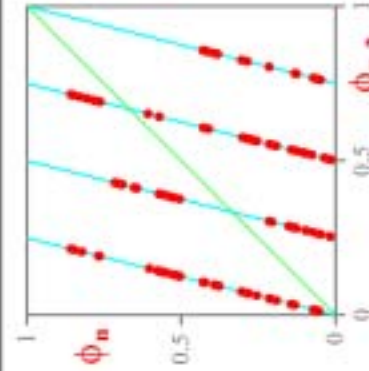
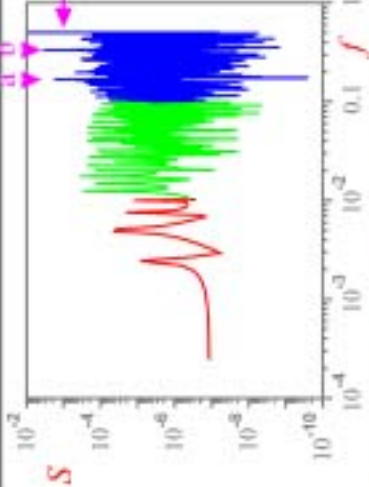
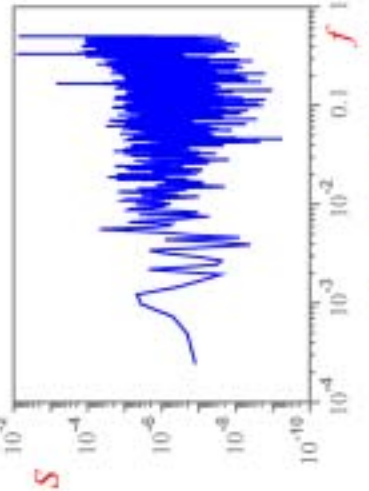
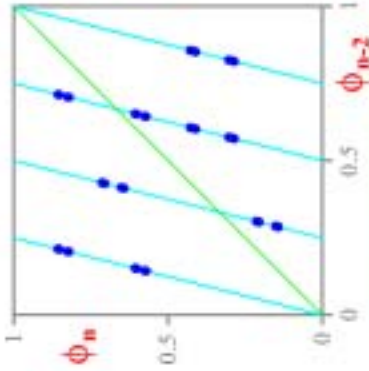
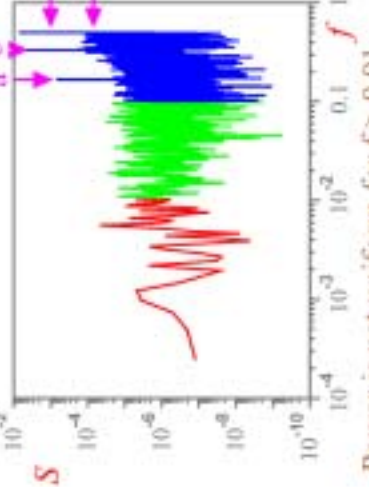
$B_N[\alpha, \beta, \tau]$	Power spectrum	Bernoulli σ_τ -shift map	Characteristic features	N
$B_{38}^{[1,4,2]}$	 <div>38</div>	 <div>Attractor 1</div> $\phi_{n-2} \mapsto \phi_n$	 <p>Power is not uniform for $f > 0.01$. Sharp peaks a ($f = 1/6$), b ($f = 1/3$), and c ($f = 1/2$) imply period-6, period-3, and period-2 modes</p>	<div>38</div> <div>52</div> <div>155</div> <div>211</div>
$B_{38}^{[2,4,2]}$	 <div>38</div>	 <div>Attractor 2</div> $\phi_{n-2} \mapsto \phi_n$	 <p>Power is not uniform for $f > 0.01$. Sharp peaks a ($f = 1/6$), b ($f = 1/3$), and c ($f = 1/2$) imply period-6, period-3, and period-2 modes. A broad peak d ($f = 1/3$) relates to period-3 mode.</p>	<div>38</div> <div>52</div> <div>155</div> <div>211</div>

Table 14-5. (Continued)

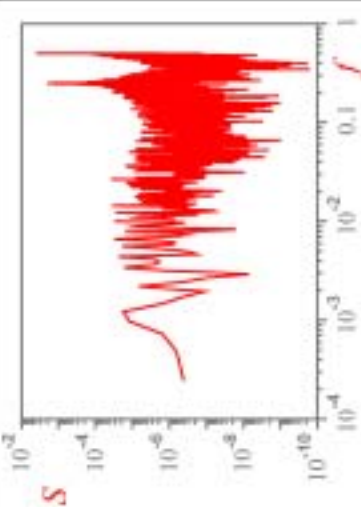
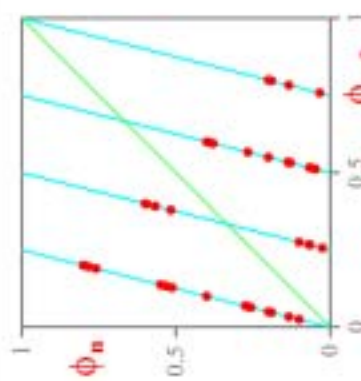
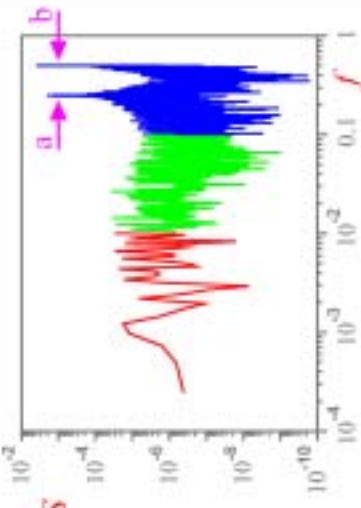
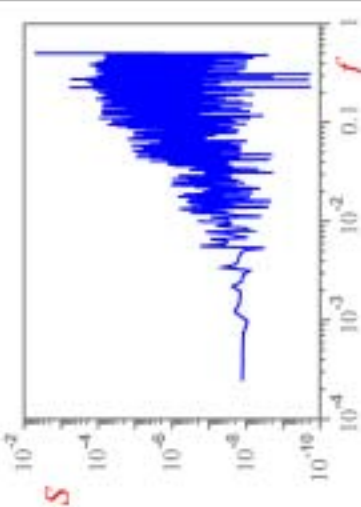
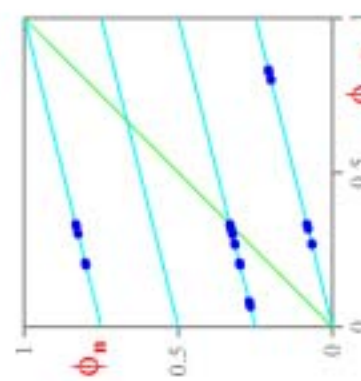
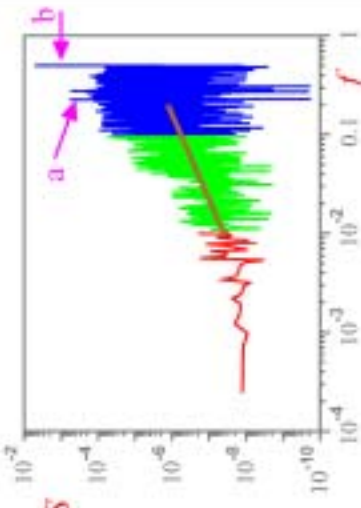
$B_N[\alpha, \beta, \tau]$	Power spectrum	Bernoulli σ_τ -shift map	Characteristic features	N
$B_{134}^{[1,4,2]}$	 <div>134</div>	 <div>Attractor 1</div> $\phi_{n-2} \mapsto \phi_n$	 <p>Power is not uniform for $f > 0.01$. Sharp peaks a ($f = 1/4$) and b ($f = 1/2$) imply period-4 and period-2 modes.</p>	<div>134</div> <div>148</div> <div>158</div> <div>214</div>
$B_{134}^{[2,1/4,2]}$	 <div>134</div>	 <div>Attractor 2</div> $\phi_{n-2} \mapsto \phi_n$	 <p>Mild ascent over $0.01 < f < 0.2$. A broad peak a ($f = 1/4$) implies period-4 mode. A sharp peak b ($f = 1/2$) implies period-2 mode.</p>	<div>134</div> <div>148</div> <div>158</div> <div>214</div>

Table 15-1. $B_N^{[25]}[\alpha, \beta, \tau]$ characterization for eight noninvertible Bernoulli rules with three Bernoulli attractors.

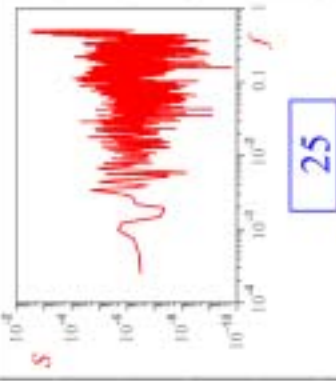
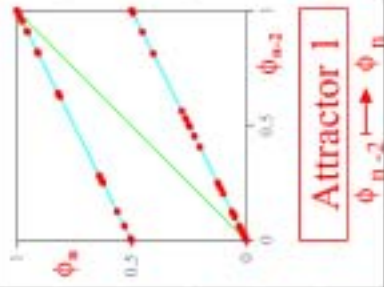
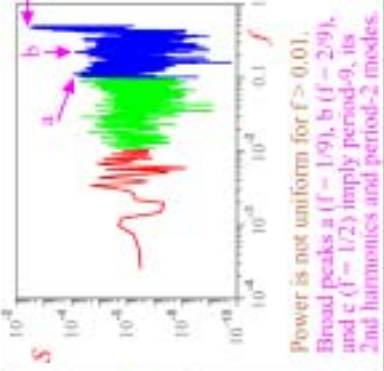

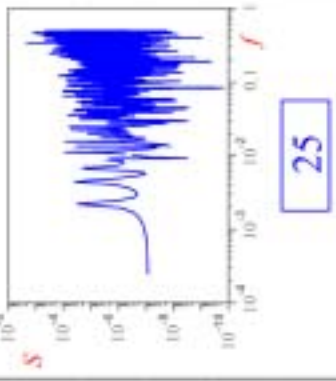
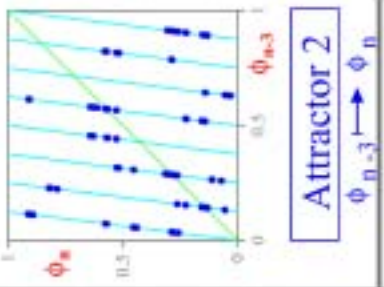
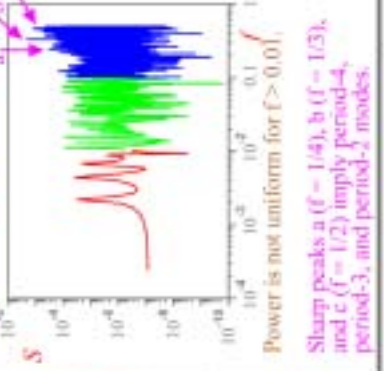
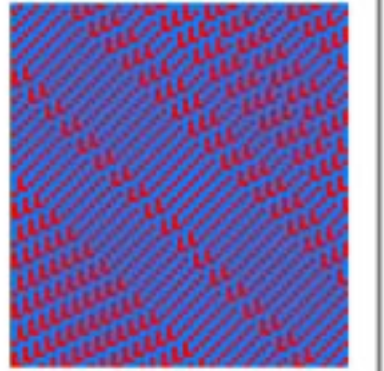
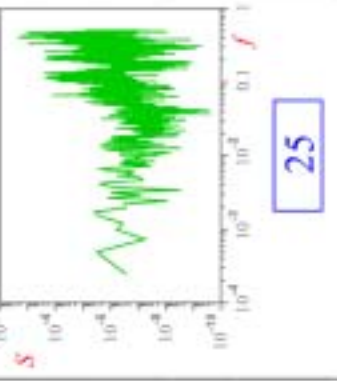
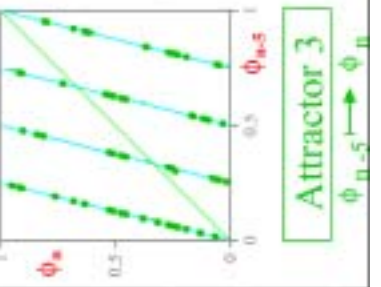
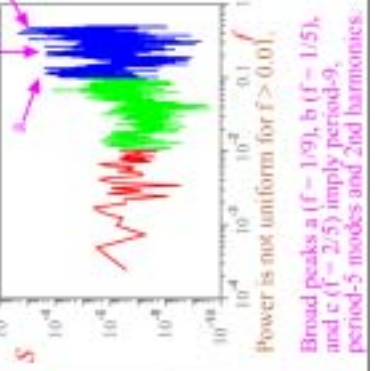
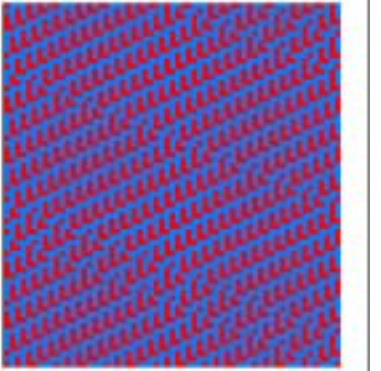
$B_N^{[25]}[\alpha, \beta, \tau]$	Power spectrum	Bernoulli σ_τ -shift map	Characteristic features	Characteristic output patterns	N
$B^{[25]}_{25}[1, 1/2, 2]$			 <p>Power is not uniform for $f > 0.01$. Broad peaks a ($f = 1/9$), b ($f = 2/9$), and c ($f = 1/2$) imply period-9, its 2nd harmonics and period-2 modes.</p>		<div>25</div> <div>61</div> <div>67</div> <div>103</div>
$B^{[25]}_{25}[2, 8, 3]$			 <p>Power is not uniform for $f > 0.01$. Sharp peaks a ($f = 1/4$), b ($f = 1/3$), and c ($f = 1/2$) imply period-4, period-3, and period-2 modes.</p>		<div>25</div> <div>61</div> <div>67</div> <div>103</div>
$B^{[25]}_{25}[3, 4, 5]$			 <p>Power is not uniform for $f > 0.01$. Broad peaks a ($f = 1/9$), b ($f = 1/5$), and c ($f = 2/5$) imply period-9, period-5 modes and 2nd harmonics.</p>		<div>25</div> <div>61</div> <div>67</div> <div>103</div>

Table 15-2. (Continued)

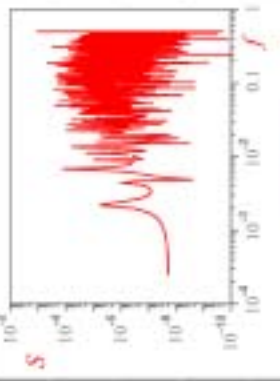
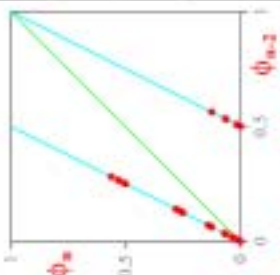
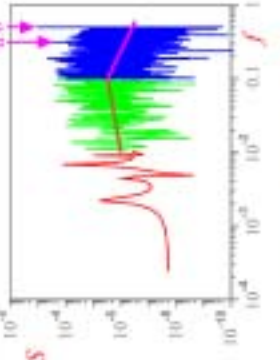

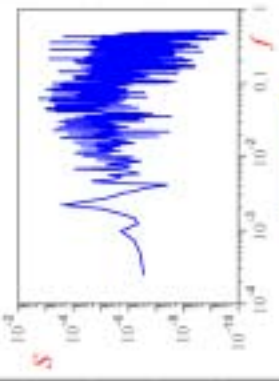
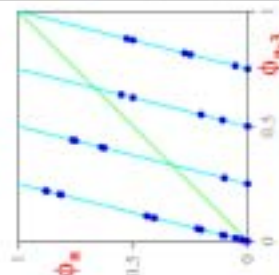
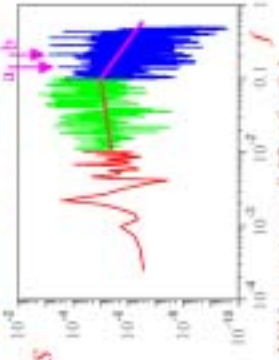
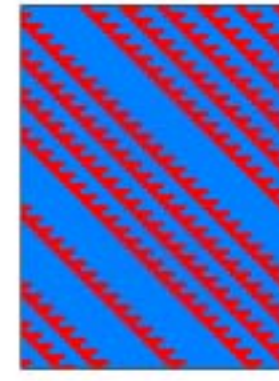
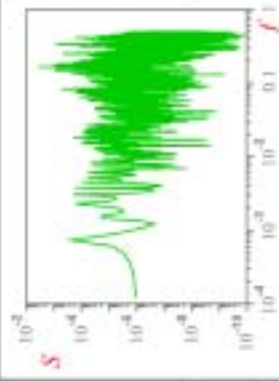
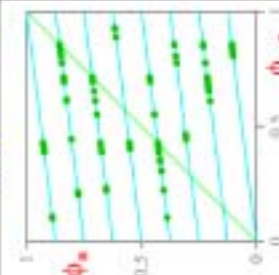
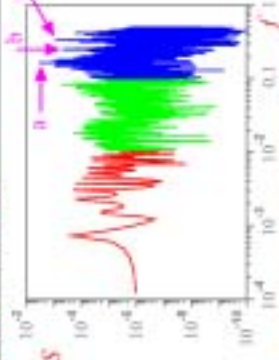

$B_N[\sigma, \beta, \tau]$	Power spectrum	Bernoulli σ_τ -shift map	Characteristic features	Characteristic output patterns	N
$B^{[74]}[1,2,1]$			 <p>Mild ascent over $0.02 < f < 0.1$. Mild descent over $0.1 < f < 0.5$. Sharp peaks a ($f \approx 1/3$) and b ($f \approx 1/2$) imply period-3 and period-2 modes.</p>		<div>74</div> <div>88</div> <div>173</div> <div>229</div>
$B^{[74]}[2,4,2]$			 <p>Mild ascent over $0.02 < f < 0.1$. Mild descent over $0.1 < f < 0.5$. Sharp peaks a ($f \approx 1/7$) and b ($f \approx 1/5$) imply period-3, period-2, and its higher harmonics.</p>		<div>74</div> <div>88</div> <div>173</div> <div>229</div>
$B^{[74]}[3,1/8,3]$			 <p>Power is not uniform for $f > 0.01$. A broad peak a ($f \approx 1/6$) implies period-6 mode. Sharp peaks b ($f \approx 1/4$) and c ($f \approx 1/3$) are period-4 and period-3 modes.</p>		<div>74</div> <div>88</div> <div>173</div> <div>229</div>

Table 16. Explicit σ_τ -shift dynamics for Bernoulli Rules.

N	shift		$ \mathcal{O} $ pixels			τ -iteration				Plus complementing	
			1	2	3	1st	2nd	3rd	5th	Yes	No
2	X		X			X					X
3		X	X				X				X
6	X			X			X				X
7		X		X			X				X
9		X	X				X				X
10	X		X			X					X
11		X	X			X					X
14	X		X			X					X
15		X	X			X					X
16		X	X			X					X
17	X		X			X					X
20		X		X			X				X
21	X		X				X				X
24		X	X				X				X
25	X				X						X
27	X		X								X
31		X	X								X
34	X		X								X
35	X		X			X					X
38	X			X							X
39		X		X							X
42	X				X						X
43		X	X			X				X	
46	X		X			X					X
47		X	X			X				X	
48	X		X			X					X
49		X	X			X					X
52		X		X							X
53	X			X							X
56		X	X			X					X
57	X		X			X					X
58	X		X			X					X
59	X		X			X					X
61		X			X						X

Table 16. (Continued)

N	shift		$ \mathcal{O} $ pixels			τ -iteration				Plus complementing	
			1	2	3	1st	2nd	3rd	5th	Yes	No
62	left	X	X								X
	right	X									X
63	left		X			X					X
	right										X
65	left	X									X
	right	X									X
66	left	X	X			X					X
	right										X
67	left	X	X				X				X
	right										X
74	left	X				X					X
	right	X									X
80	left		X								X
	right										X
81	left	X	X			X					X
	right										X
83	left	X	X			X					X
	right										X
84	left		X			X					X
	right	X									X
85	left	X	X			X					X
	right										X
87	left	X	X			X					X
	right										X
88	left	X									X
	right										X
98	left	X	X								X
	right										X
99	left	X	X								X
	right										X
103	left	X	X								X
	right										X
111	left	X									X
	right										X
112	left	X	X								X
	right										X
113	left	X	X								X
	right										X
114	left		X								X
	right										X
115	left	X	X								X
	right										X
116	left	X	X								X
	right										X
117	left	X	X								X
	right										X
118	left	X	X								X
	right										X
119	left	X	X								X
	right										X
125	left	X	X								X
	right										X

Table 16. (Continued)

N	shift		$ \sigma $ pixels			τ -iteration				Plus complementing	
			1	2	3	1st	2nd	3rd	5th	Yes	No
130	X		X			X					X
131		X	X				X				X
134	X		X			X					X
138	X		X			X					X
139	X		X			X					X
142	X		X			X					X
143	X		X			X					X
144		X	X			X					X
145	X		X				X				X
148	X			X			X				X
152		X	X			X					X
155	X			X			X				X
158	X			X			X				X
159	X			X			X				X
162	X		X			X					X
163	X		X			X					X
170		X	X				X				X
171	X		X			X					X
173	X			X			X				X
174	X		X			X					X
175	X		X			X					X
176		X	X			X					X
177	X		X			X					X
184		X	X			X					X
185	X		X			X					X
186	X		X			X					X
187	X		X			X					X
188	X		X			X					X
189	X		X			X					X
190	X		X			X					X
191	X		X			X					X
194	X		X			X					X
208		X	X			X					X

Table 16. (Continued)

N	shift		$ \mathcal{O} $ pixels				τ - iteration				Plus complementing	
	left	right	1	2	3	1st	2nd	3rd	5th	Yes	No	
209		X	X			X					X	
211		X		X			X				X	
		X		X				X			X	
212		X	X			X					X	
	X		X	X		X	X	X			X	
213		X	X			X	X	X			X	
	X		X			X					X	
214		X		X				X			X	
	X			X				X			X	
215		X		X			X	X			X	
	X			X				X			X	
226	X		X				X	X			X	
		X	X			X	X	X			X	
227	X		X									
		X	X			X	X	X				

N	shift		$ \mathcal{O} $ pixels				τ - iteration				Plus complementing	
	left	right	1	2	3	1st	2nd	3rd	5th	Yes	No	
229		X	X			X					X	
230		X		X			X				X	
	X				X			X			X	
231		X	X			X	X	X			X	
240		X	X			X					X	
241		X	X			X					X	
242		X	X			X					X	
243		X	X			X	X	X			X	
244		X	X			X					X	
245		X	X			X	X	X			X	
246		X	X			X	X	X			X	
247		X	X			X	X	X			X	

τ -iteration from any binary bit-string *initial state* (configuration) \mathbf{s}^t on *any* attractor of *any* Bernoulli rule $[N]$, one simply transcribes the dynamics specified from the entries marked by a “cross” (X) in row N .

Let us use this direct “read-out” procedure to predict the *attractor* evolution dynamics of the four Bernoulli rules $[N] = [74], [99], [85]$ and $[11]$ from the dynamic patterns $\mathcal{D}_{[N]}[\mathbf{x}(0)]$ exhibited in Fig. 17. Let \mathbf{s}^t denote any row on the attractor regime (i.e. pick $t > T_\delta$) of these four patterns. The dynamical evolution of $[74]$ from \mathbf{s}^t can be predicted by looking at the first subrow (corresponding to attractor $\alpha = 1$) of row $N = 74$ of Table 16 and read out the following precise evolution rules for $[74]$:

Shift string \mathbf{s}^t to the **left** by **1 pixel** to obtain the **first iteration** \mathbf{s}^{t+1} .

 (39)

Repeating the same procedure we obtain the same pattern shown in the upper left corner of Fig. 17.

Similarly, if we go to the second subrow (corresponding to attractor $\alpha = 2$) of row $N = 99$ in Table 16, we would read out the following evolution rule for $[99]$:

Shift string \mathbf{s}^t to the **right** by **1 pixel** to obtain the **first iteration** \mathbf{s}^{t+1} .

 (40)

Repeating the same procedure we obtain the periodic pattern (after the transient regime) shown in the upper right corner of Fig. 17, where the highlighted area denotes the attractor regime.

For $[N] = [85]$, we read out from row $N = 85$ in Table 16:

Shift string \mathbf{s}^t to the **left** by **1 pixel** and then **complementing** (changing color) to obtain the **first iteration** \mathbf{s}^{t+1} .

 (41)

Repeating the same procedure we obtain the dynamic pattern in the lower left corner of Fig. 17.

Finally, For $[N] = [11]$, we read out from sub-row 2 (corresponding to attractor $\alpha = 2$) of row $N = 11$ in Table 16:

Shift string \mathbf{s}^t to the **right** by **1 pixel** and then **complementing** (changing color) to obtain the **first iteration** \mathbf{s}^{t+1} .

 (42)

Repeating the same procedure we obtain the pattern in the lower right corner of Fig. 17.

The four Bernoulli rules chosen in Fig. 17 are all described by a forward *time-1 map* $\rho_1[N](\phi_{n-1} \mapsto \phi_n)$; i.e. $\tau = 1$. Consider next the four rules $[74]$ ($\alpha = 2$),¹⁰ $[3]$, $[6]$, and $[9]$ shown in Fig. 18 where $\tau = 2$.

For $[74]$, we go to the second sub-row of row $N = 74$ in Table 16 to read out:

Shift string \mathbf{s}^t to the **left** by **2 pixels** to obtain the **second iteration** \mathbf{s}^{t+2} .

 (43)

Repeating the same procedure we obtain the same pattern shown in the upper left corner of Fig. 18, where only even rows are printed out for easier verification of the above evolution procedure. In order to generate all rows, we would need to iterate also from row \mathbf{s}^{t+1} .

The other three patterns in Fig. 18 are obtained by exactly the same read out procedure.

Finally, Fig. 19 shows the dynamic patterns of four Bernoulli rules $[74]$ ($\alpha = 3$), $[9]$, $[25]$ ($\alpha = 2$) and $[25]$ ($\alpha = 3$) with $\tau = 5$.

To predict the periodic pattern of $[74]$ ($\alpha = 3$), we go to the third subrow of row $N = 74$ and read out:

Shift string \mathbf{s}^t to the **right** by **3 pixels** to obtain the **third iteration** \mathbf{s}^{t+3} .

 (44)

Repeating the same procedure we obtain the pattern shown in the upper left corner of Fig. 19, where only every third row is printed out for easier verification. Clearly, in order to obtain the entire attractor, it is necessary to repeat the above procedure from rows \mathbf{s}^{t+1} and \mathbf{s}^{t+2} as well.

To appreciate the predictive power of the σ_τ -shifting rule, it would be instructive to apply Table 16 to all 112 Bernoulli rules exhibited in Table 5 of Part II [Chua *et al.*, 2003].

5.3. Two limiting cases: Period-1 and palindrome rules

Notice that $\sigma = 0$ is not included in the above formulation of the σ_τ -shifting rule. It is possible to enlarge the class of Bernoulli rules significantly by including $\sigma = 0$ as a *limiting case* without

¹⁰ Although we have chosen the same rule $[74]$ from Fig. 17, our initial state here belongs to the basin of attraction of attractor $\alpha = 2$.

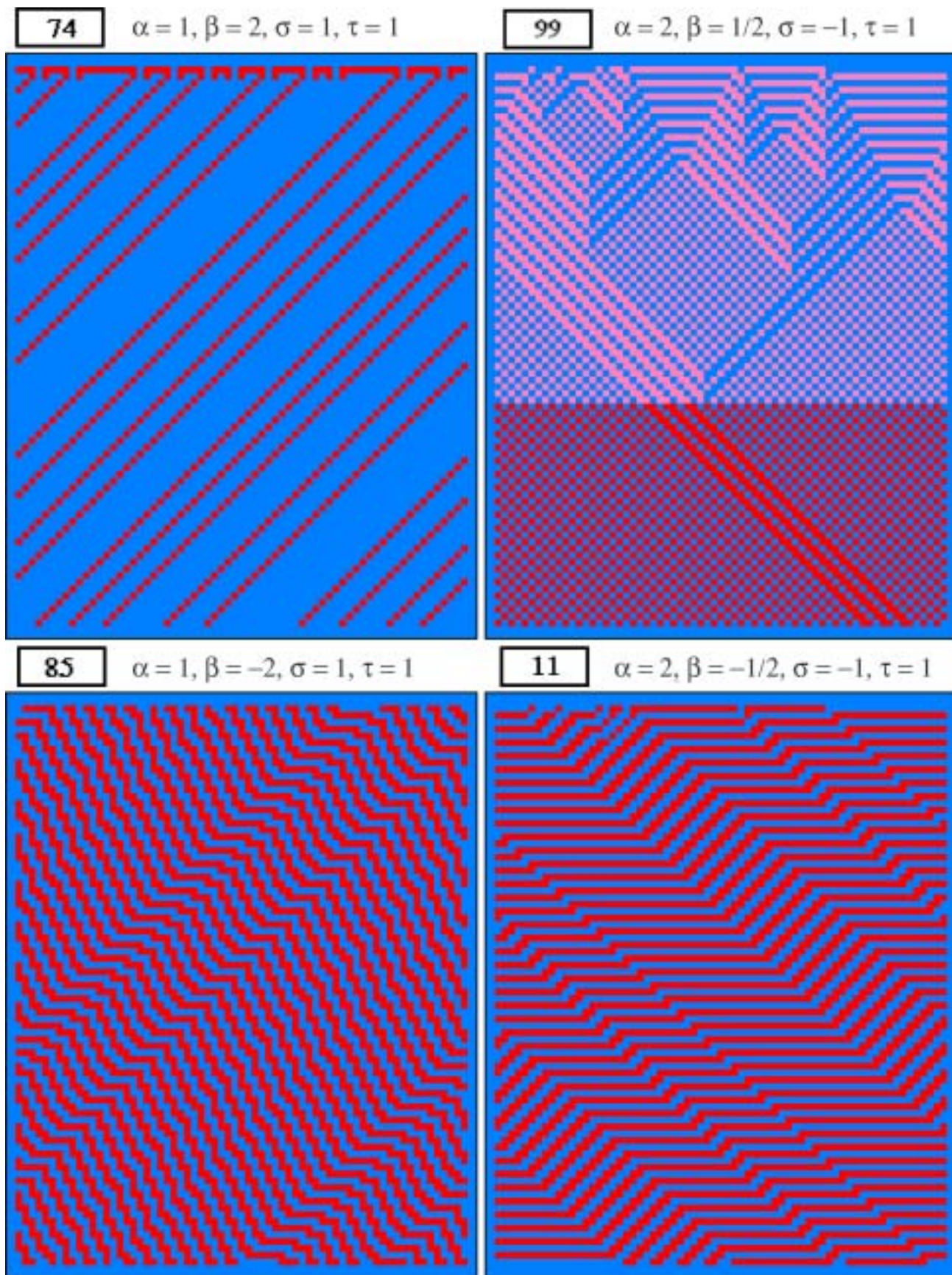


Fig. 17. Dynamic patterns of Bernoulli rules [74], [99], [85], and [11]. The dimension of each pattern is 66 rows \times 84 columns.

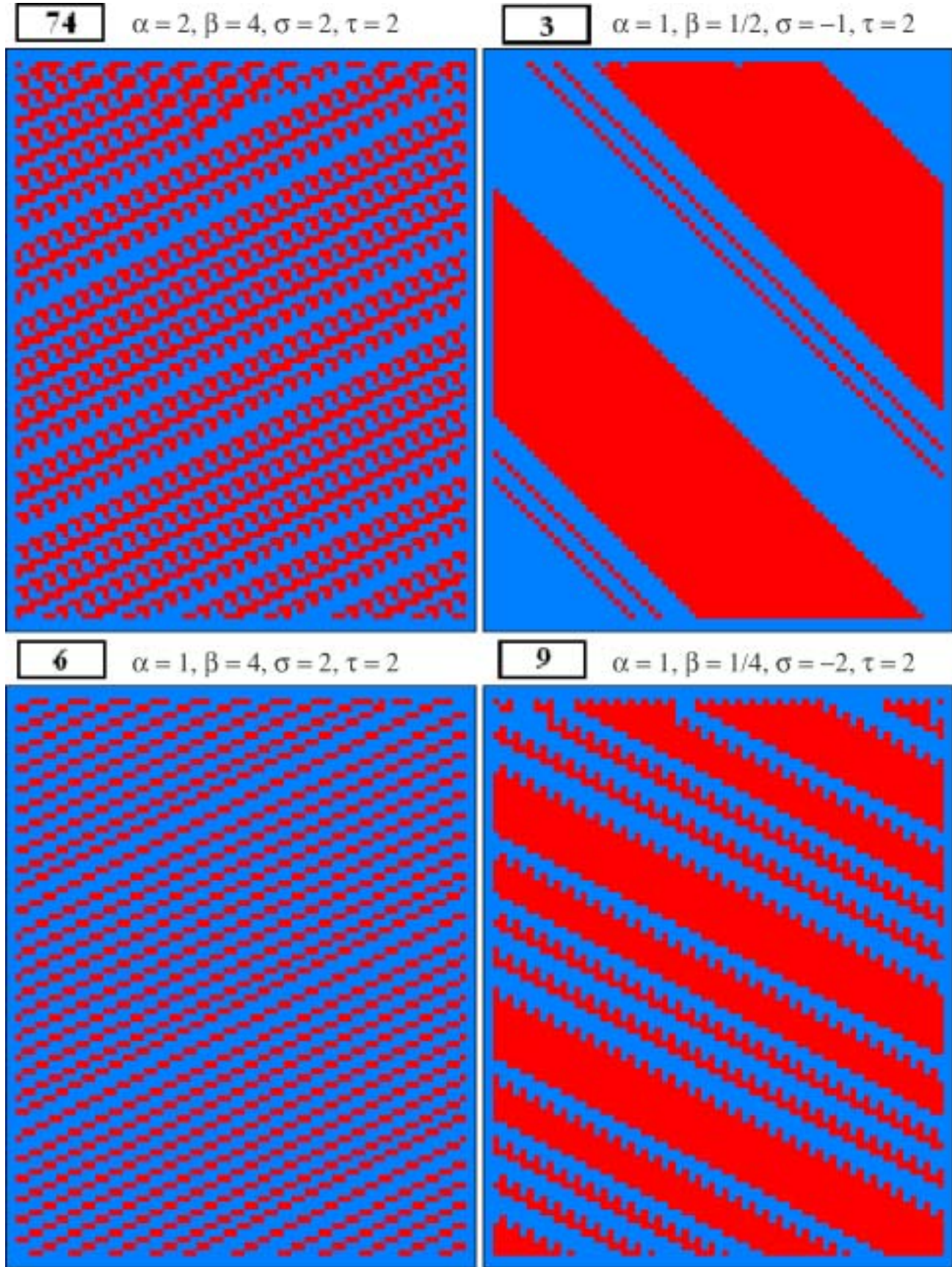


Fig. 18. Dynamic patterns of Bernoulli rules **74** ($\alpha = 2$), **3**, **6**, and **9**. The dimension of each pattern is 66 rows \times 84 columns. Only *alternate* rows $n = 0, 2, 4, \dots$ are shown.

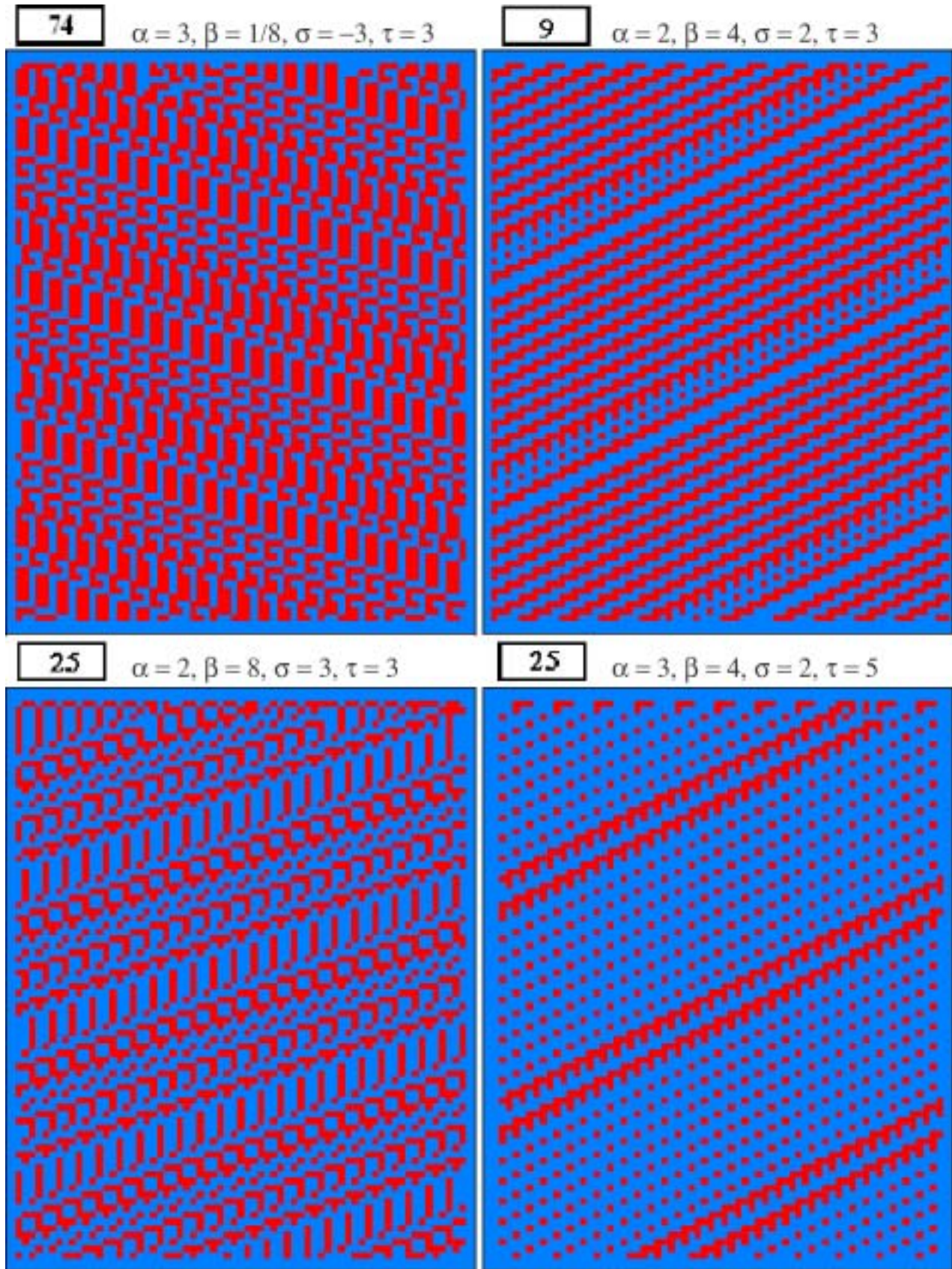


Fig. 19. Dynamic patterns of the four Bernoulli rules $\boxed{74}$ ($\alpha = 3$), $\boxed{9}$, $\boxed{25}$ ($\alpha = 2$) and $\boxed{25}$ ($\alpha = 3$). Successive rows represent three iterations in all cases except $\boxed{25}$ ($\alpha = 3$) where only every fifth iteration is printed. The dimension of each pattern is 66×84 for $\boxed{74}$ ($\alpha = 3$) and $\boxed{25}$ ($\alpha = 2$), 67×84 for $\boxed{9}$, and 65×84 for $\boxed{25}$ ($\alpha = 3$).

changing the original statements of the σ_τ -shifting rule.

Limiting Case 1: $\boxed{\beta = +1 = 2^0}$

In this case, since $\sigma = 0$ and $\beta > 0$, both statements (a) and (b) in Case 1 of the σ_τ -shifting rule imply that no pixel is shifted either left or right. In other words, any point on an attractor of N which follows the σ_τ -shifting rule with $\beta = +1$ is a *fixed-point*, and hence a *period-1* attractor. Conversely, any period-1 point on a period-1 attractor satisfies the σ_τ -shifting property with $\sigma = 0$. We can thereby conclude:

Corollary 1. *The dynamics of all period-1 rules from Tables 3–6 satisfies the σ_τ -shift rule with $\sigma = 0$, for all period-1 initial states.*

Limiting Case 2: $\boxed{\beta = -1 = -2^0}$

In this case, since $\sigma = 0$ and $\beta < 0$, both statements (a) and (b) in Case 2 of the σ_τ -shifting rule are satisfied, implying that although any initial state \mathbf{s}^t on an attractor does not shift its position, it changes *sign* in *each* iteration. This implies that \mathbf{s}^t is a period-2 point. The converse, however, is *not* true. In fact, only certain rather special period-2 patterns exhibit the above “sign-alternating” property. In particular, the following result can be proved to be the only period-2 rules satisfying *limiting case 2*:

Corollary 2. *Period-2 Palindromes: All period-2 rules which obey the σ_τ -shift property are necessarily palindromes in the sense that any initial configuration string \mathbf{s}^t corresponding to an attractor must be symmetrical with respect to the center of \mathbf{s}^t .¹¹*

Among the 25 period-2 rules listed in Tables 7 and 8, only the seven bilateral rules $\{19, 23, 50, 51, 55, 178, 179\}$ are palindromes and only these seven rules obey the σ_τ -shift property with $\beta = -2^0$.

5.4. Resolving the multivalued paradox

A cursory glance of Tables 13–15 reveals that the graph of the forward time- τ map $\rho_\tau[N]$ of all Bernoulli rules with $\beta < 1$ (equivalently, $\sigma < 0$)¹²

is a subset of a *multivalued* function consisting of $2^{|\sigma|}$ parallel straight lines with slope equal to $\beta = 2^{-\sigma}$, $\sigma = 1, 2, 3$. This observation seems to contradict the fact that all time- τ maps must be *single-valued* functions on the unit interval. This paradox can be resolved by observing that every point on the graph must project to a *different* point on the horizontal axis. In other words, if we draw very thin projection lines through all points on the graph, as in Figs. 3–7, these lines will merely interleave each other. This will always be the case even as $I \rightarrow \infty$; namely, between every two projection lines, there will be more lines, sandwiched in between, *ad infinitum*. It is mind boggling to imagine a function with such an intricate structure [Niven, 1967]. How can one guarantee the iteration of such Bernoulli rules for large values of I can be reliably carried out on a computer? How can one be sure that the inevitable computing errors due to truncation will not affect the outcome for large values of I ?

The answer to the above questions comes from our σ_τ -shifting rule. For $|\beta| < 1$, \mathbf{s}^{t+1} is always obtained by shifting \mathbf{s}^t to the right by $|\sigma| = 1, 2$ or 3 pixels. Hence every bit of \mathbf{s}^t will eventually arrive at the right boundary located at $\phi_{n-\tau} = \phi_{\text{end}} \approx 1.0$ (depending on I). If the *end* bit is equal to a “1”, such as

$$\phi^t = 0.001010 \cdots 0101 \quad (45)$$

then the σ_τ -shifting rule and the *periodic* boundary condition in Fig. 1 imply (assuming $|\sigma| = 1$) the following unambiguous outcomes:

$$\phi^{t+1} = 0.1001010 \cdots 010 \quad (46)$$

$$\phi^{t+2} = 0.01001010 \cdots 01 \quad (47)$$

$$\phi^{t+3} = 0.101001010 \cdots 0 \quad (48)$$

\vdots

etc.

It is now clear that the *rightmost* bit at time t determines the *leftmost* bit at time $t + 1$, assuming $|\sigma| = 1$. Hence, there is never any loss of accuracy because the *computation* is *discrete*, not continuous.¹³

¹¹The palindromes \mathbf{s}^t in Corollary 2 are assumed to be represented as binary bit strings. Corollary 2 is also true for a decimal \mathbf{s}^t as $I \rightarrow \infty$.

¹²For each Bernoulli rule $\mathbf{B}_{[N]}[\alpha, \beta, \tau]$ with $\beta = 2^\sigma > 0$, its bilateral twin $\mathbf{B}_{[N]^\dagger}[\alpha, \beta^\dagger, \tau]$ has $\beta^\dagger = 2^{-\sigma} < 1$.

¹³Assuming the computer has a sufficiently long word length.

It is instructive to illustrate the above *right shifting rule* on rule [240] whose *characteristic function* $\chi_{[240]}^1$ is shown in Fig. 4(b). Now recall the first few digits of the *decimal* expansion of a binary bit string

$$\bar{\mathbf{x}} = [x_0 x_1 \cdots x_{I-1} x_I] \quad (49)$$

is given by Eq. (13); namely,

$$\begin{aligned} \phi &= \frac{1}{2}x_0 + \frac{1}{4}x_1 + \frac{1}{8}x_2 + \cdots + \frac{1}{2^I}x_{I-1} + \frac{1}{2^{I+1}}x_I \\ &= 0.5x_0 + 0.25x_1 + 0.125x_2 + \cdots \\ &\quad + \frac{1}{2^I}x_{I-1} + \frac{1}{2^{I+1}}x_I \end{aligned} \quad (50)$$

It follows from Eqs. (49) and (50) that if the leftmost bit is a “0”, i.e. $x_0 = 0$, then $\phi < 0.5$ and the *lower* straight line (with slope $\beta = 1/2$) in Fig. 4(b) for [240] will be selected. On the other hand, if the leftmost bit is a “1”, i.e. $x_0 = 1$, then Eq. (50) implies that $\phi > 0.5$ and hence the upper branch in Fig. 4(b) will be selected.

1010110001111100000010000000100111010101010100111010110010101110101

via Eq. (50). Observe the *end* (rightmost) **bit** of the above bit string is a “1”. To obtain the next iteration via the σ_1 -*shifting rule* for $N = 240$ in Table 16, we simply **shift** the above bit string by **one pixel** (since $\tau = 1$) to the right (since $\sigma < 0$),

1101011000111110000001000000010011101010101010011101011001010111010

in the next iteration, whose *decimal* value (calculated from Eq. (50)) is equal to

$$\phi_1 = 0.836884024048529 \dots$$

It is truly amazing that while the two *decimal* numbers ϕ_0 and ϕ_1 above reveal no discernible relationship between them, their binary codes betray the hidden secret of rule [240] as simply a trivial **Bernoulli right shift of one pixel!**

Note the cobweb diagram starting from the nearby point ⑥ evolves into an entirely different orbit, a manifestation of *extreme* sensitivity. Indeed it is well known that the *Bernoulli shift* (for $I \rightarrow \infty$)

In other words, if the *end* (rightmost) bit is $x_I^t = 1$ at time t , then the Bernoulli σ_1 -shifting rule of [240] will shift the end bit “1” to the *right*, thereby reappearing as the first bit in the next iteration in view of the periodic boundary condition indicated in Fig. 1(a). Since the first bit in the next iteration now reads $x_0^{t+1} = 1$, we have $\phi^{t+1} > 0.5$ and the dynamics must follow the *upper* branch of $\chi_{[240]}^1$. Conversely, if the end bit is $x_I^t = 0$, then the Bernoulli *right* shifting rule for [240] will shift the bit “0” to make the first bit equal to $x_0^{t+1} = 0$ in the next iteration, and the dynamics must follow the *lower* branch of $\chi_{[240]}^1$.

The *right shifting rule* of [240] dynamics described above is illustrated with the help of the Lameray (cobweb) diagram shown in Fig. 20. Observe that the two points ① and ⑥ are extremely close to each other. The decimal coordinate

$$\phi_0 = 0.673768048097057 \dots$$

of point ① is calculated from the following 66-bit string (the same $I = 65$ is used throughout Figs. 3–7)

which, in view of the *periodic boundary condition* depicted in Fig. 1(a), is equivalent to inserting a “1” at the *leftmost position* of the above right-shifted string to obtain the following 66-bit string

is as *chaotic* as a *coin toss*, [Nagashima & Baba, 1999] and its chaotic attractor has a Lyapunov exponent [Devaney, 1992]

$$\lambda = \beta = 2 > 1 \quad (51)$$

To understand how the outcome of the Bernoulli rule [240] emulates an ideal “*coin toss*” *Gedanken experiment*, let us look at the evolution of the “*inverse*” Bernoulli rule [170] which *must* have identical dynamics,¹⁴ as $I \rightarrow \infty$.

The *characteristic function* $\chi_{[240]}^1: [0, 1] \rightarrow [0, 1]$ of the Bernoulli rule [170] in Fig. 4(a) can be

¹⁴For an infinitely long bit string ($I \rightarrow \infty$), it is more illuminating to show that there is a one-to-one correspondence between the iterates of the Bernoulli rule [170] and the outcome of an ideal coin-toss.

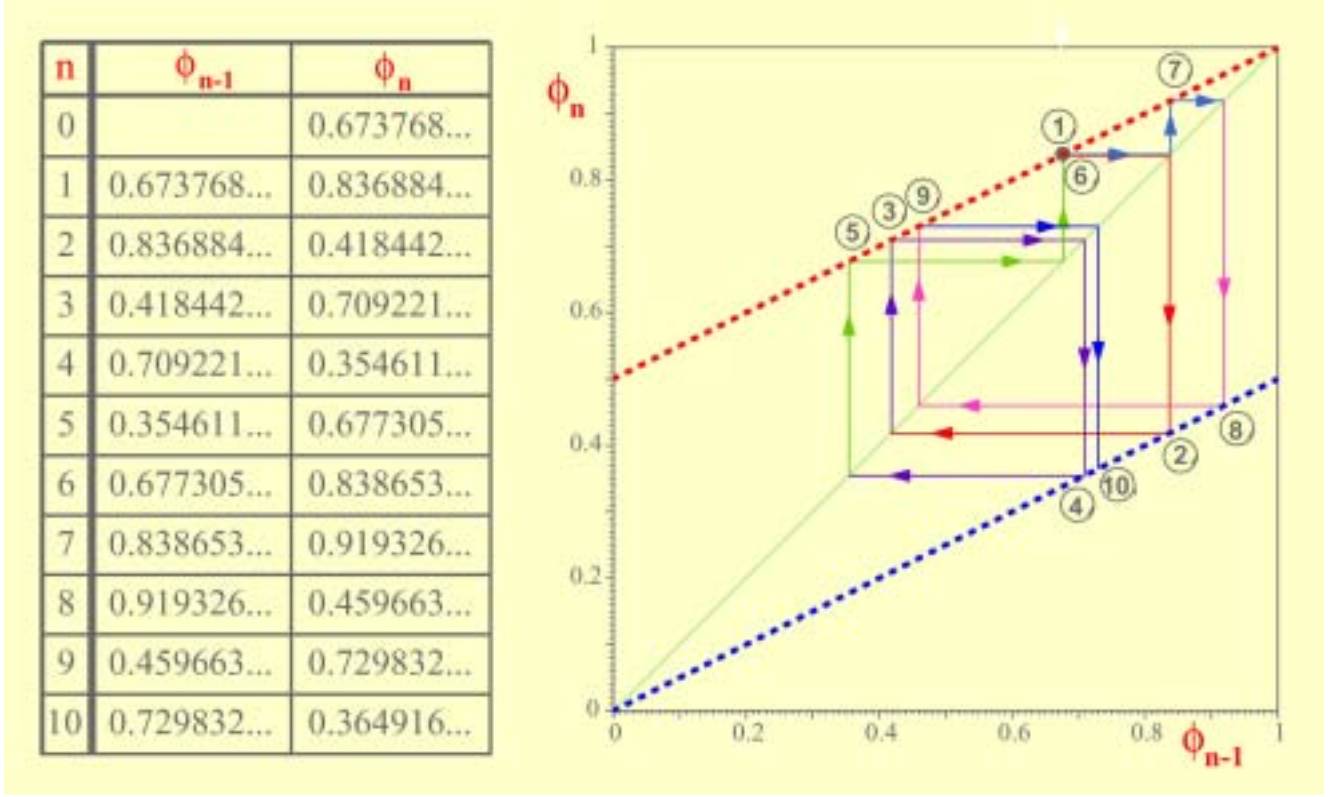


Fig. 20 Cobweb diagram of Bernoulli rule [240] showing a succession of ten iteration points (1), (2), (3), ..., (9), (10) undergoing the σ_1 -shifting evolution dynamics. Points (1) and (6) appear as a single point since they differ by only 0.003537.

described analytically by

$$\chi_{[170]}^1 = 2 \phi_{[170]} \bmod 2 \quad (52)$$

for all $\phi_{[170]} \in [0, 1]$. This means that *every* point of the unit interval $[0, 1]$ corresponds to a semi-infinite binary bit string:

$$\begin{aligned} [x_0 x_1 x_2 \cdots x_i \cdots x_{I-1} x_I] \\ \mapsto 0. \bullet x_0 x_1 x_2 \cdots x_{I-1} x_I \end{aligned} \quad (53)$$

where $I \rightarrow \infty$.

Now since, except for a set of *measure zero* (corresponding to the set of all *rational numbers*), every point in $(0, 1)$ is an *irrational*¹⁵ number [Niven, 1967] whose binary expansion can be identified with a *particular* coin toss experiment, the ensemble of *all* possible ideal *coin-toss* experiments must correspond to the set of *all* points on $[0, 1]$. Hence, to exhibit *any* member of this coin-toss ensemble using the Bernoulli rule [170], we simply choose an *arbitrary* point from the unit interval $[0, 1]$; namely, Eq. (53), and apply the Bernoulli *left* shifting rule

$\sigma_1[[170]]$ to read out the *first* digit x_0^{t+n} from each iteration $t + n$, $n = 1, 2, \dots, \infty$. The outcome of this binary output string is clearly a member of the ideal coin-toss ensemble. It is in the above sense of a *Gedanken* experiment that we claim the Bernoulli rule [170], and its *inverse* rule [240], is as *chaotic* as an ideal coin toss, as $I \rightarrow \infty$.

It also follows from the above discussion that the Bernoulli rules [170] and [240] are both *ergodic* [Billingsley, 1978] in the sense that the iterates $\phi_1, \phi_2, \dots, \phi_t$ from almost every initial state $\phi_0 \in [0, 1]$ would visit *every* point, infinitely often, on the two parallel lines (with slope $\beta = 2$ for [170] and slope $\beta = 1/2$ for [240]) of the characteristic functions $\chi_{[170]}^1$ and $\chi_{[240]}^1$ in Fig. 4 as $t \rightarrow \infty$. This is the reason why the *time-1* map $\rho_1[170]$ and the *characteristic function* $\chi_{[170]}^1$ (resp. $\rho_1[240]$ and $\chi_{[240]}^1$) are identical functions. In other words, there are no gaps in the graph of $\rho_1[170]$.

An examination of Table 2 shows that there are two other Bernoulli rules whose graphs also coincide

¹⁵The hallmark of an *irrational* number is that its binary expansion in Eq. (53) contains every possible *finite* sequences of bit “0” and bit “1” *infinitely often* [Billingsley, 1978].

with their characteristic functions; namely, rule [15] and [85]. An examination of Table 2 shows that only four out of 112 Bernoulli rules are *ergodic* over the unit interval $[0,1]$. All other Bernoulli rules have *gaps*,¹⁶ as is evident from their *graphs* (indicated by red or blue dots) in Tables 13–15.

The four *ergodic* Bernoulli rules [15], [85], [170], and [240] are *invariant* in the sense that their orbits are *invariant orbits* (recall Sec. 4.4). Observe that although their characteristic functions $\chi_{[N]}^1$ have only two fixed points, there are *infinitely* many fixed points $\chi_{[N]}^\tau$ as $\tau \rightarrow \infty$. This follows from Eq. (54) (for [170]) that the *graph* of the τ th-iterated characteristic function

$$\chi_{[170]}^\tau = 2^\tau \phi_{[170]} \bmod 2 \quad (54)$$

consists of 2^τ parallel lines with slope $\beta = 2^\tau$.¹⁷ Since each intersection of these lines with the main diagonal is a fixed point of $\chi_{[170]}^\tau$, it follows that as $\tau \rightarrow \infty$, the number of fixed points tend to infinity. Note, however, that the fixed points of all Bernoulli rules with $\beta > 0$ are *unstable* because the slope of their characteristic function at these points have a slope $\beta > 1$. Hence, unless one chooses the *exact* coordinates of these fixed points, they are not observable. Such fixed points are therefore said to be *not robust*.

6. Predictions from Power Spectrum

The *graph* of the time-1 map of each attractor in Table 2 is derived using a *randomly-generated* initial configuration. The fact that *the same graphs* are generated as long as the random configurations are in the corresponding basins of attraction confirms the validity of using *randomly-generated* bit strings as “probing” inputs [Wiener, 1958]. In addition to providing the graphs of both *forward* and *backward time-1 maps* for each vignette in Table 2 we have also recorded the *power spectrum* for the *forward time-1 map* $\rho_1[N]$ and displayed it in the center frame of each vignette. The spectra of the *period-1*, *period-2* and *period-3 rules* in Table 2 do not provide any new information. They merely confirm the periodicity of the attractors. In this final section, we will examine the spectra of the 112 Bernoulli rules in Tables 10–12.

6.1. Characteristic features of Bernoulli rules

The power spectrum of one prototype member of each group $\mathbf{B}_{[N]}[\alpha, \beta, \tau]$ of Bernoulli rules having identical Bernoulli σ_1 -shift maps is displayed in Column 2 of Tables 13–15, respectively. A careful analysis of these spectra reveals certain generic features of all Bernoulli rules belonging to each of the 34 distinct groups $\mathbf{B}_{[N]}[\alpha, \beta, \tau]$ listed in Table 13–15. Such generic features include the presence of various *robust periodic modes*, as well as the rate of increase or decrease of the power spectrum at various frequency ranges. This information is highlighted and annotated in column 4 of each group in Tables 13–15.

The presence of a sharp *spike* at some frequency f_p indicates that the Bernoulli rule has a *robust natural oscillating mode* at this frequency. As a demonstration of its *prediction* ability, Fig. 21 shows the power spectrum of Bernoulli rules [14] and [81]. An inspection of these two spectra reveals a spike at $f = 1/4$ in both cases. These spikes imply the presence of a stable and hence robust *period-4* point. The location of the four period-4 points of [14] are identified on the characteristic function $\chi_{[14]}^1$, in Fig. 22(a). Observe that the points on the two attractors associated with $\mathbf{B}_{[14]}[1, 2, 1]$ (red) and $\mathbf{B}_{[14]}[2, -1/2, 1]$ (blue) of the Bernoulli rule [14] in Fig. 21, are found at the tip of a *sub-group* of vertical lines in Fig. 22(a), as expected. Observe that there are many points in Fig. 22(a) which do not lie on the attractors. Here, we have superimposed the two red parallel lines from Fig. 21 where attractor 1 resides, and the two blue parallel lines where attractor 2 resides onto $\chi_{[14]}^1$ in Fig. 22. It is interesting to note that although the four period-4 points ①, ②, ④, ③ in Fig. 22 lie at the intersection of these two sets of parallel lines, they are *not* a part of attractors 1 and 2 because points belonging to two different attractors *cannot* intersect, by definition of an attractor.

Note that it is generally not possible to identify *period- τ points* of $[N]$ directly from the characteristic function $\chi_{[N]}^1$ unless $\tau = 1$. A much more effective way to search for period- τ points of any rule $[N]$ is to plot the graph of the τ th-iterated *characteristic function* $\chi_{[N]}^\tau$ and look for points on $\chi_{[N]}^\tau$ which lie on the main diagonal $\chi_{[N]}^\tau = \phi_{[N]}$. As

¹⁶We conjecture that the set $\Lambda_i[N]$ corresponding to each attractor α of all *noninvariant* Bernoulli rules are *Cantor sets* [Alligood et al., 1996].

¹⁷See $\mathbf{B}_{[25]}[2, 8, 3]$ in Table 15-1 for an example when $\tau = 3$.

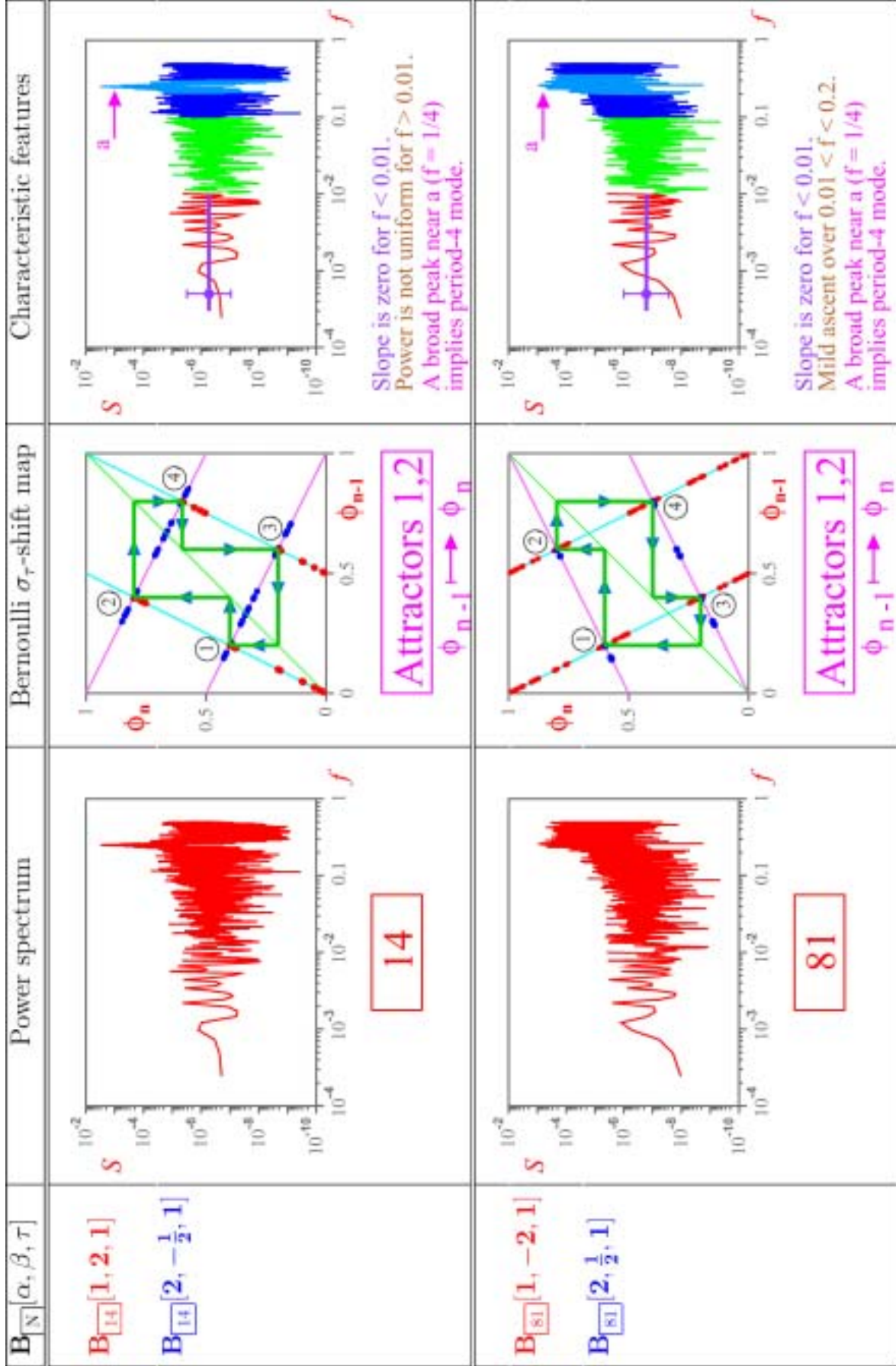


Fig. 21. Spectra of Bernoulli rules 14 and 81 and their σ_1 -shift map showing locations of four period-4 fixed points of ρ_{14}^4 and ρ_{81}^4 , respectively.

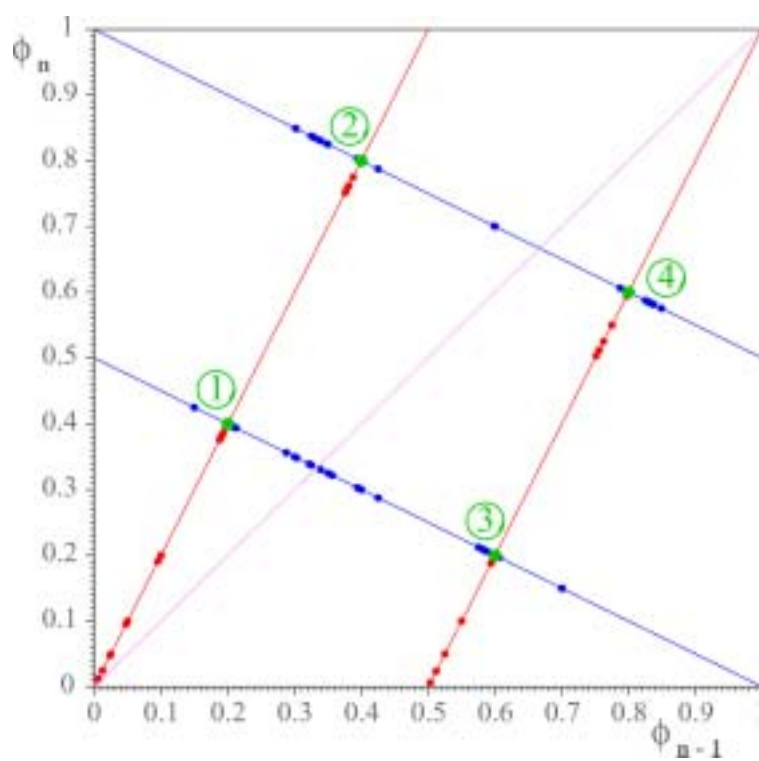
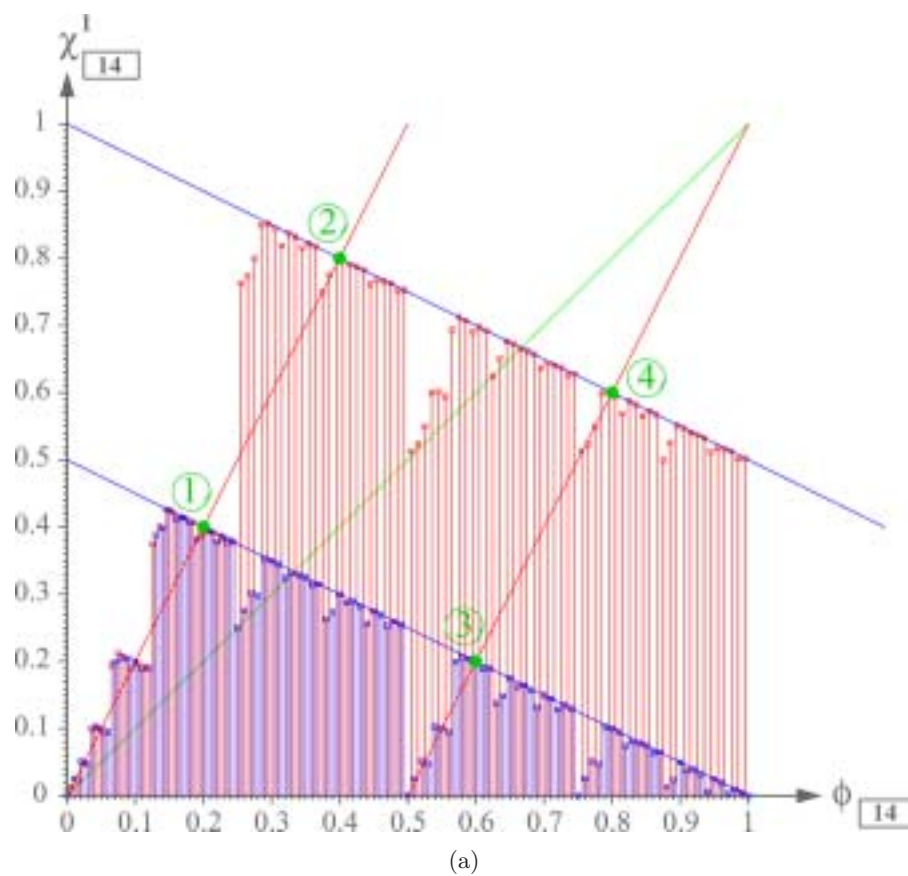
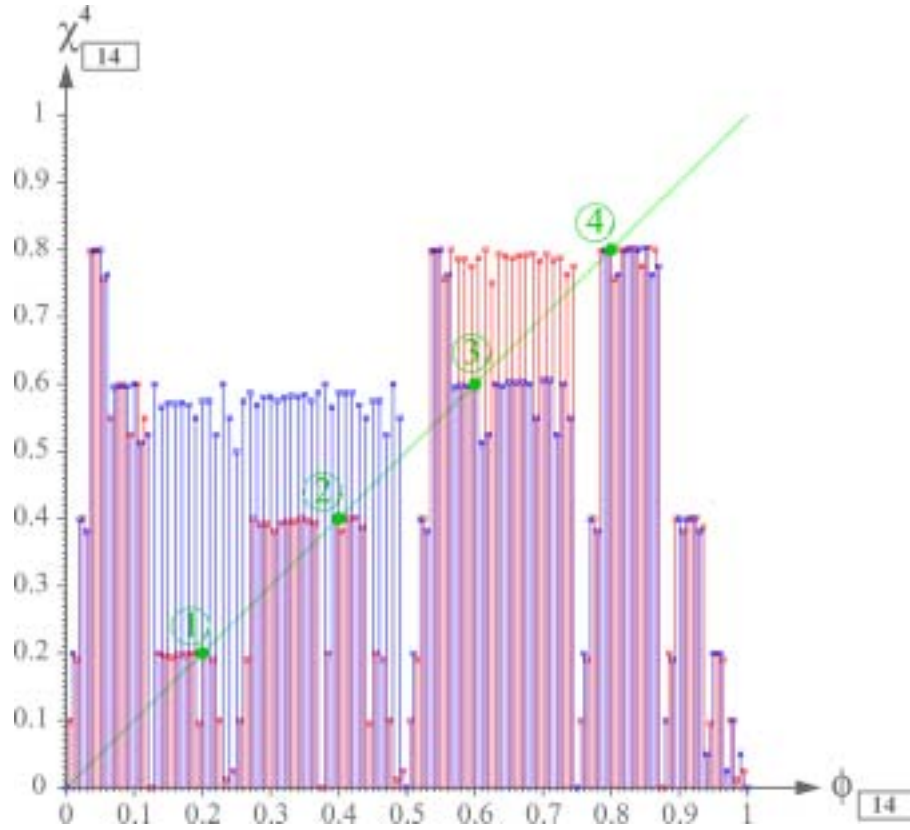
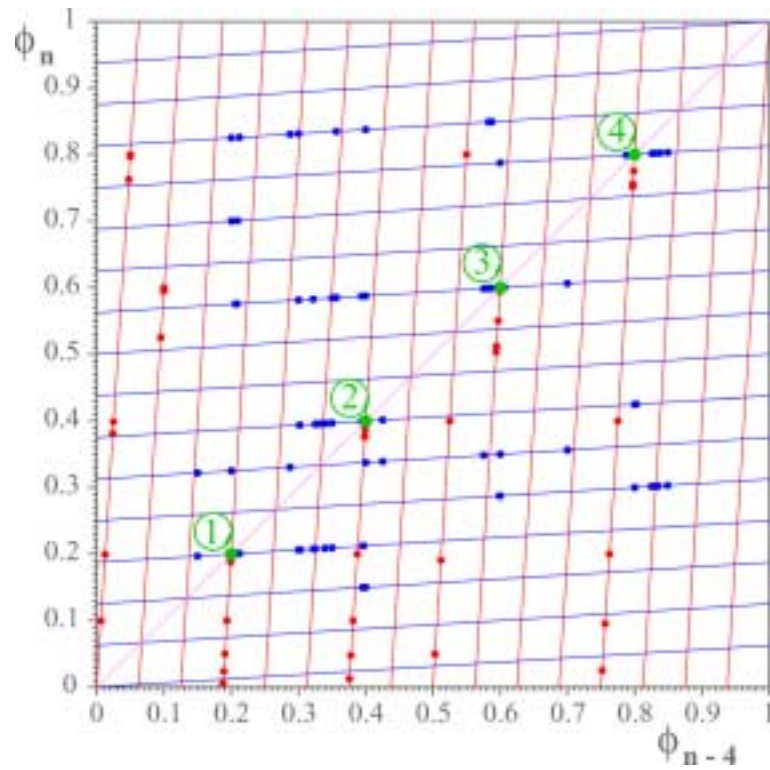


Fig. 22. Characteristic function χ_{14}^1 (top) and time-1 map ρ_{14}^1 (bottom) of Bernoulli rule $\boxed{14}$.



(a)



(b)

Fig. 23. Fourth-iterated characteristic function χ_{14}^4 (top) and time-4 map ρ_{14}^4 (bottom) of Bernoulli rule [14].

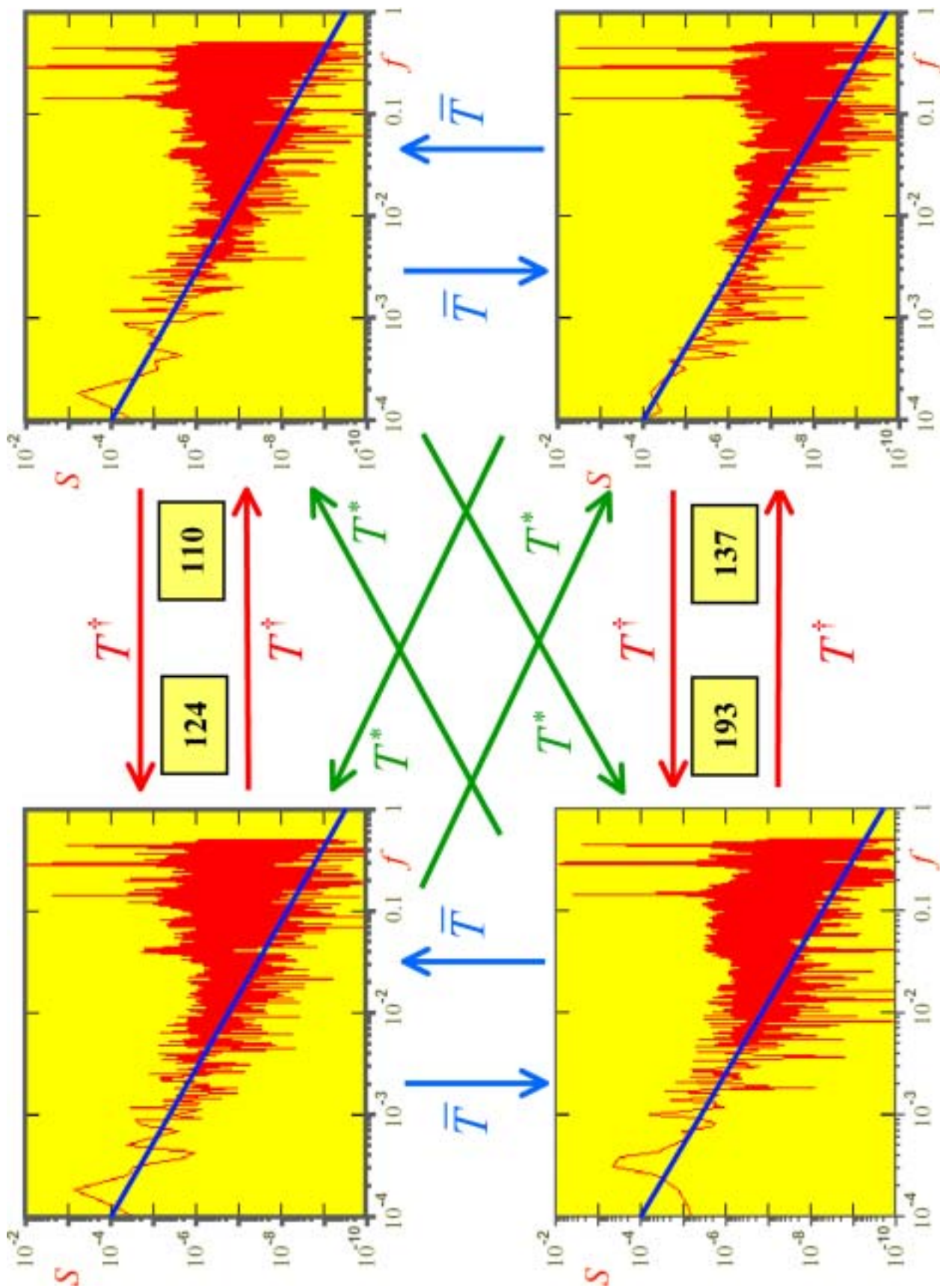


Fig. 24. The power spectrum of four global equivalent rules [110], [124], [137], and [193] capable of *universal computation* all exhibit a $1/f$ power-frequency characteristics.

an illustration, we plot χ_{14}^4 in Fig. 23 (top) and note that indeed there are four points, labeled ①, ②, ③, and ④, which lie precisely on the main diagonal, and the coordinates of these four points are precisely those identified earlier in Fig. 22, as expected. It is even more illuminating to examine the *time-4 map* $\rho_4[14]$ of [14], shown in the bottom of Fig. 23. This is a map showing $\rho_{n-4} \mapsto \rho_n$, i.e. only every fourth iterates of χ_{14}^1 are printed. Observe that, by definition, all points of χ_{14}^4 must lie on the 16 parallel lines of slope $\beta = 2^4 = 16$ for attractor 1, and $\beta = 2^{-4} = 1/16$ for attractor 2.

Observe that although we were able to identify the precise location of the four period-4 points, we would not have undertaken the time-consuming procedure had we not known that a *period-4 point* must exist for both Bernoulli rules [14] and [81]. The *power-spectrum* therefore provides valuable clues on what to look for.

6.2. Turing-universal rules: $\{[110], [124], [137], [193]\}$ exhibit $1/f$ power-frequency characteristics

A careful examination of the power spectrum of all 256 rules in Table 2 reveals that the four globally-equivalent *Turing universal* rules [110], [124], [137], and [193], and only these four rules, exhibit a $1/f$ power-frequency characteristics with a slope equal to approximately -1.5 , as exhibited in Fig. 24 [Schroeder, 1991]. This interesting observation suggests that there might exist a fundamental relationship between universal computation and the ubiquitous $1/f$ phenomena.

7. Concluding Remarks

We have completely characterized the long-term (time-asymptotic) behaviors of 206 one-dimensional CA rules with three inputs. Each CA rule can have several *attractors* and *invariant* orbits. A single *randomly* chosen initial state (configuration) is used as a probe to determine uniquely the precise characteristics of the attractor whose basin of attraction contains the “probing” random configuration.

A CA rule $[N]$ is either *bilateral* (when $T^\dagger[N] = N$), or *nonbilateral*. It can be either *invertible* (when its forward and backward time-1 maps are symmetrical with respect to the main diagonal) or *noninvertible*.

There are 45 *invertible* and 24 *noninvertible period-1* rules. Each *period-1* rule generally has a continuum of *period-1* attractors (as $I \rightarrow \infty$), clustered along the main diagonal. Among the *period-1* rules, there are 12 rules which always tend to the homogeneous “0” attractor, and another 12 rules which always tend to the homogeneous “1” attractor, regardless of the initial state (configuration), except for the *isles of Eden* states possessed by [40], [96], [235], and [249].

There are 17 *invertible period-2* rules all of which are *bilateral*. There are also eight *noninvertible period-2* rules, all of which are *nonbilateral*. Each *period-2* rule generally has a continuum of *period-2* attractors (as $I \rightarrow \infty$), clustered symmetrically with respect the main diagonal.

There are four *nonbilateral period-3* rules which can be either *invertible* or *noninvertible*.

There are 112 Bernoulli rules whose asymptotic behavior is completely characterized by a σ_τ -shifting rule.

The *period-4* attractor exhibited by [14] and [81] represents a very interesting *bifurcation* point separating two distinct attractors that warrant further in-depth analysis.

The remaining 50 rules consist of 18 *noninvertible* but *bilateral* rules (listed in Table 17) and 32 *noninvertible* and *nonbilateral* rules (listed in Table 18). The qualitative long-term dynamics of these rules will be studied in Part V.

An in-depth analysis on the characterizations of the long-term behaviors of these rules represents challenging future research problems. By invoking the *global equivalence* principle developed in [Chua *et al.*, 2004], the above list of 50 currently intractable rules reduces to the study of only 10 *noninvertible* but *bilateral* rules and only eight *noninvertible* and *nonbilateral* rules.

A compendium of the characteristic properties and relevant data of all 256 CA rules are collected in Table 19. Except for the 18 rules listed in Table 17, the *attractors* of all *bilateral* rules have been completely characterized and annotated in appropriate columns of Table 19. In addition, all *invertible attractors* of CA rules are completely characterized. Such attractors are closely related to the *time-reversal* concept from physics, and will be discussed in-depth in Part V.

It is important to emphasize that *Table 19* can be used to *predict*, by inspection, the global *asymptotic dynamics* (as $t \rightarrow \infty$) from *any* initial state (configuration) belonging to *any* robust attractor

Table 17. 18 *Noninvertible bilateral* rules.

\mathcal{E}_m^κ	N	$T^\dagger[N]$	$\overline{T}[N]$	$T^*[N]$	κ
\mathcal{E}_3^2	18	18	183	183	2
\mathcal{E}_4^2	22	22	151	151	2
\mathcal{E}_{18}^2	54	54	147	147	2
\mathcal{E}_{24}^2	73	73	109	109	2
\mathcal{E}_{26}^2	90	90	165	165	2
\mathcal{E}_6^3	105	105	105	105	3
\mathcal{E}_{32}^2	122	122	161	161	2
\mathcal{E}_{33}^2	126	126	129	129	2
\mathcal{E}_{37}^2	146	146	182	182	2
\mathcal{E}_7^3	150	150	150	150	3

Table 18. 32 *Noninvertible nonbilateral* rules.

\mathcal{E}_m^κ	N	$T^\dagger[N]$	$\overline{T}[N]$	$T^*[N]$	κ
\mathcal{E}_7^2	26	82	167	181	2
\mathcal{E}_9^2	30	86	135	149	2
\mathcal{E}_{15}^2	41	97	107	121	2
\mathcal{E}_{17}^2	45	101	75	89	2
\mathcal{E}_{21}^2	60	102	195	153	2
\mathcal{E}_{29}^2	106	120	169	225	2
\mathcal{E}_{31}^2	110	124	137	193	2
\mathcal{E}_{39}^2	154	210	166	180	2

Table 19. Summary of characteristic properties and identification data for 256 CA rules.

N	\mathcal{E}_m^κ	S_m^w	Period k			σ_τ -shift		Bilateral		Invertible		Table Index
			1	2	3	σ	τ	Yes	No	Yes	No	
0	\mathcal{E}_1^I	S_0^I	X					X		X		3, 5
1	\mathcal{E}_2^I	S_1^I		X				X		X		7
2	\mathcal{E}_3^I	S_1^I				1	1		X	X		10
3	\mathcal{E}_4^I	S_2^I				-1	2		X		X	10
4	\mathcal{E}_5^I	S_1^I	X					X		X		3
5	\mathcal{E}_6^I	S_2^I		X				X		X		7
6	\mathcal{E}_7^I	S_2^I				2, -2	2, 2				X	11
7	\mathcal{E}_7^I	S_3^I				-1	2		X	X		10
8	\mathcal{E}_8^I	S_1^I	X					X		X		3, 5
9	\mathcal{E}_2^I	S_2^I				-2, 2	2, 3		X		X	11
10	\mathcal{E}_9^I	S_2^I				1	1		X	X		10
11	\mathcal{E}_{10}^I	S_3^I				-1, 1	1, 1		X	X		10
12	\mathcal{E}_{11}^I	S_2^I	X					X		X		4
13	\mathcal{E}_{12}^I	S_3^I	X					X		X		4
14	\mathcal{E}_{13}^I	S_3^I				1, -1	1, 1		X	X		10
15	\mathcal{E}_{14}^I	S_4^I				-1	1		X	X		10
16	\mathcal{E}_3^I	S_1^I				-1	1		X	X		10
17	\mathcal{E}_4^I	S_2^I				1	2		X	X		10
18	\mathcal{E}_3^I	S_2^I						X		X		17
19	\mathcal{E}_{15}^I	S_3^I		X				X		X		7
20	\mathcal{E}_7^I	S_2^I				-2, 2	2, 2		X		X	11
21	\mathcal{E}_7^I	S_3^I				1	2		X	X		10

N	\mathcal{E}_m^κ	S_m^w	Period k			σ_τ -shift		Bilateral		Invertible		Table Index
			1	2	3	σ	τ	Yes	No	Yes	No	
22	\mathcal{E}_4^I	S_1^I						X			X	17
23	\mathcal{E}_{16}^I	S_4^I		X				X		X		7
24	\mathcal{E}_5^I	S_2^I				-1	1		X	X		10
25	\mathcal{E}_6^I	S_3^I				-1, 3, 2	2, 3, 5		X		X	12
26	\mathcal{E}_7^I	S_3^I							X		X	18
27	\mathcal{E}_1^I	S_4^I				-1, 2	2, 2		X		X	11
28	\mathcal{E}_8^I	S_3^I		X					X		X	8
29	\mathcal{E}_2^I	S_4^I		X					X		X	8
30	\mathcal{E}_9^I	S_4^I							X		X	18
31	\mathcal{E}_7^I	S_5^I				-1	2		X	X		10
32	\mathcal{E}_{17}^I	S_1^I	X					X		X		3, 5
33	\mathcal{E}_{10}^I	S_2^I		X				X		X		7
34	\mathcal{E}_{18}^I	S_2^I				1	1		X	X		10
35	\mathcal{E}_{19}^I	S_3^I				-1, 1	2, 1		X	X		10
36	\mathcal{E}_{11}^I	S_2^I	X					X		X		3
37	\mathcal{E}_{12}^I	S_3^I		X				X		X		7
38	\mathcal{E}_{13}^I	S_3^I				2, 2	2, 2		X		X	11
39	\mathcal{E}_1^I	S_4^I				-1, 2	2, 2		X		X	11
40	\mathcal{E}_{14}^I	S_2^I	X						X	X		3, 5
41	\mathcal{E}_{15}^I	S_3^I							X		X	18
42	\mathcal{E}_{20}^I	S_3^I				1	1		X	X		10
43	\mathcal{E}_{21}^I	S_4^I				-1, 1	1, 1		X	X		10

Table 19. (Continued)

N	\mathcal{E}_m^K	S_m^π	Period k			σ_τ -shift		Bilateral		Invertible		Table Index
			Period k			σ_τ -shift		Bilateral		Invertible		
			1	2	3	σ	τ	Yes	No	Yes	No	
44	\mathcal{E}_{16}^2	S_3^3	X						X			4
45	\mathcal{E}_{17}^2	S_4^3							X			18
46	\mathcal{E}_3^3	S_4^5				1	1		X			10
47	\mathcal{E}_{10}^1	S_5^1				-1, 1	1, 1		X			10
48	\mathcal{E}_{18}^1	S_2^1				-1	1		X			10
49	\mathcal{E}_{19}^1	S_5^1				1, -1	2, 1		X			10
50	\mathcal{E}_{22}^1	S_1^1		X				X				7
51	\mathcal{E}_{23}^1	S_4^1		X				X				7
52	\mathcal{E}_{13}^2	S_3^3				-2, -2	2, 2		X			11
53	\mathcal{E}_1^3	S_4^5				1, -2	2, 2		X			11
54	\mathcal{E}_{18}^2	S_4^3						X				17
55	\mathcal{E}_{15}^1	S_5^1		X				X				7
56	\mathcal{E}_{19}^2	S_3^3				-1, 1	1, 1		X			10
57	\mathcal{E}_{20}^2	S_4^3				-1, 1	1, 1		X			10
58	\mathcal{E}_4^3	S_4^6				1, -1	1, 2		X			10
59	\mathcal{E}_{19}^1	S_5^1				-1, 1	2, 1		X			10
60	\mathcal{E}_{21}^2	S_4^4							X			18
61	\mathcal{E}_6^2	S_5^1				1, -3, -2	2, 3, 5		X			12
62	\mathcal{E}_{22}^2	S_5^3		X		-1, 1	2, 1		X			9, 10
63	\mathcal{E}_4^1	S_6^1				-1	2		X			10
64	\mathcal{E}_8^1	S_1^1		X					X			3, 5
65	\mathcal{E}_2^2	S_2^3				2, -2	2, 3		X			11

Table 19. (Continued)

N	\mathcal{E}_m^K	S_m^π	Period k			σ_τ -shift		Bilateral		Invertible		Table Index
			1	2	3	σ	τ	Yes	No	Yes	No	
88	\mathcal{E}_{25}^2	S_3^3				-1, -2, 3	1, 2, 3		X		X	12
89	\mathcal{E}_{17}^2	S_4^3							X		X	18
90	\mathcal{E}_{26}^2	S_4^4						X			X	17
91	\mathcal{E}_{12}^2	S_5^3			X			X		X		7
92	\mathcal{E}_5^3	S_4^5	X						X		X	4
93	\mathcal{E}_{12}^1	S_5^1		X					X		X	4
94	\mathcal{E}_{27}^2	S_5^3	X					X		X		3
95	\mathcal{E}_6^1	S_6^1			X			X		X		7
96	\mathcal{E}_{14}^2	S_2^2	X						X		X	3, 5
97	\mathcal{E}_{15}^2	S_3^3							X		X	18
98	\mathcal{E}_{19}^2	S_3^3				1, -1	1, 1		X		X	10
99	\mathcal{E}_{20}^2	S_4^3				1, -1	1, 1		X		X	10
100	\mathcal{E}_{16}^2	S_3^3	X						X		X	4
101	\mathcal{E}_{17}^2	S_4^3							X		X	18
102	\mathcal{E}_{21}^2	S_4^4							X		X	18
103	\mathcal{E}_6^3	S_5^3				-1, 3, 2	2, 3, 5		X		X	12
104	\mathcal{E}_{28}^2	S_3^2	X					X		X		3
105	\mathcal{E}_6^3	S_4^7						X			X	17
106	\mathcal{E}_{29}^2	S_4^2							X		X	18
107	\mathcal{E}_{15}^2	S_3^2							X		X	18
108	\mathcal{E}_{30}^2	S_4^3		X				X		X		7
109	\mathcal{E}_{24}^2	S_5^2						X			X	17

N	\mathcal{E}_m^K	S_m^π	Period k			σ_τ -shift		Bilateral		Invertible		Table Index
			1	2	3	σ	τ	Yes	No	Yes	No	
110	\mathcal{E}_{31}^2	S_5^3							X		X	18
111	\mathcal{E}_2^2	S_6^2				-2, 2	2, 3		X		X	11
112	\mathcal{E}_{20}^1	S_3^1				-1	1		X	X		10
113	\mathcal{E}_{21}^1	S_4^2				1, -1	1, 1		X	X		10
114	\mathcal{E}_4^3	S_4^5				-1, 1	1, 2		X	X		10
115	\mathcal{E}_{19}^1	S_5^1				1, -1	2, 1		X	X		10
116	\mathcal{E}_3^3	S_4^6				-1	1		X	X		10
117	\mathcal{E}_{10}^1	S_5^1				1, -1	1, 1		X	X		10
118	\mathcal{E}_{22}^2	S_5^3			X	1, -1	2, 1		X	X	X	9, 10
119	\mathcal{E}_4^1	S_6^1				1	2		X	X		10
120	\mathcal{E}_{29}^2	S_4^3							X		X	18
121	\mathcal{E}_{15}^2	S_5^2							X		X	18
122	\mathcal{E}_{32}^2	S_5^3						X			X	17
123	\mathcal{E}_{10}^2	S_6^2		X				X		X		7
124	\mathcal{E}_{31}^2	S_5^3							X		X	18
125	\mathcal{E}_2^2	S_6^2				2, -2	2, 3		X		X	11
126	\mathcal{E}_{33}^2	S_6^3						X			X	17
127	\mathcal{E}_2^1	S_7^1			X			X		X		7
128	\mathcal{E}_{26}^1	S_1^1	X					X		X		3, 5
129	\mathcal{E}_{33}^2	S_2^3						X			X	17
130	\mathcal{E}_{34}^2	S_2^2				1	1		X	X		10
131	\mathcal{E}_{22}^2	S_3^3			X	-1, 1	2, 1		X	X	X	9, 10

Table 19. (Continued)

N	\mathcal{E}_m^κ	S_m^π	Period k			Σ_{τ} -shift		Bilateral		Invertible		Table Index
			Period k			σ	τ	Yes	No	Yes	No	
			1	2	3							
132	\mathcal{E}_{35}^2	S_2^2	X					X		X		3
133	\mathcal{E}_{27}^2	S_3^2	X					X		X		3
134	\mathcal{E}_{36}^2	S_3^2				2, -2	2, 2		X		X	11
135	\mathcal{E}_9^2	S_4^2							X		X	18
136	\mathcal{E}_{27}^1	S_2^1	X						X	X		3, 5
137	\mathcal{E}_{31}^2	S_3^2							X		X	18
138	\mathcal{E}_{28}^1	S_3^1				1	1		X	X		10
139	\mathcal{E}_3^3	S_4^6				1	1		X	X		10
140	\mathcal{E}_{29}^1	S_3^1	X						X		X	4
141	\mathcal{E}_5^3	S_4^3	X						X		X	4
142	\mathcal{E}_{30}^1	S_4^2				1, -1	1, 1		X	X		10
143	\mathcal{E}_{13}^1	S_5^1				1, -1	1, 1		X	X		10
144	\mathcal{E}_{34}^2	S_2^2				-1	1		X	X		10
145	\mathcal{E}_{22}^2	S_3^2			X	1, -1	2, 1		X	X	X	9, 10
146	\mathcal{E}_{37}^2	S_3^2						X			X	17
147	\mathcal{E}_{18}^2	S_4^2						X			X	17
148	\mathcal{E}_{36}^2	S_3^2				-2, 2	2, 2		X		X	11
149	\mathcal{E}_9^2	S_4^2							X		X	18
150	\mathcal{E}_7^3	S_4^3						X			X	17
151	\mathcal{E}_4^2	S_5^2							X		X	17
152	\mathcal{E}_{38}^2	S_1^2				-1	1		X	X		10
153	\mathcal{E}_{21}^2	S_4^2							X		X	18

Table 19. (Continued)

N	\mathcal{E}_m^K	S_m^n	Period k			σ_{τ} -shift		Bilateral		Invertible		Table Index
			Period k			σ_{τ} -shift		Bilateral		Invertible		
			1	2	3	σ	τ	Yes	No	Yes	No	
198	\mathcal{E}_{40}^2	S_4^1		X					X		X	8
199	\mathcal{E}_8^2	S_5^3		X					X		X	8
200	\mathcal{E}_{37}^1	S_3^1	X					X		X		3
201	\mathcal{E}_{30}^2	S_4^3		X				X		X		7
202	\mathcal{E}_8^3	S_4^3	X						X		X	4
203	\mathcal{E}_{16}^2	S_5^3	X						X		X	4
204	\mathcal{E}_{38}^1	S_4^1	X					X		X		3
205	\mathcal{E}_{24}^1	S_5^1	X					X		X		3
206	\mathcal{E}_{29}^1	S_5^1	X						X		X	4
207	\mathcal{E}_{11}^1	S_6^1	X						X		X	4
208	\mathcal{E}_{28}^1	S_3^1				-1	1		X		X	10
209	\mathcal{E}_3^1	S_4^1				-1	1		X		X	10
210	\mathcal{E}_{39}^2	S_4^3							X		X	18
211	\mathcal{E}_{13}^2	S_5^3				-2, -2	2, 2		X		X	11
212	\mathcal{E}_{39}^1	S_4^2				-1, 1	1, 1		X		X	10
213	\mathcal{E}_{13}^1	S_5^1				-1, 1	1, 1		X		X	10
214	\mathcal{E}_{16}^2	S_5^2				-2, 2	2, 2		X		X	11
215	\mathcal{E}_7^2	S_6^2				-2, 2	2, 2		X		X	11
216	\mathcal{E}_8^1	S_4^3	X						X		X	4
217	\mathcal{E}_{16}^2	S_5^3	X						X		X	4
218	\mathcal{E}_{41}^2	S_5^3	X					X			X	3
219	\mathcal{E}_{11}^2	S_6^3	X					X			X	3

Table 19. (Continued)

N	\mathcal{E}_m^κ	S_m^π	Period k			σ_τ -shift		Bilateral	Invertible		Table Index
			1	2	3	σ	τ		Yes	No	
220	\mathcal{E}_{29}^I	S_5^I	X						X		4
221	\mathcal{E}_{11}^I	S_6^I	X						X		4
222	\mathcal{E}_{35}^2	S_6^2	X					X			3
223	\mathcal{E}_5^I	S_7^I	X					X	X		3
224	\mathcal{E}_{33}^I	S_3^I	X						X		3, 5
225	\mathcal{E}_{29}^2	S_4^3						X		X	18
226	\mathcal{E}_9^3	S_4^6				1, -1	1, 1	X	X		10
227	\mathcal{E}_{19}^2	S_5^3				-1, 1	1, 1	X	X		10
228	\mathcal{E}_8^3	S_4^3	X					X		X	4
229	\mathcal{E}_{25}^2	S_5^3				-1, -2, 3	1, 2, 3	X		X	12
230	\mathcal{E}_{38}^2	S_5^3				-1	1	X	X		10
231	\mathcal{E}_5^2	S_6^3				-1	1	X	X		10
232	\mathcal{E}_{39}^I	S_4^I	X					X	X		3
233	\mathcal{E}_{28}^2	S_5^2	X					X	X		3
234	\mathcal{E}_{33}^I	S_5^I	X					X	X		3, 6
235	\mathcal{E}_{14}^2	S_6^2	X					X	X		3, 6
236	\mathcal{E}_{37}^I	S_5^I	X					X	X		3
237	\mathcal{E}_{23}^2	S_6^2	X					X	X		3

N	\mathcal{E}_m^κ	S_m^π	Period k			σ_τ -shift		Bilateral	Invertible		Table Index
			1	2	3	σ	τ		Yes	No	
238	\mathcal{E}_{27}^I	S_6^I	X						X		3, 6
239	\mathcal{E}_8^I	S_7^I	X						X		3, 6
240	\mathcal{E}_{34}^I	S_4^I				-1	1		X		10
241	\mathcal{E}_{20}^I	S_5^I				-1	1		X		10
242	\mathcal{E}_{32}^I	S_5^I				-1	1		X		10
243	\mathcal{E}_{18}^I	S_6^I				-1	1		X		10
244	\mathcal{E}_{28}^I	S_5^I				-1	1		X		10
245	\mathcal{E}_9^I	S_6^I				-1	1		X		10
246	\mathcal{E}_{34}^2	S_6^2				-1	1		X		10
247	\mathcal{E}_3^I	S_7^I				-1	1		X		10
248	\mathcal{E}_{33}^I	S_5^I	X						X		3, 6
249	\mathcal{E}_{14}^2	S_6^2	X						X		3, 6
250	\mathcal{E}_{31}^I	S_6^I	X					X	X		3, 6
251	\mathcal{E}_{17}^I	S_7^I	X					X	X		3, 6
252	\mathcal{E}_{27}^I	S_6^I	X						X		3, 6
253	\mathcal{E}_8^I	S_7^I	X						X		3, 6
254	\mathcal{E}_{26}^I	S_7^I	X					X	X		3, 6
255	\mathcal{E}_I^I	S_8^I	X					X	X		3, 6

Note :

1. The four rules $\{62, 118, 131, 145\}$ (shaded in yellow in columns N and \mathcal{E}_m^κ) belonging to \mathcal{E}_{22}^2 possess not only *non-invertible* period-3 attractors but also *invertible* Bernoulli rules.
2. The Rules with no data provided in the “period k ” and “ σ_τ -shift” columns have very large periods.

listed in this table. Moreover, for the six “orbit-invariant” rules [15], [51], [85], [170], [204] and [240], Table 19 actually *predicts* their *complete* dynamical evolutions *over all times*, i.e. *both transient and steady state regimes*, and *for all initial states*. This follows by default because all orbits of these six rules are *invariant*, and therefore do not have a transient regime.

The *main* result of this paper is no doubt the gallery of *graphs* of both *forward* and *backward time-1 maps* of all 256 CA rules. Since these graphs do *not* depend on the *initial state* (configuration), they completely characterized the *long-term asymptotic behaviors* of all rules, including the 50 complex rules listed in Tables 17 and 18. They are, in some sense, the *generalized Green's functions* for *cellular automata*.

Perhaps the most intriguing unsolved problem is to discover the relationship between the four *Turing-universal rules* [110], [124], [137], and [193], and the ubiquitous $1/f$ power spectrum exhibited by these four rules, and only these rules.

Acknowledgments

This paper is supported in part by the MURI contract no. N00014-03-1-0698, the DURINT contract no. N00014-01-0741, the MARCO Microelectronics Advances Research Corporation FENA Award no. 442521/WK57015, and the NSF grant CHE-0103447.

References

- Alligood, K. T., Sauer, T. D. & Yorke, J. A. [1996] *Chaos: An Introduction to Dynamical Systems* (Springer-Verlag NY).
- Billingsley, P. [1978] *Ergodic Theory and Information* (Robert Keirger Publishing Company, Huntington).
- Chua, L. O. & Kang, S. M. [1977] “Section-wise piecewise-linear functions: Canonical representation, properties and applications,” *Proc. IEEE* **65**, 915–929.
- Chua, L. O., Desoer, C. A. & Kuh, E. S. [1987] *Linear and Nonlinear Circuits* (McGraw-Hill, NY).
- Chua, L. O. [1998] *CNN: A Paradigm for Complexity* (World Scientific, Singapore).
- Chua, L. O. & Roska, T. [2002] *Cellular Neural Networks and Visual Computing* (Cambridge University Press).
- Chua, L. O., Yoon, S. & Dogaru, R. [2002] “A nonlinear dynamics perspective of Wolfram's new kind of science. Part I: Threshold of complexity,” *Int. J. Bifurcation and Chaos* **12**, 2655–2766.
- Chua, L. O., Sbitnev, V. I. & Yoon, S. [2003] “A nonlinear dynamics perspective of Wolfram's new kind of science. Part II: Universal neuron,” *Int. J. Bifurcation and Chaos* **13**, 2377–2491.
- Chua, L. O., Sbitnev, V. I. & Yoon, S. [2004] “A nonlinear dynamics perspective of Wolfram's new kind of science. Part III: Predicting the unpredictable,” *Int. J. Bifurcation and Chaos* **14**, 3689–3820.
- Devaney, R. L. [1992] *A First Course in Chaotic Dynamic Systems: Theory and Experiment* (Addison-Wesley, Reading, MA).
- Hirsch, M. W. & Smale, S. [1974] *Differential Equations, Dynamical Systems, and Linear Algebra* (Academic Press, NY).
- Moore, E. F. [1962] “Machine models of self-reproduction,” *Proc. Symp. Appl. Math.* **14**, 17–33.
- Nagashima, H. & Baba, Y. [1999] *Introduction to Chaos* (Institute of Physics Publishing, Bristol).
- Niven, I. [1967] *Irrational Numbers* (The Mathematical Association of America, NJ).
- Poincare, H. [1897] *Les Methodes Nouvelles de la Mechanique Celeste*, Vol. I and II (Gauthier-Villars, Paris).
- Schroeder, M. [1991] *Fractals, Chaos, Power Laws* (W. H. Freeman and Company, NY).
- Shilnikov, L. P., Shilnikov, A. L., Turaev, D. V. & Chua, L. O. [1998] *Methods of Qualitative Theory in Nonlinear Dynamics: Part I* (World Scientific, Singapore).
- Tang, Y. S., Mees, A. I. & Chua, L. O. [1983] “Synchronization and chaos,” *IEEE Trans. Circuits Syst.* **9**, 620–626.
- Wiener, N. [1958] *Nonlinear Problems in Random Theory* (John Wiley, NY).
- Wolfram, S. [2002] *A New Kind of Sciences* (Wolfram Media, Champaign Illinois, USA).